



HAL
open science

Shape, rhythms and growth heterogeneities of a leaf: unfurling and nutation of *Averrhoa carambola*

Mathieu Rivière

► **To cite this version:**

Mathieu Rivière. Shape, rhythms and growth heterogeneities of a leaf: unfurling and nutation of *Averrhoa carambola*. Physics [physics]. Université Sorbonne Paris Cité, 2017. English. NNT: 2017USPCC040 . tel-01907869

HAL Id: tel-01907869

<https://theses.hal.science/tel-01907869>

Submitted on 29 Oct 2018

HAL is a multi-disciplinary open access archive for the deposit and dissemination of scientific research documents, whether they are published or not. The documents may come from teaching and research institutions in France or abroad, or from public or private research centers.

L'archive ouverte pluridisciplinaire **HAL**, est destinée au dépôt et à la diffusion de documents scientifiques de niveau recherche, publiés ou non, émanant des établissements d'enseignement et de recherche français ou étrangers, des laboratoires publics ou privés.

Thèse de doctorat de Physique

Shape, rhythms and growth heterogeneities of a leaf

*Unfurling and nutation of *Averrhoa carambola**

Par Mathieu Rivière

Dirigée par Stéphane Douady, Alexis Peaucelle & Julien Derr

Soutenue publiquement le 20 novembre 2017 devant le jury composé de

Présidente	Pr. Naomi Nakayama	University of Edinburgh
Rapporteur	Dr. Olivier Pouliquen	CNRS–Université d’Aix-Marseille
Rapporteur	Pr. Richard Smith	Max Planck Institute
Examineur	Pr. Atef Asnacios	Université Paris Diderot
Directeur de thèse	Dr. Stéphane Douady	CNRS–Université Paris Diderot
Co-directeur de thèse	Dr. Alexis Peaucelle	INRA
Co-directeur de thèse	Dr. Julien Derr	Université Paris Diderot



This work is licensed under a Creative Commons
Attribution-NonCommercial-ShareAlike 4.0 International License.



Acknowledgements

Voilà ! Il aura fallu trois ans pour mener à bien cette thèse. Mais trois ans et un bonhomme ne suffisent en fait pas. Si, à la fin, j'ai bien tenu le crayon seul, de nombreuses personnes ont contribué à façonner cette thèse d'une manière ou d'une autre. Je veux ici les remercier, toutes et tous, pour leur concours indispensable à ces travaux et à cette tranche de vie !

Je voudrais commencer par remercier mes directeurs de thèse. Ils étaient trois, ce qui peut paraître beaucoup. Pourtant, il aurait été difficile de faire ne serait-ce qu'avec un de moins !

Tout a commencé avec Julien qui, fin 2011, nous racontait dans l'un de ses cours qu'il travaillait sur la forme et la posture des feuilles. Merci donc, en premier lieu, de m'avoir fait découvrir la physique des plantes et des formes. Merci à toi de n'avoir jamais compté ton temps pour m'aider, de l'enfer du debug à celui de la rédaction entre autres, et de m'avoir toujours accueilli avec un grand sourire ! Merci de m'avoir toujours pris dans tes valises, à Clermont ou à Grenoble. Tu m'as toujours encouragé à aller plus loin et à peaufiner mon travail. C'est aussi à toi que je dois mon apprentissage éclair de la langue nippone ! Bref, domo arigato gozaimasu Julien-sensei !

J'ai ensuite rencontré Stéphane lors de mon stage de M2. J'aimerais te remercier, si ça a un sens, de t'intéresser à autant de choses et de les étudier de façon passionnante et amusante. Merci d'avoir été si généreux, en partageant avec moi tes nombreuses questions, tes idées mais surtout ton goût pour l'observation et la description. Merci de m'avoir freiné dans mes fuites en avant, vers plus de précision, de détails, ... et de m'avoir rappelé le sens de l'expérience et la beauté des résultats simples. Merci aussi d'avoir été attentif et attentionné, d'avoir souvent résolu les doutes et la démotivation en quelques mots. Je n'ai pas encore décidé si je devais te remercier pour m'avoir fait tomber dans Naruto ou pas, mais merci pour tout le reste !

Enfin, j'ai rencontré Alexis pendant la construction de mon projet de thèse. Merci pour tout ce que tu m'as transmis sur la paroi, l'AFM et les immunos. Grâce à ta patience, je sais enfin ce qu'est un homogalacturonan ! Merci aussi pour toute

ton aide et le travail que tu abattu sur ces fronts-là. Merci aussi de m'avoir emmené à Cambridge avec toi et d'avoir veillé à ce que tout se passe bien sur place, au labo et pendant notre temps libre. Notre travail — énergique ! — là-bas a été plaisant et gratifiant. J'y ai trouvé un nouveau souffle à un moment où ma motivation n'était pas au plus haut. Merci enfin d'avoir tout fait pour me rassurer, me faire connaître un maximum de choses et de personnes !

Merci à vous trois pour votre simplicité, votre gentillesse et votre enthousiasme inusable ! J'ai beaucoup apprécié travailler avec vous. Grâce à vous j'ai beaucoup appris et j'ai aussi passé de très bons moments.

I would like to thank all the members of the jury: Naomi Nakayama, Olivier Pouliquen, Richard Smith and Atef Asnacios. They have accepted to read this manuscript unaware of the numerous delays that would come. I am thus thankful for their kind patience and understanding. I have appreciated their detailed reports very much. This has been very helpful in the process of preparing the defence but also in my personal thinking about my research. Thanks to their diverse knowledge and competences, the discussion has been a truly enriching and enjoyable moment.

Je remercie chaleureusement Emmanuel de Langre et Olivier Hamant qui, en prenant part à mon comité de thèse, ont suivi mes travaux ces trois dernières années. Leur regard extérieur m'a beaucoup apporté scientifiquement — en me permettant d'affiner mes questionnements et ma démarche — mais aussi humainement. Merci pour votre aide et votre bienveillance !

I would like to thank the people from the Center for Research and Interdisciplinarity. Their support has made this thesis possible. I would like to thank particularly David Taresté, Sofie Leon and Elodie Kaslikowski for their assistance and follow-up, notably in the last moments of my thesis.

Merci à Bruno Moulia, Nicole Brunel et Valérie Légué et à toute l'équipe du laboratoire PIAF de nous avoir accueillis quelques jours, à Clermont-Ferrand, Julien et moi. A leur contact nous avons pu apprendre les rudiments de l'histologie végétale et s'essayer à l'art de la coupe à main levée ou au microtome. Merci aussi à Bruno pour les discussions intéressantes et toujours encourageantes sur le retournement des feuilles !

Many thanks to Elliot Meyerowitz who has invited me to work and present my research in his team at the Sainsbury Laboratory in Cambridge. There, I have been able to perform the immunolabelling experiments. A million thanks to Raymond

Wightman who has kindly arranged every detail of my two visits and took time to explain me and help me with the Cryo-SEM, the confocal and the Raman. Thank you also for sharing your enthusiasm about Wetherspoons with me!

Merci à Franck Hétroy-Wheeler, Julien Pansiot et Florence Bertails-Descoubes au LJK à Grenoble avec qui une collaboration a démarré en 2016 pour les mesures d'élongation en 3D. Merci pour leur temps, leur accueil et leur investissement. Je remercie aussi tous les étudiants qui se sont impliqués dans ce projet "Carambole".

Vient maintenant le tour du MSC, mon laboratoire de ces presque quatre dernières années. Tout d'abord, un immense merci à tous ceux qui se sont occupés des plantes quand plus personne n'était là pour elles. Leur contribution à ce travail a été cruciale ! Je pense notamment à Michael qui les a si souvent sauvées ! Merci à Cyprien d'avoir pris le temps de me mettre sur les rails pour les notions et calculs de mécanique. J'espère que toutes les idées qu'on a discutées pourront être mises en place à terme. Merci à Etienne pour les nombreuses discussions sur les plantes, la science, la thèse et les postdocs. Merci à Marc, notamment pour son esprit de solidarité entre utilisateurs de Arch Linux. Merci à Sylvain de n'avoir jamais cédé à ses envies de déforestation de la 811 pendant ma thèse.

Je voudrais aussi adresser mes remerciements à Arnaud, Yann et Laurent qui nous ont aidés pour la construction de la "cage" d'acquisition 3D et d'autres projets un peu moins encombrants. Merci à Wilfrid sans qui je serais encore en train d'installer Arch sur mon PC. Merci aussi à Maéva, Nadine, Carole, Lucie et Marlène pour leur patience et leur aide inestimable dans toutes les tâches administratives.

Plus généralement, je remercie toutes les personnes que j'ai eu le plaisir de côtoyer au MSC. Merci de faire du MSC c'est endroit si particulier. C'était une véritable chance d'y travailler !

Merci à tous celles et ceux qui ont partagé mon quotidien au labo, c'est à dire la 911 et ses satellites. Merci aux membres historiques — Claire, Sébastien et Amandine — pour leur accueil lorsque j'étais encore un jeune stagiaire de M2. Il y avait aussi Olivier, dit "Chou-fleur", ses interminables rouleaux de calculs, son bureau toujours impeccablement rangé et sa passion pour les élastiques. Caroline qui a sans doute fait de notre salle le labo de physique au fumet le plus agréable de ce monde. Renaud, ses facéties et ses empilements de canettes. Romain Pousse, ma référence sociologie et mercato, célèbre pour sa capuche et son bonnet mais surtout pour sa capuche par dessus son bonnet. Solène, qui a bien pris soin de mes BD et qui m'a fait découvrir certains plaisirs simples de la vie comme les romans de Cavanna ou l'élevage de méduses en laboratoire. Tanguy, ses fulgurances géniales et

nos nombreuses conversations — intéressantes et soutenues — en japonais qui m’ont permis de maintenir mon niveau, voire peut-être même de l’améliorer. Antoine, aussi doué pour rebondir sur la moindre référence à Kaamelott que dans l’art délicat de relancer les discussions à table. Raphaël, l’homme aux multiples casquettes : confection de skates, management de stagiaires, vente en gros et demi-gros de pasta italienne ou de riz japonais, ... Paul, dont la créativité se manifeste de nombreuses façons, et notamment par sa manière de saluer si particulière et sans cesse renouvelée. Quentin, dont les quiches — et la modestie — sont sans égales et m’ont marqué à tout jamais. Je n’oublie pas sa jolie moustache. Il y avait aussi Babak, Julien P. et Adrien que j’aurais aimé côtoyer plus longtemps !

Il y a enfin eu tous les stagiaires qui sont passés par là — notamment Clara avec qui j’ai pu un temps travailler — et qui ont tous participé à la bonne ambiance de la mezzanine.

Il y aurait naturellement beaucoup de choses à dire encore. On a beaucoup travaillé (surtout Tanguy), mais on a aussi beaucoup ri. Je crois que sans vous ça aurait été un peu moins bien, alors merci d’avoir été là !

Pour finir, je veux évidemment remercier toutes les personnes qui n’étaient pas au labo mais qui m’ont accompagné tout au long de l’aventure. Je pense à tous mes amis, précieuses rencontres faites aux différentes étapes de mon parcours. Ceux des premiers temps, à Villefranche, pour la plupart rencontrés aux alentours du Tricot. A Lyon, la fameuse bande à Guillemot et ceux, non moins fameux, de la Martin. A Paris, la fine équipe du magistère de P7 et enfin, last but not least, les amis du M2. Mention spéciale à Romain “Bobby D” Grasset, avec qui j’ai partagé un appartement et une passion pour la saucisse au Roquefort.

Mention très spéciale à Marie. Merci pour ta présence à mes côtés et ton soutien indispensables. Merci à toute ma famille pour leurs encouragements et leur intérêt pour ce que je faisais. Enfin, merci à mes parents pour tout, tout simplement.

Merci à toutes et tous ! Thank you all!

Abstract

Plant growth—the irreversible volume increase of a cell or an organ—remains an exciting biological puzzle. Growth is essential to the shape regulation of the developing organ. It is also the key for every plant, developing or mature, to adapt to its environment.

The cellular mechanisms of plant growth rely on a competition between the inner pressure of the cell and the elastic properties of the cell wall. Heterogeneities of these mechanical properties across the tissue result in differential growth and eventually lead to growth motions at higher scales. These macroscopic motions can thus be read as an outward signal of the cellular mechanisms underlying shape regulation and growth itself. Here, we propose to take benefit from the intimate link between growth and its related motions to gain a new insight on growth through a multiscale approach, from the organ to the cell wall level.

The compound leaves of *Averrhoa carambola* display two marked motions—unfurling and nutation—that are widespread among developing leaves. Our approach consists in assuming that different phases of the motion correspond to different growth status within the tissues of the organ.

In the first place, we show that the shape of the leaf results from an active regulation, especially of its macroscopic mechanical properties. The kinematics of the two latter motions are then compared to the associated growth. Doing so, we put forward the specific patterns of growth and growth heterogeneities underlying the development of the leaf. Based on these findings, we build a kinematic model for nutation which—accordingly with previous findings—suggests the occurrence of local contractions during growth. The mechanics of the cell wall are then investigated. Our results suggest that spatial heterogeneities of cell wall rigidity within the leaf are correlated with the direction of the nutation. Finally, immunohistochemistry reveals heterogeneities in the repartition of de-methylesterified pectins within the leaf, possibly consistent with the direction of nutation.

Résumé

Titre français : Forme, rythmes et hétérogénéités de croissance d'une feuille

Sous-titre français : Déroulement et nutation chez *Averrhoa carambola*

Chez les végétaux, la croissance est essentielle à la régulation de la forme de tout organe en développement mais aussi à l'adaptation des organes matures à leur environnement.

A l'échelle de la cellule, la croissance est le résultat de la compétition entre la pression interne de la cellule et la rigidité de sa paroi. Des hétérogénéités de ces propriétés mécaniques à l'échelle du tissu mènent alors à une croissance différentielle puis à des "mouvements de croissance" à l'échelle de l'organe entier. Ces mouvements macroscopiques peuvent alors être interprétés comme une manifestation des processus de croissance microscopiques. Nous proposons dans cette thèse de mettre à profit ce lien intime entre croissance et mouvements afin d'approcher la croissance d'une nouvelle manière : de l'organe à la cellule.

Nos travaux portent sur les feuilles composées d'*Averrhoa carambola* qui montrent deux mouvements typiques des feuilles en croissance : le déroulement et la nutation.

Nous montrons dans un premier temps que la forme de la feuille en croissance est régulée de manière active. Nous étudions ensuite la cinématique du déroulement et de la nutation. Ce faisant, nous mettons en évidence une relation particulière entre croissance et croissance différentielle à partir de laquelle nous construisons ensuite un modèle cinématique de nutation. Conformément à de précédents résultats, ce modèle suggère que la croissance peut s'accompagner de contractions locales. A l'échelle du tissu, la mécanique des parois cellulaires est ensuite étudiée. Nos résultats suggèrent que les hétérogénéités spatiales de rigidité de la paroi sont corrélées à la direction du mouvement de nutation. Enfin, des hétérogénéités de composition de la paroi, possiblement corrélées à la nutation, sont révélées par immunohistochimie.

Contents

1	Introduction	1
1.1	Plant motions: diversity and ubiquity	1
1.1.1	Are plant motions exceptional?	1
1.1.2	Early conceptions about plant motions	4
1.1.3	Classical plant motion nomenclature	6
1.2	Origin of growth motions	8
1.2.1	Differential growth drives the motion	8
1.2.2	Microscopic mechanisms of plant growth	11
1.2.3	A quick picture of the cell wall	14
1.3	Study of plant motions	17
1.3.1	What have we already learnt from plant motions?	17
1.3.2	The classical nomenclature called into question	18
1.4	Problematic and approach	22
2	Description of <i>Averrhoa carambola</i> as a model	23
2.1	General information on <i>Averrhoa carambola</i>	24
2.2	<i>Averrhoa carambola</i> compound leaves	26
2.2.1	Shape and anatomy of the leaves	26
2.2.2	Histology of the rachis	29
2.2.3	Geometrical parametrization	31
2.3	The different motions of the leaf	33
2.3.1	Motions of the growing leaf	33
2.3.2	Motions of the mature leaf	39
2.4	Discussion and conclusion	43
3	Hook shape of the growing leaf	45
3.1	Kinematics of leaf unfurling	47
3.1.1	Experimental approach	47
3.1.2	Bent zone and growth zone	49
3.2	Macroscopic mechanics of the hook	52

3.2.1	Experimental approach	52
3.2.2	Data analysis	55
3.2.3	A first look at shape and self-weight	57
3.2.4	Mechanical properties in time	59
3.2.5	Links with lignification	63
3.3	Discussion and partial conclusion	65
4	Characterizing the nutation motion	71
4.1	Experimental method	72
4.1.1	Quantities of interest	72
4.1.2	Experimental set-up	73
4.1.3	Data analysis	75
4.2	Results	76
4.2.1	Curvature variations and associated differential elongation	76
4.2.2	Relation between elongation and differential elongation	80
4.2.3	Nutation described as an oscillation	86
4.3	Discussion and partial conclusion	96
5	From motions to growth	103
5.1	Growth measurements	103
5.1.1	Experimental protocol	103
5.1.2	Results	106
5.1.3	Impact of projection effects on elongation measurements	109
5.2	Kinematic model of growth and nutation	112
5.2.1	Definition of the growth and nutation model	112
5.2.2	Results	117
5.3	Discussion and partial conclusion	124
6	Towards the microscopic aspects of plant growth	131
6.1	Mechanical heterogeneities within tissues	132
6.1.1	Atomic force microscopy as a tool for plant mechanics	132
6.1.2	Experimental protocol	133
6.1.3	Data analysis	138
6.1.4	Results	140
6.2	Cell wall composition heterogeneities	145
6.2.1	Preliminary results	148
6.3	Discussion and partial conclusion	151
7	Conclusion & prospects	155

Appendices	173
A Graviception, proprioception and hook shape	175
A.1 The graviproprioceptive model	175
A.1.1 Origin of the model	176
A.1.2 A suitable model for <i>Averrhoa carambola</i> ?	177
A.2 Adaptation of the model	177
A.2.1 Definition of the model	177
A.2.2 Growth-dependent parameters	178
A.3 Results	179
B Mechanics of the rachis: additional insights	181
B.1 Viscous deformation of the rachis	181
B.2 Useful calculations	181
C Kinematic model of nutation: useful calculations	185
C.1 Angular amplitude of the motion	185
C.2 Threshold of contraction	186
C.3 Amplitude of the second harmonic term	187

Chapter 1

Introduction

Contents

1.1 Plant motions: diversity and ubiquity	1
1.1.1 Are plant motions exceptional?	1
1.1.2 Early conceptions about plant motions	4
1.1.3 Classical plant motion nomenclature	6
1.2 Origin of growth motions	8
1.2.1 Differential growth drives the motion	8
1.2.2 Microscopic mechanisms of plant growth	11
1.2.3 A quick picture of the cell wall	14
1.3 Study of plant motions	17
1.3.1 What have we already learnt from plant motions?	17
1.3.2 The classical nomenclature called into question	18
1.4 Problematic and approach	22

1.1 Plant motions: diversity and ubiquity

1.1.1 Are plant motions exceptional?

Plants move. This short and simple statement often leads to a delicate mix of contradictory ideas. As a matter of fact, the notion of plant motion is often regarded through the prism of two opposed conceptions. On the one hand, the plant kingdom is usually defined in opposition with the animal kingdom because of the apparent stillness of plants. On the other hand, examples of moving plants come easily to

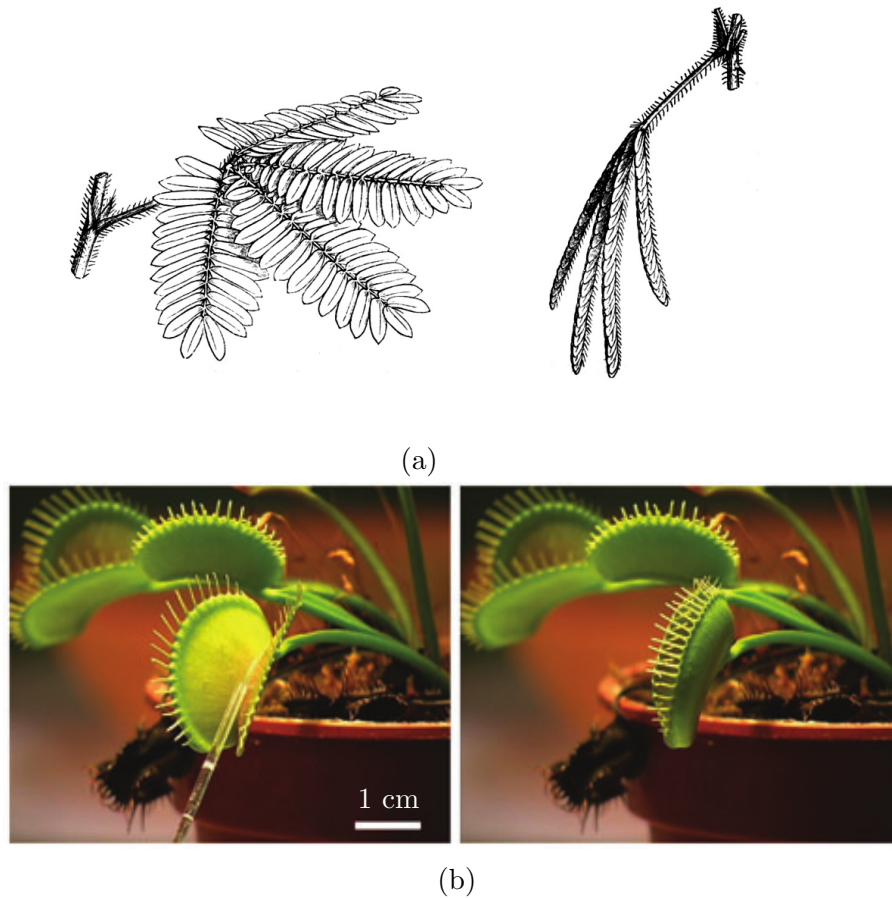


Figure 1.1: **Two examples of well-known plant motions.** (a) *Mimosa pudica*. When touched, the leaves pack against each other in a couple of seconds. If the perturbation is a bit more violent, the entire leaf fall down as pictured here. (Drawings from P.H.W. Taubert's *Leguminosae*, 1891). (b) *Dionaea muscipula* might be the most famous carnivorous plant. The inner part of the trap contains several hairs. If a prey touches at least three of these hairs, the trap closes in less than a second (Forterre, 2013).

mind. Among these examples, the most popular might be the fast motions of carnivorous plants—such as *Dionaea muscipula* also known as the Venus Flytrap—and of the so-called sensitive plant—*Mimosa pudica* (see figure 1.1). The paradox arising from the contradiction between the common idea of motionless plants and the rapidity of the two latter motions resolves itself in a compromise: plant motions must be exceptional.

It is interesting to note how this idea pervades our cultural environment. In the late 19th century, stories about man-eating plants began to spread. These legendary plant-monsters were usually described as moving in threatening ways, revealing the

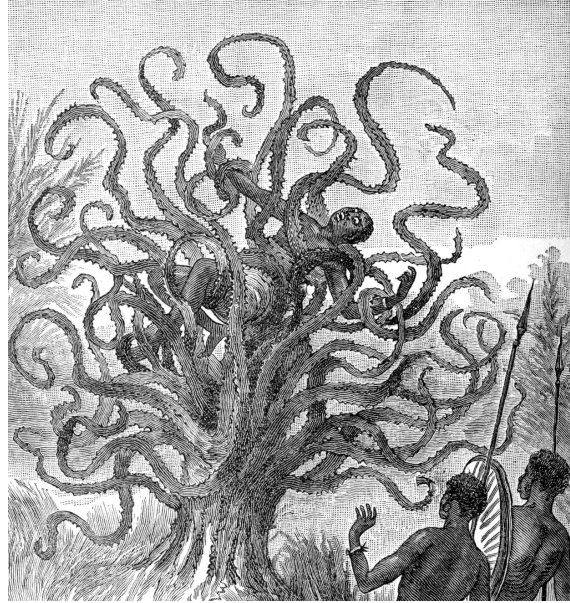


Figure 1.2: **The legendary man-eating tree Ya-te-veo.** This plant was described as an ensemble of stems similar to ‘many huge serpents in an angry discussion, occasionally darting from side to side as if striking at an imaginary foe’. Text and illustration from J.W. Buel’s *Sea and Land*, 1887.

uneasiness about plant motion at these times¹ (see figure 1.2). Nowadays, many novels involve moving plants or plant-like beings. From Carroll’s animated and talkative flowers to Rowling’s Whomping Willow or Tolkien’s Ents, plant motions may take various aspects. They are however systematically astonishing or horrific, associated with magic or witchcraft. In this sense, these outrageous depictions not only reveal our uneasiness about plant motions but might also reinforce our preconceptions on plant stillness.

On another note, the etymology of the noun ‘plant’ itself carries the idea of being ‘*chained to a place*’ (Marder, 2015). Certain phrases—such as ‘to be rooted to the spot’ in English—also reveal the strong connection that is made between plants and immobility. We see here how our everyday language implies a very specific definition of motion: locomotion². It is true that the position of individual plants is fixed in space, but motions are not restrained to locomotion. The motions of *Dionaea muscipula* and *Mimosa pudica* already show that plant motility lies in the position and orientation of their different organs relative to each other (see figure 1.1), that is to say in changes of the posture of the plant (Mouliia et al., 2006).

¹Note that Charles Darwin published his works on insectivorous plants at about the same period, in 1875.

²From the Latin *loco* (place, location) and *motio* (motion, movement)

In fact, there exist numerous motions of this kind. So, why would we think plant motions are uncommon? The characteristic time scale involved in plant motions can vary from milliseconds to several hours (Skotheim & Mahadevan, 2005; Forterre, 2013). In consequence, many plant motions—actually most of them—are beyond our perception. Our eyes only grasp the most rapid and spectacular plant motions, contrasting with our daily experience of plant stillness. Many plants and organs display such motions. Carnivorous plants exhibit different capturing strategies and motions, adapted to their surroundings (Forterre et al., 2005; Vincent et al., 2011). In some cases, seed dispersal is performed in a violent and fast way, thanks to bursts (Endo et al., 2010) or catapulting motions (Llorens et al., 2016). Nevertheless, a patient and careful observation of *any* plant—maybe with the help of a dedicated device—is likely to reveal beautiful motions. Slow motions have been observed in roots (Barlow et al., 1994), hypocotyls (Silk & Erickson, 1978), stems (Bastien et al., 2013) and leaves (Dornbusch et al., 2014). It would be excessive to state that we are totally unaware of such slow motions. But do we really regard them as motions? For instance, why would not we regard the growth of a tree as an upward motion? Another fundamental distinction actually makes that slow motions do not match our ‘animal’ experience of motion. The slow changes of shape coming with slow motions seem or are irreversible, contrary to our daily experience of reversible motions. So, we might more readily regard them as deformations—which they are—than motions.

Despite the fact that they are relatively difficult to observe, slow plant motions have likely been known for a long time, in all civilisations. In Ancient Greece for instance, in the 4th century BCE, philosophers Anaxagoras and Empedocles already defended the idea that plants were capable of motion (Whippo & Hangarter, 2006). To the best of my knowledge, the first report about plant motion was written at the beginning of the 3rd century BCE by Androstenes of Thasos³. He described how the leaves of the tamarind would close and pack against each other at night and open anew on the morning (Theophrastus, 1916). Such motions were then referred as ‘sleep movements’.

Considering that slow plant motions are a universal phenomenon and that they have been known for at least 2,500 years, how can we explain that they remain such a surprise to us?

³An admiral of Alexander the Great, sent to explore the Persian gulf. Parts of his report *The Navigation of the Indian sea* survive through later works such as Theophrastus’ *Enquiry on Plants* (3rd century BCE).

1.1.2 Early conceptions about plant motions

The evolution of the notion of plant motion cannot be separated from that of plant sensitivity (Whippo & Hangarter, 2009). Because plant motions had been observed, it seems that this notion was not contested in itself. On the contrary, the notion of plant sensitivity failed to gain support among the Greek philosophers. The vision according to which plants were insensitive actually prevailed. This vision relied on a hierarchy of living beings—formalized by Aristotle—established on the base of their different abilities. This hierarchy of nature persisted in time. It led to the emergence of the *scala naturae* in the Christian world during the Middle Ages. Since plants were considered to be deprived of sensitivity, the motions they displayed were seen as the direct result of an external action onto them. In this way, plant motions were completely passive: they did not *perform* motion but rather *underwent* motion. As a result, the study of plant motions remained disregarded until the end of the Renaissance (Whippo & Hangarter, 2006).

The end of the 16th century is a landmark in the study of plant motions. At these times, several naturalists began questioning the insensitivity of plants. For instance, Giambattista della Porta (1535–1615) studied the attraction of roots for water. The renewed interest in plant motions is however mostly due to the discovery of the American flora. European explorers were confronted for the first time to the rapid motions and touch-responsiveness of the *Mimosa pudica* or similar plants (see figure 1.1a). The motions of the *Mimosa pudica* were overall studied in England by the scientists of the Royal Academy (Whippo & Hangarter, 2009). However, during the 17th century, the proposed mechanisms to account for plant motion mainly kept relying on passive mechanical processes.

Webster unearthed that plant sensitivity had actually been supported the idea of sensitive plants during the 17th century (Webster, 1966). Their ideas found no echo at the time, but they opened the way to a fundamental shift in the approach to plant motions: from external, passive mechanisms to internal active mechanisms.

A first stone was laid by Augustin Pyrame de Candolle and Henri Dutrochet. De Candolle proposed that the slow re-orientation of plants toward light resulted from differences in the maturation of the tissues exposed to due to their different exposition to light (de Candolle, 1832). Dutrochet went even further and proposed that motions were driven by changes in the inner turgor pressure⁴ within the plant tissues (Bell, 1959). The mechanisms that they proposed remained passive (Whippo

⁴Turgor pressure will be detailed in section 1.2.2

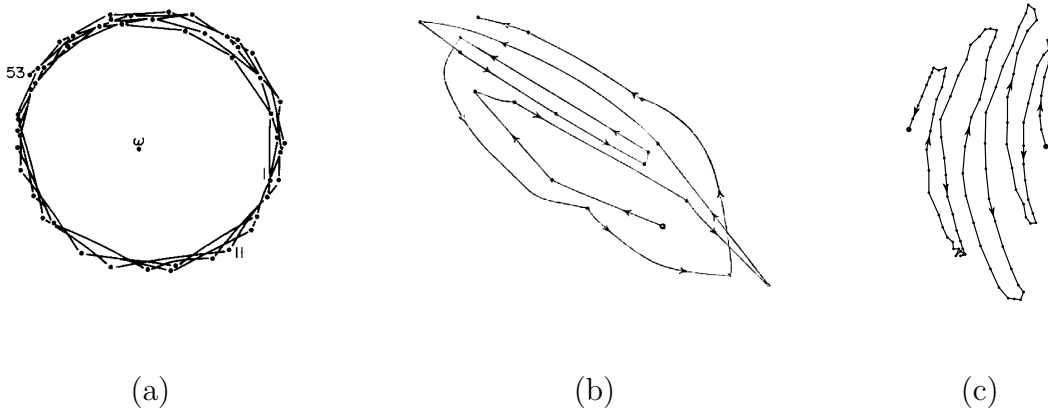


Figure 1.3: **The ubiquitous nutation motions.** Charles and Francis Darwin evidenced the ubiquity of periodical oscillatory motions in plants called nutations. Here are pictured three typical trajectory types (a) Circular nutation referred as circumnutation of *Phaseolus vulgaris* tendrils (Millet et al., 1984) (b) Elliptical circumnutation of *Brassica oleracea* seedlings (Darwin & Darwin, 1880). (c) Nutation of *Averrhoa carambola* leaves.

& Hangarter, 2009), but they sought the origin of plant motions in physiological—rather than purely mechanical—phenomena.

The final step was achieved by Sachs and Wiesner, two German botanists. They tackled the question of the active character of plant motions. By depriving a plant of oxygen, Julius von Wiesner observed that motion ceased (Bell, 1959), suggesting that an energetic input from the plant is needed in order to move. The 18th and 19th centuries were characterized by the interest of botanists in the influence of external cues—such as the gravity or the light—on plants. At that time, Wiesner and Sachs also studied the relationship between the ‘intensities’ of a given stimulus and that of the response motion (Bell, 1959; Whippo & Hangarter, 2009). They showed that the relation linking these intensities was not trivial, supporting the idea of *active* plant motions.

The 19th century also saw the publication of three books of Charles Darwin dedicated to plants and their motions: *The movements and Habits of Climbing Plants* in 1865, *Insectivorous Plants* in 1875 and finally *The power of movement in Plants* in 1880. The latter one, written jointly with Francis Darwin, mostly deals with the slow circumnutation revolving motion (see figure 1.3). It is still unanimously referred as a founding text to the study of plant motions nowadays. Darwin’s works greatly contributed to the awareness on the ubiquity of plant motions.

In summary, we see that the idea that plants are not able to *perform*—in an active way—motion is deeply rooted in the history of thought and science. The progressive accumulation of observations about plant motions led to reconsider the question of plant sensitivity. This allowed to slowly shift from passive mechanical to active

physiological mechanisms to account for plant motions during the 19th century.

1.1.3 Classical plant motion nomenclature

The increasing diversity of the observed plant motions led botanists to try and classify motions. Historically, plant motions have mainly been distinguished thanks to three different criteria: (i) Is the motion triggered by an external stimuli or not? (ii) Does the direction of the motion depend on that of the stimulus? (iii) What is the mechanism of the motion? (Firn & Myers, 1989). The second criterion allows to distinguish two classes of motions—tropisms and nastic motions—which is often used as a complete classification.

A *tropism*⁵ is a slow (re-)orientation motion of an organ in response to an anisotropic stimulus in the environment. Here, the important point is that the direction of the motion directly depends on the direction of the anisotropy. Tropisms are not always obvious in nature and are more easily observed in the case of a brutal change of the environmental conditions. Two important and illustrative examples are phototropism and gravitropism. Gravitropism corresponds to the re-alignment of an organ with respect to the vertical, *i.e.* the direction of the acceleration of gravity (see figure 1.4a). Phototropism characterizes the re-orientation of an organ depending on the orientation of the source of light (see figure 1.4b). Actually, tropisms can be aimed toward or away from the anisotropy. For instance, gravitropism can be positive or negative, *i.e.* an organ may align with the downward (e.g. most roots) or upward vertical (e.g. most stems) respectively. Of course, many other tropisms exist. We can mention the hydrotropism of roots or the impressive thigmotropism⁶ helping climbing plants enrolling around a support (see figure 1.4c), for example.

When the direction of the motion is independent from the stimulus, it is said to be a *nastic motion*⁷. The most iconic nastic motion might be thigmonasty. The closure motions of *Mimosa pudica* and *Dionaea muscipula* are two examples of thigmonasty (see figure 1.1). Changes of temperature can also result in closure or opening motions—referred as thermonasty—in some flowers, such as tulips. The direction of a nastic motion is generally imposed by an anatomical constraint. In the case of thigmonasty for example, the direction is imposed by the pulvini. The pulvini is a soft tissue capable of inflating differentially and thus to act as joint.

⁵From the Greek word ‘tropos’ meaning a ‘turning’.

⁶The Greek prefix ‘thigmo’ corresponds to ‘touch’

⁷From the Greek word ‘nastos’ meaning compact, evoking a closure motion.

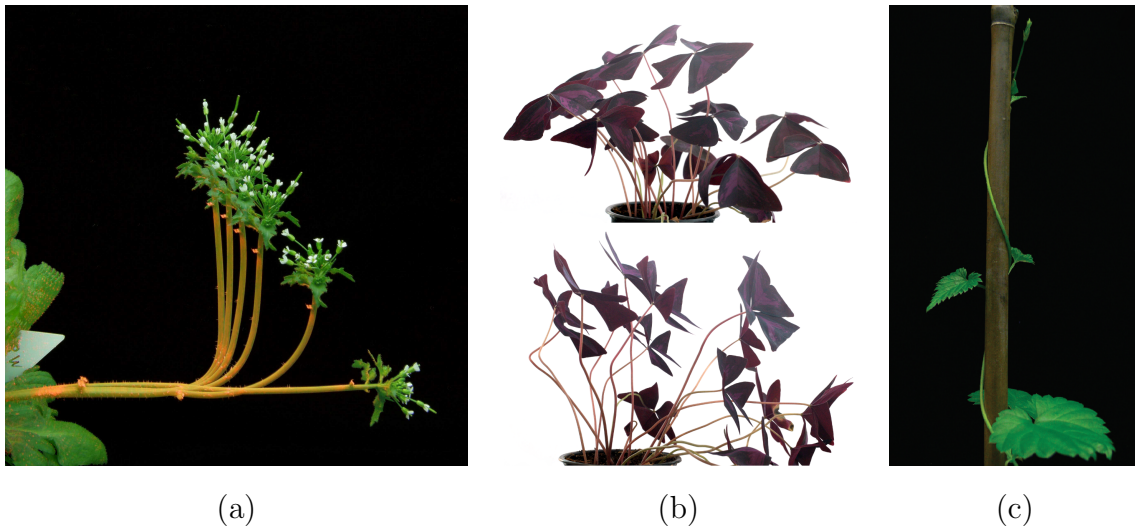


Figure 1.4: **Three examples of tropisms.** (a) Gravitropism of an *Arabidopsis thaliana* inflorescence stem (courtesy of Renaud Bastien). (b) Phototropism of *Oxalis triangularis* leaves. (c) Thigmotropism of a *Humulus lupulus* twining stem (Isnard & Silk, 2009).

In the previously mentioned motion, a trigger is clearly identified. Such motions are said to be paratonic. But there exist autonomic motions, for which no clear trigger is identified (Firn & Myers, 1989). For example, autonomic motions contain epinasty and hyponasty which correspond to changes in the height of an organ during growth (Dornbusch et al., 2014). Nyctinasty—corresponding to ‘sleep movements’—are also autonomic motions in the sense that the rhythm of this motion does not entirely depend on the alternation of day and night⁸.

At last, the question of the mechanism underlying the motion is asked. It is clear from the previous paragraphs that at least two kinds of mechanisms are necessary to explain plant motions. As a matter of fact, tropisms seem to be irreversible motions—as long as the triggering anisotropy is maintained—while most nastic motions are reversible. In addition to that, it has been observed that plant motions occurred on various very different time scales, suggesting different mechanisms (Skotheim & Mahadevan, 2005). In this thesis, however, we will focus on the case of slow irreversible motions. The mechanisms of fast motions are thus out of our scope, but the curious reader can refer to (Forterre, 2013) for a detailed review, for example.

⁸This will be detailed in section 1.3.1

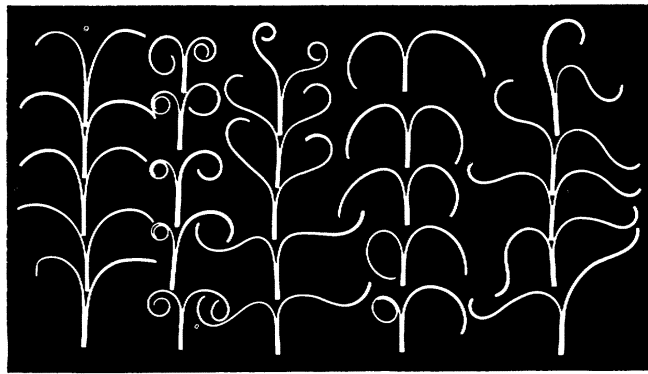


Figure 1.5: **Differential growth and curvature.** Slit stems of *Pisum sp.* exhibit an outward curvature in water (left column). By tuning the concentration in growth hormones of the baths, this curvature can be enhanced or reversed. (Thimann & Schneider, 1938)

1.2 Origin of growth motions

It is now clear that slow motions are inherent to the plant kingdom. Contrarily to animals, plants do not have muscles though. So, what are the mechanisms underlying plant motions?

1.2.1 Differential growth drives the motion

Tropisms have been interpreted in terms of differential mechanisms—i.e. mechanisms relying on some kind of inhomogeneities—for a long time. For instance, Theophrastus already explained phototropism by the differential desiccation of the shaded and enlightened faces of the bending organ (Whippo & Hangarter, 2009). To my knowledge, Robert Sharrock has been the first to propose that tropisms resulted from growth inhomogeneities between the opposed faces of the bending organ (Sharrock, 1660). De Candolle later built up a passive explanation to phototropism relying on differential growth (de Candolle, 1832). At last, Charles and Francis Darwin proposed that circumnutation resulted from differential growth (Darwin & Darwin, 1880).

Differential growth basically corresponds to elongation heterogeneities within the tissues of a growing organ. Because the tissues are cohesive, if a given part of the organ elongates relatively more or faster than the rest of the organ, mechanical stress will build up in the tissues. This is what is called ‘residual stress’. If the different layers of the considered tissue grow at different rates, these inner tensions can be revealed by slitting the organ in half (see figure 1.5, left column). Doing so,

the tensions are released and curvature reveals the previous state of tension. In this example, the resulting outer curvature shows that the inner tissues of the stem were compressed by the outer ones. By stimulating the growth of the inner tissues, this curvature can be exaggerated (see figure 1.5, columns 2 and 4). On the contrary, stimulating the growth of the outer tissues reverses the curvature (see figure 1.5, columns 3 and 5). This demonstrates how growth can affect the internal mechanics of the tissue and eventually its shape.

However, growth inhomogeneities not only occur between the different layers of a growing tissue, but can be found along elongating organs or between the opposing faces of elongating organs (Tomos et al., 1989). The phrase ‘differential growth’ will be used to designate the latter case in this whole thesis. In the simple case where the two opposing faces of a growing organ have different elongation rates, the resulting inner tensions make the organ bend toward the least-growing face (see figure 1.6). In this way, we see how growth and differential growth can give rise to motions. The nature of the resulting motions indeed depends on the time and spatial patterns of differential growth (Bastien & Meroz, 2016).

Differential elongation has been experimentally evidenced in a variety of cases. The basic method simply consists in comparing the elongation rates of the two opposite faces of the moving organ. The phototropism of coleoptiles, epicotyls and hypocotyls (Franssen et al., 1981; Baskin, 1986) and epi/hyponastic motions of *Arabidopsis thaliana*’s rosette leaves (Dornbusch et al., 2014) have been shown to rely on differential elongation. Differential elongation have also been evidenced in the (circum)nutations of roots (Chavarría-Krauser et al., 2008), epicotyls (Baskin, 1986) and *Helianthus annuus* seedlings (Berg & Peacock, 1992). Interestingly enough, in the case of nutation, the two last cited studies put forward out of phase oscillations of the elongation rates of the opposite faces of the considered organ.

In some other studies, the differential elongation of tissues is assumed and can thus be directly quantified by the curvature variations of the moving organ (we will detail it in Chapter 4).

We have seen that some slow motions—tropisms, some specific nastic motions and circumnutation—are induced by differential elongation. The question of the origin of these elongation inhomogeneities is now asked. To better understand how differential elongation—and motions—emerge, it is now essential to take a look at the cellular growth processes themselves.

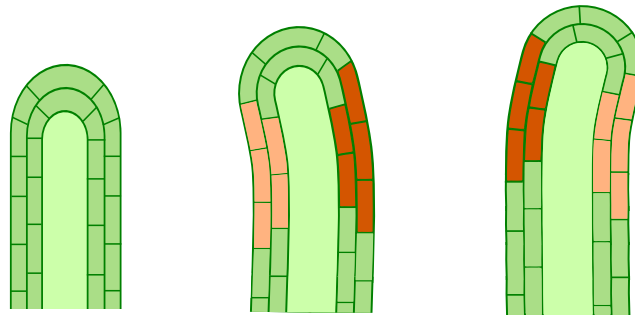


Figure 1.6: **Illustration of the principle of differential growth.** The two sides of the growing organ elongate with different rates. Since the tissues are cohesive, this results in a bending towards the side with the smallest elongation rate. Growth heterogeneities can eventually be reversed, giving rise to oscillatory motions for instance. Adapted from (Mugnai et al., 2007).

1.2.2 Microscopic mechanisms of plant growth

It is now necessary to precisely define the word ‘growth’. In the scientific literature, growth usually refers to the irreversible increase in volume of an organ. The growth of an organ relies on two contributions: the growth of individual cells and mitosis—*i.e.* cell divisions. In plants, mitosis—contrarily to growth—is mostly confined to specific tissues of growing organs called meristems. In this study we will rather focus on the contributions of cellular growth. Plant growth unfolds in two distinct and successive phases. *Primary growth* consists in an elongation of cells while *secondary growth* refers to the radial enlargement of cells.

Like animals, plants are eukaryotes. Their cells contain a nucleus and several organelles within a membrane (see figure 1.7). A number of differences however exist between animal and plant cells. The most important of these differences is the cell wall. In plants, the protoplast⁹ is encased within a semi-permeable and rigid cell wall. Cell walls form an extracellular matrix, preventing plant cells to move relative to one another but also constraining their size and shape. In this way, we see that plant growth necessarily implies to irreversibly deform the cell wall. The cell wall thus plays a major role in the mechanics of plant cells. This has been ingeniously underlined by showing that plant protoplasts and animal cells shared comparable mechanical behaviours (Durand-Smet et al., 2014).

Plant and animal cells contain water storage organelles: vacuoles. In mature plant cells, the vacuole is unique and can take up to 90% of the cell volume. The

⁹The protoplast designates the plasma membrane and its content.

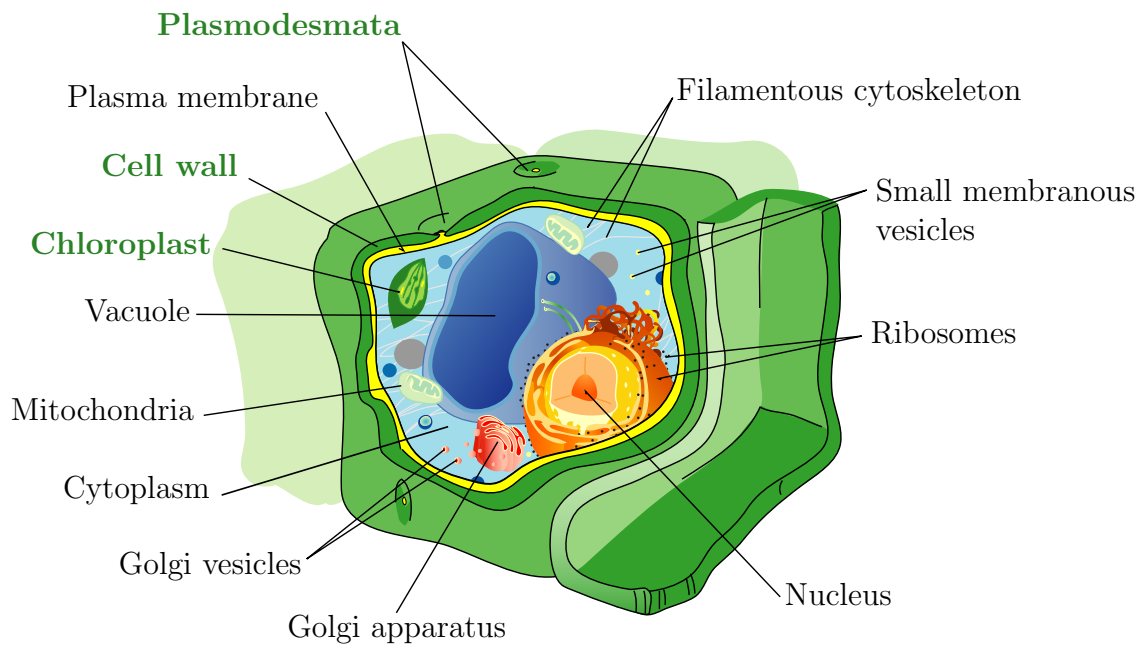


Figure 1.7: **Illustration of the plant cell structure.** Plant and animal cells share most of their organelles and structures. Plant specific structures and organelles are indicated in bold green letters. (Illustration from the Wikicommons project. Artist: Lady of Hats.)

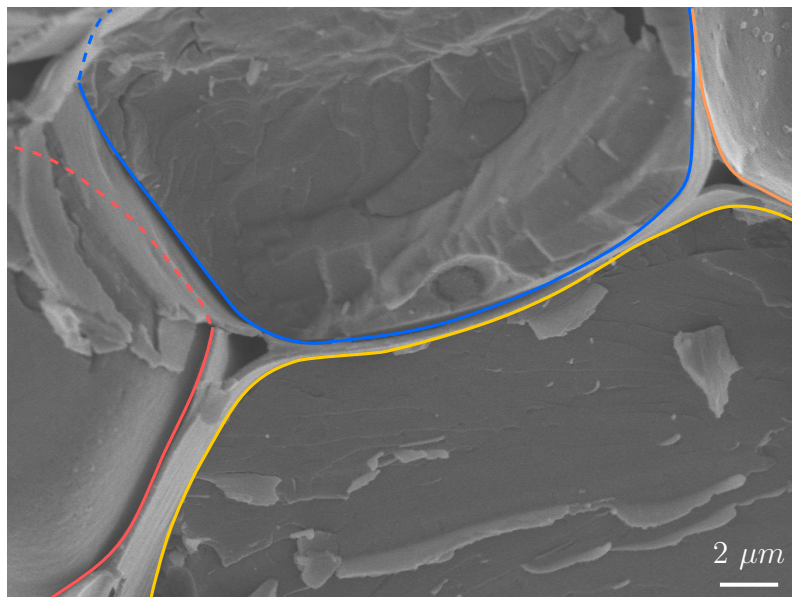


Figure 1.8: **Four cells and their cell walls.** On this Cryo-SEM image of *Averrhoa carambola* inner tissues, we can distinguish four different cells, surrounded by cell walls (outlined by plain color lines). Note the presence of intercellular spaces where neighbouring cell walls separate.

water content of the cell is regulated by osmosis¹⁰. Water uptake results in an volume increase of the protoplast. This increase in volume is however limited by the rigid cell wall. When the protoplast of the cell is in contact with the cell wall, the cell is said to be turgid. Because further water uptake is not possible, a hydrostatic pressure rises within the cell to keep water from entering it. This turgor pressure needs to be equal to the osmotic pressure. Turgor pressure values are usually of the order of a few atmospheres. It thus appears here that the volume increase of a cell is driven by osmosis and that turgor pressure is the source of cell wall deformation.

Finally, let us mention that—at the tissue level—neighbouring cell walls are tied together by an intermediary layer called the middle lamella (see figure 1.8 for a close view of a plant tissue). Cells are not perfectly joined and we often see intercellular spaces. The communication between cells is allowed by small apertures in the cell wall called plasmodesmata (see figure 1.7).

From the last paragraph, we see that plant growth is based on two contributions: the irreversible extension of the cell wall and water uptake. These are at the base of the plant growth model of Lockhart which was later augmented by Ortega (Lockhart, 1965; Ortega, 1985). In the Lockhart-Ortega model, the cell wall is submitted to variations of the turgor pressure P . Below a critical threshold P_c , the cell wall responds in a viscoelastic way. Above P_c , the cell wall yields and is irreversibly deformed. The cell wall is thus modelled as an elasto-visco-plastic material. In the case of an elongating cell, the rate of change of the cell length L is given by

$$\frac{dL}{dt} = \underbrace{m(P - P_c)}_{\text{irreversible}} + \underbrace{\frac{L_0}{\epsilon_L} \frac{dP}{dt}}_{\text{elastic}} \quad (1.1)$$

as shown in (Proseus et al., 1999). Here, ϵ_L is the elastic modulus¹¹ of the cell wall, m is its irreversible extensibility¹² and L_0 is the initial length of the considered cell. From equation (1.1), we clearly see the superposition of irreversible and elastic contributions here.

The Lockhart-Ortega model emphasizes the role of turgor pressure as the driving phenomena of cell growth. Turgor pressure is indeed essential to growth since too low turgor pressures have been found to inhibit growth (Cosgrove, 1987). But it has been argued that the active regulation of the rheological properties of the cell

¹⁰Cells solutes usually in higher concentration than their surroundings. Water movements thus arise to equilibrate concentrations.

¹¹ ϵ_L depends on both the geometry of the cell wall and its Young's modulus.

¹² m not only depends on the geometry and rheology of the cell wall, but also on all the other factors affecting growth (Proseus et al., 1999).

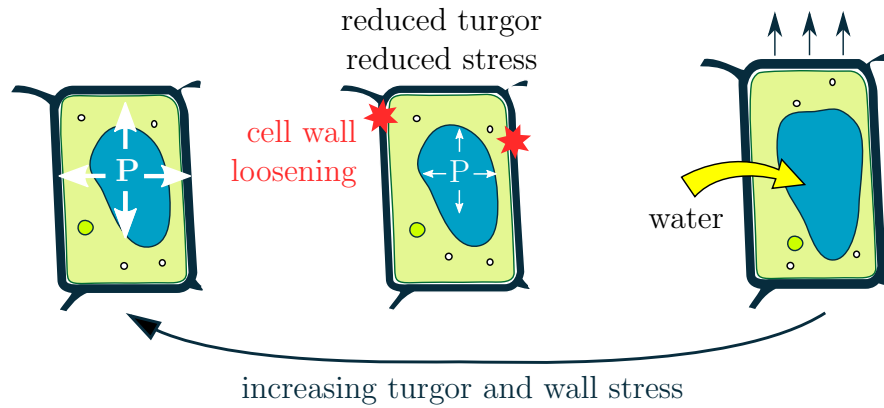


Figure 1.9: **Putative cellular growth scenario.** Red stars represent cell wall loosening. While the turgor pressure provides the mechanical energy for elongation, cell wall loosening and stress relaxation rule it. Inspired from (Cosgrove, 2015).

wall (P_c, m, ϵ_L) are at the basis of growth control (Cosgrove, 1987; Schopfer, 2006). It has been observed that the mechanical status of the cell wall is modified during growth. In growing cells, it has been observed that m increases with the rate of elongation of the cell. This is what is referred to as the cell wall loosening. In the same time, P and P_c also decrease. More surprisingly, a correlation between the elongation rate and the elastic modulus of growing cells has been established. It was observed that growing cells were softer than non-growing cells (Geitmann & Ortega, 2009).

From these observations, a simple primary growth scenario can be imagined (see figure 1.9). First¹³, the cell wall is set under tension by the inner turgor pressure of the cell. Then, the cell wall loosens, leading to a relaxation of its inner stresses. This could be the result of growth hormones such as auxin. Because the cell wall stress decreases, the inner turgor pressure also decreases. Doing so, it allows water uptake and thus cell elongation. Elongation ceases when the mechanical equilibrium between turgor and the cell wall stress is reached (Cosgrove, 2015). Finally, this cycle can start anew.

Together with the Lockhart-Ortega model, this simple picture of growth helps us understanding the mechanisms of growth. However, several aspects of growth were not assessed here. First, in the case of elongating cells, growth is highly anisotropic. No account on anisotropic growth was given. How can the directionality of growth be explained? Second, we are here mainly concerned by plant motions and the

¹³Here the mechanism is decomposed for pedagogical purposes. In reality the presented steps occur simultaneously.

associated differential growth. So, how is differential growth generated within plant tissues? We have seen that the mechanical properties of the cell wall play a great role in plant growth. Hence, growth inhomogeneities might be caused by any kind of mechanical inhomogeneities within the walls of the growing tissue. But then, from what arise the cell wall rheological properties and their possible inhomogeneities? To try and answer these questions, we now need to take a closer look at the cell wall.

1.2.3 A quick picture of the cell wall

The cell wall is usually described as a complex, composite material. The main component of the cell wall—which has logically focused most of the attention—is cellulose. Cellulose is arranged in microfibrils which are embedded within a matrix of polysaccharides (see figure 1.10). Two main families of cell wall polysaccharides were defined, based on their chemical composition and solubility: insoluble hemicelluloses and soluble pectins. The most abundant hemicelluloses are xyloglucans. Arabinoxylans and mannans are generally found in lesser amounts within plant tissues. The most abundant pectins are rhamnogalacturonans I and homogalacturonans. Other pectins include xylogalacturonan, arabinans and rhamnogalacturonans II for instance. Finally, several other structural proteins (< 5%) and solutes can be found in the cell wall (Cosgrove, 2005).

The extensibility of the cell wall results from the different bonds that can be formed between its components. It is quite intuitive that the more the components of the cell wall are linked together, the stiffer the cell wall is. It was classically thought that a tethered network of cellulose microfibrils and xyloglucans bore most of the load within the cell wall. Pectins and other wall components were thus regarded as having little impact on the cell wall rheology. The ‘tethered network’ hypothesis and the preponderant role of cellulose-xyloglucans links have however recently been challenged and pectins—especially homogalacturonans—began to raise more and more interest (Peaucelle et al., 2012).

Homogalacturonans can form Ca^{2+} -mediated cross-links. The ability of homogalacturonans to form such cross-links directly depends on their chemical status. The methyl-esterification of homogalacturonans actually blocks the possibility to form cross-links. Homogalacturonans are usually synthesized in a highly methyl-esterified state but can later be specifically demethyl-esterified via the action of pectin methyl esterase (Cosgrove, 2005; Peaucelle et al., 2012). It is thus expected that cell walls containing highly methyl-esterified homogalacturonans will be softer

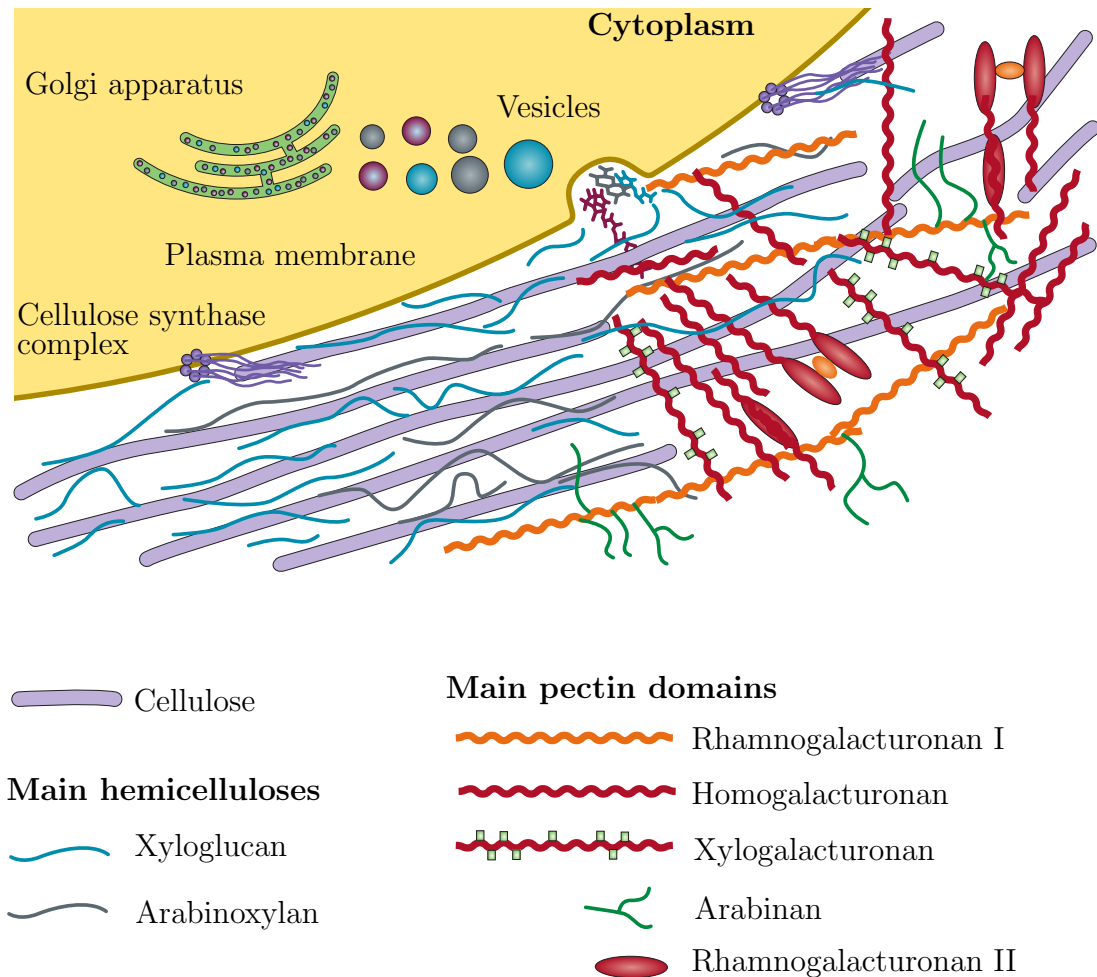


Figure 1.10: **Illustration of the structure of the primary cell wall.** The cell wall lies beyond the plasma membrane. It is basically an entangled network of cellulose, hemicelluloses and pectins. Pectins and hemicelluloses are synthesized by the Golgi apparatus and transported to the cell wall by vesicles. Cellulose microfibrils are synthesized by cellulose synthase complexes in the membrane. For clarity, pectines were drawn solely on the right half of the picture. Illustration taken from (Cosgrove, 2005)

than those presenting low rates of methyl-esterification. In this way, it is further expected that de-methyl-esterification is associated with growth processes. In roots and in the pollen tube, studies revealed such a correlation (Palin & Geitmann, 2012). But studies in the shoot apical meristem brought observations challenging the classical view. It was found that low rates of methylesterification were associated with softer cell walls and growth (Peaucelle et al., 2008, 2011). Several hypotheses and mechanisms have since been proposed to conciliate the *a priori* contradictory observed roles for pectins and methylesterification (Chebli & Geitmann, 2017).

More importantly, in both cases mechanical and chemical gradients have been found to be correlated with growth. We thus see here how biochemical gradients can lead to mechanical inhomogeneities and differential growth within the tissues.

What about the growth directionality? By essence, turgor pressure applies isotropic stress on the cell wall. Then, how is it possible to explain the highly anisotropic growth of an elongating organ? The anisotropy of growth must rely on cell wall anisotropies, leading to stress anisotropies. It has been shown that growth anisotropy is mostly dictated by the orientation of the cellulose microfibrils in the cell wall (Baskin, 2005). Highly anisotropic microfibril orientation will lead to anisotropic stress within the cell wall and favor elongation in the orthogonal direction. However, cellulose might not be the only actor in anisotropic cell growth. A recent study has indeed shown that anisotropic demethyl-esterification precedes the anisotropic cellulose microfibril orientation (Peaucelle et al., 2015).

Finally, we have seen how the biochemical status of the cell wall is dynamic and tightly connected to growth. Biochemical gradients across the tissues are likely to give rise to mechanical inhomogeneities, to differential growth and *in fine* to macroscopical motions. In this sense, plant motion is a multiscale phenomenon. From the biochemistry of the cell wall to the bending of the whole organ, we see how strong and intimate are the links between motions and growth. In summary, macroscopic growth motions are an outward signal of microscopic growth processes.

1.3 Study of plant motions

When confronted with plant motions, our preconceptions are challenged and our curiosity is naturally aroused. In this sense, plant motions are a formidable motor for advances in plant sciences research. In this section, I want to try and show the importance of plant motions in the improvement of our knowledge on plants and nature.

1.3.1 What have we already learnt from plant motions?

First, as discussed in section 1.1.2, plant motions have led several generations of philosophers and scientists to rethink the place of plants in nature. Among all the possible questions, the question of plant sensitivity has been of paramount importance for further investigations on plants (Whippo & Hangarter, 2009).

Many of the plant sensitivities have been discovered through the motions they are associated to. The specific mechanisms of plant sensitivities and their biochemical pathways have naturally been investigated and are still active domains of research. Among them, the mechanisms of mechanosensing (Moullia et al., 2015), photosensitivity (Galvão & Fankhauser, 2015) and graviception (Pouliquen et al., 2017).

The study of gravitropism also led to further advances in our understanding of plant posture regulation. A recent phenomenological model of gravitropism have indeed revealed the essential role of proprioception in tropisms (Bastien et al., 2013, 2015).

Because of their tight links with growth, plant motions also helped understanding the processes of plant growth. With plant sensitivity being accepted, plant motions have finally been regarded as the possible outcome of physiological processes. In consequence, this led scientists like von Sachs and von Wiesner to question the role of the cell wall mechanics and of turgor pressure in growth and motions (Bell, 1959). As discussed in sections 1.2.2 and 1.2.3, these domains are still very active nowadays.

It was also in an attempt to understand the mechanisms of phototropic bending that the existence of a growth substance was postulated in the early 20th century. In 1926, Frits W. Went demonstrated the existence of such a substance. He isolated it from the apex of phototropically stimulated *Avena sativa* (Went, 1926). This was the discovery of the plant growth hormone auxin¹⁴, which was later identified as indole-3-acetic acid.

The study of plant motions also contributed to more general advances in general biology. For the record, Robert Hooke came to be the first to describe a biological cell during his works on the *Mimosa pudica* motions.

The study of plant motions have also been of great importance to chronobiology¹⁵. Nyctinasty was not only the first example of biological rhythm, but it remained the only known example until the 20th century and the discovery of human rhythms (McClung, 2006). During the 18th and 19th centuries, the works of Jean-Jacques Dortous de Mairan and Augustin Pyrame de Candolle showed that

¹⁴The word auxin is derived from the ancient Greek word ‘auxein’, meaning increasing or growing.

¹⁵Chronobiology is the study of biological rhythms

the nyctinasty of *Mimosa pudica* actually relied on an endogenous rhythm (Somers, 1999; McClung, 2006). The rhythm of nyctinasty is actually only forced by the diurnal rhythm¹⁶

At last, works on plant motions are also motivated by possible technological outcomes. In the beginning of the 21st century, plant motions have indeed become a source of inspiration for adaptive materials and structures. The passive motions of plant organs and fruits—opening of some flowers, pine cones or seed pods—have drawn much attention and led to production of different kinds of passive actuators (Reyssat & Mahadevan, 2009; Armon et al., 2011; Schleicher et al., 2015). Such actuators usually rely on the anisotropic mechanical properties of the used materials. Tropisms and differential growth have also provided some inspiration for bio-inspired robots for example (Sadeghi et al., 2016).

1.3.2 The classical nomenclature called into question

Plant motions have contributed to advances in our general knowledge on plants, and specifically in the mechanisms of growth. What can we learn more from plant motions? While it is true that motions have been extensively studied, it appears that the traditional classification has naturally led to regard plant motions in the framework of tropisms and nastic motions. It has however been argued that the study of plant motions could benefit from a reconsideration of the classification of motions (Firn & Myers, 1989). As a matter of fact, this nomenclature presents several shortcomings.

First, it is difficult to determine the position of certain motions within this classification. Autotropism and circumnutation might be the two most pathological cases. Autotropism corresponds to the observed tendency of plants to grow straight, aligned with themselves. But, in that case we see that the directionality of the motion is necessarily imposed by an *inner* symmetry, in contradiction with the very definition of tropism (Firn & Myers, 1989). Circumnutation and nutation are also difficult to fit in this classification. As a matter of fact, the originally suggested autonomic character of these motions (Darwin & Darwin, 1880) is still debated nowadays (Baskin, 2015). Notably, many experiments were conducted on the influence of gravity on nutation. According to our current knowledge on nutation, it is possible that nutation is based on autonomic oscillations which amplitude is enhanced by graviception (paratonic). Furthermore, the mechanism underlying (circum)nutation might depend on both irreversible growth and reversible volume

¹⁶The diurnal rhythm corresponds to the alternation of day and night.

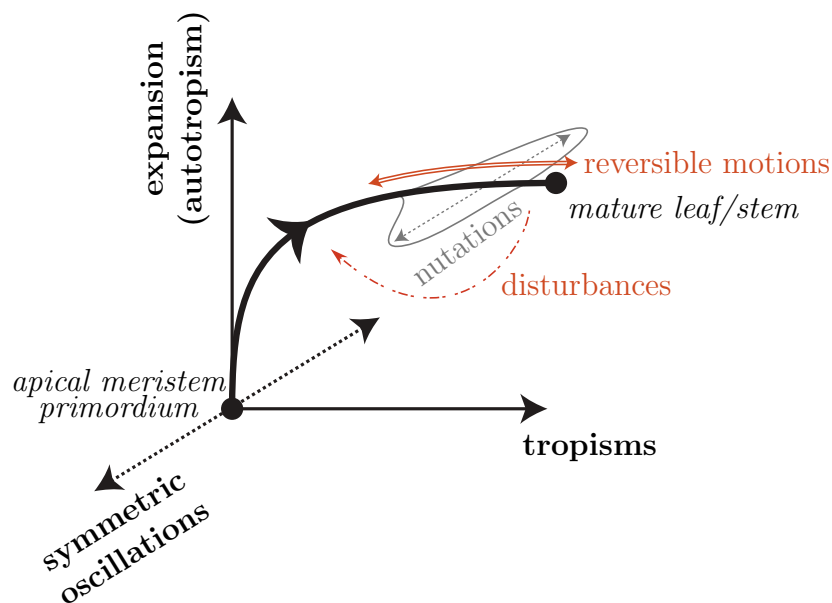


Figure 1.11: **Succession of motions on the developmental time line.** An organ will first take shape via autotropism. The integration of more and more external cues—tropisms—then allows to achieve successful posture regulation. Before the end of the development, oscillatory motions appear. Finally, a perturbation of the mature organ may lead to posture correction and will induce a reversion to a previous state, evidenced by a renewed anisotropic growth and motions. (Rivière et al., 2017).

changes. Differential growth has indeed been measured between the faces of nutating organs (Baskin, 1986; Berg & Peacock, 1992). But reversible processes have also been found to be involved in nutation. Local contractions have indeed been measured at the organ level (Berg & Peacock, 1992; Stolarz et al., 2008) and at the cellular level (Caré et al., 1998). These contractions have been shown to be reversible and have been proposed to be linked to turgor pressure variations. Therefore, we see how difficult it is to determine the position of nutation within the traditional classification of motions.

Second, the two main categories that emerge from the traditional nomenclature of motions—tropisms and nastic motions—are inconsistent in the sense that they do not rely on a single mechanism. For example, the *Mimosa pudica*'s seismonasty resort on differential turgor changes and quick water displacements (Dumais & Forterre, 2012) while epinasty and hyponasty rely on differential growth (Dornbusch et al., 2014).

We see here how resorting on a classification leads to a fragmented and somewhat inconsistent picture of plant motions. It seems that at least a piece of information is

lacking in order to recover the logic of plant motions. We have recently proposed that the consistency and continuity of plant motions could be recovered by considering their succession during development. The complete reasoning supporting this idea is slightly out of scope and will not be discussed in this thesis. It has however been developed in a review (Rivière et al., 2017). Basically, the succession of motions was described to be organized in four phases (see figure 1.11).

First comes a shaping phase. The preferential elongation axes of the organ are established, and motions consequently arise, guided by autotropism.

Then, the organ enters a phase of posture regulation. At this stage, the integration of *external* cues—i.e. tropisms—becomes useful in leading growth and motions, to ensure a successful posture control. The end of growth is then accompanied by a phase of oscillatory motions such as nutation. We have hypothesized that these last developmental motions are a manifestation of autotropism before definitively freezing both shape and posture (Rivière et al., 2017).

When the growth of the organ is over, two kinds of motions are still possible: reversible motions and posture correction via tropisms (see figure 1.11, red arrows). Our observations suggests that reversible motions are in fact the repetition of the motions performed during the posture regulation phase. Their velocities and the mechanism they rely on are necessarily not the same anymore, but their trajectories and effects are similar (Rivière et al., 2017). Finally, in the case of an environmental perturbation requiring a re-orientation of the mature organ growth is reactivated to correct posture. This posture correction then implies to go back to the posture regulation phase described earlier, and to go through the same time the succession of their associated motions again.

In conclusion, we have seen how plant motions were actually unified under the prism of organ development. Considering their logic and their arrangement in time dissolves the apparent frontier between nastic motions and tropisms, but also between autonomic and paratonic motions. Doing so, it becomes possible to understand plant motions as a single phenomenon, strongly connected to other developmental phenomena such as growth. This picture of plant motions we have built might, however, be limited by exceptions and counter-examples.

1.4 Problematic and approach

In conclusion, slow plant motions have been known for a long time but remained overlooked until the pioneering works of Charles and Francis Darwin (Darwin & Darwin, 1880). Since then, a majority of works have focused on mature motions such as tropisms and nastic motions. Circumnutation and nutation are also among the most studied motions: the origin of these oscillations remains unanswered. So, a majority of works have focused on a stimuli-response approach, often without any insight on growth.

In contrast, in this thesis we chose to focus on plant growth motions—motions displayed only during the development of an organ. Because of their strong link with growth, we regard these motions as an *outward signal* of growth and developmental processes of the plant. Following this idea, we will explore the connections between the motions and several aspects of plant development: elongation kinematics, mechanics and biochemistry.

To do so, we will follow the succession of the motions in the course of the development, as described earlier, and across the different scales. Our study is mostly dedicated to the characterization of growth, mechanical and biochemical patterns that underlie the development of an organ. An emphasis will thus be put on heterogeneities, time and space variations. Those will be sought at several scales: from the global shape of the organ to the cell wall. Our basic statement is that different phases of the motion will correspond to different phases in growth. In consequence, the oscillatory motions will be of particular interest all along this work.

The first step of this work is now to define our plant and motions of interest.

Chapter 2

Description of *Averrhoa carambola* as a model

Contents

2.1	General information on <i>Averrhoa carambola</i>	24
2.2	<i>Averrhoa carambola</i> compound leaves	26
2.2.1	Shape and anatomy of the leaves	26
2.2.2	Histology of the rachis	29
2.2.3	Geometrical parametrization	31
2.3	The different motions of the leaf	33
2.3.1	Motions of the growing leaf	33
2.3.2	Motions of the mature leaf	39
2.4	Discussion and conclusion	43

Arabidopsis thaliana has been one of the most studied model organisms of plant sciences since the 1990s. Nevertheless, in the context of plant motions, we will focus on another plant: *Averrhoa carambola*. In this chapter, the specificities of *Averrhoa carambola* will first be discussed. Then, we will detail the numerous typical motions exhibited by *Averrhoa carambola* leaves. Consistently with the ideas developed in Chapter 1, we will do so by following the developmental course of the leaves. A geometrical framework will also be established in order to properly describe motions throughout this thesis.

2.1 General information on *Averrhoa carambola*

Since the works of Carl von Linné, botanists have named plants using binomial names. Binomial names are usually made of two words. The first word names the genus and the second word names the species. A final addition to the binomial name can be made—the ‘authority’—and designates the person who first named the plant. The complete name of our plant of study is *Averrhoa carambola* L. The genus ‘*Averrhoa*’ directly refers to the Moorish astronomer Averroes (Quattrocchi, 1999). The name of the species supposedly derived from a Sanskrit word—*karamphala*¹, meaning ‘food appetizer’—originally designated the fruit of the tree. Finally, the authority refers to Carl von Linné—meaning the plant has been known in Europe at least since the 18th century.

The *Averrhoa* genus belongs to the *Oxalidaceae* family which gathers 875 dicots². The only other member of this genus is *Averrhoa bilimbi* whose motions were already mentioned by Charles and Francis Darwin (Darwin & Darwin, 1880).

The exact geographical origin of *Averrhoa carambola* is not known with certainty, but it seems to have originated in South-East Asia. Several authors have proposed that carambola is from the Malay peninsula, Indonesia or Sri Lanka (Litz & Griffis, 1989; Manda et al., 2012; Patil et al., 2012). Nowadays, carambola trees are distributed across a wide variety of tropical regions, from South East Asia to the Caribbean.

Averrhoa carambola is an evergreen tree which can be up to 15 m in height (Litz & Griffis, 1989). Its flowers are pink to purple and its fruits are oblong with five sharp lobes. Carambola fruits have a waxy skin which is yellow-green when the fruits are unripe and turns orange-yellow at maturity. Carambola fruits are famously known as ‘star fruits’ because of the star shape of their slices. Another remarkable characteristic of *Averrhoa carambola* are its leaves which will be described in section 2.2.

Like most of species belonging to the *Oxalidaceae* family, the carambola tree is well suited to tropical climates (Patil et al., 2012). It adapts easily to any cultivation condition however. The minimum prerequisites seem to be that it is well irrigated and not exposed to frost for too long (Litz & Griffis, 1989). This makes *Averrhoa*

¹or *karmaranga*, to *karambal* in Marathi and finally to *carambola* in Portuguese (Manda et al., 2012)

²Right after germination, dicot seedlings possess two leaf-like storage organs called cotyledons.

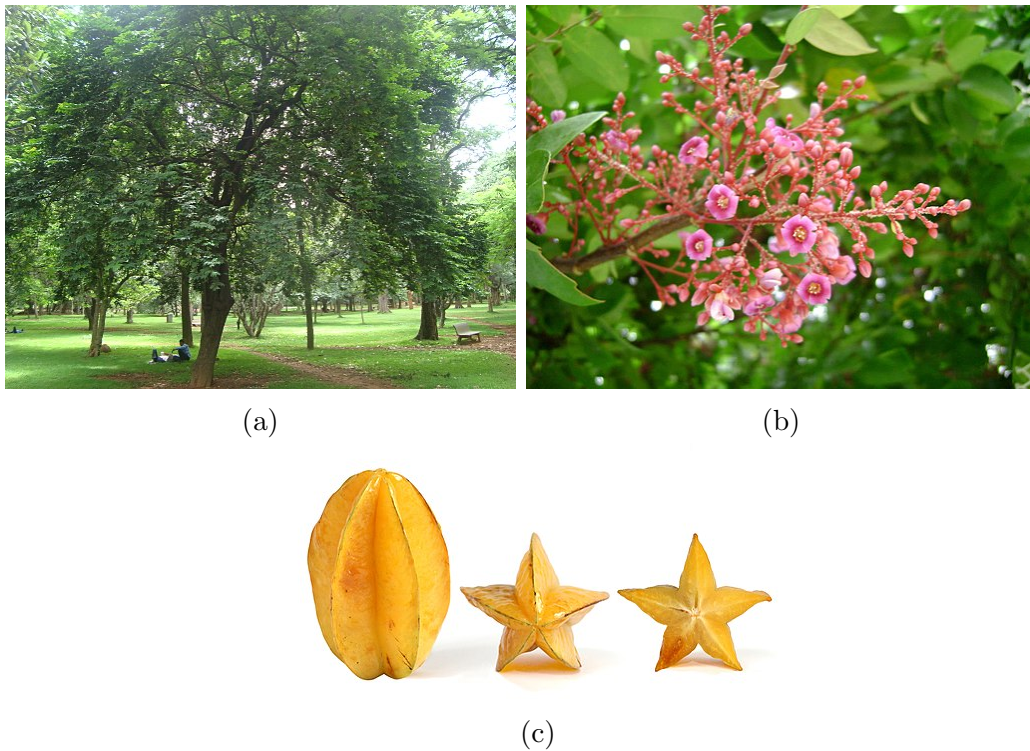


Figure 2.1: **Carambola tree, flower and fruit.**

carambola a quite robust plant and easy to grow in the sheltered conditions of a laboratory.

Carambola trees have been cultivated for centuries in South East Asia . In present days, carambola trees are cultivated in many regions of the world. They are mainly cultivated for their fruits. Starfruits appear to be a good source of proteins and fibers as well as potassium or copper (Manda et al., 2012). They are used in various food or drink preparations, from Malaysia to Hawaii (Manda et al., 2012; Patil et al., 2012).

Averrhoa carambola is involved in many medicinal uses were it is traditionally cultivated. Fruits, roots, leaves and flowers are all used to treat diverse ailments and diseases (Saghir et al., 2013). They are mainly used to counteract skin conditions, fever, headaches and stomach aches, but are sometimes used against serious diseases such as diabetes or malaria (Patil et al., 2012). For these reasons, the majority of the available literature about *A. carambola* deals with pharmacological and clinical assays. Many tests were conducted on the possible uses of star fruits extracts. For instance their antioxidant capacity, anti-ulcer activity, hypoglycaemic activity or hypotensive activity revealed promising for pharmacological applications (Patil et al.,

2012). Carambolas contain high amounts of oxalic acid and also small quantities of a neurotoxin. For this reason, star fruit consumption is dangerous – and can be fatal – to people suffering certain kidney conditions (Patil et al., 2012; Saghir et al., 2013).

2.2 *Averrhoa carambola* compound leaves

Leaves play a fundamental role in plant metabolism. They are the seat of photosynthesis, the process turning light energy into chemical energy. Leaves also play a role in water uptake and osmotic regulation through transpiration. At last, some leaves can store water and nutrients. The usual leaf is constituted by the following elements: the blade or the lamina is a thin photosynthetic tissue ; the vascular network (midvein and secondary veins) that ensures the transport of nutrients ; and the petiole connecting the leaf to the stem. Finally, the bud is located at the connection between the petiole and the stem. Leaves are usually almost symmetric along their midveins but present a strong anatomical asymmetry between their upward and downward faces³. These faces are referred to as adaxial and abaxial faces respectively.

Different types of leaves Despite a clear—and almost unique—physiological role, leaves present an astonishing diversity of shapes. Leaf shape differences lie in the blade characteristics. Botanists resort to numerous terms to describe and classify the shape of a leaf that answer the following questions: What is the global shape of the leaf? What are the shapes of its apex, base and margin?

In particular, the blade can be more or less divided. These divisions create indentations—more or less deep—and lobes of various sizes and shapes. In some cases, indentations are so deep that the blade is discontinuous and forms independent leaflets. Such leaves are called compound leaves, in opposition with simple leaves. Several degrees of blade division, or pinnation, exist: simply pinnate or compound (eg. *Juglans*, chestnut tree), bipinnate (eg. *legumiceae*, *Caesalpinia* sp., *Mimosa pudica*) or even tripinnate (eg. *Moringa oleifera*). In compound leaves, the midvein is completely disconnected from the blade and is in the perfect continuity of the petiole. We call it the rachis. By definition, the rachis starts after the first leaflet. Each leaflet is connected to the rachis by a second order petiole called the petiolule.

³This is often referred as bilateral symmetry

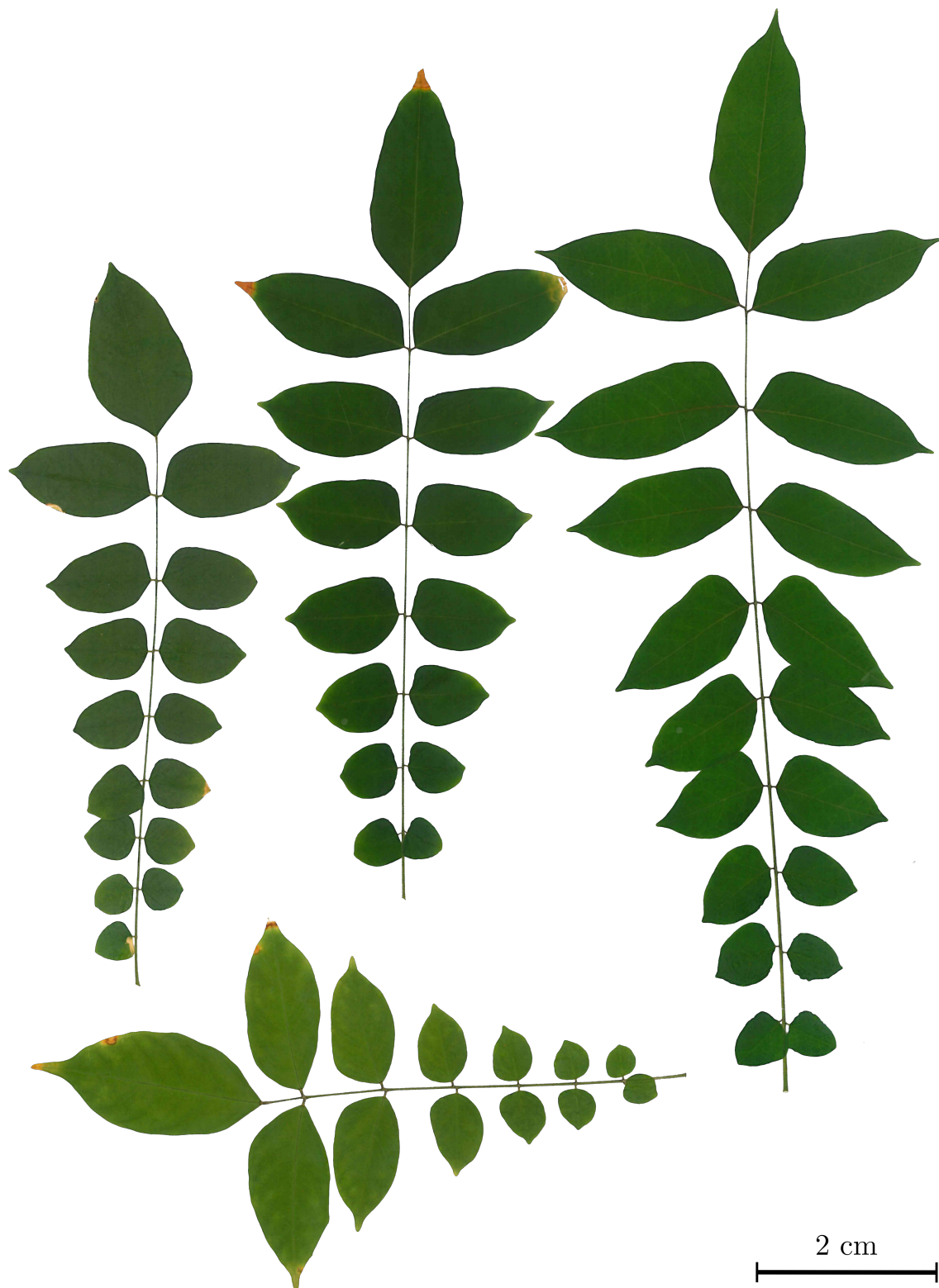


Figure 2.2: **Herbarium:** four mature leaves of *Averrhoa carambola*. Each leaf has an odd number of leaflets. The aspect ratio of leaflets increases from the petiole to the apex (position effect). The asymmetry of leaflets around their midveins is particularly visible for leaflets close to the apex. The presented leaves were not taken on the same plant and had not the same position on the principal stem.

2.2.1 Shape and anatomy of the leaves

Averrhoa carambola leaves belong to the category of compound leaves. The most important characteristic of compound leaves is the arrangement of their leaflets. Carambola leaves are imparipinnate, *i.e.* once-compound, with an odd number of leaflets. Leaves usually bear from 5 to 19 leaflets, depending on the age of the branch or stem they are connected to. The leaflet arrangement on the rachis is said to be alternate. This means that the leaflets are placed on the opposing lateral sides of the rachis, with their petiolules being not perfectly aligned (see figure 2.2). In the case of *Averrhoa carambola*, two facing petiolules are usually close enough. In addition to that, two successive petiolules on the same lateral face of the rachis are well separated. This creates the impression that leaflets are grouped in pairs, except for the apical one which stands alone. To further describe carambola leaves, we can take a look at the rachis. The rachis is almost circular, with a radius of about 1–2 *mm* at its basal end. As we get nearer to its apex, the rachis becomes thinner and thinner. The rachis is densely covered with unicellular short hairs called trichomes. At last, the bud is located at the connection between the stem – or the branch – and the petiole, on the adaxial face of the petiole (see figure 2.3).

The global shape of the leaf evolves throughout its development. During the growth of the leaf, the rachis is hook-shaped, as for many other compound leaves. When the leaf reaches maturity, its rachis is straight and makes a certain angle with the vertical which is called the gravitropic set-point angle. Carambola leaves usually have $\theta_{gsa} \simeq 30^\circ$. At last, all the leaflets of the leaf are coplanar when maturity is reached.

The shape of a leaflet can be described with the usual morphological glossary dedicated to leaves. Leaflets are laminar and elliptic, but their shape is not the same along the rachis. There is a gradient of the aspect ratio of the leaflets along the rachis (see figure 2.2). The closer we get to the apex, the bigger the aspect ratio. Leaflets are also slightly asymmetric around their midvein. The half-blade which is the closest to the base of the leaf is in general thinner. This is however not the case for the apical leaflet which is completely symmetrical. The apical part of the leaflet ends up in a short tapering tip. It is said to be acuminate. Depending on the position of the considered leaflet on the rachis, the tip is more or less prominent. The basal part of the leaf is rounded near the petiole and becomes more and more acute near the apex. The margin of the leaflets is completely smooth, with no indentation at all and are said to be entire. At last, to achieve a complete description of the leaflet, let us describe its vascular network. Secondary veins derive from the midvein in a

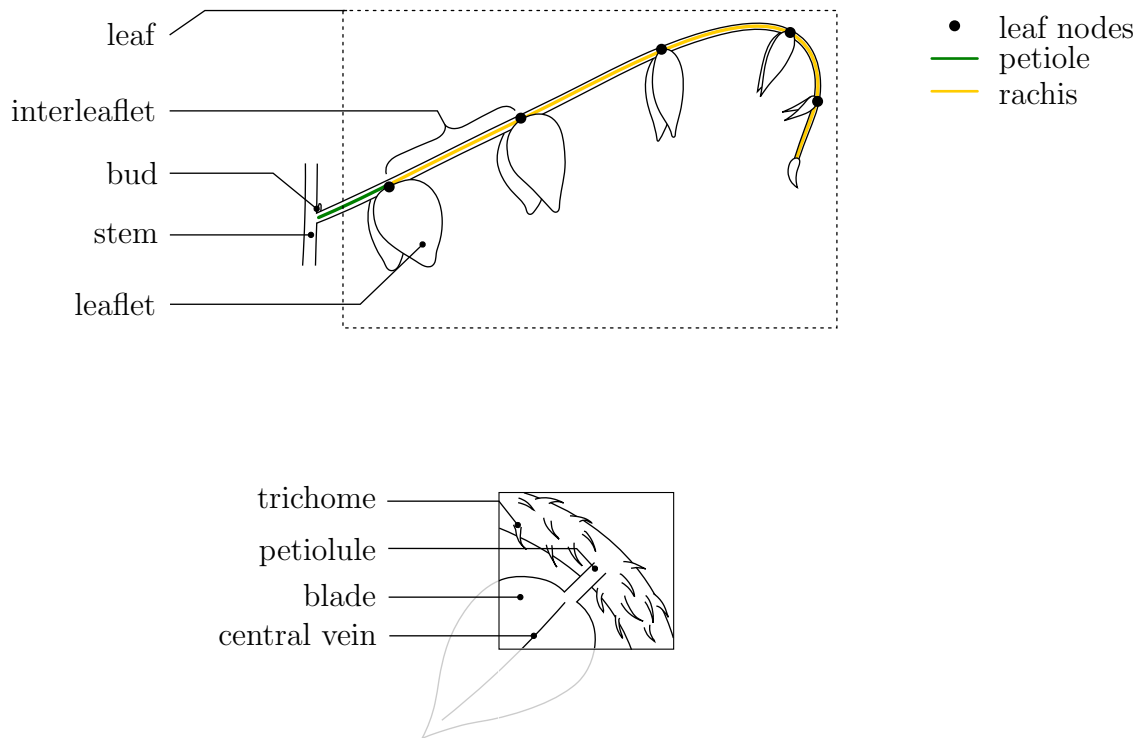


Figure 2.3: **Drawing of a growing *Averrhoa carambola* compound leaf.**

alternate fashion. Near to the margin of the leaflet, they branch to their neighbour and form closed loops in which are enclosed most of the higher order veins. Such a venation pattern is pinnate and brochidodromous.

In order to precisely describe the development and motions of *Averrhoa carambola* leaves, let us define smaller units of the rachis, by analogy with the stem. The attach points of leaflets will be referred as ‘leaf nodes’. Two successive leaf nodes define an interleaflet (topological equivalent of an internode). A numbering convention can then be established to label the successive interleaflets. Strictly speaking, the petiole is not part of the rachis and is set to 0. The following interleaflets are numbered from 1 onwards.

2.2.2 Histology of the rachis

As we will later discuss it, the rachis is of particular importance for the global shape and most of the motions of *Averrhoa carambola* leaves. According to the differential growth hypothesis, some tissues of a moving leaf have to grow in an anisotropic manner. What are the tissues that are likely to display such a growth behaviour? In order to answer this question, let us take a look at the inner anatomy of the rachis. In the following paragraphs, we will describe the anatomy of a *mature* rachis.

A striking characteristic of the rachis is its hairiness. The trichome coverage of an organ is also used by botanists to precisely describe it. The trichomes of the rachis are sharp and lightly curved, soft with a single tip (unbranched). *Averrhoa carambola* rachis is said to be villous. Right beneath the trichomes, one can see the epidermis of the rachis. The epidermis consists in a single layer of cells delimiting the environment and the plant. Under the epidermis lies the cortex. It is composed of several layers (here four) of thin-walled cells. Some of these cells – mostly those on the adaxial face of the rachis – enclose chloroplasts (see the greenish half-ring in fig.2.4) or amyloplasts.

Beneath the outer layers we have just described, we find a ring of thick-walled cells. They form what we call bast fibres or sclerenchyma. The sclerenchyma cells are actually lignified. Their walls have been made impermeable by the deposition of lignin, an hydrophobic substance. As a result, all the cells belonging to the bast fibre ring are dead.

We now enter the innermost tissues of the rachis. Among these tissues, we find the vascular tissues that allow the transport of water and nutrients within the plant. As we will see it in Chapter 3, the vascular tissues form isolated bundles in the young rachis. Quite the contrary, for a mature rachis, the vascular tissues form a complete ring. This ring has replaced the initial provasculature via the maturation of the cambium. We first encounter the phloem which is composed by thin-walled cells and ensures the transport of photosynthesis products from the leaf to the others parts of the plant. Under the phloem lies the xylem. The main purpose of the xylem is to transport basic nutrients and water from the roots to the upper parts of the plant. It contains bigger cells than the phloem and is totally lignified⁴. At last, the most central tissue of the rachis is a parenchyma. It is made of very large cells, in comparison with the rest of the stem, with thin walls. This is what we call the medullar parenchyma, medulla or pith. The pith is involved in both the transport and the storage of nutrients.

The description of the inner tissues of the rachis reveals its strong anatomical similarities with stems. This organization and succession of tissues is typical of plant stems. The rachis of *Averrhoa carambola* is thus likely to follow the same developmental path than a typical stem. From a young stem to a mature stem, the most significant changes take place within the vascular tissues. Phloem and xylem are initially procambium cells that will differentiate during primary growth. Pith cells also considerably expand. At last, at the boundary with dermal tissues,

⁴The word ‘xylem’ actually derive from the Greek word for wood.

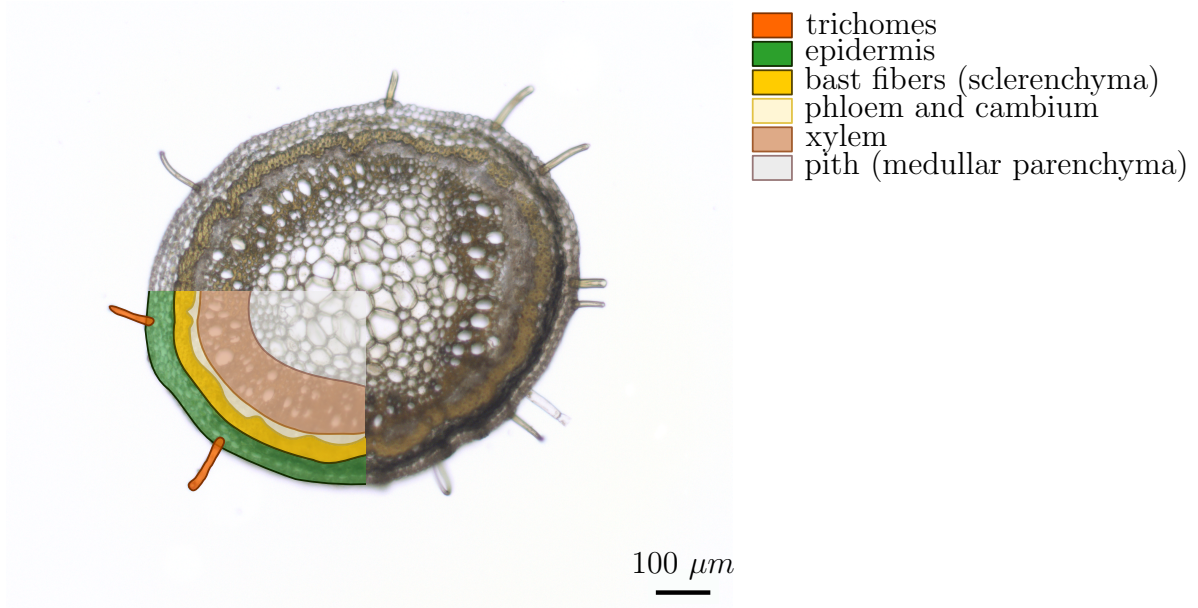


Figure 2.4: **Transverse cut of the rachis of *Averrhoa carambola*.**

bast fibres are initially absent. We have now pinpointed three different tissues that display important anatomical changes during the rachis development. In conclusion, these tissues (the pith, phloem and xylem precursors and bast fibres precursors) may be linked to differential growth – and to the observed motions.

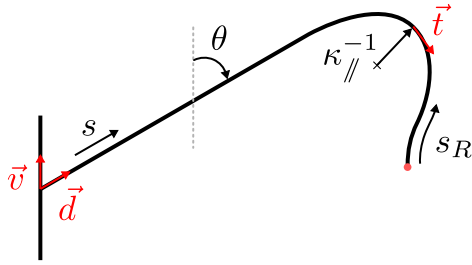
2.2.3 Geometrical parametrization

It is now necessary to set a geometrical framework to describe—in a proper and consistent way—both the shape and the motions of the leaves. As we will see later, the motions are performed by only two distinct anatomical elements of the leaf: the rachis and the leaflets.

The first step is to reduce the rachis to a curve, typically its midline. The geometrical parametrization of the rachis can be broken down into two independent parts. Depending on the studied motion we consider two different planes. For each of these planes, it will be possible to define at least an arc length, a local orientation and a local curvature for the midline of the rachis. By reducing the rachis to a line, we lose some information about its shape. This is why we also define the local thickness of the rachis which is set equal to $2R$ where R is the radius of the rachis.

Two directions are remarkable in the anatomy of the leaf: the vertical, roughly indicated by the stem, and the direction defined by the rectilinear, mature parts of the rachis. These two directions are represented by the vectors \vec{v} and \vec{d} respectively

side view parameters:



top view parameters:

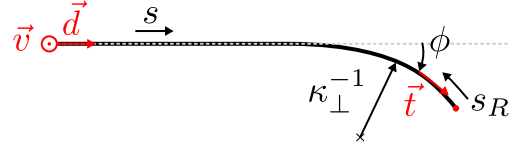


Figure 2.5: **Geometrical parameters describing the rachis.** We define the arc length s , the reverse arc length s_R . The local orientation of the rachis with respect to the vertical is described by θ . The local orientation with respect to its principal direction \vec{d} is given by ϕ . The corresponding curvatures are κ_{\parallel} and κ_{\perp} respectively.

(see figure 2.5). They define a plane (π) that will correspond to our side-view takes. We define two arc lengths spanning the rachis' midline: s from the base to the apex, and s_R in the other way. A local tangent vector $\vec{t}(s)$ can be associated to the midline, and we define the local orientation θ of the rachis with respect to the vertical as $\theta(s) = (\vec{v}, \vec{t}(s))$. Finally, the curvature of the rachis in (π) is labelled as κ_{\parallel} .

All the motions of the rachis that do not occur in (π) will be referred as out-of-plane motions. To describe these motions, we use a second set of geometrical parameters that correspond to a top view of the rachis. As in the previous case, we define the arc length s and the reverse arc length s_R . Here, a natural choice for the local orientation of the rachis is $\phi = (\vec{d}, \vec{t}(s))$. It corresponds to the angle of deflection of the rachis with respect to its principal direction. Finally, the curvature of the rachis in the top view parametrization is labelled as κ_{\perp} .

It is essential to note here that the motions—hence the shapes—we will describe and study are in three dimensions. This is why the geometrical quantities defined above need to be considered carefully. They actually all correspond to projected quantities and do not account for the 3D geometry of the organ. In the top view in particular, because of the typical hook shape of the leaf, the apical end of the rachis is seldom visible. As a result, the s and s_R cannot span the complete rachis.

To completely describe the shape of the leaf, it is necessary to specify the orientation and position of the leaflets. In a first approach of the mature leaf, we have stated that leaflets were all flat and coplanar, with the petiolules orthogonal to the rachis. Actually, the petiolules are not always orthogonal to the rachis (see fig-

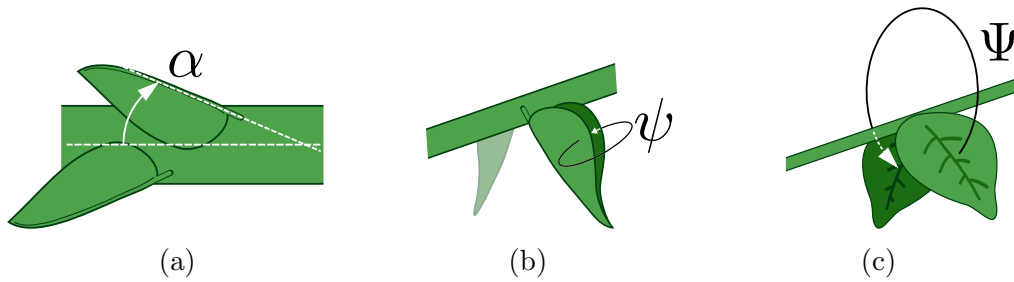


Figure 2.6: **The different angles orientating leaflets.** (a) α is the angle between the rachis and the leaflet, (b) ψ characterizes the opening or flatness of a leaflet, (c) Ψ quantifies the alignment of the two leaflets of a given pair.

ure 2.6a). The angle α varies between 0 and $\pi/2$. Leaflets can also be more or less flat. The degree of flatness of a leaflet is quantified by the angle ψ between its two half-blades (see figure 2.6b). At last, two leaflets of a given pair are can be more or less aligned. In other words, the angle Ψ defined by the two midveins might not be exactly equal to π (see figure 2.6c). Moreover, Ψ could not be equal from a pair of leaflet to another one, or could even evolve in time.

2.3 The different motions of the leaf

Averrhoa carambola is a restless plant. Its leaves are particularly animated, displaying a wide variety of motions throughout the life of the plant. More precisely, the mobile parts of the leaf are the rachis and the leaflets. The rachis only performs growth motions. It bends itself in spectacular ways during its development and stops moving once it reaches a straight shape. Leaflets exhibit several types of motions during their development, and contrary to the rachis, they remain mobile when the leaf reaches maturity. Leaflets move around two essential anatomical axes: the rachis and their own midvein. I will now describe all the motions of the Carambola leaves in the following paragraphs, with an emphasis on growth motions.

2.3.1 Motions of the growing leaf

The growth of *Averrhoa carambola* leaves is mesmerizing to observe. It is during growth that the great variety of the motions of the leaves is plain to see. The growth phase is actually complete from the point of view of motions: growing leaves perform all the different types of movement they are able to. These specific motions are naturally growth motions in the sense that they occur during the primary growth of the leaf. It is not clear, a priori, that these motions rely on a differential elongation mechanism *only*. Their typical time scales vary from a dozen of hours to several

days which clearly categorizes them as growth motions (Forterre, 2013). All these different motions come one after another in a specific and robust order.

Carambola leaves do not develop inside of a closed bud. They develop at the apical end of the principal stem or of a branch⁵. For this reason, it is difficult to state when the leaf begins its development and what exactly is the first motion. During the first developmental stages, when a structure becomes clearly visible at the tip of the stem, the leaf is reduced to a small and compact organ with a cylindrical shape. The leaflets are packed against the rachis and are barely distinguishable by the eye. By comparing this initial state with the typical shapes of a growing and a mature leaf, we see that numerous steps and motions are necessary.

From adaxial hook to abaxial hook The motion I will describe here can be separated into two successive steps and corresponds to the establishment of the typical hook shape described earlier. These two steps consist in slow and opposite bending motions. The typical time scale of the complete motion is of the order of one week but is extremely variable. Once the leafling has initiated its growth and motion, it might stop at any moment for several days to several weeks. Most of the time, brutal environmental changes seem to cause such a ‘freezing’.

First, the rachis progressively elongates and bends adaxially near its apex. If this bending is completely due to differential growth, the adaxial face has to grow faster than the abaxial face. At this moment, the rachis is almost vertical, fairly flat except at its apical end. The leaflets close to the basal end of the rachis can now be easily seen, the outline of the other ones can be distinguished. This could be called the ‘upward’ phase of the motion.

Then comes the ‘downward’ phase of the motion. The leafling keeps growing, but the rachis then bends abaxially, hypothetically through a reversed anisotropy of growth (adaxial growth faster than abaxial growth). This eventually leads to a complete reversion of the curvature of the rachis, that is to say that $\kappa_{//}$ changes sign on a major part of the rachis. This ‘reversing’ motion finally results into the hook shape that is typical of many compound leaves growth.

It is interesting to try and describe the ‘reversing’ motion in terms of the classical nomenclature of plant motions. If we take a step back, we see that this motion is also a change in the global orientation of the leaf. Globally, θ first gets closer to 0 and then increases. Since the changes of orientation occur in the plant

⁵This is what botanists call a *terminal and naked bud*.

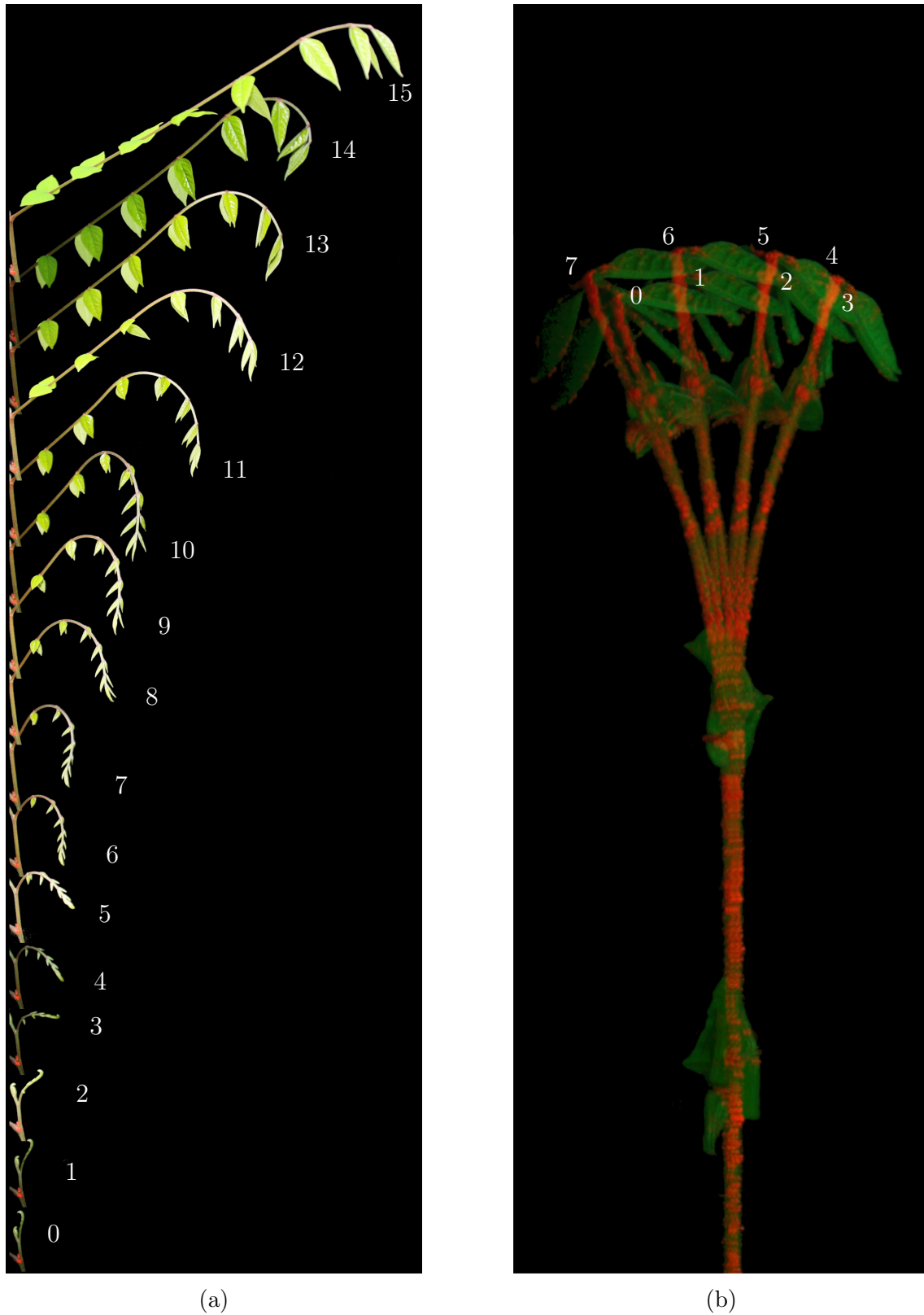


Figure 2.7: **Growth motions of *Averrhoa carambola* rachis.** (a) Reversing motion (0 – 5) followed by the unfurling motion (6 – 15). The typical hook propagates along the rachis (6 – 14) until it almost reaches the apex (15). Pictures were taken every 1000 *min.* (b) Top view of nutation. Pictures were taken every 15 minutes.

(π) and relatively to the vertical, it appears natural to think about gravity. This motion could then be ascribed to a shift from negative to positive gravitropism⁶.

Unfurling The rachis is now hook-shaped. This hook generally extends on a length equivalent to three interleaflets. The final shape of the rachis is rather rectilinear however. This means that the rachis now needs to straighten up *i.e.* $\kappa_{//}$ has to globally nullify. The straightening of the rachis requires an adaxial bending. Once again, this is hypothetically achieved thanks to differential growth where the adaxial part of the rachis would grow in a slower way than its abaxial part.

This straightening motion is progressive and localized. The basal end of the hook unbends— $\kappa_{//}$ locally tends toward 0—while the apical end of the hook remains bent. This process is often referred as the ‘hook maintenance’ in the literature. The hook maintenance results in the translation of the hook along the rachis. It looks like an unrolling or rather an unfurling motion. This translation stops when the hook reaches the apical end of the leaf and the rachis is completely straight. The unfurling motion is usually completed in 8 to 12 days, depending on the vivacity of growth.

The unfurling motion is concerted with growth. The growth behaviour of the rachis can be described by the displacement of a growth zone of fixed length as in stems and roots (Silk et al., 1989; Peters & Tomos, 2000; Bastien et al., 2013). The observation of the unfurling motion easily reveals that once an interleaflet becomes straight its elongation rate rapidly decays. Once the hook outreaches the apical boundary of the interleaflet, its shape is almost fixed. Notably, θ is constant along this interleaflet and is set to the so-called gravitropic set-point angle θ_{gsa} .

As we will see in Chapter 3, this hook shape is typical of numerous compound leaves that eventually reach a flat and straight shape. So, it is likely that the unfurling motion is as widespread in compound leaves as the hook shape.

Nutation The emergence of the final, straight and flat shape of the rachis is a completely three-dimensional phenomena. It is not only accompanied by curvature variations in (π), but also by out-of-plane curvature variations. The rachis bends and unbends in a pseudo-periodical way, as if it were oscillating around a straight state ($\kappa_{\perp} = 0$ along the whole rachis).

⁶The relation between graviception, proprioception and the hook shape is quickly addressed in Appendix A. However, a beforehand reading of Chapters 3, 4 and 5 is recommended.

As already discussed in Chapter 1, many plant organs undergo some oscillatory motions. These are characterized by pseudo-periodical curvature oscillations. In the case of *Averrhoa carambola*, the leaf swings in a pendulum-like manner, from right to left. This motion is simply called nutation⁷.

The typical period τ_{nut} of *Averrhoa carambola* nutation varies between 1.5 hours and 2.5 hours. The angular amplitude $\Delta\phi$ – defined as the amplitude of the local orientation of the apex ϕ_{apex} – of nutation usually varies from 5° to 25° . All the nutation and circumnutation motions are also characterized by their bending zone (Millet et al., 1988), the region where curvature varies in time. This bending zone translates itself along the rachis as time goes. In this sense, nutation is localized. Assuming that nutation only relies on the differential elongation of tissues, the bending zone must be where the differential elongation takes place. The elongation asymmetry associated with nutation is set between the lateral faces of the rachis (not the abaxial and adaxial ones). Starting from a straight state,

- (i) the left side of the rachis could grow faster than the right one for example. This would result in a bending: κ_\perp would increase, the left and right sides would now be the concave and convex sides of the rachis respectively.
- (ii) At some point, ϕ_{apex} would reach its maximum value $\Delta\phi$ and the elongation asymmetry would start to reverse its direction.
- (iii) From here, the whole process is reversed. The left side now grows faster than the right one. The rachis is bending in the opposite direction and reaches a straight state anew: κ_\perp and ϕ_{apex} both decrease and globally nullify.
- (iv) The rachis goes beyond its principal direction given by \vec{d} : κ_\perp and ϕ_{apex} both decrease and become negative. The concave side is now the right one, and the convex side is the left one.

This describes half a period of nutation. From this simple description of nutation we first expect that – at any moment of the nutation motion – the concave and convex sides of the rachis will present different growth status. We also expect that ϕ_{apex} , or $\max(\kappa_\perp)$, and the signal of differential elongation are in quadrature.

A careful observation of nutation reveals some of its interesting and puzzling features. In this paragraph, I propose to list these observations. First, the rachis does not perform nutation during the complete growth process. It seems that the

⁷From the latin word *nutatio* meaning ‘nodding’ or ‘swaying’.

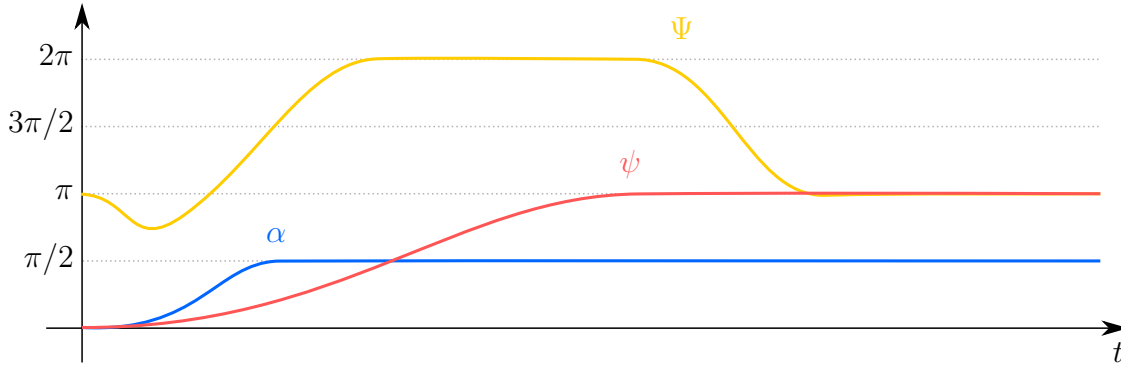


Figure 2.8: **Idealized growth motions of the leaflets.**

nutations motion does not start before the hook has outreached the first or second pair of leaflets. Further than that, the variations of curvature seem to be systematically localized at the basal end of the hook, where the rachis is eventually achieving its unfurling motion.

Taking a closer look at the position of the nutation initiation point – the basal end of the bending zone – it appears that the bending zone leapfrogs from a given interleaflet to the following one.

At last, both the amplitude and the frequency of nutation seem to vary during the day and the night. In most cases, a clear difference is visible in the nutation behaviour between night and day.

Leaflets growth motions Leaflets are already formed and clearly visible before the first reversing motion of the leafing. At this moment, all the leaflets are folded in two along their midveins and packed against the rachis. Their midveins are turned away from the rachis and their lower half-blades are resting on the adaxial face of the rachis. By the end of the development of the leaf, the leaflets will be entirely opened and their midveins orthogonal to the main plane (π) of the rachis. We can imagine from the initial and final states of the leaflets that they have to go through several rotations, around different axes.

The succession of rotations begins with a slight upward rotation of the whole leaflet (Ψ slightly decreases). Then, the leaflet rotates around the point of attachment of the petiole on the rachis. When the reversing of the leafing begins, leaflets start to get away from the axis of the rachis and α consequently increases up to $\alpha \simeq \pi/2$. At the same time, the leaflet begins to fall slowly *i.e.* Ψ increases. At the moment when the hook shape of the rachis is set, the leaflet points downward ($\Psi \simeq 2\pi$) and its midvein faces the base of the leaf. Then, while the unfurling of the rachis is progressing, the leaflet unfolds and opens up. The angle ψ goes from

almost 0 to almost 2π . Once the blade of the leaflet is entirely flat, Ψ increases until $\Psi \simeq \pi$ and the two leaflets of the pair are orthogonal to the (π) plane again. From this point, the leaflet will not display any growth motions. Its development is not over though. When the rachis is locally straight around a given leaflet, it starts its areal expansion. This final step can last several days.

It is important to note that leaflets do not perform these motions in a concerted manner. More precisely, the two leaflets of a given pair usually move in a coordinated way, but the motions of two different pairs of leaflets will be time-delayed: when the basal pair of leaflets is completely open, the leaflets of the tip are still packed against the rachis. This remark can actually be generalised to all the other growth motions by considering the time-delays between larger anatomical units of the leaf: its interleaflets.

2.3.2 Motions of the mature leaf

Similarly to many other leaves, *Averrhoa carambola* leaves remain mobile once their growth is over. The diversity of motions is now much reduced since—under normal conditions—the only moving part are now the leaflets. More precisely, leaflets are animated by their petiolules and now only move around a single anatomical axis: the rachis. There is no more motion of the half-blades around the midvein. All the mature mature motions that I will present in the following paragraphs consist in variations of Ψ .

The typical time and length scales involved in mature motions indicate that they belong to the class of ‘hydraulic movements’ that include growth and swelling motions (Dumais & Forterre, 2012). Mature motions however present a fundamental difference with the preceding motions: they are completely reversible. The mechanism underlying the motions of the mature leaf is by definition necessarily different from differential growth. They must rely on a differential swelling mechanism like the motions of *Mimosa pudica* leaves for example (Tamiya et al., 1988; Vanden Driessche, 2000).

Therefore, the following motions rely on a pulvini-like mechanism, localized in the petiolule of each leaflet. To make the leaflet fall, some of the cells of the abaxial face of the petiolule have to be partially plasmolysed while the adaxial face stays turgid. On the contrary, to make leaflets raise again, the abaxial cells have to increase their water content and become turgid again.

The diversity of *Averrhoa carambola* mature motions mostly lies in the typical time scales⁸, the extent to which Ψ is modulated and the sensitivities associated to

⁸These motions remain faster than growth motions though.

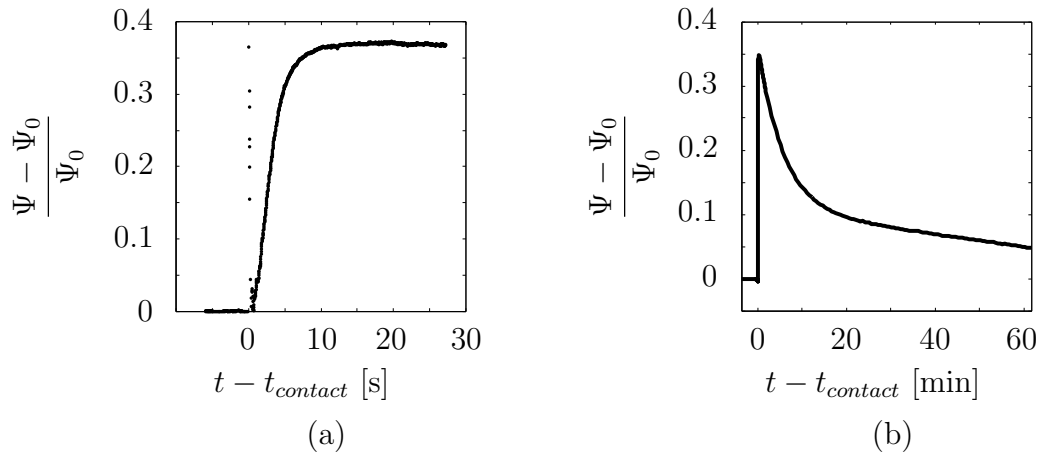


Figure 2.9: **Seismonastic motion of *Averrhoa carambola***. The instant $t = 0$ corresponds to the moment of the perturbation. (a) Closure response of the leaflets. Oscillations after contact correspond to artefacts due to the global motion of the leaf. (b) Closure and opening over an hour. These graphs correspond to different experiment run on the same pair of leaflets.

the different motions.

Seismonasty *Averrhoa carambola* leaflets are sensitive to the touch, or more generally to mechanical stimuli. This similarity between the carambola and the *Mimosa pudica* has struck some naturalists as soon as 1783 (Bruce, 1785). Like for *Mimosa pudica*, it is possible to trigger leaflets independently. Carambola leaflets however respond to mechanical stimuli in a lesser way. More violent stresses are needed to trigger the reaction motion which is also slower than in the case of *Mimosa pudica* and the petiole is not mobile. Carambola leaflets quickly fall and Ψ reaches a plateau in a dozen of seconds (see figure 2.9a). Here, an exponential fit on the closure motion revealed a characteristic closure time $\tau \simeq 2$ s. Leaflets then slowly recover their original orientation. Twenty minutes after the mechanical perturbation, Ψ is still 10% superior to its initial value (see figure 2.9b). For the experiment pictured in 2.9a, the total recovery of the initial position of the leaflets was observed 2 h after contact.

It is interesting to note that the maximum value of Ψ is generally different from 2π . In his letter, Robert Bruce states that leaflets ‘*move themselves downwards, frequently in so great a degree that the two opposite almost touch one another by their under sides*’. I have not been able to reproduce such motion in the lab with a simple pat though. I have tried applying repeated mechanical stimuli of the leaflets once Ψ is stabilized on a maximum value. But no further evolution of Ψ was noticed.

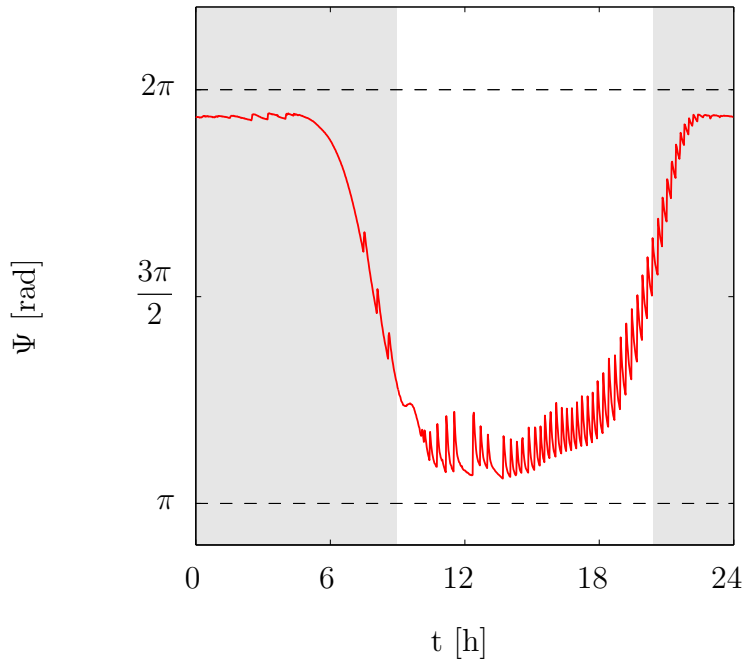


Figure 2.10: **An example of the nyctinastic motion of *Avertrhoa carambola*.** The leaflets rise during the day and fall down at night. In this case, the closure motion is perturbed by grouped and incessant ‘nervousness’ motions. Gray/white backgrounds indicate night/day respectively.

It is possible that a simple pat is not sufficient to trigger a complete fall down of the leaflets. Continuous or periodical mechanical stimulation (eg. plant on a shaking platform⁹) could be strong enough to make the leaflets go to $\Psi \simeq 2\pi$.

Nyctinasty Like many other plants, such as the *Mimosa pudica*, *Avertrhoa carambola* displays nyctinastic motions. More precisely, the position of its leaflets evolve according to the alternation of day and night (see fig. 2.10). During daytime, *Avertrhoa carambola* leaflets are usually aligned ($\Psi \simeq \pi$). At night, the leaflets fall down until they almost touch each other ($\Psi \simeq 2\pi$). Finally, at dawn, the leaflets raise again and recover the alignment characteristic of daytime ($\Psi \simeq \pi$). Thus, nyctinastic motions involve a single rotation of the leaflets around the axis of the rachis in *Avertrhoa carambola*. Note that, however, the extent of this rotation vary from a plant to another. The closing value of Ψ might thus be much less than 2π in some cases. The ascending and descending motions of the leaflets are initiated a few hours earlier than dawn and dusk respectively. This suggests that the plant has adapted its own (circadian) rhythm to the environmental condition in which it lives.

⁹We have observed that the leaflets completely fall down after a train ride which can be shaky!

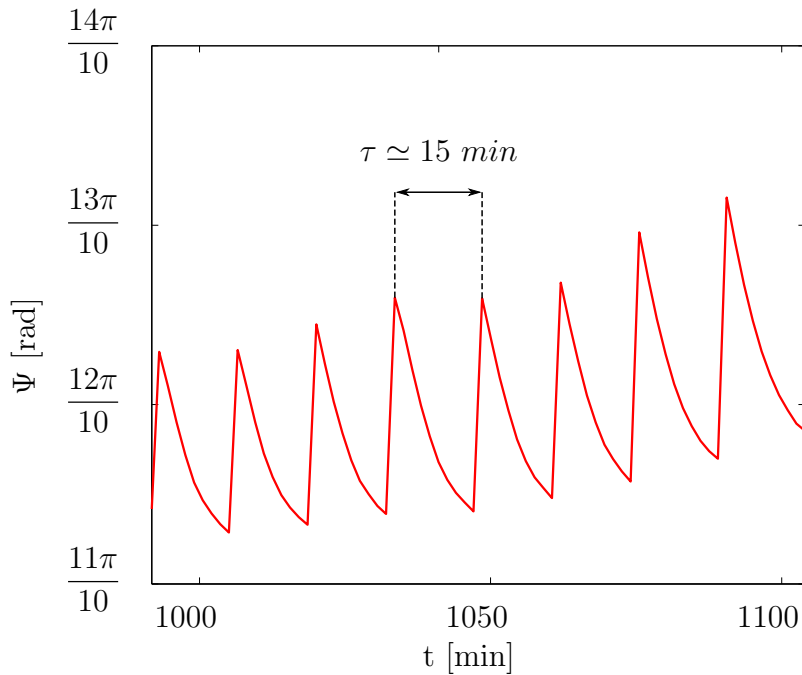


Figure 2.11: **Zoom on the ‘nervousness’ jolts.** Leaflets are animated by sudden falls during daytime. Here, they repeat with a characteristic period of about 15 min (same data than in fig. 2.10).

‘Nervousness’ motions The qualitative difference between the ascending and descending phases of nyctinasty is puzzling. We see that while the ascending phase of the motion is smooth, the descending motion is quite jolty. The descending phase of nyctinasty is accompanied by a succession of ‘nervousness’ motions until the leaflets reach their night position. Such jolts have already been reported for *Averrhoa carambola* (Ulrich, 1911), but also in the case of *Averrhoa bilimbi* (Darwin & Darwin, 1880). Like in the case of the seismonasty, Ψ reaches a maximum value Ψ_{max} in a few seconds and slowly decreases. The value of Ψ_{max} is not always the same for a given leaflet. In the exposed example, the jolts are spaced of about 15 min (see fig. 2.11). The behaviour presented here is somewhat extreme as the leaflets undergo numerous jolts. In other cases, the number of jolts was much more reduced.

We refer at these jolts as ‘nervousness’ motions since they are not clearly associated to any sensitivity and seem completely autonomic. They could be triggered by some air displacements (wind?), but considering the difficulty to trigger nastic responses by patting the leaflets this is not the most likely. The leaflets jolt mostly during daytime, making light a possible cue for these motions. But its influence is not clear as jolts remain in its absence. These nervousness jolts might be tightly connected to the osmotic regulation within the pulvini of the petiolules.

Finally, we see how the motions that remain at maturity are similar—at the level of their trajectories—to the developmental motions of the leaflets for *Averrhoa carambola*.

2.4 Discussion and conclusion

Averrhoa carambola compound leaves display a wide variety of motions. Its different motions and their succession is also a perfect illustration of the vision of plant motions developed in Chapter 1. The rachis unfurls in a typical hook shape and, in the same time, is animated by a quite enhanced nutation motion. The leaflets, initially folded and packed against the rachis, slowly unpack and unfold. When they reach maturity, *Averrhoa carambola* leaflets also display two kinds of reversible motions: seismonasty and nyctinasty. These two motions have different time scales but share the same trajectory. Their trajectories recall the unpacking of the leaflets during growth, consistently with the idea that reversible plant motions are a regression of some irreversible plant motions. The motions displayed by *Averrhoa carambola* actually span the most of the known motions in the plant kingdom. They also occur at several scales—from the petiolule to the whole rachis—and with different timescales—from seconds to days.

Arabidopsis thaliana has been the usual plant model since the 1990s and should naturally be considered for the study of plant motions. Among the strong advantages *Arabidopsis thaliana* provides the experimentalist are the wide palette of available mutants. As a matter of fact, its genome has been entirely sequenced and allows proper biological investigations of the genetic regulation of growth and motions. Despite this incontestable advantage, the motions of *Arabidopsis thaliana* are little diversified. The leaves of its rosette go through successive epinastic and hyponastic motions throughout their development (Dornbusch et al., 2014) that could be interpreted as an oscillatory motion. Its inflorescence stems also display circumnutation (Schuster & Engelmann, 1997) and, when mature, are able to correct their posture thanks to tropisms (Bastien et al., 2013). Finally, no reversible motion is kept at the maturity stage. So, *Arabidopsis thaliana* is a powerful plant model to explore the genetic aspects of growth, posture regulation and their associated motions. But it does not allow a complete study of plant motions. A comprehensive approach of plant motions can be carried out on plants showing a wider diversity of motions. A lot of questions can be addressed on growth and motions—outside the field of genetics—on the grounds of biological physics and histology. These questions can then lead to hypothesis on genetic regulations that will then be testable on the

model *Arabidopsis thaliana*. Conversely, the study of plant motions is also a way to test the generality of recent findings on the growth of *Arabidopsis thaliana*.

In this sense, *Averrhoa carambola* is a strong model for the study of plant motions. The rachis of its compound leaves—and its growth-driven motions—is of particular interest to understand the interplays between growth and motions. Consistently with the vision developed in Chapter 1, we are now going to study the motions in the logic of their succession: unfurling, then nutation.

Chapter 3

Hook shape of the growing leaf

Contents

3.1 Kinematics of leaf unfurling	47
3.1.1 Experimental approach	47
3.1.2 Bent zone and growth zone	49
3.2 Macroscopic mechanics of the hook	52
3.2.1 Experimental approach	52
3.2.2 Data analysis	55
3.2.3 A first look at shape and self-weight	57
3.2.4 Mechanical properties in time	59
3.2.5 Links with lignification	63
3.3 Discussion and partial conclusion	65

The most striking characteristic of growing *Averrhoa carambola* leaves is their hooked shape. This hook shape is found in many plant organs such as hypocotyls or inflorescence stems. Among compound leaves, the typical hook shape of the growing rachis is found across a large span of genera, species and places (see figure 3.1). These leaves eventually reach straightness through the unfurling motion introduced in chapter 2. *Averrhoa carambola* is a typical illustration of this behaviour.

This motion and its associated shape are puzzling. The maintenance of a steady hook shape during growth—which is by essence a dynamic process—is a first surprise. Wendy Silk perfectly captured this apparent paradox in one of her titles ‘Steady form from changing cells’ (Silk, 1992). Such a behaviour necessarily implies specific kinematics for both curvature and elongation. This is why, in a first section, we will discuss the kinematics of leaf unfurling. Another source of questions is

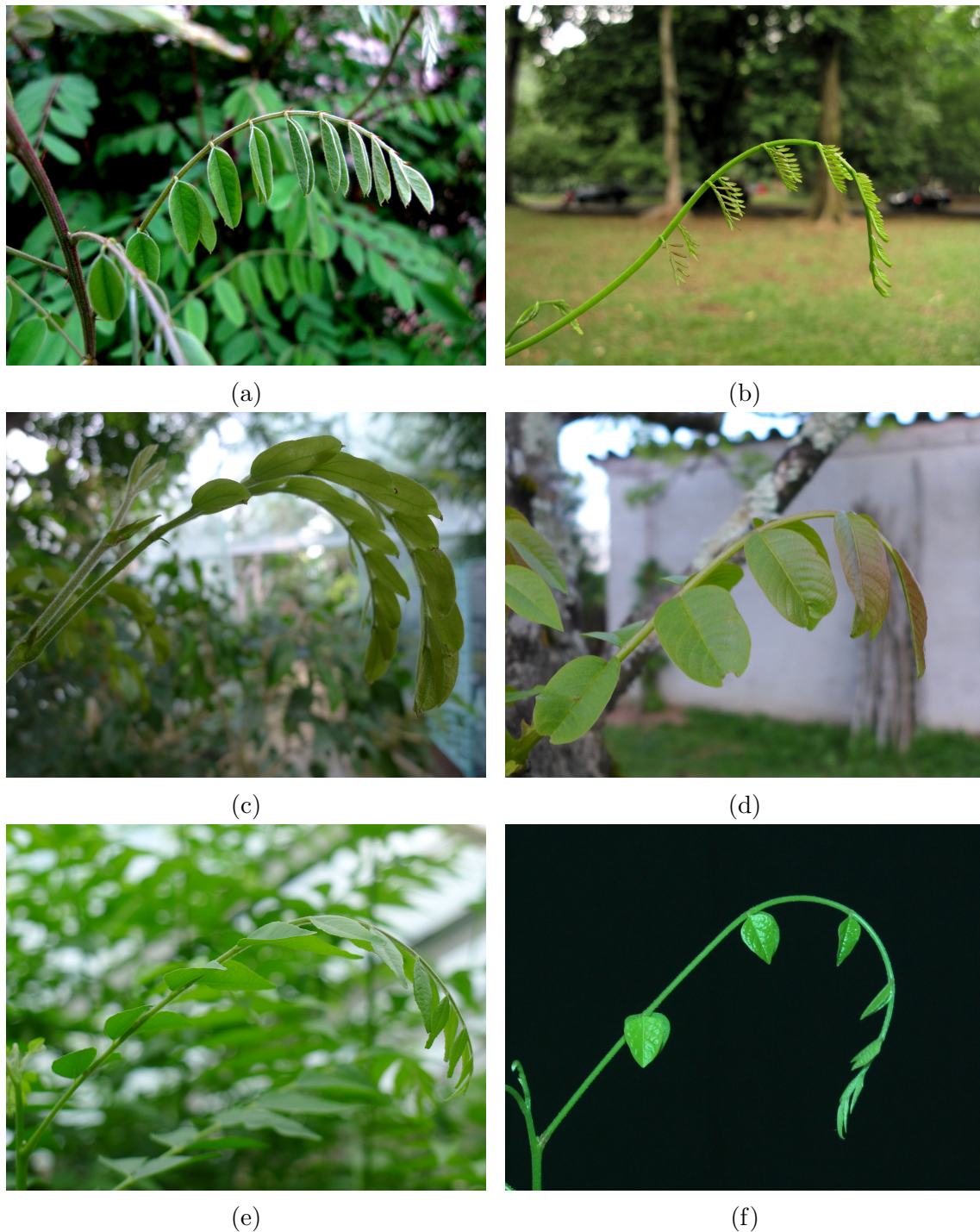


Figure 3.1: **Six examples of hooked rachis in compound leaves.** (a) *Amorpha fruticosa* (b) *Sandora wallichii* (c) *Calliandra haematocephala*, Jardin des Plantes, Paris (d) *Juglans regia*, Villefranche de Rouergue, France (e) *Murraya koenigii*, Cambridge University Botanic Garden (f) *Averrhoa carambola* cultivated in the laboratory. Images (a) and (b) from (Rivière et al., 2017) supplemental information.

the hook shape itself. Such a curved shape naturally evokes buckling phenomena. Could the leaf then be a passive outcome of the interplay between its self-weight and mechanical properties? The active/passive character of motions and shapes will be discussed in a second section through the analysis of the mechanical properties of the rachis.

This third chapter will thus be driven by two major questions: how can we explain the hook shape? How does this shape evolve in time?

3.1 Kinematics of leaf unfurling

The unfurling motion consists in the progressive unbending of the rachis in its principal direction of growth. The maintenance of a hook—and its eventual opening—at the apical part of the rachis may resort on specific time and spatial patterns of curvature variations. For these reasons, a proper quantification of the curvature is likely to reveal mechanisms underlying the unfurling. To this end, we will set our work in the framework designed by Erickson and Silk for the study of plant motions, inspired from fluid dynamics (Silk & Erickson, 1979).

This thesis is rooted in previous unpublished results in the team, notably obtained by Amina Saadani and Yoann Corre, two former interns. I will now detail the used approach and the results it has brought.

3.1.1 Experimental approach

For the described experiment, we want to analyse the spatial and time evolution of the side-view curvature $\kappa_{//}$ of the rachis. A camera was thus placed in the plane (π) and pictures were taken every 5 minutes.

The pictures are then analysed in order to extract the curvature of the rachis. Images are made binary—*i.e.* black and white only—by applying a threshold on their green channels. The contours of the rachis are determined and the skeletons are then derived by an algorithm that was previously developed in the team (Couturier, 2009). The algorithm is based on the Voronoi diagram of the contour. The Voronoi diagram of a given set of points—often referred as seeds—basically consists in dividing the plane into regions based on the distance to each seed. Each seed is associated to a single region—called a Voronoi cell—which contains the points of the plane that are closed to the considered seed than to any other seed. These cells are obtained by using the perpendicular bisector of all the segments defined by the considered seeds with all the other ones. Voronoi cells are thus polygons which

vertices are equidistant to at least three seeds. In the case of a closed shape, the Voronoi vertices which are located within the shape define its midline.

Voronoi-based algorithms for skeleton extraction have proven to be efficient in a large diversity of cases. They have been successfully used for hypocotyls and coleoptiles (Bastien et al., 2013), diverse networks such as in lungs (Clément et al., 2012), intestines or gastric organs. Here, the leaflets make it difficult to use this technique. The first reason is that leaflets hide significant parts of the rachis during the day, when $\Psi = \pi$. The hidden proportion of the rachis also evolves during acquisition because of the nervousness and nyctinastic motions of the leaflets. The second reason is that leaflets make the global shape of the leaf more complex than a single cylindrical rachis. As a result, Voronoi-based skeletons systematically fail around leaflets. In such cases, further numerical treatment is thus needed. The retrieved skeleton is affected by the contour of the leaflets at a range that partly depends on the smoothing process that is applied to the raw skeleton. One of the possible workarounds is to fit the skeleton with Bézier curves. Bézier curves are parametric curves that are used for their smoothness and regularity. By doing so, we retrieve a smooth skeleton and get rid of the artefacts due to the leaflets.

The different needed geometrical quantities are then derived from the skeleton in a straightforward manner. The arc length s of the skeleton is defined as the cumulative distance from the base of the skeleton to its apex. The local orientation θ of the rachis is obtained from the Cartesian coordinates of the skeleton, and the curvature $\kappa_{//}$ is obtained by differentiating θ with respect to s .

The evolution of $\kappa_{//}$ is then represented by using spatio-temporal diagrams. A spatio-temporal diagram is a graph displaying both the space and time evolution of a given quantity. Basically, the two axes are the arc length s of the skeleton and time t . The quantity of interest—the curvature $\kappa_{//}$ of the rachis in (π) —is represented by a heat map. A spatio-temporal diagram essentially is a matrix. Creating the spatio-temporal diagram of a given experiment thus requires to interpolate the represented data on a regular space-time grid.

Finally, let us define the usual vocabulary used to characterize the growth behaviour of a plant organ. The following definitions will be used in this whole thesis. Growth is generally understood as the irreversible volumic increase of the considered organ. Since we are dealing with the primary growth of *Averrhoa carambola* leaves, growth manifests itself through the elongation of the rachis. To measure the growth of a complete organ or any subsection, the relative growth rate (RGR) is

used (Erickson & Sax, 1956). Let L be the length of the organ of interest. Then, the relative growth rate is given by

$$RGR = \dot{E} = \frac{1}{L} \frac{dL}{dt} \quad (3.1)$$

and simply corresponds to the relative elongation of the considered part of the organ. The growth behaviour of an organ can also be studied in a more local way, to precisely know the spatial variations of elongation along an organ for example. Doing so however requires to keep track of material points and build small increments of the studied organ of length, say, δl . The relative elemental growth rate (REGR) is then defined in an analogous manner than the RGR (Erickson & Sax, 1956):

$$REGR = \dot{\varepsilon} = \frac{1}{\delta l} \frac{d\delta l}{dt} \quad (3.2)$$

Of course, the relative growth rate simply corresponds to the spatial average of the relative elemental growth rate over the length of the considered organ.

3.1.2 Bent zone and growth zone

The results presented in this section were all obtained on the same *Averrhoa carambola* leaf, during an acquisition that lasted for 250 hours, that is to say almost 10.5 days. The spatio-temporal diagram of the curvature $\kappa_{//}$ is shown in figure 3.2. For the purpose of this graph, the profiles $\kappa_{//}(t)$ had been smoothed thanks to a moving average over 5 h .

First, this spatio-temporal diagram shows us the extent of the total elongation of the rachis. The total length $L(t)$ of the rachis is indicated by a solid black line on the left obtained from the extremities of $\kappa_{//}(t)$ profiles. The length of the rachis is initially of 2 cm and increases up to 25 cm on the duration of the experiment. We also see changes in the relative growth rate (RGR). We can distinguish three regimes of increasing RGR: from $t = 0 h$ to 50 h , from 50 h to 175 h and finally the RGR approximately stays constant up to the end of the experiment.

Second, we distinguish on the diagram three different types of motions. From $t = 0 h$ to 70 h , the rachis is strongly curved at his base. Curvatures decreases along the rachis to end with a negative curvature at the apex. This negative curvature is the signature of the end of the reversal motion at the apical extremity of the leaf. Then, the region of strong curvature translates along the rachis until $t = 110 h$. From this moment, the position of the bent zone with respect to the apex is almost constant. Its position $s_c(t)$ is marked with a dotted line in figure 3.2. For any point

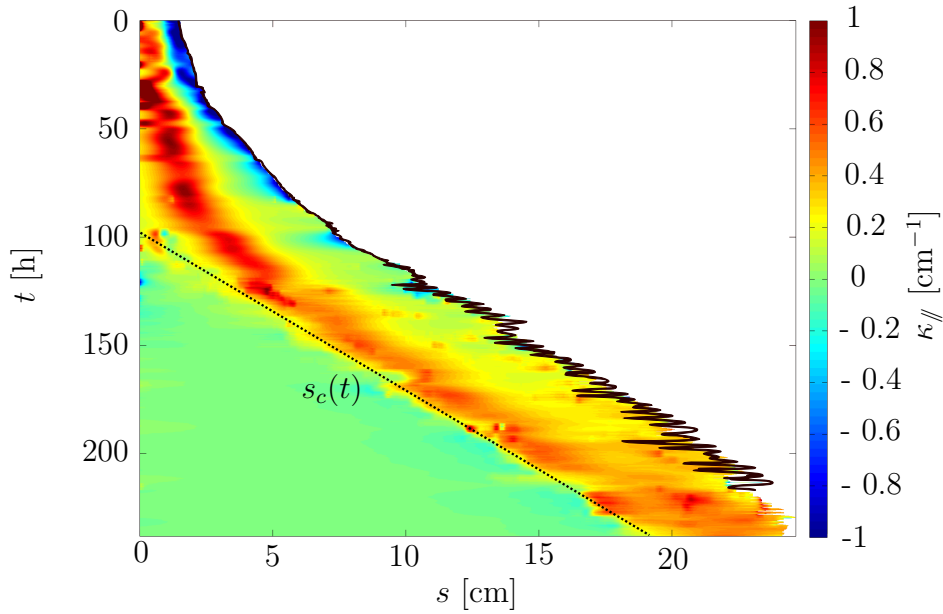


Figure 3.2: **spatio-temporal diagram of $\kappa_{//}$ along the rachis.** The arc length used in this graph is the regular arc length s . The point $s = 0$ is situated at the base of the leaf. The total length $L(t)$ of the rachis is indicated by a plain black line. The arc length $s_c(t)$ indicates the position of the bent zone. Courtesy of Yoann Corre.

such that $s < s_c$, $\kappa_{//} \simeq 0 \text{ m}^{-1}$. So we see here that the rachis has shifted from a totally curved shape to the typical hook shape of compound leaves, with a straight part and a curved part near the apex. The rachis is now unfurling. At last, we notice that $L(t)$ oscillates from $t = 120 \text{ h}$. These oscillations of the total length of the rachis are not physical. They actually correspond to the out-of-plane motions of the rachis, that is to say nutation. Since the rachis bends and unbends in a plane orthogonal to (π) , its apparent length in the retrieved images is affected.

We have just seen that a bent zone at fixed distance from the apex underlies the unfurling motion. According to our description of plant motions in Chapters 1 & 2, we expect the unfurling motion to be driven by differential growth. So, we can wonder what are the relationships between the bending zone and the growth behaviour of the rachis. The global RGR of the rachis gave us information on the global kinematics of growth but fails in providing local information on growth. To go beyond this limitation, we are now going to study the trajectories of the leaflets along the rachis (see figure 3.3a). This will give us information on the elongation of each interleaflet of the rachis. Let us consider the first interleaflet, which is limited by the trajectories 1 and 2. We see that the gap between the trajectories quickly increases between $t = 0$ and $t \simeq 120 \text{ h}$. Then, this distance remains constant until the end of the experiment. The distance between the two trajectories is indeed the length of the

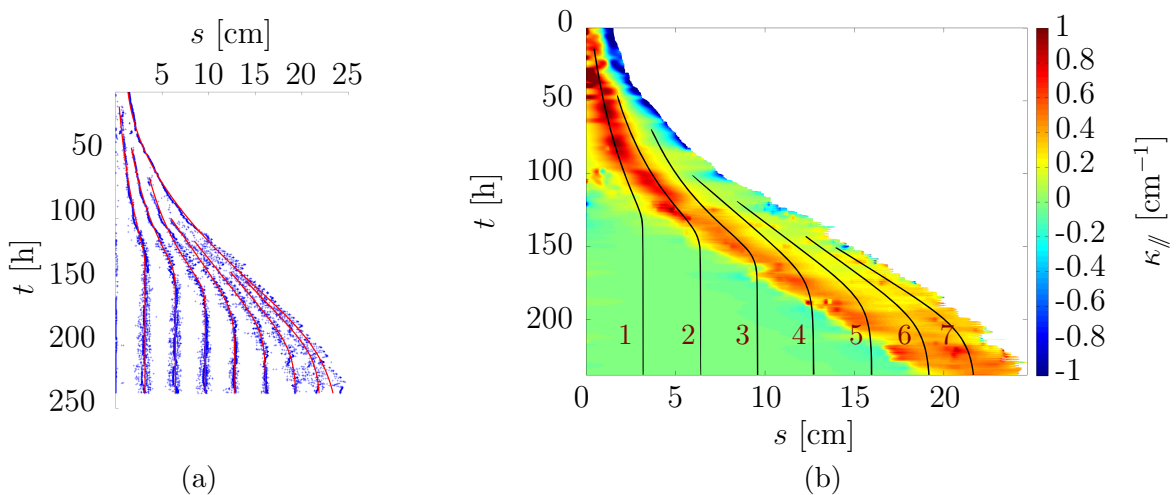


Figure 3.3: **Evidence of a growth zone.** (a) Displacement of the leaflets along the rachis. Raw data: blue dots, Fitted trajectories: red lines. (b) Trajectories of the leaflets overlaid over the spatio-temporal diagram of κ_{\parallel} . Courtesy of Yoann Corre.

considered interleaflet. So, the interleaflet goes through an elongation phase which stops around $t = 120$ h. Looking at the other interleaflets, we see that the closer to the apex, the later they reach their final length. The duration of the experiment prevents us from observing the end of the elongation phase for interleaflets 6 and 7 for instance. Altogether, these observations support the hypothesis of an elongation zone, near the apex of the leaf. Do the organ elongate and bend on the same exact region? Or does a spatial shift exist between the two considered zones?

The overlay of the fitted trajectories over the spatio-temporal diagram of curvature previously presented brings some elements of answer to this question (see figure 3.3b). We have discussed earlier the fact that the bending zone is properly defined from $t \simeq 110$ h. Let us now take a look at the elongation behaviour of the successive interleaflets from the same moment. The positions of the leaflets are all almost constant in the zone of low curvature of the rachis. We thus see that for all the interleaflets, most of their elongation is performed in the bent zone. This is not perfectly verified as the petiole of the leaf finishes its elongation outside of the bending zone. But we see that, later in the experiment, interleaflets closer to the apex end their elongation while still being in the bent zone. In a first approximation, the bending zone and the growth zone thus appear overlay. However, it is possible that the elongation zone shrinks in time.

In summary, the analysis of these results have brought forward two major features of *Averrhoa carambola* leaves during growth. We have seen that both curvature and elongation occur in spatially defined regions of the rachis. The bending zone,

corresponding to the region where the rachis unfurls and to the position of the hook, develops quickly after the reversal motion. It is located at a constant distance from the apex. The zone of elongation also corresponds to a limited part of the rachis, near the apex. Although these two regions do not perfectly overlap, they seem to have a significant overlay.

3.2 Macroscopic mechanics of the hook

The specificity of curvature and elongation kinematics during leaf unfurling has been unravelled. The hook shape itself remains to be explained. The bending of the rachis could be regarded as a passive bending resulting from the self-weight of the rachis. Self weight is known to partially affect the shape of mature leaves (Mouliat et al., 1994). One can wonder to what extent the shapes and motions displayed by compound leaves during their growth are active or passive. In addition, leaves stiffen during their growth. Could a combination of these two phenomena explain the shape of growing leaves?

3.2.1 Experimental approach

In their respective experiments, Silk and Mouliat actively bent the studied organs with weights. Here, to test the influence of the self-weight on the shape of the leaf, it appears natural to modify the amplitude or the direction of the weight. To do so, we simply flipped the plants upside-down. This results in an inversion of the arrow of the weight and in a more or less prominent bending along the rachis. The basic idea is then to compare the shape of the rachis in their normal and reversed configurations. If the rotated leaf does not change its shape, this would suggest that the self-weight has no direct mechanical role in the establishment of the shape.

Determination of mechanical quantities of interest

It is possible to extract the macroscopic mechanical properties of the rachis from its shape thanks to beam theory (Silk & Beusmans, 1988). Some simplifications are thus needed. The rachis is assumed to be axisymmetric, with an homogeneous density and isotropic mechanical properties. Moreover, we will neglect the mechanical role of leaflets here.

When a beam is under the action of a given torque—or moment of force —, its curvature $\kappa_{//}$ is modified and differs from its spontaneous curvature—the curvature when no loading is applied— $\kappa_{//}^0$. Let us consider two configurations (+) and (−) of

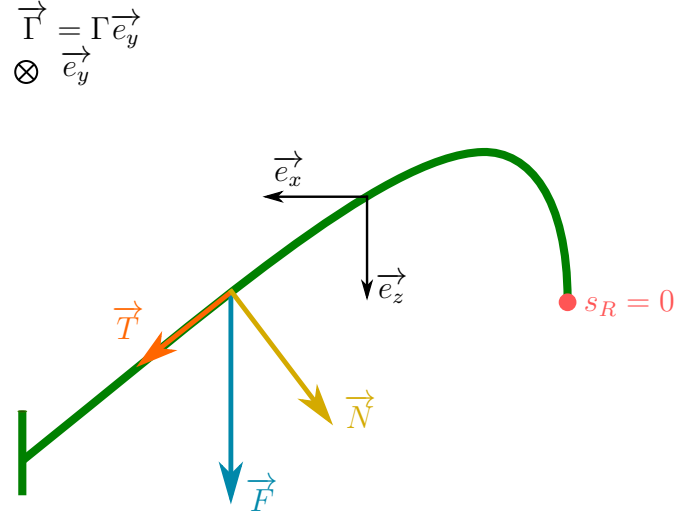


Figure 3.4: **Parametrization of our mechanics problem.** In this part of the study, the reverse arc length s_R will be used as it is more convenient. We define a global right handed Cartesian coordinate system (\vec{e}_x, \vec{e}_z) . Consider an arbitrary force \vec{F} applied on the rachis at $s_R = s$. \vec{F} can be decomposed into two components, relative to the local geometry of the rachis: a tangential component \vec{T} and a normal component \vec{N} . The sign convention for an arbitrary torque Γ is indicated.

the same object undergoing the two corresponding torques Γ_+ and Γ_- . According to beam theory, it is possible to express these two torques as follows:

$$\begin{cases} \Gamma_+(s) = B(s)(\kappa_{\parallel}^+(s) - \kappa_{\parallel}^0(s)) \\ \Gamma_-(s) = B(s)(\kappa_{\parallel}^-(s) - \kappa_{\parallel}^0(s)) \end{cases} \quad (3.3)$$

where s is the arc length along the beam, B is the flexural rigidity and κ_{\parallel}^0 is the spontaneous curvature of the beam (Feynman et al., 1964). Simply put, the flexural rigidity B corresponds to the resistance an objects opposes to a change of curvature. A simple one-dimensional analogy can be done with Hooke's law for a spring $F = k(x - x_0)$ to better grasp equations (3.3). The quantity B is furthermore linked to the Young's modulus of the considered material through the relation $B = EI$ where I is the second moment of area of the considered object. Finally, the flexural rigidity B and the spontaneous curvature κ_{\parallel}^0 are given by:

$$B = \frac{\Gamma_+ - \Gamma_-}{\kappa_{\parallel}^+ - \kappa_{\parallel}^-} \quad ; \quad \kappa_{\parallel}^0 = \overline{\kappa_{\parallel}} - \frac{\overline{\Gamma}}{B} \quad (3.4)$$

where $\overline{\Gamma}$ and $\overline{\kappa_{\parallel}}$ are the torques and the curvatures averaged over the two conformations respectively.

In our case, the two considered conformations are the initial shape and the shape when the leaf is upside-down. In a first approach, we assume that the torque is only caused by the self-weight of the rachis. In other words, we neglect the mechanical action of the leaflets. We also assume that the rachis is cylindrical.

Let us now consider the frame and parametrization described in figure B.2. Let us consider the free-body diagram of the studied leaf. The left part of the leaf— $0 \leq s_R \leq s$ for instance—has a weight $\vec{P}(s)$ such that

$$\vec{P}(s) = P(s)\vec{e}_z = \rho g \pi \int_0^s R^2(s_R) ds_R \vec{e}_z \quad (3.5)$$

where g is the gravitational acceleration, ρ is the volumetric mass density of the rachis and R its radius. This weight exerts a torque of force $\Gamma(s)$ on the right part of the rachis which is defined with respect to the apical end of the leaf— $s_R = 0$. Its intensity can be computed by the spatial integration of the normal component of the weight \vec{N} (see Appendix B for a complete derivation of this property).

$$\Gamma(s) = \int_0^s N(s_R) ds_R \quad (3.6)$$

Altogether, the previous paragraphs show that it is possible to extract the macroscopic mechanical properties of the rachis from a few simple geometrical quantities. Provided an assumption on the density of the rachis ρ , the knowledge of the arc length s , the radius R and the curvature $\kappa_{//}$ of the rachis allow to determine its flexural rigidity B . A reasonable approximation for ρ is—like for many soft biological tissues—to take $\rho = \rho_{water} = 1 \text{ kg.m}^{-3}$.

Experimental protocol

In order to collect all the needed quantities, we designed the following protocol. The studied plant is firmly fixed to a clinostat¹. The leaves that are not studied are gently tied to the stem so that they do not hide the leaf of interest when flipped. We deposit a small point of paint on the petiole of the studied leaf to make data analysis easier. Also, a scale was inserted in the experimental setup.

The motor of the clinostat has been interfaced with Python. In consequence, it can easily be programmed to perform any cycle of rotations². Then, a camera—

¹A clinostat is a slow rotating device usually used to counteract the effects of gravity. The perpetual rotation of the plant prevents the sedimentation of the statoliths and supposedly disrupts gravisensing.

²For instance, it is possible to set up random rotations at random moments, to assess the global mechanical characteristics of the rachis.

controlled with gphoto—is placed in front of the clinostat, and can take pictures during the rotation or after it is complete.

Side-view pictures of the studied leaf are taken at short time intervals (approximately 1 every second) in order to track the evolution of their curvature. The two most important pictures are: the initial one, and the one corresponding the moment when the leaf reaches the upside-down position. The viscous response to this perturbation can be observed if we maintain the plant upside-down for longer times (see Appendix B). In any case, the leaf should not be left upside-down more than 30 min. This duration of 30 min results from a trade-off. On the one hand, we want to observe the evolution of the shape in time in case of viscous relaxation. On the other hand, we want to avoid any gravitropic response from the plant. It has been shown that gravitropic responses can be triggered by stimulations of only 3 minutes in the case of *Arabidopsis thaliana* stems (Fukaki et al., 1996). *Averrhoa carambola* stems are usually woodier than those of *Arabidopsis thaliana*. For this reason, we expect gravitropic motions of *Averrhoa carambola* plants not to be triggered by short gravistimulations. Moreover, no gravitropic response was observed during the experiments and the growth of the studied leaves did not appear to be disturbed.

As a matter of fact, it is possible to study the evolution of the elasticity of the rachis in time. Doing so, we would make it possible to correlate the changes in mechanics with the histological changes taking place in the rachis. The evolution of mechanics can be tracked in two different ways. One approach would be to select a group of similar leaves (same number of leaflets for instance) but at different growth stages. Thus, by performing the previously described experiment once on each leaf there is no more gravisensing issue. The comparison of the obtained results becomes less clear as several individuals (and therefore biological variability) are involved though. another approach consists in performing the same experiment every day on the same leaf. The main drawback of this method is that we are not absolutely certain that the rotation of the plant has no effect on the development of the leaf and eventually on its mechanics.

We have chosen the second method for our experiments since we did not notice any gravitropic response nor abnormal growth behaviour for the studied leaves.

3.2.2 Data analysis

From the pictures that are the raw output of our experiment, we first want to extract geometrical quantities such as $\kappa_{//}$, s_R and R . I propose to describe the main steps required to achieve this goal in the following paragraphs.

Skeleton extraction

The most important step of our data processing is the skeleton extraction *i.e.* to reduce the rachis to a single line. One of the major difficulties in the skeletonization of the rachis is the presence of the leaflets. Segmentation-based techniques are hard to apply since it is difficult to tell apart the leaflets from the rachis based on their colors. Moreover, leaflets hide parts—sometimes large parts—of the rachis and sometimes make it difficult to reconstruct the rachis by numerical methods. On the contrary, the eye is good at completing and guessing curves. From here, several methods could indeed be applied. Considering the low number of images per experiment, we have chosen to digitalize the shape of the rachis thanks to a pen tablet and the vector graphics editor Inkscape. This kind of digitalization has been used in the past for experiments of this kind (Silk & Beusmans, 1988; Moulia et al., 1994). The rachis is first drawn by hand on the pen tablet and is recorded as a set of connected cubic Bézier curves by Inkscape. At first, the retrieved shape—or path in the terms of vector graphics—is quite rough as it is affected by the motions of the hand. This roughness can be smoothed out by progressively decreasing the number of cubic Bézier curves constituting our path. While we do this, it is necessary to adjust the parameters of the remaining Bézier curves to make the path fit to the rachis. In particular, it is important to ensure that the last and first control points of two consecutive Bézier curves and their common end/start point are aligned. Doing so, we make sure that $\kappa_{//}$ is continuous.

Geometrical quantities

The next step is to compute all the geometrical quantities that are relevant to our study: the reverse arc length s_R , the curvature $\kappa_{//}$ and the radius of the rachis R . The skeleton is first rasterized: we obtain a list of pixels with coordinates (x, y) . Then, the reverse arc length is simply computed as the cumulative distance from the apex to the base of the rachis.

We then need to evaluate the radius R of the rachis. In order to do this, the local orientation of the skeleton with respect to the vertical θ is determined in each point. This allows us to determine the normal to the skeleton in each point. The value of pixels in the green channel is then evaluated along the normal to the skeleton. In an ideal case, the histogram is expected to look like a Heaviside distribution: 0 outside of the rachis, 1 on the rachis. The width of the step gives the diameter of the rachis, $2R$. In real cases, the value profile is smoother. Such a profile can be fitted by the sum of two hyperbolic tangent functions—or equivalently by two error functions. The retrieved value of R is indeed impacted by the presence of leaflets.

Aberrant points are discarded thanks to a simple median filtering. Missing R values are recovered by fitting the R vs. s relationship to a linear one. In other words, we assume that the radius of the rachis decreases linearly as one gets closer to the apex.

Finally, we want to get the curvature of the rachis. Rather than resorting to its Cartesian definition—involving a double derivative—or to the spatial derivative of θ , we have estimated $\kappa_{//}$ by locally fitting the rachis with a circle.

Mechanical quantities

All the geometrical and physical quantities have now been gathered to allow the evaluation of the mechanical quantities of interest. It is necessary to acquire these quantities for both conformations of the leaf: the normal one, and the upside-down one. From this point, the derivation of the spontaneous curvature $\kappa_{//}^0$ and of the flexural rigidity B is straightforward.

Specific precautions should however be taken in order to ensure that the two skeletons are evaluated consistently. That is to say that they should have the same number of points, but also that these points effectively correspond to the same material points on the rachis. This is needed because the evaluation of B at a given point requires the knowledge of the geometrical quantities at this same material point for the two configurations.

3.2.3 A first look at shape and self-weight

One of our goals is to understand the influence of the self-weight of the rachis on its own shape. To do so, as previously explained, we simply flip the plant upside-down and observe the deformation of the rachis. In this section, I will show the evolution of a single leaf over five days of experiment. A single acquisition per day was performed.

The simple experiment consisting in reversing the direction of the leaf self-weight is illustrated in figure 3.5. A young leaf is flipped upside-down and the shapes of the initial and final states are compared in the two first panels (left and center). We can hardly see any difference in the shape of the rachis between the two conformations. The right-most panel of figure 3.5 presents the superimposition of the two shapes—the flipped conformation has been rotated. We notice that the rachis is globally displaced upward, as it could have been reasonable expected. This displacement is tenuous though. Colored arrows indicate the position of the apex for the two



Figure 3.5: **Superposition of the normal and flipped configurations of the leaf (day 1).** The arrows in the right-most panel indicate the position of the apex for the normal configuration (blue) and the flipped configuration (yellow).

conformations. The position of the apex indeed integrates the deformation of the whole rachis. We see that here the displacement of the apex resulting from the reversal of the weight is small compared to the length of the rachis. This suggests a reduced influence of the deformations of the rachis due to its own weight in its shape. Does this observation extend to the further developmental stages of the leaf?

The repetition of this experiment over five successive days is presented in figure 3.6. The evolution of the shape of the rachis during its development is represented by the plain-lined skeletons. We see that the evolution of the shape is indeed consistent with the description of the unfurling motion in chapter 2 and in section 3.1. A bent zone persists throughout the development of the leaf. The hook follows the apex and the part of the rachis the closest to the stem is now straight. The observation of the skeletons also shows us that the mean curvature of the bent zone gets lower and lower. We also see that, at first, the rachis is completely curved. The length of bending zone L_{bz} is at least equal to the total length of the rachis, in a completely analogous manner than the growth zone behaviour.

More importantly, the skeletons corresponding to the flipped conformation of the rachis are shown in dotted line. The deformation of the rachis due to the reversal of the direction of its weight appears to become greater and greater in time. This is obvious when we compare the first and last pair of skeletons. Unlike in the case of the first skeleton, the displacement of the apex is not negligible in the case of the last skeleton. From the third day of experiment, deformations become so intense that we clearly see inflexion points on the flipped rachis conformation skeletons, characterizing local changes of sign of $\kappa_{//}$.

Contrary to the previously discussed case, the great deformation of the rachis during the experiment suggests an important role of the deformations due to self-weight in the normal shape of the rachis. The importance of self-weight for the shape of the

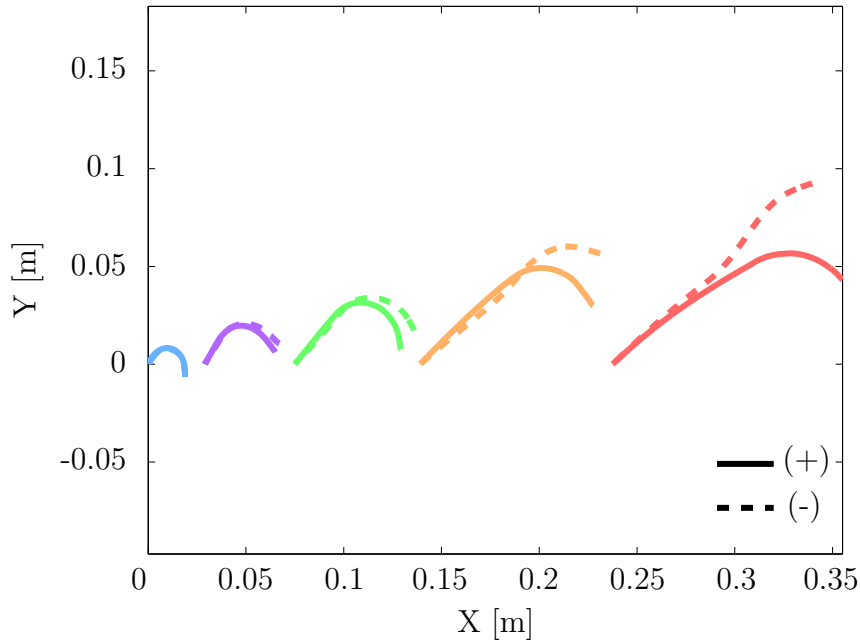


Figure 3.6: **Evolution of the shape of the rachis in time.** For each day of the experiment, the skeletons corresponding to the normal (+) and flipped (-) conformations are superimposed. The skeletons are arranged from the earlier stages of development (left) to the later ones (right).

rachis seems to progressively increase in time, from negligible to important. How can we explain these differences of behaviour? Considering the fact that *Averrhoa carambola* rachis stiffen during their growth, could this be a signature of a change in the mechanical properties of the rachis? At last, can we properly quantify the importance of self-weight in the shape of the rachis?

3.2.4 Mechanical properties in time

The shape of the rachis results from the external mechanical actions it undergoes, but also from its intrinsic mechanical properties. This is what expresses equation (3.3). The two quantities that determine the curvature the rachis adopts under a given torque are its flexural rigidity B and its spontaneous curvature $\kappa_{//}^0$. In normal conditions, the rachis is only submitted to the action of its own weight. Understanding the observed shape of the rachis thus requires the knowledge of its own weight, B and $\kappa_{//}^0$. The protocol discussed in section 3.2.1 allows us to determine the latter ones.

In this section, we will try and go a step further in the understanding of the shape of the rachis than in section 3.2.3. We are going to seek in the intrinsic

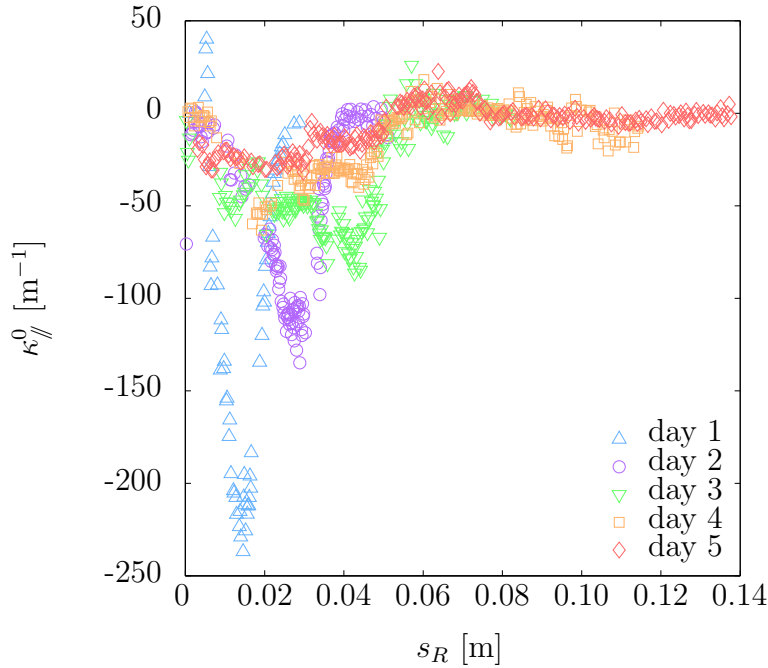


Figure 3.7: **Evolution of the spontaneous curvature κ_{\parallel}^0 of the rachis in time.** The arc length used here is the reverse arc length s_R or the distance to the apex. The point $s_R = 0$ is then the apex of the leaf. The colors attributed to the different days of the experiment correspond to those initially defined in figure 3.6.

mechanical parameters of the rachis an explanation for its shape. The repetition of this experiment over 5 days on the same leaf will also allow us to track the evolution of these quantities in time.

Among the parameters that characterize the mechanical behaviour of the rachis, its spontaneous curvature is of particular interest. It is the curvature the rachis would adopt in the absence of any load. In other words, it is the ‘natural’ curvature of the rachis. The successive profiles of κ_{\parallel}^0 are shown in figure 3.7. The most striking feature of this figure is that the rachis has a non-zero spontaneous curvature. Put differently, the rachis is naturally curved. This strongly supports the active character of shape regulation in *Averrhoa carambola*. The exact influence of the self-weight on the rachis shape still needs to be properly investigated and quantified though.

Looking at each individual κ_{\parallel}^0 profile, we notice that the rachis can be divided in two distinct parts:

1. A bent zone, close to the apex where most of the spontaneous curvature is concentrated.

2. A straight zone, close to the principal stem of the plant. In this part, the spontaneous curvature is almost homogeneous and equal to 0.

These two regions change in time and in space. In particular, the global decrease of the spontaneous curvature values in time is blatant. At first developmental stages, the spontaneous curvature is large ($\max \kappa_{//}^0 = 240 \text{ m}^{-1}$ at day 1), but the $\kappa_{//}^0$ profile becomes flatter and flatter in time, meaning that the rachis tends to straighten itself. This can be viewed as an extension of the straight zone of the rachis. This behaviour is indeed consistent with the unfurling motion of the rachis over the days, as it has previously been described. In the same time, the length L_{bz} of the bent zone increases in time. At the beginning of the experiment, we see that the rachis is completely curved. The length L_{bz} of the bent zone appears to be limited by the size of the rachis. From the second day of the experiment, the bent zone extends. Then, L_{bz} stabilizes during the two last days of the experiment. At this stage, the bent zone seems to have reached its complete length. The duration of the experiment prevents us from observing the decrease of L_{bz} . Such a decrease should be expected, considering the description of the unfurling motion 2.7: the bent zone disappears to leave a completely straight rachis. We also note that the position of the maximum of $\kappa_{//}^0$ is not fixed and tends to translate toward the base of the leaf.

The second quantity which is necessary to characterize the flexural behaviour of the rachis is the so-called flexural rigidity B . The rigidity profiles are shown for each day of the experiment in figure 3.8. We first notice that B is strongly inhomogeneous along the rachis. It spans a remarkably large interval of values, from 10^{-12} N.m^2 to 10^{-4} N.m^2 , that is to say eight orders of magnitude. Note however that the results shown in figure 3.8 have to be considered carefully. This is specifically true near the apex where the torque exerted by the self-weight on the rest of the rachis is negligible. This results in tiny variations of $\kappa_{//}$ and in a great error on B . However, there is a clear tendency in the profile of B . In contrast with $\kappa_{//}^0$, we notice that all the B profiles are collapsing on a single ‘master curve’. In other words, the profile of B does not vary much on the duration of the experiment. Thanks to the spatial stability of the B profile, we can define three different zones of fixed position. These three zones are then defined both by their position relative to the apex and by the local rate of change of B . The three zones are the following:

1. A soft region near the apex. In this part of the rachis, B varies between 10^{-12} N.m^2 and 10^{-7} N.m^2 . Here, the soft region extends up to 2 cm away from the apex. The rate of change of B is not a relevant information here, because of the possible large errors on the values of B .

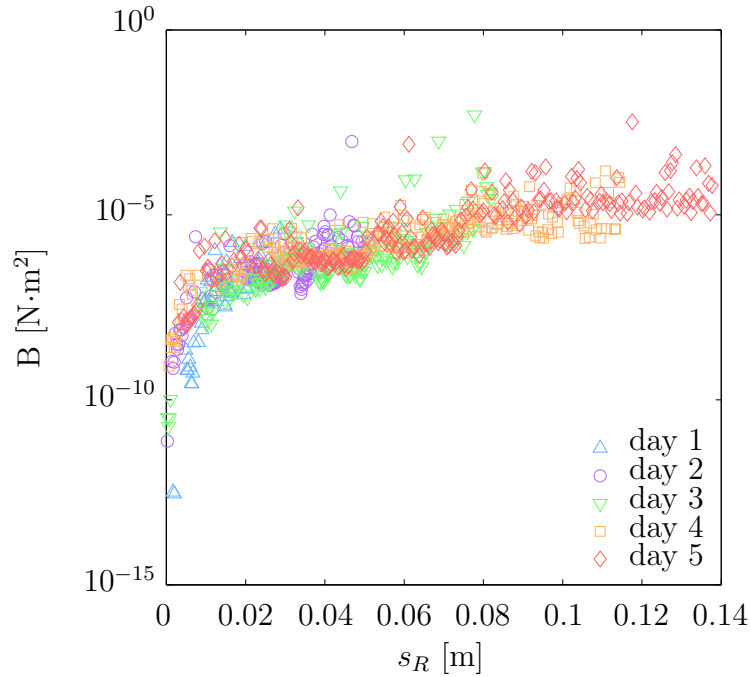


Figure 3.8: **Evolution of the flexural rigidity B along the rachis in time.** The arc length used here is the reverse arc length s_R or the distance to the apex. The point $s_R = 0$ is then the apex of the leaf. The colors attributed to the different days of the experiment correspond to those initially defined in figure 3.6.

2. A transition region in which the rigidity evolves slowly along the rachis. Here, it is located between 2 *cm* and 10 *cm* away from the rachis.
3. A rigid region in which the flexural rigidity is almost constant. This zone corresponds to the parts of the rachis which are close to the petiole and the petiole itself. Here the final value of the flexural rigidity is $B \sim 10^{-5} \text{ N.m}^2$.

The previous division of the rachis enhances the fact that a material point of the rachis is going to become stiffer and stiffer throughout the growth process. Material points will all start in the soft region, near the apex, where new material is synthesized and then migrate to the following regions. The rachis also becomes globally stiffer, as it can be seen by comparing the B profiles for the first and the last day for instance. These results do not show the complete development of the leaf. But we can reasonably expect the profile of B to slowly become homogeneous. At this point, a question naturally arises: what are the biological processes which make the rachis stiffen?

3.2.5 Links with lignification

In most vascular plants, the maturation of some specific tissues implies the deposition of lignin³ on the cell walls. This is what we call lignification. Lignification is known to affect the physical properties of the cell walls. Lignin being an hydrophobic component, they make conductive tissues such as secondary xylems impermeable and facilitate water transport (Barceló, 1997). In addition to that, lignin deposition stiffens the tissues. It has been shown that the higher the lignin content, the higher the rigidity of the cell wall (Ruggeberg et al., 2008; Speck & Burgert, 2011). We have observed that the inner tissues of the mature rachis of *Averrhoa carambola* contain, for a large part, xylem and bast fibers that are lignified tissues (see figure 2.4). Lignification is thus a possible candidate to explain the strong gradient of flexural rigidity along the growing rachis (see figure 3.8).

Together with Clara Billard, a bachelor intern in the lab during spring 2016, we have studied the lignification status of the inner tissues of a growing *Averrhoa carambola* leaf. The lignified tissues were evidenced thanks to a classical dual staining technique with carmine (red stain, cellulosic walls) and iodine green (greenish-blueish stain, lignified tissues). The lignification rate of each hand-cut sample was then evaluated by measuring the ratio of the area of lignified tissues with the total area of the sample. Such a method is not very accurate. It depends on the thickness of the sample, on the time of exposure to the stain and on the quality of the final picture. This method nevertheless provides interesting qualitative results.

The successive samples are show in figure 3.9a. We immediatly see that there is a gradient of lignification along the rachis, with highly lignified tissues near the stem and less lignified tissues at the apex. This global tendency is confirmed by the quantification of the lignification ratio of each sample (see figure 3.9b). The lignification rate is of 17% in the first sample and drops to 7% in sample 5. The lignification rate then increases again in sample 6, but this is likely due to the inaccuracy of our method. In the same time, we see that the higher levels of lignin are reached where the local curvature is minimal. Can we pinpoint the presence of a lignification zone, in a similar manner than for $\kappa_{//}$ or B ?

We see in the sample corresponding to the first interleaflet that a complete ring of bast fibers has already formed underneath the outermost layers of the rachis. Closer to the centre, we see that the secondary xylem is developing⁴. It forms an incomplete

³From the latin word *lignum* meaning wood.

⁴We can tell it is still developing thanks to the comparison with figure 2.4 where a full ring of xylem is visible, taking most of the room in between the bast fibres and the central medullar

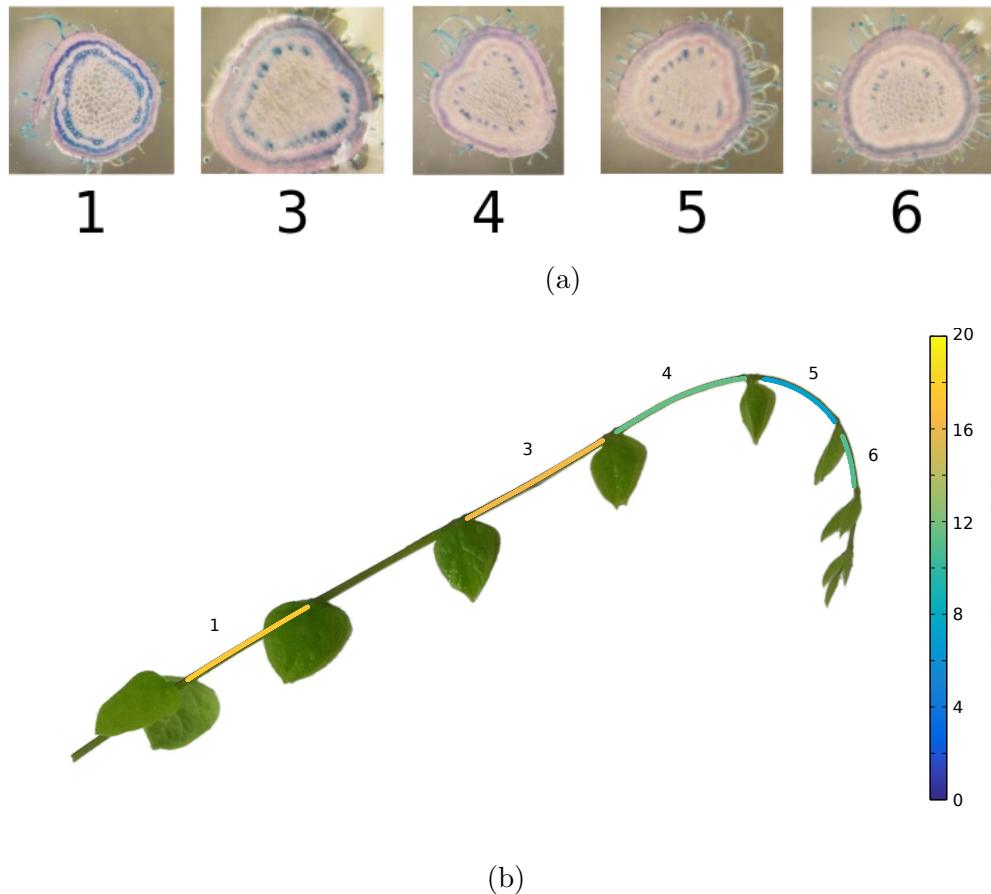


Figure 3.9: **Evaluating the lignification status of the growing rachis.** (a) Cross-sections of a rachis colored with Carmine and Iodine green. The number of the interleaflet to which the sample belongs is indicated. (b) Lignification rate per interleaflet. The lignification rate computed from each sample in (a) is shown on its corresponding interleaflet.

ring, slightly thicker than the bast fibres ring. The following samples show less and less complete bast fibres rings. The secondary xylem is already greatly reduced in interleaflet 3 compared with interleaflet 1. For interleaflets from 4 to 6, the iodine green stain only reveals disjoint vessels. We also see that their number keeps decreasing when we go toward the apex. If we follow the usual direction for tissue development—from the apex to the stem —, we thus see that vessels are lignified early on. The number of lignified vessels increases in time. Their lignification seem to take place from the abaxial face to the adaxial one. On the contrary, the ring of bast fibres seems to develop from the adaxial face to the abaxial one.

Finally, we see that there is a lignification gradient oriented from the apex to the petiole of the leaf. This lignification gradient is accompanied with a maturation gradient of the tissues which underlies the formation of support tissues of the plant (bast fibres). It is difficult to clearly evidence a lignification zone in the rachis. It seems that the lignin deposition starts in the earlier developmental stages of the tissues and seems to occur everywhere, but at different paces. The region where lignification appears to be the quickest is near the petiole, with the formation of thick rings of bast fibers and secondary xylem.

3.3 Discussion and partial conclusion

Our experiments allowed us to explore several aspects of the unfurling motion of *Averrhoa carambola* leaves and their associated hook shapes. Two major questions were asked: how can we explain the hook shape? How does this shape evolve in time? We are now going to discuss the previously described results in order to extract an answer to these questions.

Shape is actively regulated throughout development The hook shape of growing compound leaves—among which *Averrhoa carambola* leaves—is characterized by a prominent curvature near the apex of the rachis (see figure 3.5, left-most panel for instance). This curvature has been quantified (see figure 3.2) and the radius of curvature $1/\kappa_{\parallel}$ has been found to be approximately ten times superior to the typical radius of the rachis. The question was asked from what this curved shape could result from. The natural idea of the influence of the self-weight on the shape was explored in section 3.2. By flipping the leaf upside-down, we have shown that the role of the deformations due to the self-weight of the leaf on its shape is

parenchyma.

negligible at first developmental stages (see figure 3.5). This suggests that the hook shape results from an active process at early stages at least.

A proper characterization of this behaviour has been carried out by the determination of the mechanical properties at play: the flexural rigidity B and the spontaneous curvature $\kappa_{//}^0$. We have neglected the mechanical actions applied by the leaflets on the rachis. As a result, torques are thus underestimated and so is B , but $\kappa_{//}^0$ is overestimated. Our results are sufficient however to give us tendencies and orders of magnitude. For the most early stage of the experiment, B was found to be low (compare with other curves, see figure 3.8). However, the rachis is almost not deformed when flipped. This is because the shape is indeed ruled by both $\kappa_{//}^0$ and B as shown in equation (3.3). In other words, soft tissues are not a sufficient condition to get a curved rachis. Most of the contribution to the shape of the rachis is actually contained in the spontaneous curvature (see figure 3.7, light blue). Consistently with the previous paragraph, we show here that the hook shape is actively regulated by the plant at the earliest developmental stages.

We then noted that the deformations of the rachis due to its self-weight during the experiment seemed to increase for the latest stages of the experiment (see figure 3.6). This suggests that, as the development progresses, the shape of the leaf is more and more impacted by the deformations due to its own weight. The question of the mechanisms underlying the evolution of the hook shape—*i.e.* the unfurling motion—was thus asked. We have shown that the unfurling motion is characterized by the propagation of a bent zone at a fixed length of the apex (see figure 3.2). The repetition of the flip experiment allowed us to track the evolution of the B and $\kappa_{//}^0$ profiles in time. We have put forward that the B profile is steady: all curves overlay on a ‘master curve’ (see figure 3.8). On the contrary, $\kappa_{//}^0$ exhibited strong changes on the duration on the experiment. It goes from a peak distribution and evolves toward a homogeneously null distribution (see figure 3.7). This indicates that the rachis tends to a naturally straight shape and corresponds to the definition of the unfurling motion. Thus, despite the increasing impact of the deformations due to the self-weight on the shape of the rachis, $\kappa_{//}^0$ keeps underlying the changes associated to the unfurling motion. Altogether, this suggests an active regulation of the shape of rachis throughout the development.

Differential growth seems to occur where the elongation rate drops

If the curvature of the rachis is actively controlled, it might now be asked what drives the changes of $\kappa_{//}$ in time. According to the description of the unfurling motion detailed in Chapter 2, we expect that changes in $\kappa_{//}$ are driven by differential

growth. Let us consider a small material element of the rachis. This element starts its development in the bent zone, near the apex and progressively drifts towards the straight part of the rachis (see figure 3.2). In other words, the considered element unbends itself downstream of the bending zone. Differential growth necessarily takes place in this specific region. Referring to figure 3.3b, we see that, in most cases, elongation has almost stopped downstream of the bent zone. In consequence, differential growth is likely to occur in a region where elongation is getting lower and lower. The results presented in section 3.1 do not allow us to go further in this direction. We can however take this observation as a working hypothesis for the rest of our work.

Growth, curvature, rigidity and lignification interplays The analysis of the previous results also led us to define four different antagonisms along the rachis: bent/straight (see figure 3.2), growing/not growing (figure 3.3b), soft/stiff (figure 3.8) and low/high lignification level (figure 3.9). Let us now discuss the interplays between all these zones.

Bending zone Bending zones are often defined when treating plant motions related problems. This is particularly true when it comes to circumnutation or nutation (Millet et al., 1988). Because of the nature of the hook shape, it was expected to pinpoint a bent zone in our measurements (see figures 3.5 and 3.6). Here, the main feature of this bent zone is that it is set at a constant distance from the apex (see figure 3.2). Such behaviours have already been reported in the case of hypocotyl unfurling (Silk & Erickson, 1978). It was observed that the curvature profile was approximately steady, consistently with our results. These similarities between the kinematics of hook maintenance—or unfurling—in hypocotyls and compound leaves are striking and may indicate a common regulation process for hook-shaped organs.

Growth zone It also appeared that the elongation of tissues is confined to the apical region of the rachis (see figure 3.3b). This behaviour is often called ‘tip growth’. It has been observed for a diversity of cylindrical plant organs such as hypocotyls (Silk & Erickson, 1978) and roots (Silk et al., 1989; Bizet et al., 2015). This behaviour seems to be considered a widespread feature of plant growth and is often used when modelling the growth and/or motions of complete plant organs (Bastien et al., 2013).

Growth and curvature interplays We have already discussed the fact that the growth zone and the bent zone almost overlap in section 3.1.2. The growth zone however seems to be shrinking in time (see figure 3.3b) and an increasing

discrepancy is set between the two zones. The position of the curved part of the rachis nevertheless constitutes a good approximation of the position of the growing zone in our case.

Rigidity zones The analysis of the flexural rigidity profiles has brought forward three different zones on the rachis. The global behaviour of B was found to be monotonic increasing, with 5 orders of magnitude between the apex and the base of the rachis. We see that the minimum of B (the softest rigidity zone we defined) is likely to be included in the growth zone. This behaviour contrasts with measurements made on the apical region of growing roots (Beusmans & Silk, 1988). Silk and Beusmans had found that the root presented a maximum of extensibility away from the apex and from the growth zone. We have already discussed the possibly large errors on B in section 3.1.2 to which this discrepancy could be partly ascribed. Moreover, it should be remembered that in both studies the mechanical properties of the rachis are probed in a direction orthogonal to the growth direction. Would the behaviour of the first zone be confirmed, how could we understand it? The behaviour of the first rigidity zone (very soft, and quick increase of B) may be explained by the maturation of the cell walls. Because the first rigidity zone is located at the apex, it is comprised in the growth zone and might be the place where cell divisions occur and new material is synthesised. The mechanical properties of dividing plant cells may be different from mature cells. Gradients of cell wall composition—other than lignin—along the elongation zone of growing organs have already been measured (Zhang et al., 2014). For example, the contents in crystalline cellulose were found to increase from the apex to the base. Moreover, the division of a mother cell into two daughter cells requires the synthesis of a new physical border between the two daughters. This step is called cytokinesis. The newly formed border is initially reduced to the thin middle lamella. The middle lamella and the primary cell wall are two distinct tissues that have different compositions and mechanical properties (Zamil & Geitmann, 2017). We thus see that the composition of the young primary cell wall is dynamic and may explain the observed rigidity profile.

Lignification zone The second rigidity zone shows a more progressive increase of B and the third zone presents almost homogeneous B . We had observed that the tissues of *Averrhoa carambola* leaves are lignified relatively quickly after growth. It has been shown that the higher the lignin content in a tissue, the higher its rigidity (Speck & Burgert, 2011). Lignification was thus a possible explanation for this stiffening of the rachis (see figure 3.8). The differential staining of transverse cuts of the rachis revealed a gradient of lignification in the rachis from the base to the apex (see figure 3.9). In our experiment, interleaflet 1, already straight and several

interleaflets away from the bent/growth zone was by far the most lignified. The lignification level drops after the third interleaflet and seems almost homogeneous after that. Thus, it seems that the lignification zone is significantly delayed/shifted from the bent/growth zone. Its position is however compatible with the second and third rigidity zones defined earlier.

The technical limitations of the used technique have already been discussed in section 3.2.5. The used technique however easily provides global information on lignification. More quantitative results could be obtained thanks to spectrophotometry (Ruggeberg et al., 2008) or more sophisticated chemical staining methods (Lion et al., 2017). An obvious additional drawback of this experiment lies in the fact that it only shows lignification status of the tissues at a given time. The spatial and time patterns of lignification are still unclear and several types of lignification dynamics could be imagined. In order to properly establish a link between lignification, growth and curvature kinematics it is needed to track the evolution of lignification within tissues in a non-invasive and non-destructive way. Lignification causes the tissues to become stiffer and more dense (wider cell walls). It might thus be possible to detect the resulting density/stiffness inhomogeneities and to follow their evolution thanks to X-ray imaging for example.

Wrap-up: posture regulation and associated sensitivities We have seen that the posture of *Averrhoa carambola* leaves is actively regulated during their development. The unfurling motion is the manifestation of this regulation of curvature. The straightening of the rachis brings the idea of autotropism to mind. The question of the sensitivities associated to the unfurling, the hook shape and posture regulation may now be asked. Proprioception—the sensitivity to local curvature and self-alignment—was shown to be of prime importance in gravitropism (Bastien et al., 2013). It was proposed by the same authors that a mechanism for proprioception could rely on the sensitivity to mechanical strain and/or stress. Would the rachis rely on its strain to regulate its posture, it would then be necessary for it to be deformable under its own weight. Here, we show that the mechanical properties $(\kappa_{\parallel}^0, B)$ of the rachis dramatically change in time and in space. The spatial patterns of B and κ_{\parallel}^0 could possibly be regulated to maintain a zone of high ‘curvature strain’ $(\kappa_{\parallel} - \kappa_{\parallel}^0)/(\kappa_{\parallel}^0) = \Gamma/(B\kappa_{\parallel}^0)$. We see that the strain in curvature directly depends on the applied torque—which basically depends on the distance to the apex of the considered point —, B and κ_{\parallel}^0 . The maintenance of a zone with high bending strain would ensure a differential stress of the abaxial and adaxial faces of the rachis which could in turn trigger differential growth.

The trajectory of a set of material points during the development of the leaf would then be the following. After a given number of cell divisions at the apex,

a set of cells would first see their primary cell walls mature and their elongation would begin shortly afterwards (first rigidity zone + growth zone + bent zone). Then, the elongation rate of the considered set of material points will decrease and they will unbend (end of growth zone and bent zone). The rigidity of the set of point keeps increasing and their curvature keeps decreasing (second rigidity zone + straight zone + lignification zone). In this part, the sensitivity to the weight being maximal, adjustments of the curvature of the rachis are still possible by differential growth. At last, the considered set of points is perfectly straight. Its shape and elongation are freed by lignification (lignified zone + straight zone).

We have shown in this chapter that the leaf actively controls its curvature at the earliest stages of development. Later on, its curvature is partially impacted by its own weight. This is however accompanied by strong changes in the spontaneous curvature of the rachis, suggesting an active control of the curvature throughout the whole development.

Chapter 4

Characterizing the nutation motion

Contents

4.1	Experimental method	72
4.1.1	Quantities of interest	72
4.1.2	Experimental set-up	73
4.1.3	Data analysis	75
4.2	Results	76
4.2.1	Curvature variations and associated differential elongation	76
4.2.2	Relation between elongation and differential elongation	80
4.2.3	Nutation described as an oscillation	86
4.3	Discussion and partial conclusion	96

The growth of *Averrhoa carambola* compound leaves is not solely accompanied by the slow unfurling motion. A closer observation reveals a periodical swaying motion of the rachis in the perpendicular direction: the nutation. Nutation contrasts with the unfurling motion in several ways. In particular, compared to the time scale of growth, their respective time scales correspond to two extreme cases. Despite their opposed natures, could the unfurling and nutation motions share common growth patterns and kinematics?

Nutation and circumnutation have been heavily studied, mostly since the works of Charles and Francis Darwin at the end of the nineteenth century. Their apparent autonomous character and their periodicity have drawn most of the attention. Many studies investigated the possible interactions of nutation motions with external cues

such as gravity. In contrast, fewer studies have been dedicated to understanding the kinematics of nutation and its relation to growth.

In this fourth chapter, we will try to answer the following questions: what are the characteristics of nutation? What are its kinematics?

4.1 Experimental method

4.1.1 Quantities of interest

Before discussing our experimental set-up, let us identify the relevant parameters to describe and characterize the nutation of *Averrhoa carambola* leaves.

In many studies, the nutation motion is described in terms of tip position or tip angle. Such quantifications of nutation are handy in the sense that they are easy to understand and to measure. We have however discussed in Chapter 2 that a more complete description of the nutation motion could be achieved by measuring the local curvature of the nutating organ rather than the angle or position of a single point. In this chapter, we will use both descriptions depending on the specific addressed question. Our reduced measurement of the nutation is given by the deflection Δy of the apex with respect to the principal growth direction of the rachis \vec{d} . Since nutation is an out-of-plane motion, a more complete quantification of nutation is given by the curvature κ_{\perp} along the rachis.

We then want to link the motion to the elongation behaviour in a similar manner than what has been done in Chapter 3 for the unfurling motion. As discussed in Chapter 1, the elongation behaviour of an organ undergoing growth motions can be described by two components: elongation rate and differential elongation. The elongation of the rachis can either be quantified by the relative elemental elongation rate $\dot{\epsilon}$ or in an averaged way by the relative growth rate \dot{E} . Differential elongation is more tricky to measure. Under the hypothesis that nutation is driven by nutation only, it can however be estimated. It is possible to establish a relationship between the variation of curvature and the amount of differential growth (Bastien, 2010):

$$\frac{D\kappa_{\perp}}{Dt} = \frac{1 - R^2\kappa_{\perp}^2}{R}\dot{\delta} \quad (4.1)$$

$$\frac{\partial\kappa_{\perp}}{\partial t} + v\frac{\partial\kappa_{\perp}}{\partial s} = \frac{1 - R^2\kappa_{\perp}^2}{R}\dot{\delta} \quad (4.2)$$

where $v = \int_0^s \dot{\epsilon}(s', t) ds'$ is the speed at the considered arc length. Here, the typical time scale of nutation is much smaller than the typical time scale of elongation. Thus,

$v \frac{\partial \kappa_{\perp}}{\partial s} \ll \frac{\partial \kappa_{\perp}}{\partial t}$. We can then approximate the amount of differential elongation as:

$$\dot{\delta} \simeq \frac{R}{1 - R^2 \kappa_{\perp}^2} \frac{\partial \kappa_{\perp}}{\partial t} \quad (4.3)$$

This equation will allow us to approximate the amount of differential elongation of the tissue, under the hypothesis that nutation is driven by differential growth only.

In the previous chapter, we have formulated the hypothesis that differential growth occurs where the relative elemental growth rate of the tissue drops. We will be able to access the differential elongation rate thanks to the proxy of curvature, but the REGR $\dot{\varepsilon}$ will not be directly accessible. Like in section 3.1, we can retrieve coarse information on the growth field—the relative growth rates RGR—for each interleaflet thanks to the trajectories of the leaflets. A quantity equivalent to the RGR has thus to be built for the differential elongation of the tissues. The RGR actually correspond The ‘relative differential elongation rate’ \dot{D} for each leaflet can be defined as :

$$\dot{D} = \frac{1}{L_i} \left| \int_{s_{min,i}}^{s_{max,i}} \dot{\delta}(s) ds \right| \quad (4.4)$$

where $L_i = s_{max,i} - s_{min,i}$ is the length of the considered interleaflet. Here we take the absolute value of the score because the sign of $\dot{\delta}$ is purely conventional and we are actually interested in the magnitude of differential elongation within the tissues.

4.1.2 Experimental set-up

Nutation being an out of plane motion, it is not relevant anymore to take pictures in the plane (π) of growth. To capture the evolution of the κ_{\perp} in time, we place a camera above the leaf of interest, orthogonal to the vertical direction. The main drawback to top-view pictures is that it is not possible to observe the whole rachis. Growing *Averrhoa carambola* leaves are indeed hooked and their apical part is most of the time invisible from above. The apparent spatial extension of the rachis can be affected in several ways. First, global motions of the rachis can result in phases of apparent contraction or elongation of the rachis. It has already been discussed that it is most of the time not possible to observe the complete rachis. But the observable portion of the rachis however evolves as the rachis periodically—and partially—furls and unfurls. Global changes of the orientation of the rachis with respect to the top camera also affect the apparent length of the rachis. Global displacements of the rachis can also result in the concealment of a part of the rachis. Finally, as the

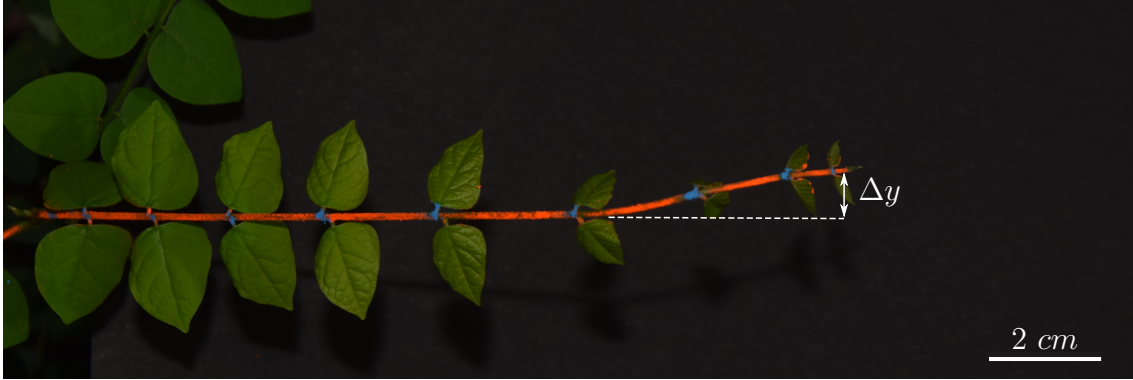


Figure 4.1: **Typical top-view image.** The prepared rachis is covered with fluorescent orange pigments. The position of the pairs of leaflets is indicated by blue fluorescent points. The deflection Δy of the rachis with respect to \vec{d} is indicated.

rachis irreversibly unfurls and grows, more of it becomes observable.

Similarly to the experiments described in section 3.1, the follow-up of κ_{\perp} profiles in time is realised by using time-lapse photography. The typical time interval for this kind of acquisition varies between 1 min and 5 min and will be indicated when needed. Images were taken with Nikon D3300 DSLR cameras piloted with the software gphoto2. The cameras were firmly fixed on a rigid structure to avoid any displacement or rotation.

Knowing that the leaf is going to considerably elongate during the experiment, the camera needs to be set quite far away the rachis in order to be able to capture the whole rachis at any time of its development. This results in a quite thin rachis on the pictures. The most important quantity for our study is the out-of-plane curvature κ_{\perp} . The quality of the skeleton is then crucial for a precise quantification of nutation. This is why I have chosen to heavily mark the rachis with fluorescent orange paint. This step allows a good contrast between the rachis, the leaflets and the black background. It thus helps overcoming two major difficulties for the skeleton extraction: a thin rachis and the presence of leaflets.

Note that according to the technique previously discussed we can only observe the painted parts of the rachis. In a first time, it is not possible to paint the complete rachis because the leaflets are packed on its adaxial face. It is then necessary to complete the paint of the plant several times during an experiment. If two painting adjustments are too spaced, this unfortunately results in a brutal increase of the apparent spatial extension of the rachis. Finally, false detections during the image analysis can result into artificially bigger skeletons.

We also want to evaluate the relative growth rate \dot{E} of each interleaflet. Like in the previous Chapter, the tracking of the leaflets enables such measurements. The detection of leaflets in top-view pictures might be difficult to handle. The reason for that lies in their nyctinasty. To go beyond this experimental difficulty, I chose to simply indicate the position of the leaf nodes along the rachis with small dots of paint. This time blue fluorescent pigments were used to enhance contrast with the orange painted rachis (see figure 4.1).

At last, the relative humidity and temperature of the room were monitored thanks to a DHT22 sensor connected to an Arduino Uno board.

4.1.3 Data analysis

The output of each one of our experiment is a set of isochronous pictures from which several quantities must now be extracted. The starting point is—as usual—the skeleton. Thanks to the heavy painting of the rachis, the points belonging to the rachis are extracted by a simple thresholding of the pictures. The skeleton is obtained by reducing the previous cloud of points to a single line. This is done by moving median filter on the Y-coordinates of the cloud of points.

Once the skeleton has been obtained, the arc length s is easily computed. The curvature κ_{\perp} is evaluated by locally fitting a circle to the skeleton. The radius of the fitted circle gives us the radius of curvature of the skeleton in the vicinity of the probed points.

Since the position of the leaflets are indicated by blue paint dots, they are also retrieved by thresholding each the blue channel of each frame. Two major difficulties have been encountered in the detection and tracking of the position of the leaflets. First, the blue spot for each pair of leaflet ‘dilutes’ in time because of the non-cohesiveness of the pigments dots and of elongation. Blue points were often painted anew but with possible errors on position. Second, for the same reasons, the spots of dry pigments could break down in several spots, making the detection and overall tracking quite messy. No infallible workaround was found at the data analysis level. Simple rules on the conservation of the number of detected points, distance between consecutive points and on the values of displacement of the tracked points however allowed to reject most of the erroneous detections. When errors could not be treated by data analysis, they were rectified by manually selecting the correct blue dots.

Curvature data are then prepared in order to be assembled in spatio-temporal diagrams. Differential elongation rates are estimated from these processed κ_{\perp} data. The resulting spatio-temporal diagrams are smoothed thanks to median and averaging 2D filters. At last, the RGR of each interleaflet is computed thanks to the trajectories of the two nodes at its extremities.

4.2 Results

I have now introduced the framework of our experiments on the nutation motion. In this section I will present the results we have obtained by trying to characterize nutation and its variations. Three main questions are addressed in this section. The first is to properly describe nutation in terms of κ_{\perp} kinematics and estimate the differential elongation behaviour of the tissues. Second, we want to explore the hypothesis formulated from the results of Chapter 3 according to which the differential elongation of tissues occurs where the elongation rate decays. Finally, we are interested in the very rhythm of nutation. Variations of the nutation rhythm could be an outward signal of some physiological processes associated to differential growth and shape regulation.

4.2.1 Curvature variations and associated differential elongation

In this section, I propose to analyse a single acquisition of nutation, for which a maximum of information is available (leaf almost completely observable, good quality of the reconstructed trajectories, top and side views available). This acquisition lasted for approximately seven days. It does not contain the complete development on the leaf as it was started when the hook was already located on the fifth interleaflet—the studied leaf had 9 pairs of leaflets and 9 interleaflets. Of course, this acquisition is not complete but it is somehow representative of the typical behaviour of nutation. For this experiment, top and side takes were shot every 2.5 min.

As it has been briefly discussed in the previous parts, the most complete way of describing nutation is to study the spatial and temporal evolution of their curvature κ_{\perp} . The spatio-temporal diagram of curvature of the presented experiment is shown in figure 4.2. The reading of this spatio-temporal diagram allows to grasp many features of the nutation of the studied leaf but also of its development. Let us now read this spatio-temporal diagram.

The spatio-temporal diagram is constituted by three different dimensions: space, time and the dimension of interest. Each column of the diagram corresponds to a

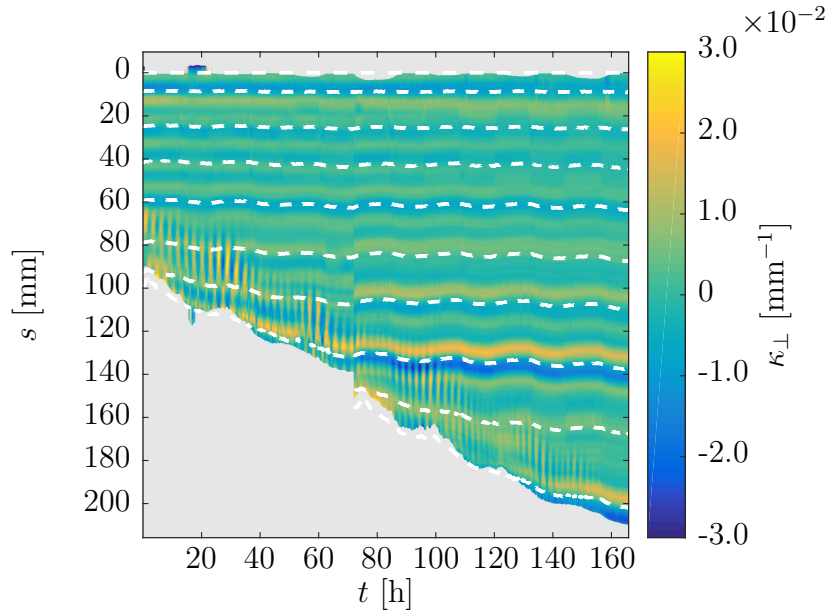


Figure 4.2: **Spatio-temporal diagram of κ_{\perp} for a nutating leaf.** The trajectories of the nodes are represented in dashed white lines. The first trajectory is on the petiole and is our reference point.

given time of the experiment. Each line corresponds to a spatial point of the rachis (defined from the reference point $s = 0$). Finally, the color code stands for the dimension of interest, which is here the curvature κ_{\perp} of the rachis.

If we now focus on a single column of the spatio-temporal diagram, we can read more about the geometry of the rachis. We can spot two obvious zones on the rachis. A zone of low curvature, on the lower interleaflets, near the petiole ; and a bent zone near the apex. If we now navigate throughout the columns of the diagram, we can read the spatial and temporal variations of curvature. We thus see that nutation is indeed characterised by a bending zone where are confined most of the κ_{\perp} variations. More precisely, κ_{\perp} oscillates from negative to positive values: the rachis is nodding from left to right. In this experiment, the curvature roughly oscillates between $\kappa_{\perp} = -3 \times 10^{-2} \text{ mm}^{-1}$ and $\kappa_{\perp} = 3 \times 10^{-2} \text{ mm}^{-1}$, which corresponds to a maximum radius of curvature of about 3 cm. At last, we can see in figure 4.2 that the nutation frequency is not constant in time. For example, the oscillations of κ_{\perp} are slower around $t = 20 \text{ h}$ than around $t = 100 \text{ h}$.

Finally, the trajectories of the nodes have been overlayed on the spatio-temporal diagram. The first trajectory $s = 0$ corresponds to a reference point on the petiole. Therefore, the first interleaflet is comprised between the second and third trajectories and so on.

Two major artefacts are visible in figure 4.2. The first one is around $t = 20 \text{ h}$. We see a brutal elongation of the rachis, with points below the reference trajectory.

This is typical of a false detection, leading to extra points in the rachis. The second one is found at $t = 70 h$. Here we see that two interleaflets appear at once. This is because I completed the paint over the rachis at this moment. Note also that at the beginning of the experiment and at the moment of the second painting, the apical-most trajectories are quite disturbed. It is possible that the stroking the rachis with the paintbrush induces some kind curvature response.

The spatio-temporal diagram of curvature has revealed a zone of bending. Let us now focus on this specific zone. To do so, we are going to estimate the differential elongation $\dot{\delta}$ associated with the nutation motion. If we assume that (i) all the curvature variations of the rachis result from differential elongation and that (ii) curvature varies rapidly in comparison with the typical time scale of elongation, we can estimate $\dot{\delta}$ from equation (4.3).

First, we need to compute the time derivative of κ_{\perp} . Note here that all the displayed geometrical quantities correspond to projected quantities. They are the orthogonal projection of the 3D geometry of the rachis in the focal plane of the camera. The bending zone clearly is the zone of interest in our case. Near the hook, the rachis is reasonably parallel to the plane of the camera allowing satisfying estimation of the κ_{\perp} and of its variations.

Second, we need to measure the radius R of the rachis. Our top-view takes do not allow a precise measurement of R as the rachis appears quite thin. Instead, R was measured in side-view takes. For the purpose of this experiment, R was only measured once, in the bending zone¹ Here, $R \simeq 0.6 mm$.

Finally, by applying equation (4.3) to the spatio-temporal diagram of curvature, we can thus build a spatio-temporal diagram for the estimated differential elongation rate $\dot{\delta}$ (see figure 4.3). The envelope of the $\dot{\delta}$ was obtained thanks to the Hilbert transform (Feldman, 2011) (see figure 4.4).

Here, the bending zone—or equivalently the zone of differential elongation—appears in an even clearer way than in figure 4.2. We clearly see that the part of the rachis which is undergoing differential growth is situated at the tip. Downstream of this zone, we have $\dot{\delta} \simeq 0$. It seems that the bending zone progressively shifts along the rachis. More precisely, it seems that the bending zone is set an almost constant distance from the apex (see figures 4.3 and 4.4).

¹The radius of the rachis however slowly increases from the apex to the petiole. Because κ_{\perp} variations are confined to a single region, the measurement of R in this specific zone are sufficient in a first approach.

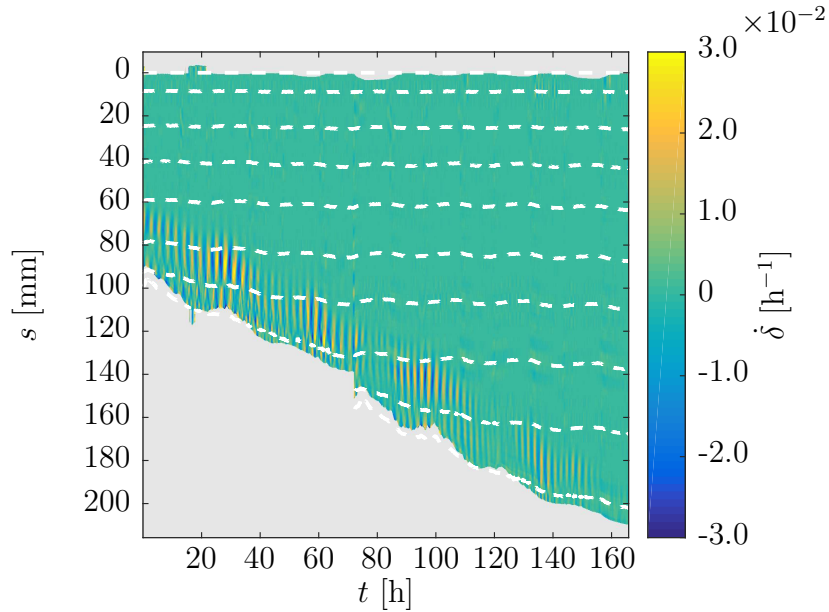


Figure 4.3: **Spatio-temporal diagram of estimated $\dot{\delta}$ for a nutating leaf.** This diagram was directly obtained from figure 4.2 by applying equation (4.3). The trajectories of the nodes are represented in dashed white lines. The first trajectory is on the petiole and is our reference point.

The analysis of figure 4.2 has revealed irregularities in the frequency of nutation. The $\dot{\delta}$ -related spatio-temporal diagrams put forward the variations of amplitude in time. As a matter of fact, we see that the amplitude of the $\dot{\delta}$ oscillations become smaller and smaller in time (see figure 4.3). In addition to this global dampening of nutation amplitude, we see that the amplitude is modulated by a slow rhythm of about $35 h$ (see figure 4.4). We can spot regular nutation ‘surges’ or ‘tides’, that is to say moments when the amplitude of nutation increases. In this case, the delay between two tides is approximately $20 h$ (see around $t = 30 h$, $t = 70 h$, $t = 110 h$ and $t = 140 h$). Interestingly enough, we see thanks to the nodes trajectories—white dashed lines—that these nutation surges appear to hop from an interleaflet to the following one, toward the apex.

Finally, we can comment on the growth behaviour of the rachis thanks to the several shown spatio-temporal diagrams. Following the spatial extension of the rachis gives a first information on the rate of growth of the rachis. Here, we see that the growth rate of the rachis is approximately constant as its spatial extension increases almost linearly.

By using the trajectories of the nodes, we can also get qualitative information on the distribution of growth along the rachis. We notice that the interleaflets with the greatest elongation rates are located near the apex. Once again, we foresee the

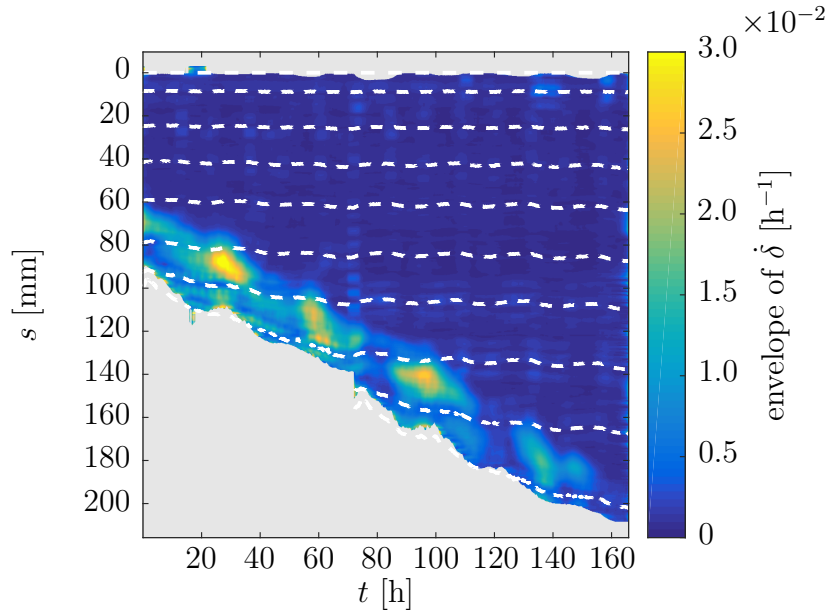


Figure 4.4: **Spatio-temporal diagram of the envelope of $\dot{\delta}$.** This diagram was obtained thanks to a Hilbert transform of the signals $\dot{\delta}(s)$ from figure 4.3. The bending zone and nutation irregularities are highlighted.

existence of an elongation zone near the apex.

4.2.2 Relation between elongation and differential elongation

In Chapter 3, we have studied the kinematics of curvature during hook maintenance. The existence of a bending zone and the clues for a growth zone have led us to hypothesize a relation between elongation and differential elongation. Can we go further and investigate this possible link? On the one hand, the previous section has put forward the existence of a zone of differential elongation in the case of nutation. On the other hand, we have a proxy for the elongation rate of rachis at our disposal. It thus seems that we now have the tools to tackle this question.

The aim here is to directly compare the elongation and differential elongation of the rachis. So, we must first get information on the elongation rate of the rachis. The trajectories of the nodes allow us to measure the apparent length of each interleaflet of the studied leaf. Trajectories are indeed affected by the global 3D motion of the leaf. To go beyond this problem, trajectories were averaged over the typical time scale of these motions ($\simeq 12 h$). We can then extract an averaged relative growth rate \dot{E} of each interleaflet. Note here that, in the limit where θ varies slowly in time—*i.e.* between a dozen of takes—the measured apparent \dot{E} is approximately

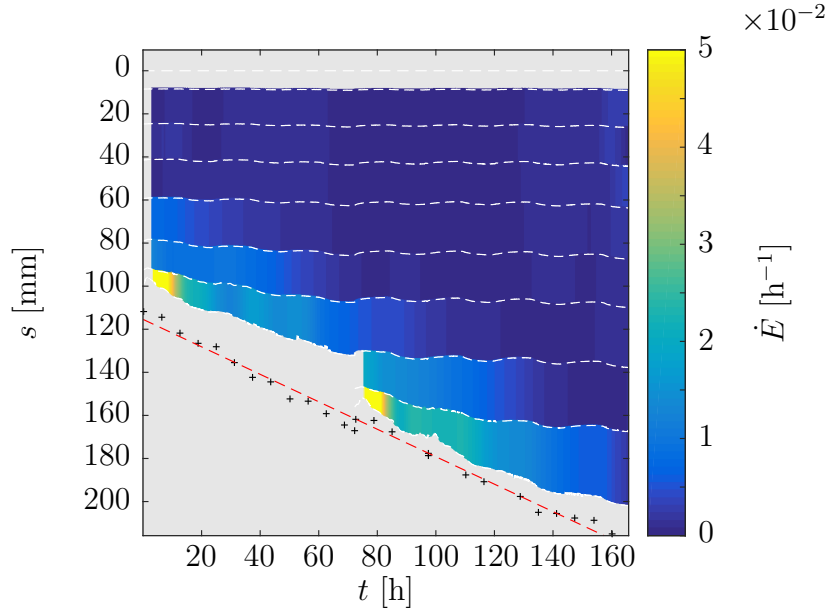


Figure 4.5: **Spatio-temporal diagram of the relative growth rate \dot{E} per interleaflet.** \dot{E} values were obtained from the trajectories of the nodes. Trajectories are indicated by white dashed lines. The position of the apex is indicated by black crosses. The fitted trajectory of the apex is indicated by the red dashed line.

equal to the true, unprojected \dot{E} . The values of \dot{E} have been computed for each interleaflet at each time and have been gathered in a spatio-temporal diagram (see figure 4.5).

As expected from the previous section, we see that the larger \dot{E} are met for the apical-most interleaflets. A given interleaflets starts by a phase of strong elongation (eg. interleaflet 6 between $t = 0 h$ and $t = 20 h$). The relative growth rate then slowly decays until it reaches $\dot{E} = 0 h^{-1}$. At this point, the growth of the interleaflet is over. We see that, later, interleaflets 7 and 8 adopt the same behaviour. Consistently with our rough descriptions of Chapter 3 and section 4.2.1, we see here clues of a growth zone.

We already have the spatio-temporal diagrams of $\dot{\delta}$ at our disposal. For the sake of consistency, however, we need to build an averaged measurement of differential elongation. Such a quantity has already been introduced (see equation (4.4)). The values of \dot{D} are thus obtained by averaging $\dot{\delta}$ over each interleaflet, at each time. Attention was paid to the fact that $\dot{\delta}$ is not always known on entire interleaflets (see figure 4.3, apical-most interleaflets). Values of \dot{D} were thus computed only when at least 85% of the interleaflet was associated to a value of $\dot{\delta}$. The resulting spatio-temporal diagram is shown in figure 4.6.

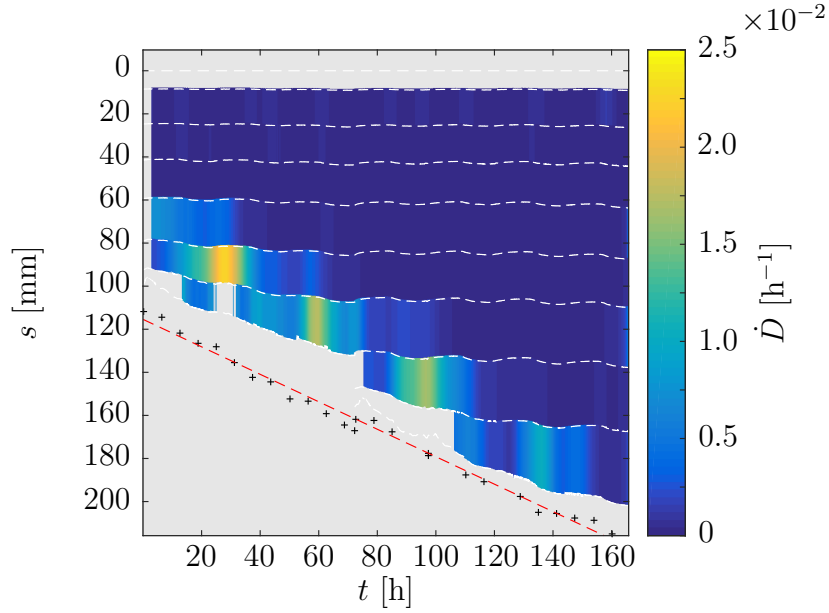


Figure 4.6: **Spatio-temporal diagram of the relative differential growth rate \dot{D} per interleaflet.** \dot{D} values were obtained by averaging data from figure 4.3 on each interleaflet. Trajectories are indicated by white dashed lines. The position of the apex is indicated by black crosses. The trajectory of the apex is indicated by the red dashed line.

The resulting spatio-temporal diagram is consistent with the previous spatio-temporal diagrams of differential elongation in figures 4.3 and 4.4. We see that for a given interleaflet, \dot{D} is first low, then increases to a maximum value and finally decreases to $\dot{D} = 0 \text{ h}^{-1}$. This behaviour is repeated sequentially by all the successive interleaflets. So, like previously, we can discern a zone of differential elongation. The position of this zone is however different from the position of the elongation zone. The peaks of \dot{D} do not occur in the apical-most interleaflets, but seemingly one interleaflet back. Finally, this diagram also underlines the slow modulation of nutation, like in figures 4.3 and 4.4.

The comparison of the spatio-temporal diagrams of \dot{E} and \dot{D} suggests that the zone of maximum differential elongation is situated downstream of the zone of maximum elongation. For instance, in figure 4.5, between $t = 0 \text{ h}$ and $t = 40 \text{ h}$ we see that the sixth interleaflet is comprised in the zone of maximum elongation. In figure 4.6, on the same time interval, we see that most of \dot{D} is contained in the fifth interleaflet. Differential elongation thus appears to take place where elongation is decaying. The same comparison is possible once again, between $t = 70 \text{ h}$ and $t = 120 \text{ h}$ and leads to the same observation.

We now want to go beyond the simple comparison of the spatio-temporal diagrams and completely take benefit from them. To investigate the spatial arrangement of elongation and differential elongation, we are going to try and build the average \dot{E} and \dot{D} profiles.

Since it appears that the elongation and bending zones are defined from the apex, we first need to set the spatio-temporal diagrams in the referential of the apex. The apex is unfortunately invisible on most top-view takes. Its position was thus determined from the side-view takes—and from the top-view takes when it was possible. The manual tracking of the apex is shown in figures 4.5 and 4.6 by small black crosses. Since the global rate of elongation of the rachis is approximately linear in this part of the experiment, we have fitted the trajectory of the apex with a linear displacement. This fitted trajectory is indicated by the red dashed line.

It is now possible to shift the spatio-temporal diagrams in the referential of the apex. Once this is done, the average profiles of \dot{E} and \dot{D} can be built. To do so, we simply average the diagrams in the time dimension. Some of the information in the shifted spatio-temporal diagrams were rejected from the analysis however. As discussed earlier, the apical-most trajectories are disturbed around $t = 10 h$ and $t = 75 h$. This causes overestimated values for \dot{E} . These specific parts were thus excluded from the analysis of both \dot{E} and \dot{D} spatio-temporal diagrams. The resulting \dot{E} and \dot{D} profiles are presented in figure 4.7.

The experimental data are represented by coloured dots in figure 4.7. Since we cannot observe the whole rachis, because and we have excluded some points from the analysis, the retrieved profiles are necessarily incomplete near the apex. They start around $s_R = 25 mm$. We observe that the average \dot{E} profile smoothly decays from the apex to the base. The hypothesis of a growth zone with saturation suggests a sigmoidal shape for the \dot{E} profile and the existence of a plateau. Unfortunately, because of the missing spatial information, we cannot observe the presence or absence of a plateau. We nevertheless see that the average \dot{E} profile decays to almost $0 h^{-1}$ in a few dozens of millimetres and stays then constant.

Let us now focus on the average \dot{D} profile. Near the apex, we see that \dot{D} increases up to a maximum value which is reached in $s_R \simeq 40 mm$. \dot{D} then decreases in a few dozens of millimetres to $\dot{D} = 0 h^{-1}$ and stays constant down to the base of the leaf. It thus seems that the average \dot{D} profile has a bell shape near the apex and is flat near the petiole.

In accordance with our hypothesis, we see that the maximum of \dot{D} is reached in a zone where \dot{E} is decaying. Moreover, we see that the characteristic lengths over which the \dot{E} profile varies and the width of \dot{D} are comparable. This supports the idea that the spatial distributions of these two quantities are tightly connected.

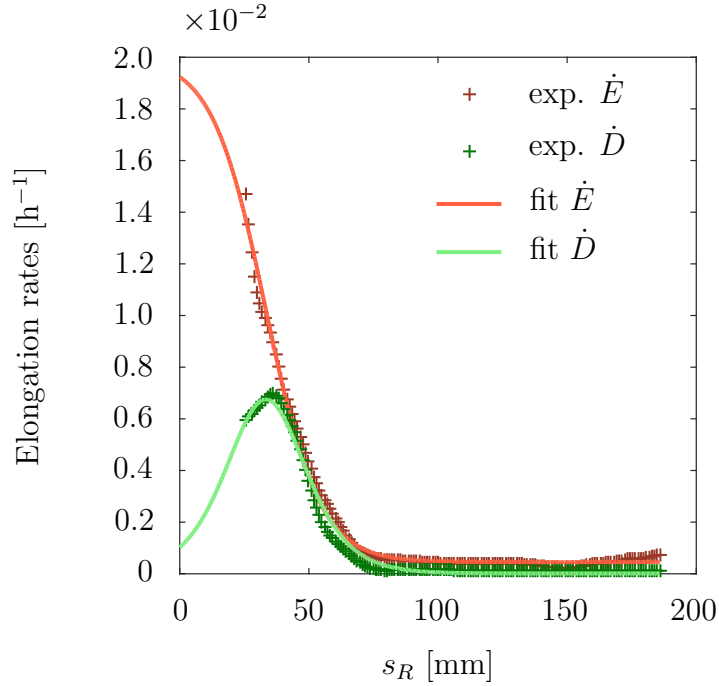


Figure 4.7: **Average \dot{E} and \dot{D} profiles.** The experimental dots were obtained by temporally averaging the re-aligned \dot{E} and \dot{D} spatio-temporal diagrams. Experimental data were simultaneously fitted with a sigmoid (equation (4.5)) and its derivative (equation (4.6)) respectively. One on ten experimental points have been plotted here.

The several spatio-temporal diagrams of elongation and differential elongation have evidenced two zones: a growth zone and a bending zone. We thus see that we need at least two characteristic lengths to describe the growth behaviour of the rachis. These lengths are the growth zone length L_{gz} and the bending zone length L_{bz} . In addition to that, the hypothesis of tip growth suggests a sigmoidal-like profile for \dot{E} which might be compatible with our experimental profile (see figure 4.7). A third length L —the characteristic length of the sigmoid—is thus needed. We have however showed in the last paragraph that \dot{D} occurs where \dot{E} varies the most. Moreover, the width L_{bz} of the \dot{D} peak is comparable to $2\Delta L$. These observations are to some extent complementary and lead us to postulate that the spatial profile of \dot{D} is proportional to the spatial derivative of \dot{E} , i.e. $\dot{D} \propto \partial_s \dot{E}$. I now propose to test this hypothesis on our experimental data presented in figure 4.7. Following the hypothesis of tip growth with a maximum elongation plateau near the apex, we propose to fit our experimental \dot{E} profile to:

$$\dot{E} = \frac{\dot{E}_0}{2} \left(1 - \tanh \left(\frac{s_R - L_{gz}}{\Delta L} \right) \right) + \dot{E}_\infty \quad (4.5)$$

where \dot{E}_0 is the maximum relative growth rate value and \dot{E}_∞ is a constant value. In consequence, the experimental profile of \dot{D} must be fitted with:

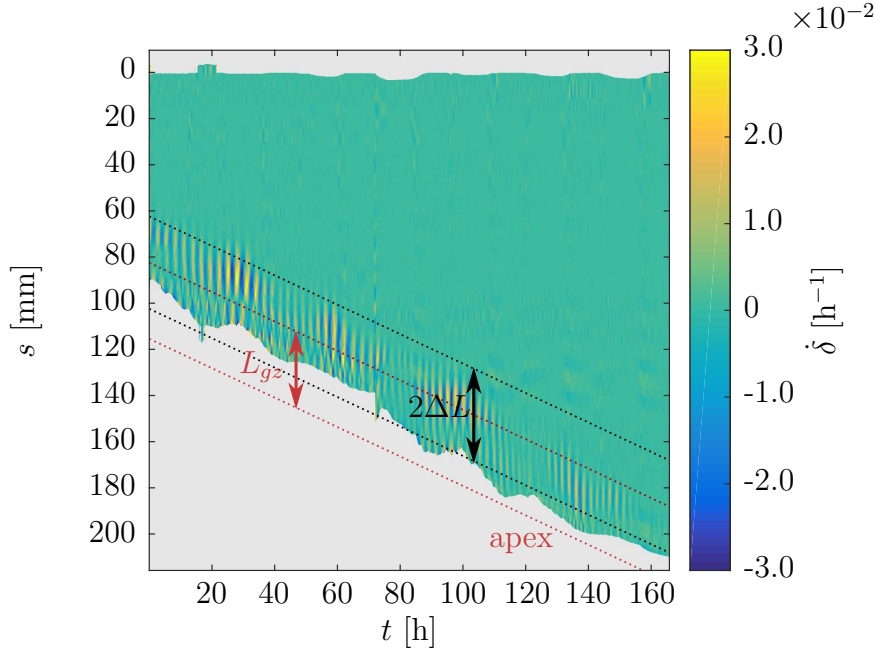


Figure 4.8: **Position of the growth and bending zones.** The growth zone is comprised between the two black dashed lines. The bending zone is comprised between the two red dashed lines.

$$\dot{D} = \dot{D}_0 \left(1 - \tanh^2 \left(\frac{s_R - L_{gz}}{\Delta L} \right) \right) + \dot{D}_\infty \quad (4.6)$$

where \dot{D}_0 is the maximum rate of differential elongation and \dot{D}_∞ is a constant value. The six parameters of the fit are thus $\{L_{gz}, \Delta L, \dot{E}_0, \dot{D}_0, \dot{E}_\infty, \dot{D}_\infty\}$. Since the fitted profiles for \dot{E} and \dot{D} share two parameters, they are performed simultaneously. Doing so greatly constrains the parameters of the fit but allows to check if our hypothesis is reasonable.

We see a good qualitative agreement between our experimental data and the fitted profiles (see figure 4.7). For our two quantities of interest, the fit gave $L_{gz} = 33.4 \text{ mm}$ and $\Delta L = 20.8 \text{ mm}$. If we accept the equations (4.5) and (4.6), it is also possible to give an experimental measurement of L_{gz} . by measuring the position of the maximum of \dot{D} . The maximum is found in $s_R = 35.9 \text{ mm}$. We thus see that L_{gz}^{exp} and L_{gz}^{fit} differ by 7%. The growth zone is bounded by the apex on one side and by $s_R = L_{gz}$ on the other side. By definition, the bending zone is delimited by the peak of \dot{D} and is thus centred around $s_R = L_{gz}$ and of length $2\Delta L$. The spatial arrangement of these zones on the spatio-temporal diagram of $\dot{\delta}$ is shown in figure 4.8.

Since the result of the coupled fitting of \dot{E} and \dot{D} gives satisfying results, we now

have clear experimental support to claim that differential elongation takes place where elongation is decaying.

The establishment of averaged spatial profiles for \dot{E} and \dot{D} revealed the intimate connection between growth and differential growth and have paved the way for further modelling of nutation. All the process that lead to their establishment was guided by the idea of steady growth patterns underlying nutation. As a result, the dynamical nature of nutation has been ignored. The several spatio-temporal diagrams that we have seen up to now however contained evidences of changes in the rhythm of nutation (see figures 4.3 and 4.4 in particular). We will now focus on this specific aspect of nutation in the following section.

4.2.3 Nutation described as an oscillation

The nutation of *Averrhoa carambola* leaves naturally evokes the pendulum motion. We have seen that nutation is characterized by rapid variations of κ_{\perp} —in comparison with the typical time scale of growth. These oscillations of κ_{\perp} are clearly pseudo-periodic in the sense that their frequency vary over a few complete motion cycles. In the same time, the amplitude of κ_{\perp} variations also appear to change. The period and the amplitude of nutation both appear to be functions of time. We have additionally seen that nutation is also characterized by a bending zone where most of the curvature variations—or equivalently the differential elongation—is confined. Finally, nutation can be described by its period τ_{nut} , its amplitude A_{nut} and the position of the bending zone. A proper characterization of the nutation motion then requires to quantify the variations of these three quantities.

Frequency and amplitude variations

When the nutation motion has been observed on long enough periods—that is to say more than 3 days—we tried to study the nutation signal Δy itself (see section 4.1.1 for definition). The experiment presented in figure 4.9 is a beautiful illustration of nutation. It lasted almost 6 days. The alternation of day and night is indicated by white and gray backgrounds respectively. The top panel of figure 4.9 shows the evolution of the deflection Δy of the leaf with respect to the principal direction of elongation \vec{d} . Once again, we see that nutation is a continuous motion. The motion does not stop, at any moment, before the end of the primary elongation. Despite being continuous, nutation is not constant or regular though. We clearly see a modulation of the Δy signal in time. Variations of the nutation period τ_{nut} can also be observed. The most obvious ones are for example between $t = 20 h$ and $t = 50 h$, where the motion decelerates and between $t = 100 h$ and $t = 120 h$ where

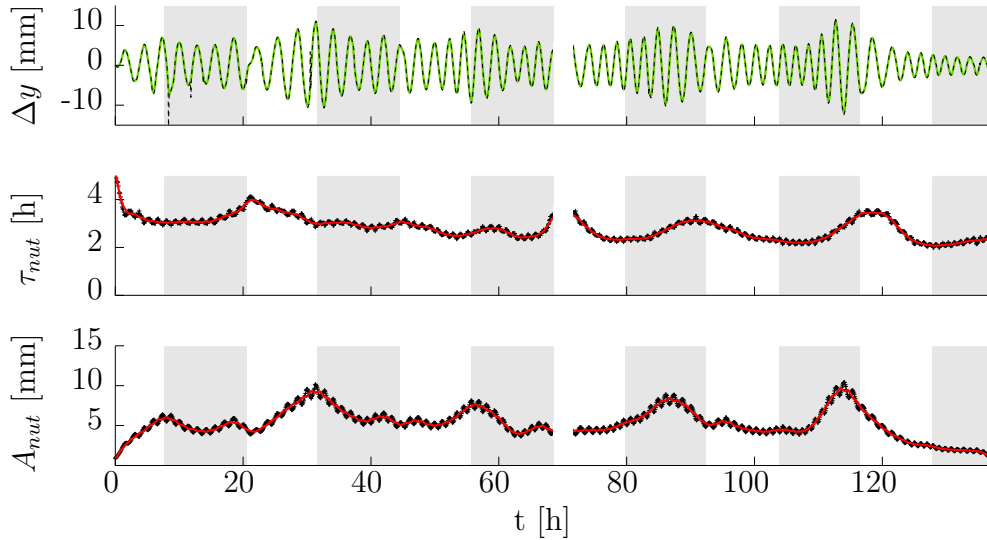


Figure 4.9: **Variations of the nutation signal in time.** Top panel: nutation signal represented by the deflection Δy of the leaf with respect to the line described by the direction vector \vec{d} . Middle panel: frequency of the nutation signal. Bottom panel: amplitude of the nutation signal. Day/night alternation is indicated by white/gray background. The black lines represent direct output from the wavelet transform. The red lines are smoothed data. The absence of data around $t = 70$ h is due to a manipulation of the plant.

the motion accelerates. We also observe variations of the amplitude of the motion. For instance, we see the amplitude increasing and decreasing around $t = 30$ h.

Nutation is thus a complex oscillatory motion, with modulations of both its frequency and amplitude. These modulations are furthermore quite quick in comparison with the mean period of the signal. As a matter of fact, A_{nut} and τ_{nut} evolve on a few complete cycles of the motion. A useful tool to analyse such signals is the wavelet transform. Like Fourier transforms, wavelet transforms allow to extract the frequency and amplitude information of a signal. Using Fourier transform however implies to work on signals with a fixed spectrum. It is also possible to use short time Fourier transform to evaluate the evolution of the frequency of a signal. But here, the rapidity of frequency changes makes wavelet transform the appropriate tool. Contrary to Fourier transforms, wavelet transforms do not use the whole signal for analysis. Rather, a mother wavelet² moves along the signal and is dilated at each step to fit the signal. In this sense, wavelet transforms allow local determinations of frequency. The results of wavelet transforms are shown in the middle and bottom panels of figure 4.9.

²A function which square is integrable

The middle panel of figure 4.9 shows the evolution of τ_{nut} . We see here that τ_{nut} is comprised between 2 h and 4 h . The period of nutation globally decreases in time, meaning a global acceleration of the motion. As previously discussed, we can however spot several local maxima in the period around $t = 20 h$, $t = 45 h$, $t = 90 h$ and $t = 120 h$. Here we do not consider the data around $t = 70 h$ because of the absence of Δy data at this moment.

The amplitude is shown in the bottom panel of figure 4.9. The amplitude of nutation A_{nut} is comprised between 0.5 cm and 1.1 cm . This means that the apex of the leaf can go through horizontal displacements of approximately 2 cm . Like for τ_{nut} , we see distinct A_{nut} variations throughout the experiment. Around $t = 20 h$, $t = 45 h$, $t = 90 h$ and $t = 120 h$, significant increases of A_{nut} were recorded. Unlike for the behaviour of τ_{nut} , no underlying monotonic tendency is seen for the amplitude. At last, we can wonder if A_{nut} and τ_{nut} evolutions are correlated. It appears quite clearly on this example that the local maxima do not necessarily occur at the same time.

One of the most interesting features of the experiment pictured in figure 4.9 is the progressive shift between the day/night cycle and the position of the local maxima of amplitude. During the first complete day of the experiment—between $t = 20 h$ and $t = 44 h$ —, we see that the amplitude is minimal at dawn, increases to a maximum at dusk and finally decreases again during the night. On the contrary, between $t = 100 h$ and $t = 124 h$, we see that the amplitude of nutation increases abruptly during the night and is maximal just before the dawn. In contrast with the behaviour of the amplitude, there is no equivalent shift for the frequency of nutation. We have already discussed the local minima of frequency, on an almost daily basis. We additionally notice that the increase of τ_{nut} at dawn gets more and more pronounced in time. The recurrent increases of the period—meaning abrupt decelerations of nutation—are likely to be due to the sudden lighting of the lamps in the cultivation room. Light is indeed known to play a role in the opening of stomata, among other environmental factors such as temperature and humidity. The opening of stomata initiates plant transpiration and may thus induce water loss within the plant tissues. This water deficit stress may in turn affect growth, nutation or any other physiological process. In the case of slow light intensity variations, the opening of the stomata is not expected to be brutal, allowing an optimal opening for equilibrated gas exchanges between the plant and its environment. In our case, the sudden lightning might cause a quick and exaggerated opening of the stomata, leading to water loss. This situation is however expected to be transient only, as water deficit stress will induce the closing of stomata and reaching an optimal

opening. Less water in cells results in reduced turgor pressures and finally reduced overall rigidity of the plant. This is visible in the morning as the leaf goes through a transient collapse, with a significant increase of θ at the base.

Can the observations made on this single leaf be generalized? More importantly, these results question the link between the rhythm of nutation and the day/night alternation. Is the progressive shift of the amplitude peaks a signature of the establishment of the circadian rhythm of the leaf? Or could it be that nutation is simply not correlated to the day/night alternation? To answer this question, further investigations were conducted.

The experiment described previously was repeated a number of times. Some of these repetitions are pictured in figure 4.10. If the extent of the nutation motion is clearly different from an experiment to another—the maximum amplitudes roughly vary between 0.5 *cm* and 2 *cm*—the shape of the signals is somehow universal. Like previously, we see that the leaves move during day and night without interruption. We also see that the leaves exhibit a succession of nutation tides. This behaviour is particularly visible in the case of the first presented experiment (see top panel of figure 4.10). The amplitude of each signal is shown in figure 4.11. Nutation tides—meaning more or less prominent bursts of amplitude—are visible all along the different experiments. We furthermore notice what seems to be a general tendency of the nutation motion. Long experiments starting from early stages³—such as experiments 2, 3 and 8—show the nutation establishing and then ending. In these cases, we see a global increase of the amplitude of nutation in the first days of development. Later on the amplitude decreases until it reaches 0 and the nutation motion completely vanishes. This decrease in amplitude can be observed for every experiment showing the ending of nutation—that is all experiments except experiment 7.

The evolution of the period of nutation revealed much less clear. Nutation tides can be accompanied by an acceleration or a deceleration of the motion. In the example of figure 4.9, we could see that the the period was globally monotonously increasing. This appears to be an isolated event in our data set. The global rhythm of nutation is however well-defined. The distribution of the periods of nutation is shown in figure 4.12 under the form of box plots. For each experiment, the box shows the first and third quartiles of the distribution. We see that most of the periods are comprised between 2.5 *h* and 3 *h*. More precisely, the medians—indicated by the line within each box—for each experiment are comprised between 2.3 *h* and 2.9 *h*.

³The roman numbers indicating the number of open leaflets in figures 4.10 and 4.11 are a good indicator of how early in the development of the leaf the experiment has begun.

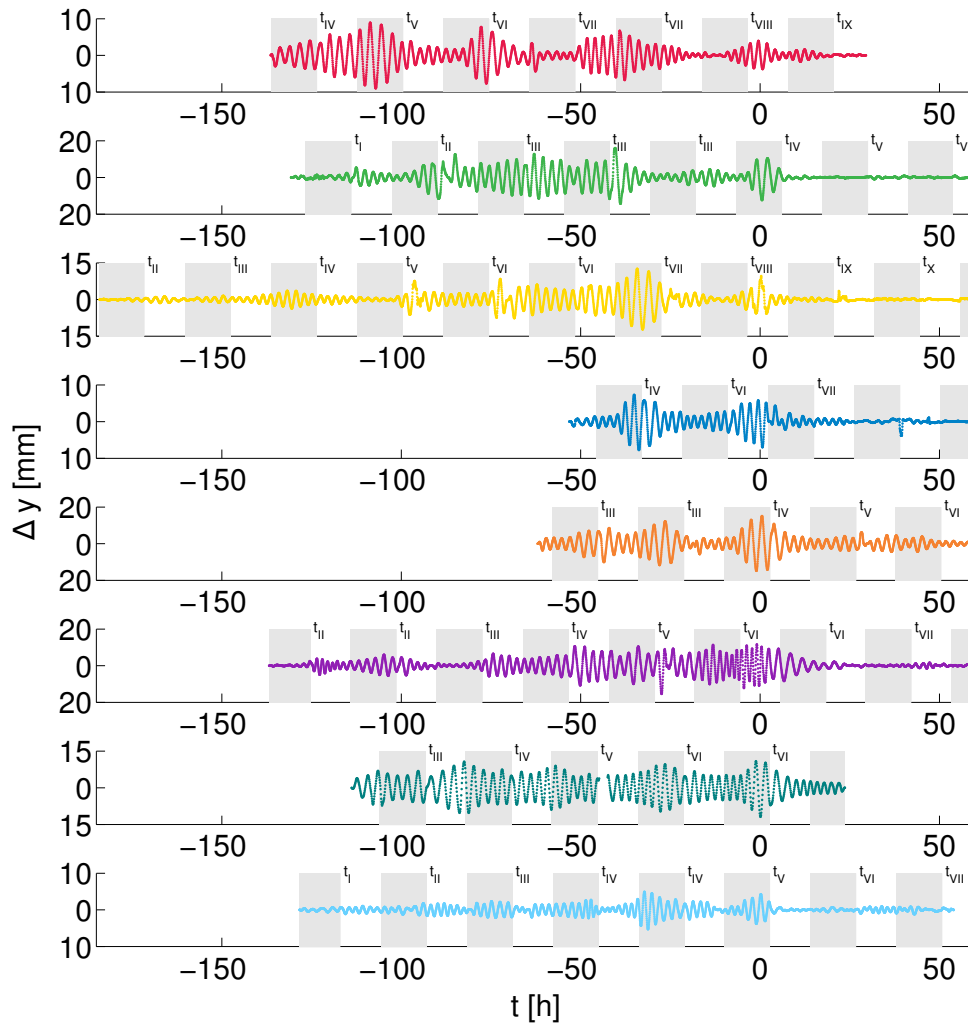


Figure 4.10: **Eight examples of nutation signals.** The signals have been aligned in order to make their last peak of amplitude coincide ($t = 0$). For each day of experiment, a Roman number indicates the number of leaflets that had opened and raised. Day/night alternation is indicated by white/gray background. The experiment shown in fig. 4.9 is the second one from the bottom. The first top panel corresponds to the experiment described in section 4.2.2.

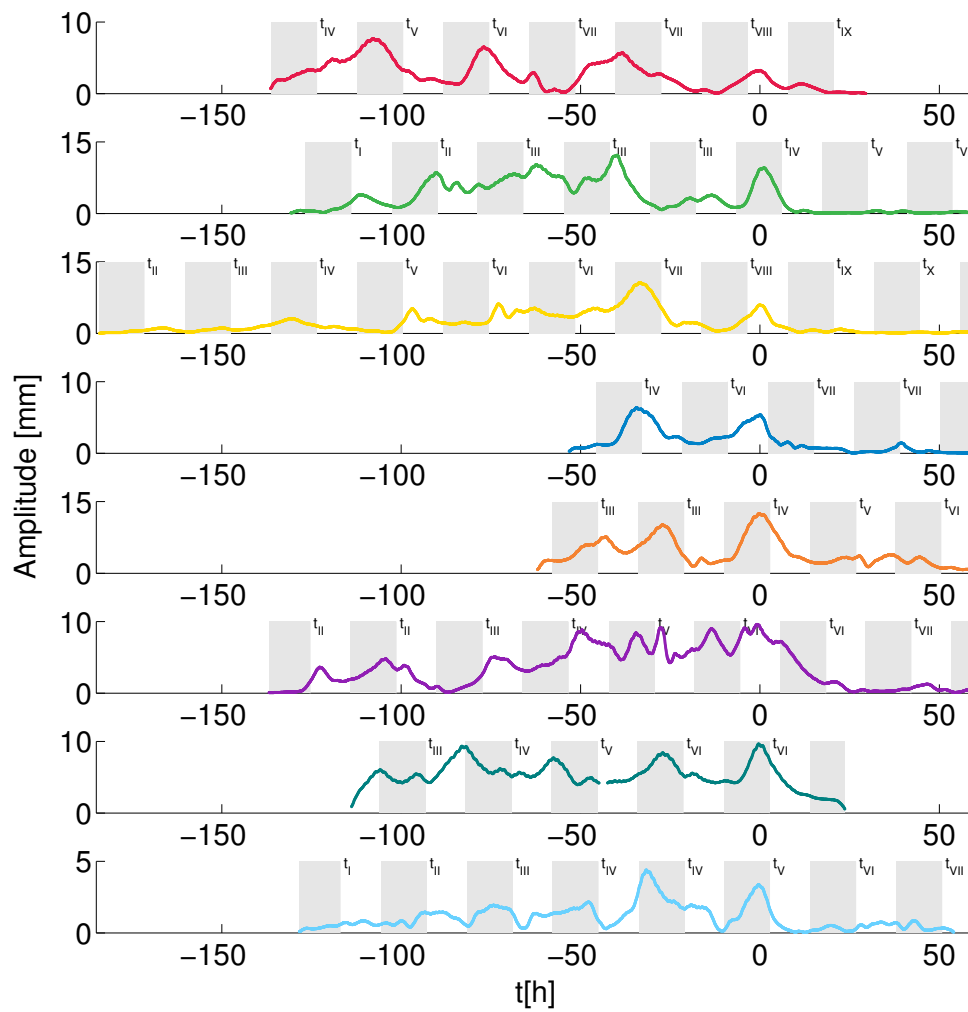


Figure 4.11: **Evolution of the amplitude of nutation in time.** The amplitudes have been determined thanks to wavelet decomposition. The signals of fig. 4.10 are shown in the same order and colours.

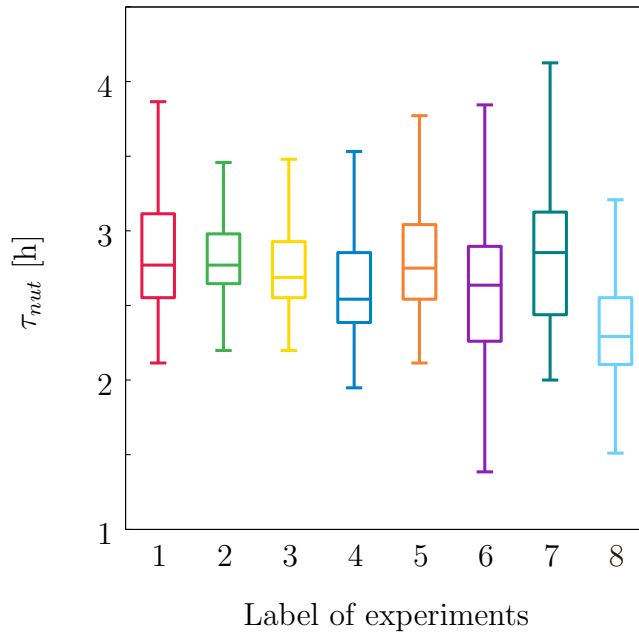


Figure 4.12: **Distributions for the nutation period.** The periods have been determined thanks to wavelet decomposition. The signals of fig.4.10 are shown in the same order and colours. Outliers are not shown in this graph.

It is thus possible to identify common behaviours to all the nutating leaves. The mismatch between their relation to the day/night alternation is however blatant. The figures 4.10 and 4.11 present the nutation signal and their amplitudes with a *ad hoc* temporal shift. The values of the time were shifted to make the last peaks of amplitude coincide. In this way, we see that the amplitude behaviours roughly coincide—peaks and decreasing amplitude—but that the day/night alternation completely disagree from an experiment to another. For example, let us focus on the two first signals in figure 4.11. We see that the amplitude peaks roughly coincide, but day and night are inverted. This discredits the hypothesis of a direct link between nutation and the day/night cycle. Rather, it seems that the periodicity of nutation tides—or amplitude peaks—is not 24 *h*.

The actual periodicity of each amplitude signal can be determined by autocorrelation. Autocorrelation consists in convolving a signal with itself. Plotting the score of autocorrelation against the quantity by which it is shifted—called lag—reveals the periodicity of the signal. A typical autocorrelation graph is shown in figure 4.13. In some cases, no peaks could be detected. To overcome this endeavour, autocorrelation signals were detrended in a first time and peaks detection was performed afterwards. Once the lags corresponding to local maxima of autocorrelation are retrieved, we can estimate the period of nutation surges. To do so, the retrieved lags

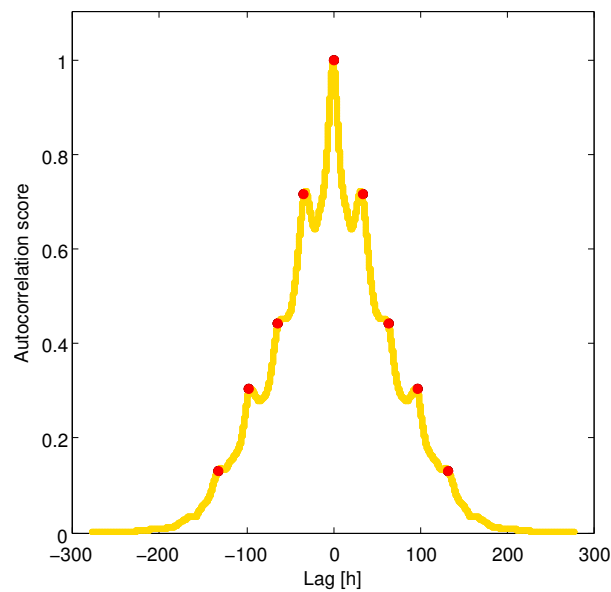


Figure 4.13: **Example of autocorrelation curve.** Data shown correspond to experiment 3. The autocorrelation score is plotted against the lag (time shift of the signal). Peaks indicate a good overlay of the original and shifted signals and thus periodicity. Peaks are indicated by red dots. Note the symmetry (and redundancy) of the signal around 0.

were divided by their peak position. In other words, we assume that peaks—except for the 0-lag peak—correspond to harmonics of the first peak. The results of this procedure are shown in figure 4.14. First, we see that most measured periods are above 26 h . Mean periods are furthermore all different from 24 h and span a wide interval, from 23 h to 35 h . In our data, three sets of behaviours are delineated:

1. Experiments 1, 3 and 4, with a mean tide period above 30 h .
2. Experiments 5, 6, 7 and 8, with a mean tide period slightly superior to 25 h , between 26 h and 29 h .
3. At last, experiment 2 has a mean surge period slightly below 24 h .

Second, for a given experiment, the values of the measured periods sometimes vary in a great extent. For instance, we see in experiment 6 that the measured periods vary from 23 h to 34 h , that is a 9 h difference between the two periods. It must however be noted that autocorrelation provides periodicity information in an averaged and smooth way. Measuring the delays between peaks directly on the graphs of figure 4.11, would provide slightly different results. In particular, if we look at the experiment 3, we can spot two peaks separated by only 24 h —around $-100 h$ and $-75 h$ —but most of the peaks are separated by a more than 30 h . This

remark can be generalized to all the signals that are sufficiently long to allow the comparison of several peak delays.

At last, we can try and compare the quick and slow rhythms of nutation. In order to understand the nature of these rhythms, it is important to know how well-defined they are. Here we are going to estimate how well the rhythm of nutation is defined, in average, from a plant to another. To do so, we compute the mean period—of the slow or quick rhythm, indifferently—for each experiment and gather all these values. From these values we extract a mean period $\bar{\tau}$ and a standard deviation σ_{τ} . Standard deviation gives information on the extent of the dispersion of data within a given distribution. To compare two different distributions, it is however needed to normalize it by the mean of its corresponding distribution. This dimensionless quantity is called the coefficient of variation: $c_v = \frac{\sigma_{\tau}}{\bar{\tau}}$. For the quick rhythm, we have $c_v^{nut} \approx 5.9\%$ while for the rhythm of tides has $c_v^{tide} \approx 15.3\%$. We see here that the mean periods of nutation tides is about 2.6 times more disperse than the mean periods of nutation. In other words, the mean rhythm of nutation is better determined than the rhythm of amplitude tides.

All in all, we see that the amplitude modulation of nutation is made on a rhythm which is mainly plant-dependent and that do not correspond to the cycle of day and night. Moreover, considering the variability of the measured periods, we can say that the periodicity of nutation surges is not robust or ill-defined. The apparent lack of correlation between the rhythm of these amplitude modulations and the day/night cycle suggests a role for an internal clock.

Comments on the displacement of the nutation zone

The position of the nutation zone is the last parameter which evolution needs to be tracked in order to completely describe the nutation as an oscillation. From the description of nutation and the last sections, it is clear that the nutation zone shifts along the rachis. We have mentioned in Chapter 2 that the point where nutation is initiated seemed to do so in a succession of hops, from an interleaflet to another. Can we confirm this behaviour to the light of the gathered data?

We have seen that the spatio-temporal diagrams were affected by some artefacts due to the 3D motions of the rachis. In particular, changes in θ —global changes or partial unfurling of the rachis—result in apparent dilations and contractions of the rachis. We have thus to make sure that the displacement of the nutation zone is independent of such effects. To do so, a first approach consists in comparing the

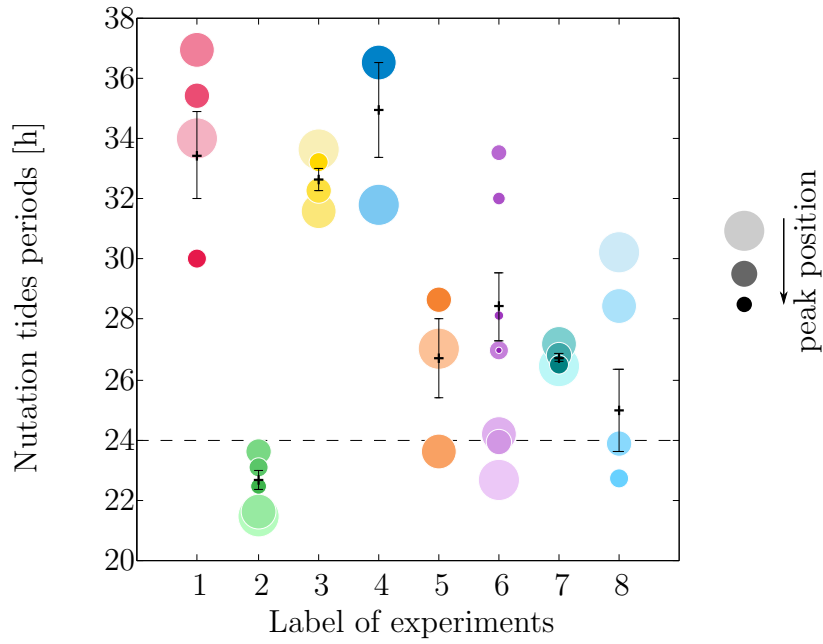


Figure 4.14: **Periods of nutation tides for each experiment.** For each experiment, black crosses correspond to the mean period. Error bars indicate standard errors. The signals of fig.4.10 are shown in the same order and colours.

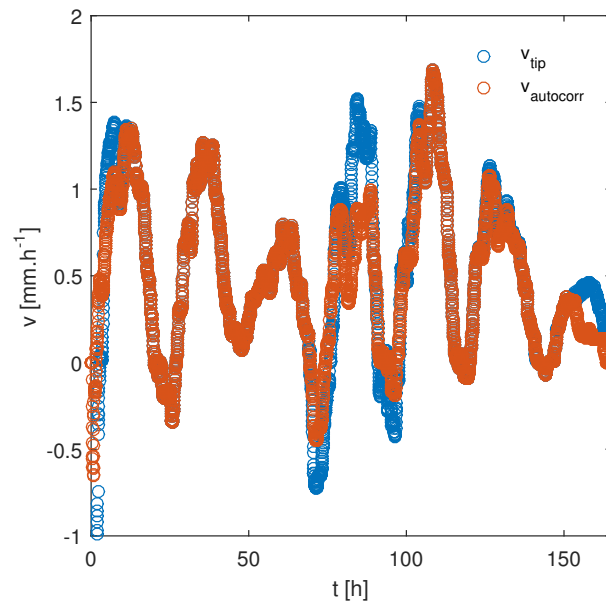


Figure 4.15: **Shifting velocity of the signal compared to the velocity of the apparent tip.** The velocity $v_{autocorr}$ at which the signal $\text{env}(\delta)$ of fig. 4.4 is shifted along the s-dimension is measured by autocorrelation.

displacement of the apparent tip and of the nutation zone. We measure the shift of our differential elongation signal thanks to autocorrelation. From this, we can extract the velocity $v_{autocorr}$ of the nutation zone and compare it to the velocity v_{tip} of the apparent tip.

Our results show that the velocity of the nutation zone mostly coincide with the velocity of the apparent tip (see figure 4.15). Some exceptions to this observation are found around obvious artefacts on the position of the tip. So, in first approximation, we can say that the zone of nutation shifts continuously by following the apex. The occurrence of hops is *a priori* excluded. Finally, we see that a continuous displacement of the nutation zone, combined with tides of nutation might create the impression of a discontinuous displacement mentioned in Chapter 2.

4.3 Discussion and partial conclusion

The shape of *Averrhoa carambola* leaves undergoes many shape changes during its growth among which the rapid nutation oscillations. In the context of posture regulation processes, such oscillations are puzzling. This fourth chapter was thus dedicated to the characterization of nutation. Like for the unfurling motion, we have first addressed the question of the kinematics of nutation. In a second time, we have explored the rhythms of nutation and their variations.

Characteristics of nutation The first question here was to characterize nutation. What are its remarkable features? We have seen that nutation is a swinging of motion the rachis. In other words, it consists in oscillations of its curvature κ_{\perp} . The analysis of the kinematics of curvature (see figure 4.2) has revealed that κ_{\perp} variations were confined to a specific region of the rachis. This region may be referred as the bending zone or the nutation zone. This confinement of the curvature variations has also been observed for the circumnutation of *Phaseolus vulgaris* (Millet et al., 1984). Although it is seldom discussed in the literature, it is very likely that all nutation and circumnutation motions share this characteristic. We have furthermore seen that this nutation zone is set at an approximately fixed distance from the apex (see figure 4.15). This behaviour recalls the bent zone in the case of the unfurling motion which relied on specific kinematics (see Chapter 3).

The nutation of *Averrhoa carambola* was shown to be characterized by two distinct rhythms. First, a short rhythm corresponding to the curvature oscillations themselves (see figure 4.10). Second, a slow rhythm corresponding to the modulation of amplitude A_{nut} of nutation (see 4.11). Such amplitude modulations are also

observed in the case of circumnutation (Schuster & Engelmann, 1997; Buda et al., 2003).

The period of nutation τ_{nut} was found to be quite variable for a given plant (see figure 4.12). It could roughly vary from 1.5 h to 4 h . Interestingly enough, the comparison of the τ_{nut} distributions revealed that the period of nutation was globally well-defined, with a low coefficient of variation for the median values. The typical period of nutation was found to be of about 2.8 h . Depending on the cases, the period of circumnutation varies between 20 min and 5 h (Mugnai et al., 2007; Stolarz, 2009). *Averrhoa carambola* is thus in the usual interval of (circum)nutation periods.

In contrast, the period of nutation tides τ_{tide} was found to be well-defined for a given plant but ill-defined from a plant to another (see figure 4.14). The mean τ_{tide} in our experiments is 28.8 h . The modulation of amplitude thus obeys to a circadian rhythm, superior to 24 h in average and suggests an internal circadian clock.

Finally, let us specify that in the case of circumnutation two rhythms are usually distinguished—short and long period nutations—corresponding to two entangled motions, of different amplitudes (Schuster & Engelmann, 1997). Their typical trajectories are epi- or hypotrochoids—i.e. the composition of a cycloid with an ellipse. The nutation of *Averrhoa carambola* does not display such complex trajectories. Trajectories might be affected in their spatial extent, but never change their shape radically. Some reports of ‘composed nutations’ have however been made in *Phaseolus multiflorus* (Heathcote, 1966). A low amplitude nutation—referred as micronutation—was superposed to the regular nutation. Our observations did not reveal such motions in the case of *Averrhoa carambola* though.

Nutation slow rhythm is decoupled from the diurnal rhythm We have just discussed the occurrence of a slow modulation of A_{nut} on a circadian basis. The comparison of all the distributions of A_{nut} revealed that nutation tides occurred at different moments of the day-night cycle from a plant to another (see figure 4.11). This observation suggests a decoupling between the rhythm of tides and the diurnal rhythm (day/night alternation). It is not clear if such a decoupling is surprising or not. On one hand, the tight connection between the diurnal rhythm and the peaks of amplitude of circumnutation has been showed in the case of *Heliantus annuus* seedlings (Buda et al., 2003; Charzewska & Zawadzki, 2006). On the other hand, it has been shown that *Arabidopsis thaliana* exhibited a circadian modulation

of nutation but, to the best of our knowledge, its link to the diurnal rhythm is not clearly understood yet (Someya et al., 2006). In our case, it is possible that the lightening of our lab is too weak to force the internal clock of the plants (illumination is about 300 *lux* and seems quite low).

The observed independence of the diurnal and nutation rhythms could suggest that the leaf has not adapted to the day and night alternation yet. As discussed in section 4.2.3, it is tempting to imagine that every leaf of the plant has its own inner clock. Then, the alignment of the circadian rhythm of the leaf could require some time to align itself on the diurnal forcing. This is however not likely. In fact, as described in Chapter 2, the leaflets of the growing leaf perform on point nyctinastic motions as soon as they reach their mature position. This rather indicates that the inner clock of the leaf—if it ever exists—is already in phase with the forcing diurnal rhythm. Another possibility coming from the previous observation would be that each leaflet would have its inner and independent clock. But in this case, the question would be asked of how leaflets adapt their inner rhythm to the forcing rhythm quicker than the rachis. It thus appears that the explanation for the rhythm of amplitude modulation is to be sought elsewhere.

Under the hypothesis of a $\dot{\delta}$ -driven nutation, the nutation tides are by definition connected to the intensity of differential elongation in the rachis. Indeed, we see that the peaks of $\dot{\delta}$ or \dot{D} coincide with the peaks of A_{nut} (compare figures 4.3 or 4.6 with the first panel of figure 4.11). It appears that the peaks of the $\dot{\delta}$ intensity occur once in the development of each interleaflet (see figure 4.4). The distance of these peaks to the apex appears to be roughly constant, recalling the behaviour of the previously discussed growth zone. We thus foresee that the rhythm of the nutation tides may be at least partially related to the growth rhythm of each plant. This could explain the variability of the tides rhythm from a plant to another, as the rhythm of elongation may depend on many parameters: resource availability (water, light and nutrients), environmental parameters (temperature, moisture), growth phase of the plant⁴ or even the global health of the plant. The question is thus asked if the diversity of nutation tides rhythm can be explained by the growth dynamics.

At last, the shape of the nutation signal somehow evokes the beats of interfering oscillators (see figure 4.10)⁵. Here, the nutation presumably results from

⁴*Averrhoa carambola* sometimes goes through growth bursts during which a single plant produces successively several leaves in a short duration (eg. 4 leaves in 3 weeks).

⁵When two oscillators with close frequencies f_1 and f_2 interact, this results in a signal of high frequency $1/2(f_1 + f_2)$ which amplitude is modulated at the slow frequency $1/2|f_1 - f_2|$.

differences of elongation between the lateral faces of the rachis. Under this hypothesis, the signal of differential elongation—and thus of nutation according to equation (5.8)—depends on this difference of elongation. It is possible to imagine that tissues do not elongate at a constant rate in the bending zone. The elongation rates of both the lateral faces of the rachis could thus undergo some oscillations. In order to generate beats of periods $\tau_{nut} = 2.8 h$ and $\tau_{tide} = 28.8 h$, the two initial periods should be $\tau_1 = 5.1 h$ and $\tau_2 = 6.2 h$. Although, such oscillations have not been reported up to now.

Differential growth occurs where mean growth decays The study of the nutation motion has allowed us to learn more about the spatial distribution and organization of growth within the tissues of the rachis. We have already discussed the existence of a growth zone in Chapter 3. Here, thanks to the trajectories of the leaf nodes, we were able to build averaged spatio-temporal diagrams of the relative growth rates \dot{E} of each interleaflet (see figure 4.5). From the observations of Chapters 2 and 3 and of the built spatio-temporal diagram, it was confirmed that *Averrhoa carambola* compound leaves undergo ‘apical growth’. That is to say that the elongation of the tissues takes place in a confined growth zone, near the apex of the rachis. Such a behaviour is classical in cylindrical plant organs and has been put forward in roots (Silk et al., 1986; Walter et al., 2002), hypocotyls (Peters & Tomos, 2000) and stems (Silk, 1992). Tip growth is sometimes used when modelling the growth of complete organs (Bastien et al., 2014). From this observation, we assumed that the distribution—set from the apex—of elongation along the rachis was approximately steady in the tissues. The construction of time-averaged profiles of \dot{E} then revealed the spatial distribution of elongation in the tissues (see 4.7, green experimental points).

Differential elongation is the other contribution to growth. The existence of a bending zone, combined with the hypothesis of a $\dot{\delta}$ -driven nutation suggested that differential elongation occurred in a restrained region of the rachis. The $\dot{\delta}$ -related spatio-temporal diagrams (see figures 4.3, 4.4 and 4.6) highlighted the bending zone, by definition. It is important to remember here that nutation may result from a combination of irreversible and reversible processes (Stolarz, 2009; Baskin, 2015). But, equation (4.3) used to build these diagrams do not allow us to discriminate irreversible and reversible length variations. This is why the amount of differential elongation is only *estimated* here. In a similar way than for \dot{E} , the average profile of \dot{D} was determined (see figure 4.7, dark red experimental points).

The comparison of the \dot{E} and \dot{D} profiles confirmed that differential elongation takes place where elongation varies the most (see figure 4.7). This suggests an intimate link between the elongation and the differential elongation. The relation between their spatial distributions has been summed up as $\dot{D} \propto \partial_s \dot{E}$. Following this relationship, a sigmoidal and its derivative were fitted of the \dot{E} and \dot{D} profiles (see plain lines figure 4.7). They showed good qualitative agreement with the experimental data. The shape of the fitted \dot{E} profile is however to be considered carefully. Our data is indeed incomplete, we do not have information on the experimental distribution of elongation in the first millimetres after the rachis. In other organs, the distribution of elongation was found to be a gaussian-like, reaching their maximum several millimetres away from the rachis and finally decaying to 0 (Walter et al., 2002; Peters & Tomos, 2000; Silk, 1992). It is thus possible that the \dot{E} profile decays near the apex. The same remark holds true for \dot{D} . In any case, our results suggest that the growth zone of the rachis does not reach any saturation plateau.

In Chapter 3, we have discussed the fact that a specific zone of the rachis seemed to offer advantageous mechanical conditions for the achievement of autotropism. Here, we have shown that differential elongation is performed in a specific zone. Could it be that these zone described in Chapter 3 and the nutation zone coincide? In this case, it would be possible to hypothesize that oscillatory motions serve in some way autotropism, or that they are a manifestation of it.

At last, what is the physiological basis of this behaviour? The oscillations of differential elongation (see figure 4.3) suggest an oscillatory behaviour for the elongation of the lateral faces of the rachis. Oscillations in the elongation of opposite faces of (circum)nutating organs have been measured (Baskin, 1986; Berg & Peacock, 1992). Although hypothesis on the physiological basis of such elongation oscillations exist (Baskin, 2015), the question of the spatial localization of these oscillations is now asked. The profiles pictured in figure 4.7 suggest a tight link between the growth rate and differential elongation. Is it possible that the intensity of growth oscillations is directly connected to the rate of elongation? It is possible to imagine that in a zone of strong elongation, all cells grow synchronously and that the global decay of the elongation rate is accompanied by more and more asynchrony within the tissues, leading thus to oscillatory behaviours.

Finally, Baskin rightly pointed out that, once again, none of the evidences of differential elongation in nutation have been properly decoupled from a possible involvement of elastic phenomena (Baskin, 2015). In our case, actual differences in the growth rates of the lateral sides of the rachis still have to be measured.

Partial conclusion The results of this chapter have drawn the general features of *Averrhoa carambola* growth and nutation rhythms and spatial organization. In particular, the tight link between elongation and differential elongation—already foreseen and discussed in the previous chapters—has been put forward. In this sense, the fourth chapter has opened the way to the modelling of growth and nutation.

This chapter has also raised new questions on the spatial organization, the dynamical aspects of elongation and the slow rhythm of nutation. Tackling these different questions implies that we go a step further in the characterization of the distribution of elongation along the rachis. We thus see that, to better understand the links between nutation and elongation, more advanced techniques need to be used.

Chapter 5

From motions to growth

Contents

5.1	Growth measurements	103
5.1.1	Experimental protocol	103
5.1.2	Results	106
5.1.3	Impact of projection effects on elongation measurements .	109
5.2	Kinematic model of growth and nutation	112
5.2.1	Definition of the growth and nutation model	112
5.2.2	Results	117
5.3	Discussion and partial conclusion	124

The study of the unfurling and nutation motions have put forward specific growth kinematics and growth patterns. Up to now, our approach has provided coarse information on the elongation field of *Averrhoa carambola* compound leaves. The upcoming chapter is devoted to the confirmation of our previous characterization by two means: actual growth measurements and a kinematic model for growth and nutation.

5.1 Growth measurements

5.1.1 Experimental protocol

Particle image velocimetry (PIV) is a common technique in fluid mechanics. The basic idea is to introduce particles in the stream of interest and to film the resulting motion of the tracers. It is then possible to extract the field of velocities of the stream by auto or cross correlation from an image to the other.

A PIV-inspired method had been previously developed in our team to measure elongation fields along plant organs (Bastien et al., 2016). I took benefit of the existing tools and methodology and adapted them to the specific case of *Averrhoa carambola*. In the following paragraphs, I will detail this method and the adjustments it required.

Experimental set-up

In our case, because plant motions and growth involve long time scales — order of the hour and the day respectively — our technique relies on time-lapse photography rather than on filming. Dry fluorescent orange pigments are carefully deposited¹ on the surface of the rachis thanks to a paintbrush. This is done in a way to create a highly textured layer that will make image analysis easier.

A camera is placed as parallel as possible to the direction of growth of the leaf. Flashes are covered with green filters for two purposes: first, ensure a strong contrast between the green rachis and the orange pigments ; second, to avoid disturbing the plant too much during the night by providing only green light (minimum of absorption). At last, because we want to capture growth and motions, pictures are typically shot every 1 to 5 minutes. This interval is to be compared with the typical 2.5 hours period of nutation which is the fastest growth motion of *Averrhoa carambola*.

In principle, it is thus possible to measure growth on the whole rachis and get information on global characteristics of growth (e.g. position and length of the growing zone) ; or to focus on a specific zone (typically on an interleaflet) and get a fine measurement of growth. In practice, as I will explain later, we always focus on a given interleaflet.

Data analysis

As already discussed in Chapter 3, Voronoi-based skeletization is not suited to the case of *Averrhoa carambola*. One of the main reasons is the presence of leaflets—not easily separable from the rachis by image analysis—hiding great proportions of the rachis and deforming the retrieved contours and skeletons. An alternative method to determine the midline of the rachis is needed. We use the fact that leaflets generally deform the lower half of the leaf’s contour rather than its higher half. The skeleton

¹The impact of pigment deposition on leaf development and viability were not assessed strictly speaking. Several risks can be thought of: intoxication, thigmomorphogenesis or reduced photosynthesis for instance. However, no major dysfunction was ever noticed for the painted leaves. The growth behaviour also seemed to be identical between painted and natural leaves.

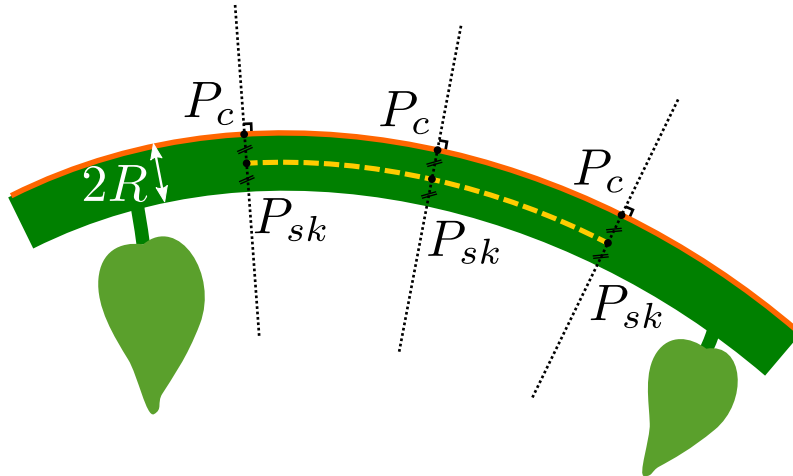


Figure 5.1: **A simple geometrical process to build the midline of the rachis.** The upper contour is drawn in orange. The constructed midline is drawn in yellow.

is then obtained by a simple geometric procedure. First, the normal direction to upper contour is determined at each point P_c . Second, a skeleton point P_{sk} is created for each P_c . This is done by placing a point at distance R from P_c on the normal to the upper contour at P_c (see fig. 5.1).

The most important step is then to measure the elongation field along the rachis of the studied leaf. To do this, we use an image-to-image correlation algorithm that has been previously developed in the lab (Bastien et al., 2016). The idea is to measure the displacement of small patterns at the surface of the rachis from an image to the following one. Let us consider two successive pictures (n) and ($n + 1$) of our complete set of pictures. A window W_n of interest is defined in picture n . This window is centered on a point of the skeleton. Its dimensions depend on the dimensions of the rachis in the considered set of images. Typically, we use a square window, slightly wider than the rachis. We now need to find this same window in the picture ($n + 1$). We first define an investigation zone of fixed length in picture ($n + 1$). It is centered on the position s_n of W_n in picture (n). For each point in the investigation zone, an investigation window W_{n+1} is defined and compared to W_n by a correlation score. In other words, W_{n+1} is translated along the skeleton. Additionally to what was initially done, we have also allowed W_{n+1} to translate along the normal to the skeleton to counter act a possible bias in the skeleton construction. The position of the maximum of correlation along the rachis is considered to be the new position of the window of interest in picture ($n + 1$). To avoid pixelation effects, the curve of correlation is locally fitted by a parabola in the vicinity of its maximum. This allows a sub-pixelar measurement of the displacement Δs of W_n . The correlation step provides the *displacement field* of

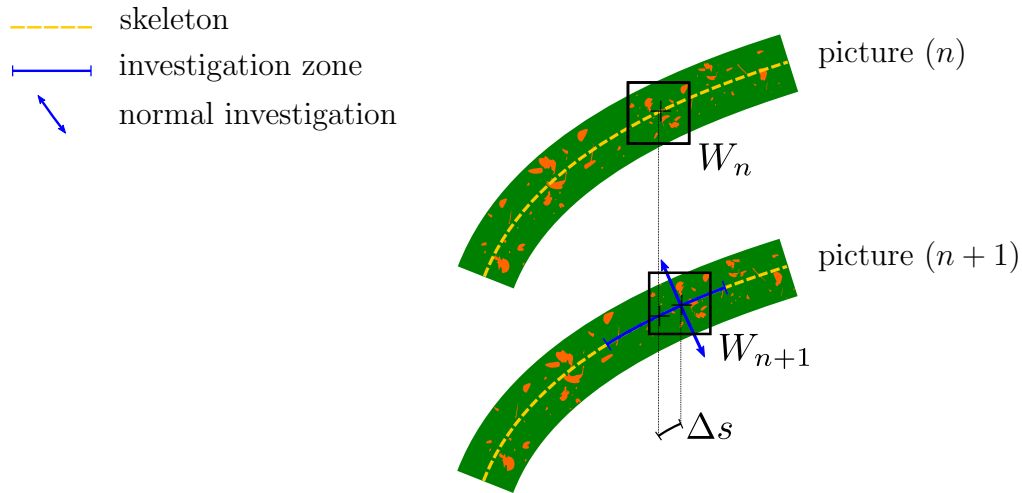


Figure 5.2: **Illustration of the image-to-image correlation principle.** A window of investigation W_{n+1} is defined in picture 2. It translates along the skeleton and its content is systematically compared to the window of interest W_n by a correlation score. The position of the maximum of correlation gives the displacement of W_n along the midline.

the considered elements along the rachis. We access the elongation field by spatially differentiating the retrieved displacement field. This procedure is repeated for each point of the skeleton in picture (n) and then for each picture of the set. Doing so, we can use the spatio-temporal representation for our experiments. Finally, the derivation of $\dot{\varepsilon}$ values can lead to quite noisy results. In order to reduce this noise, the displacement data are smoothed thanks to a median and averaging filters before being differentiated. Then, we smooth the kymograph itself by using a 2D median and averaging filters.

5.1.2 Results

A number of experiments were carried out using this protocol. In this section, I propose to describe only one of those. As described in section 5.1.1, the camera was close from the leaf and a single interleaflet was analysed. During this experiment, the time interval between two consecutive pictures is $\Delta t = 5 \text{ min}$.

The results of the image-to-image correlation step is shown in figure 5.3. Here, the results are displayed on $18.75 h$ and on a reduced part of the rachis of about initially measuring 17.5 mm . The data are cropped mainly to get rid of artefacts due to the motions of the leaflets. Doing so, we can consistently observe a part of the rachis which is never hidden by any leaflet.

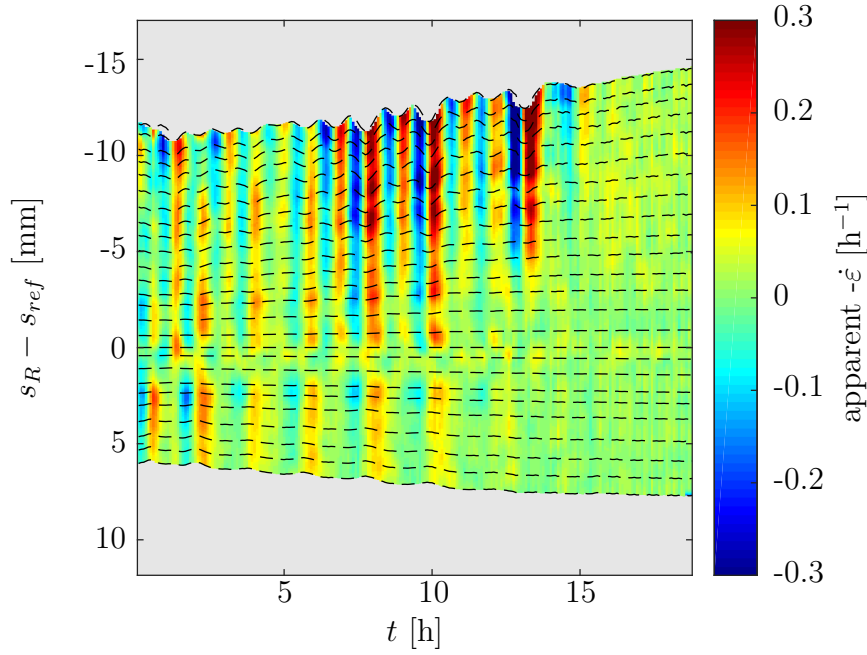


Figure 5.3: **Experimental spatio-temporal diagram of elongation.** This diagram was established for a portion of an interleaflet which was continuously observable throughout the experiment. The black dotted lines correspond to the trajectories of a given set of points.

The most striking feature of figure 5.3 are the marked oscillations of the relative elemental growth rate $\dot{\epsilon}$ in time, near the apical end of the observed interleaflet. Moreover, we see that $\dot{\epsilon}$ periodically becomes negative, thus implying local contractions of the rachis. The amplitude of these oscillations can reach 0.3 h^{-1} , meaning that the rachis could locally dilate or contract by 30% in an hour. For instance here, we see a contraction event at $t = 9.6 \text{ h}$ and a dilation event at $t = 10 \text{ h}$. These events occur on a clearly identifiable zone of length $L_{osc} \simeq 1 \text{ cm}$. On this zone, the mean value of $\dot{\epsilon}$ during the contraction event is $\dot{\epsilon}_{contract} \simeq -1.8 \times 10^{-1} \text{ h}$ and $\dot{\epsilon}_{dilate} \simeq 1.9 \times 10^{-1} \text{ h}$ during the dilation event. This values are one order of magnitude greater than the maximum of the profile of \dot{E} determined in Chapter 4 (we had $\dot{E}_0 \simeq 1.9 \times 10^{-2} \text{ h}^{-1}$). Considering their spatial extension, the contribution of these dilation and contraction events to the total growth of the observed interleaflet would be $L_{osc}\dot{\epsilon}_{event} = \pm 2 \text{ mm} \cdot \text{h}^{-1}$. Such growth rates are much greater than the average growth rate of the observed part of the leaflet, which can be obtained from the extreme trajectories, and is about $2.4 \times 10^{-1} \text{ mm} \cdot \text{h}^{-1}$. We can also compare $L_{osc}\dot{\epsilon}_{event}$ to $L_{gz}\dot{E}_0 \simeq 6.7 \times 10^{-1} \text{ mm} \cdot \text{h}^{-1}$ from Chapter 4. We have discussed in Chapter 4 the fact that growth might be inhomogeneous along the rachis. The amplitude of the oscillations here is however so great that they do not seem to be

actual growth inhomogeneities. So, what is their origin?

The observed $\dot{\epsilon}$ are actually completely artefactual. They are a result of the nutation motion of the rachis. It is important to remember that several parameters rule the apparent length of an object in a picture. The orientation of the object with respect to the camera and its distance to the camera are the two main deciding parameters. Because the rachis moves orthogonally to the focal plane of the camera, its apparent length on pictures is modified by the variations of projection effects. The relative distances between sub-elements of the rachis are also affected as it can be seen on the trajectories displayed in figure 5.3. This is why the rachis appears to periodically and violently elongate and contract in figure 5.3. The apparent variations of length due to the nutation motion furthermore dominate the variations of length driven by the growth process. This is clearly visible after $t = 15 h$, when oscillations stop and the values of $\dot{\epsilon}$ decrease by a factor 10.

Another marking feature of the measurements presented in figure 5.3 is the observation of two modes in the $\dot{\epsilon}$ oscillations. In the two previous paragraphs we have already discussed the oscillations taking place near the apical end of the observed interleaflet—here for $s_R - s_{ref} < 0$. But we also observe oscillations for $s_R - s_{ref} \geq 0$. It seems that the frequency of the oscillations for $s_R < s_{ref}$ is twice the frequency observed for $s_R \leq s_{ref}$. This is particularly visible between $t = 3 h$ and $t = 13 h$. Interestingly enough, the oscillations for $s_R \leq s_{ref}$ vanish at the same time than those for $s_R < s_{ref}$. Could they also be linked to nutation?

To further investigate this apparent frequency doubling, we use wavelet analysis once again. To make analysis easier, we focus on the spatial window defined by the initially observable portion of the interleaflet—*i.e.* $-6 mm \leq s_R - s_{ref} \leq 12 mm$. Each $\dot{\epsilon}_s(t)$ signal has then been wavelet transformed. From the coefficients of the transform, it is then possible to define an ‘energy’. This score is a way to represent the weight of a given frequency in the complete analysed signal. By assembling all the energy curves, we can visualize the dominant frequencies in the signal and their position along the rachis (see figure 5.4). The diagram clearly shows two distinct space-frequency domains. We see for $s_R - s_{ref} < -4 mm$ that most of the energy of the signal is contained in a sharp band of periods, from $\tau = 0.9 h$ to $\tau = 1.5 h$. For $s_R - s_{ref} > 2 mm$, the energy distribution is wider but shifted to higher values of τ , from $\tau = 1.2 h$ to $\tau = 3 h$. By determining the maxima of energy for each position along the rachis in figure 5.4, the periods of maximal energy were found to be $\tau_f \simeq 2.1 h$ and $\tau_{2f} \simeq 1.2 h$. Considering the large band of high energy for the slowest mode, we can reasonably state that two modes are observed in $\dot{\epsilon}$ oscillations,

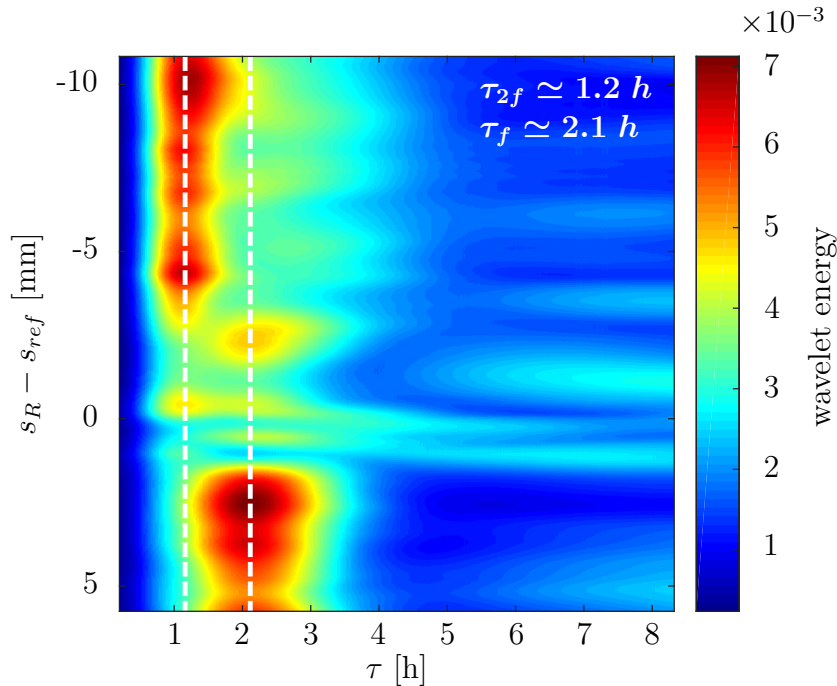


Figure 5.4: **Spatial distribution of energy for different frequencies.** Two distinct space-frequency domains are visible. For $s_R < s_{ref}$, the dominant mode is $\tau_{2f} \simeq 1.2 h$. For $s_R > s_{ref}$, the dominant mode is $\tau_f \simeq 2.1 h$. Here, τ_f roughly corresponds to the period of nutation. This graph was derived from the data shown in fig. 5.3 thanks to wavelet analysis.

one being indeed the double from the first. We see that the value of τ_f is close to the usual range for the period of nutation as seen in Chapter 4. The determination of the nutation period is uneasy here as we only have side takes at our disposal. It has however been estimated to $\tau_{nut} = 2.0 \pm 0.3 h$ by averaging measurements for successive repetitions of the motion².

In conclusion, we see that the observed basal oscillations of $\dot{\epsilon}$ seem to have the same frequency than nutation while the apical oscillations have twice this frequency.

5.1.3 Impact of projection effects on elongation measurements

As it appears, our attempt to precisely measure the elongation field along the rachis is greatly disturbed by the nutation motion. We briefly discussed in the previous section that projection effects—or more precisely their variations—are at play here. What are exactly the consequences of these variations on our measurements? Can they explain the observation of $\dot{\epsilon}$ oscillations with two distinct rhythms?

²Here the indicated error corresponds to the standard deviation of the gathered measurements.

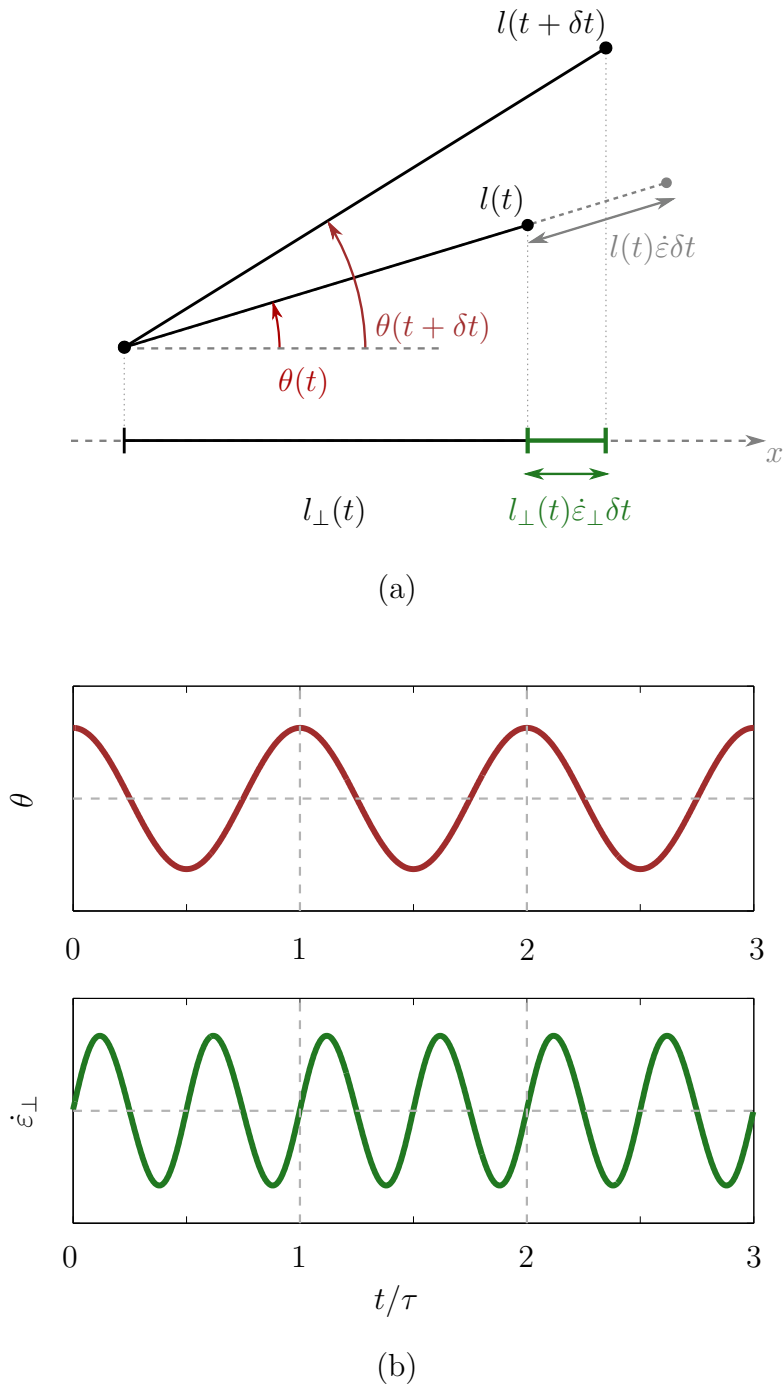


Figure 5.5: **Projection effects and apparent elongation.** (a) Geometrical quantities of the problem. A segment of length l elongates in time with an elongation rate $\dot{\epsilon}$. Its orientation with respect to the reference axis is $\theta = \theta_0 \cos(\omega t)$. Its length and elongation rate projected on the reference axis are l_{\perp} and $\dot{\epsilon}_{\perp}$ respectively. (b) In the simple case where $\dot{\epsilon} = 0$, we clearly see that $\dot{\epsilon}_{\perp}$ has twice the frequency of θ .

Let us consider a segment S of length l . This segment elongates in time with an arbitrary elongation rate $\dot{\epsilon}$. Let us now consider a reference axis (Ox) . This axis typically represents the focal plane of a camera in one of our experiments. The angle between the considered segment and (Ox) is noted θ . This angle θ is also arbitrary and can evolve in time. We now wonder what is the apparent elongation of the segment onto the reference axis (Ox) . The apparent length of S corresponds to the length l_{\perp} of its orthogonal projection onto (Ox) . So, the apparent elongation of S will correspond to the elongation of its projection, in other words to the projected elongation $\dot{\epsilon}_{\perp}$. The reader can refer to figure 5.5a for a visual summary.

The projected elongation $\dot{\epsilon}_{\perp}$ can be expressed in terms of the previously introduced geometrical parameters. It is defined as

$$\dot{\epsilon}_{\perp} \equiv \frac{1}{\delta t} \frac{l_{\perp}(t + \delta t) - l_{\perp}(t)}{l_{\perp}(t)} \quad (5.1)$$

The projected length of S is given by $l_{\perp} = l \cos \theta$ at any time, and the time evolution of $l(t)$ is known via the ‘true’ elongation rate $\dot{\epsilon}$. If we assume that the time variations of θ are small, and we limit to the first order in δt , $\dot{\epsilon}_{\perp}$ can be expressed as

$$\dot{\epsilon}_{\perp} = \dot{\epsilon} - \dot{\theta} \tan \theta \quad (5.2)$$

We see here that the projected elongation rate $\dot{\epsilon}_{\perp}$ is simply the sum of two contributions. The first term is the ‘true’ elongation rate of the observed object. The second term is a geometrical term accounting for the projection effects *and* the motion of the object. The true and measured elongation thus differ only in the case where the object of interest does move relative to the reference axis.

In our case, the rachis undergoes periodical oscillations orthogonal to the focal plane of the camera. Let us now determine the impact of such a motion on the measurement of elongation. We will simply assume that the nutation motion implies $\theta(t) = \Delta\theta \cos(\omega t)$ for example, where $\Delta\theta$ is the angular amplitude of the motion. In the simple case where S does not elongate ($\dot{\epsilon} = 0$), $\dot{\epsilon}_{\perp}$ reduces to the projection term. The angle θ and projected elongation are displayed as functions of time in figure 5.5b. We clearly see that the projection term $\dot{\theta} \tan \theta$ has twice the frequency of θ . The reason for this frequency doubling is actually quite simple to understand. If S gets closer to the reference axis (Ox) —*i.e.* $|\theta|$ decreases—then l_{\perp} increases and $\dot{\epsilon}_{\perp}$ is positive. On the contrary, if $|\theta|$ increases, l_{\perp} decreases and $\dot{\epsilon}_{\perp}$ is negative. We thus see that for half a period of θ , the projected elongation goes through a complete cycle.

How could these artefacts be overcome? First, the knowledge of the orientation of each element of the observed rachis with respect to the focal plane of the camera could help removing the projection-related artefacts in our measurements. Doing so requires supplementary cameras and substantial efforts to ensure precise calibrations. Second, note from equation (5.2) that if $\langle \Delta\theta \rangle = 0$, then $\langle \dot{\varepsilon}_\perp \rangle = \langle \dot{\varepsilon} \rangle$. But our aim was here to determine the growth behaviour as precisely as possible in space *and* in time. In this way, this technique would not provide more precise results than the technique developed in Chapter 4.

So, we see that the nutation motion induces variations of the projection effects which alter our elongation measurements. These variations result in an additive signal with twice the frequency of nutation, as seen in figures 5.3 and 5.4. But now, how can we explain the $\dot{\varepsilon}$ oscillations with the same frequency than the nutation? It also appears that getting rid of these artefacts can be quite difficult. But what can we learn on growth from our measurements anyway? Or from the motions themselves?

5.2 Kinematic model of growth and nutation

To go beyond the previously described limitations and to gain more insight on growth, a proper model is needed to reproduce the characteristics of the nutation motion. Drawing on our observations and our experimental results from Chapter 4, we have built a purely kinematic model of nutation.

5.2.1 Definition of the growth and nutation model

In this section, I will detail the construction of our kinematic model of nutation. The underlying hypotheses and the different physical limits on the parameters will be discussed.

Construction of the model

We have built our model in the frame of beam theory which is so convenient and has been used several times in similar problems (Bastien et al., 2013). In a few words, the growing rachis is reduced to an elongating 2D beam and different growth paces are imposed to its lateral faces to reproduce nutation. Here, our first and strong hypothesis lies in assuming that the nutation is driven only by the differential elongation of the tissues.

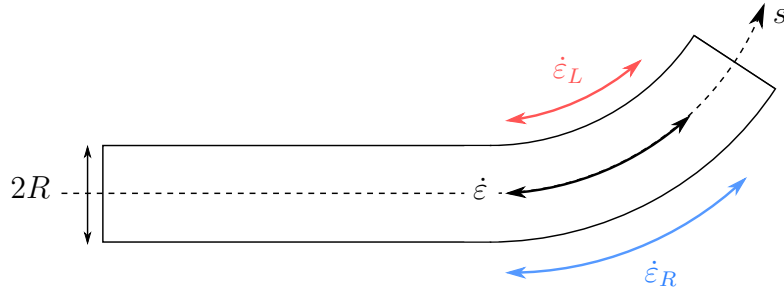


Figure 5.6: **The nutation motion in terms of beam theory.** Here is a top-view drawing of the considered 2D rachis of radius R , which midline is spanned by the arclength s . The quantities associated with the left and right lateral faces are respectively labelled L and R .

Let us now detail the geometrical parameters of our model. We consider a 2D rachis, similar to a beam, and its two opposite sides: right and left denoted (R) and (L) respectively. The width of the beam is—abusively referred as diameter— $2R$ and its total length L_{tot} . The midline of the considered beam is spanned by an arclength s orientated from the base to the apex. The geometry of the midline is furthermore described by the local orientation ϕ and its curvature κ_{\perp} . As already discussed, the total elongation of the two sides might not be equal. We thus consider the average elongation rate of the rachis $\dot{\epsilon}$ and the differential elongation rate $\dot{\delta}$:

$$\begin{cases} \dot{\epsilon} = \frac{1}{2} (\dot{\epsilon}_R + \dot{\epsilon}_L) \\ \dot{\delta} = \frac{1}{2} (\dot{\epsilon}_R - \dot{\epsilon}_L) \end{cases} \quad (5.3)$$

Here, since the rachis is perfectly symmetrical around its midline, the average elongation rate $\dot{\epsilon}$ can also be regarded as the elongation rate of the midline of the rachis. Note that the sign of the differential elongation rate $\dot{\delta}$ only results from our definition of $\dot{\delta}$ and is purely conventional. Of course, the total elongation rate of a given lateral face of the rachis will be given by:

$$\begin{cases} \dot{\epsilon}_R = \frac{1}{2} (\dot{\epsilon} + \dot{\delta}) \\ \dot{\epsilon}_L = \frac{1}{2} (\dot{\epsilon} - \dot{\delta}) \end{cases} \quad (5.4)$$

We now need to define the laws that will determine the evolution of our 2D rachis. The first step is to set the law for the elongation of the midline. As discussed in Chapters 3 & 4, the elongation of cylindrical organs is often described in terms of elongation zone. In our case, the measurements of section 4.2.2 have put forward an

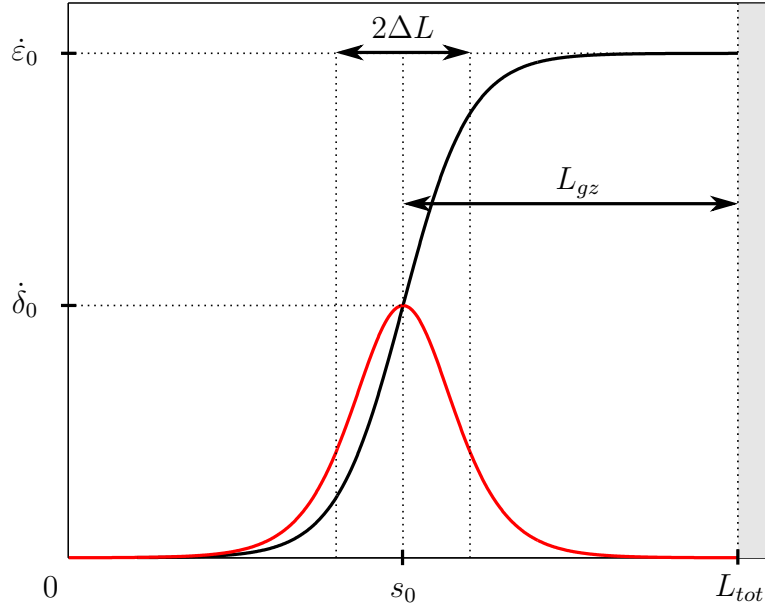


Figure 5.7: **Elongation and differential elongation laws.** The elongation rate shows a growth zone of length L_{gz} defined from the apex. The differential elongation $\dot{\delta}$ takes place where elongation is dropping. Both quantities have a characteristic length of variation ΔL .

elongation zone at the apical end of the rachis. The spatial distribution of elongation has furthermore been shown to be close to a sigmoid—with the possibility of a drop in $\dot{\epsilon}$ near the apex. A natural choice here is then to write $\dot{\epsilon}$ as

$$\dot{\epsilon}(s) = \frac{\dot{\epsilon}_0}{2} \left(1 + \tanh \left(\frac{s - s_0}{\Delta L} \right) \right) \quad (5.5)$$

where $\dot{\epsilon}_0$ is the maximum elongation rate, s_0 is the position of the growth zone and ΔL is the characteristic length of variation of $\dot{\epsilon}$. At each time, s_0 is given by $s_0 = L_{tot} - L_{gz}$ where L_{gz} is length of the growth zone³.

The next step is to define the differential elongation. Considering our observations and results from Chapter 4, differential occurs downstream to the elongation zone, where $\dot{\epsilon}$ decays. We had summarized in section 4.2.2 by saying that the spatial form of $\dot{\delta}$ is proportional to the spatial derivative of $\dot{\epsilon}$. This hypothesis was tested and was shown to fit the data in a satisfactory manner. In the frame we have established for this model, $\dot{\delta}$ is also the only motor of nutation. Then, we have seen in section 4.2.3 that nutation is an almost periodic motion, with two distinct rhythms. Here,

³Together, the two latter equations are equivalent to equation (4.5), but expressed in terms of regular arc length (s not s_R)

the nutation tides will not be treated. Instead, we will consider a perfectly periodic nutation motion, with constant amplitude. Then, we can write

$$\dot{\delta}(s, t) \propto \frac{\partial \dot{\varepsilon}}{\partial s} \sin \omega t \quad (5.6)$$

In the general case, the amplitude of differential elongation is thus proportional to $\dot{\varepsilon}_0$ up to a geometrical constant which depends on the chosen spatial form for the elongation. In our specific case, we have:

$$\dot{\delta}(s, t) = \dot{\delta}_0 \left(1 - \tanh^2 \left(\frac{s - s_0}{\Delta L} \right) \right) \sin(\omega t + \varphi) \quad (5.7)$$

At last, differential elongation being the only motor for the motion, the link between curvature variations and differential elongation needs to be established. Since we are working in the frame of the beam theory, the relation between $\kappa_{//}$ and $\dot{\delta}$ in section 4.1.1 still holds:

$$\frac{\partial \kappa_{\perp}}{\partial t} \simeq \frac{1 - R^2 \kappa_{\perp}^2}{R} \dot{\delta} \quad (5.8)$$

Recall that in the case of nutation, the advection of κ_{\perp} is negligible. This allows to approximate the total time derivative of κ_{\perp} by its partial time derivative.

The laws ruling the evolution of our model rachis have been established. The elongation laws are summed up in figure 5.7. With these three fundamental equations come a set of parameters of different natures, related to the geometry, the motion or the elongation of the considered beam. A great freedom is now possible in the choice of the values for the different parameters of the model. All the possible sets of parameters do not correspond to the physical and physiological observations of nutation however. I will now try and detail some limits in the choice of the parameters.

Restricting the range of the parameters

First, we have to keep in mind that nutation is a real motion, performed by growing plants. We have seen in Chapter 4 that the amplitude of the deflection Δy of nutation varied in time and from a plant to another. In an equivalent way, we can say that the angular amplitude of nutation $\Delta\phi$ varies. The angular amplitude of nutation can be written thanks to a short dimensional reasoning. The physical quantities at play in the bending of the beam are $\dot{\delta}_0$, ΔL , R and ω . It is then possible to show that

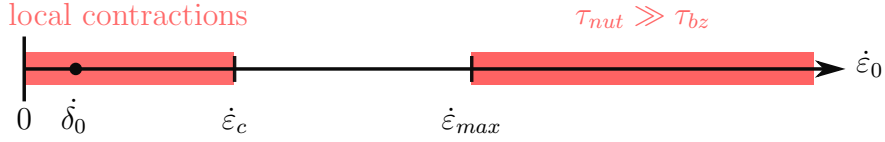


Figure 5.8: **Representation of the different limitations in the choice of $\dot{\epsilon}_0$.** In a case where $\dot{\epsilon}_0$ is the only free parameter, we see that its choice covers radically different physical situations. The possibility of local contractions is not to avoid in our simulations *a priori* but it should be kept in mind.

$$\Delta\phi = 2\frac{\Delta L}{R}\frac{\dot{\delta}_0}{\omega} \quad (5.9)$$

which appears quite natural. The length on which the motion is initiated is indeed the width of the $\dot{\delta}$ distribution, that is $2\Delta L$. We see that the longer this zone, the higher the amplitude of nutation. Conversely, the more a beam is thick, the harder it is to bend. In the same way, the higher $\dot{\delta}_0$, the higher $\Delta\phi$ (see Appendix C for an actual calculation). Finally, the faster the nutation, the lower its amplitude.

We thus see from equation (5.9) that for a given motion, elongation and geometry, there is a single possible $\dot{\delta}_0$. The question may now be asked of what values should be set for the other parameters.

The total elongation of a lateral face of the beam is given by $\dot{\epsilon} \pm \dot{\delta}$ (see equations (5.3) and (5.4)). In some cases, depending on the values chosen for $\dot{\epsilon}_0$ and $\dot{\delta}_0$, we see that the beam can locally contract (see figure 5.7). The choice of these two parameters is thus critical. It can be shown that there exists a sufficient condition on $\dot{\epsilon}_0$ and $\dot{\delta}_0$ to allow or prevent local contractions of the beam (see Appendix C for the derivation of this threshold). Supposing that in the model $\dot{\delta}_0$ is fixed, the threshold⁴ for contractions is simply given by:

$$\dot{\epsilon}_c = 4\dot{\delta}_0 = 2\Delta\phi\frac{R}{\Delta L}\omega \quad (5.10)$$

Above this threshold, local contractions of the beam are forbidden.

Another limitation on the maximum elongation rate $\dot{\epsilon}_0$ arises from the comparison of the approximation made in equation (5.8). To put it simply, we want to make sure the time scale of nutation is much smaller than the time scale of growth. More specifically, the period of nutation τ_{nut} must be at least N times smaller than τ_{bz} which is the time a material point spends in the bending zone. This comparison of

⁴Note that this threshold results from a sufficient condition and is consequently not strict.

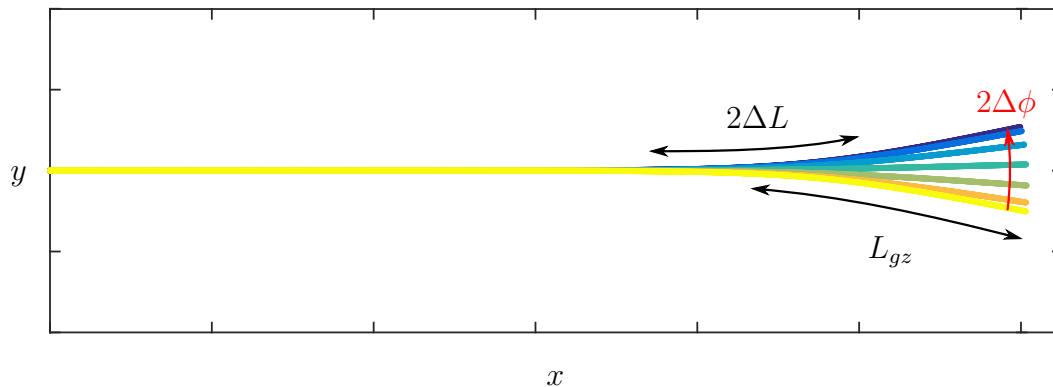


Figure 5.9: **Simulated nutation motion observed from above.** The length of the growth zone L_{gz} , the length of the bending zone $2\Delta L$ and the angular amplitude of the motion $2\Delta\phi$ are indicatively represented. The time evolution is shown by colors: from blue to yellow.

time scales leads to a new threshold in $\dot{\epsilon}_0$:

$$\dot{\epsilon}_{max} = \frac{1}{N\pi} \frac{\Delta L}{L_{gz}} \omega \quad (5.11)$$

If $\dot{\epsilon}_0$ goes beyond $\dot{\epsilon}_{max}$, not only equation (5.8) is not valid, but material points will also leave the bending zone too quickly. This gives rise to ‘non-physical’ motions and non straight final shapes for the beam.

5.2.2 Results

Our kinematic model of nutation was implemented in Matlab. Given an initial condition on the shape of the rachis—length L_0 , radius R , local orientation $\phi(s, t = 0)$ —and a set of parameters defining our model— $\dot{\epsilon}_0$, $\dot{\delta}_0$, ΔL , L_{gz} , and ω —the evolution of the rachis shape and of its different elongation rates is computed. In the following section, I want to show the different results that this model has brought.

Typical simulation result

What are the most important criteria that the results of our simulation must meet? First, the motion has to be qualitatively reproduced. Second, we want to recover measurements of $\dot{\epsilon}_\perp$ similar to our experimental measurements (see figure 5.3). In particular, we want to check that our model accounts for the observation of two distinct modes of oscillations in the measurements of $\dot{\epsilon}_\perp$ (see figure 5.4).

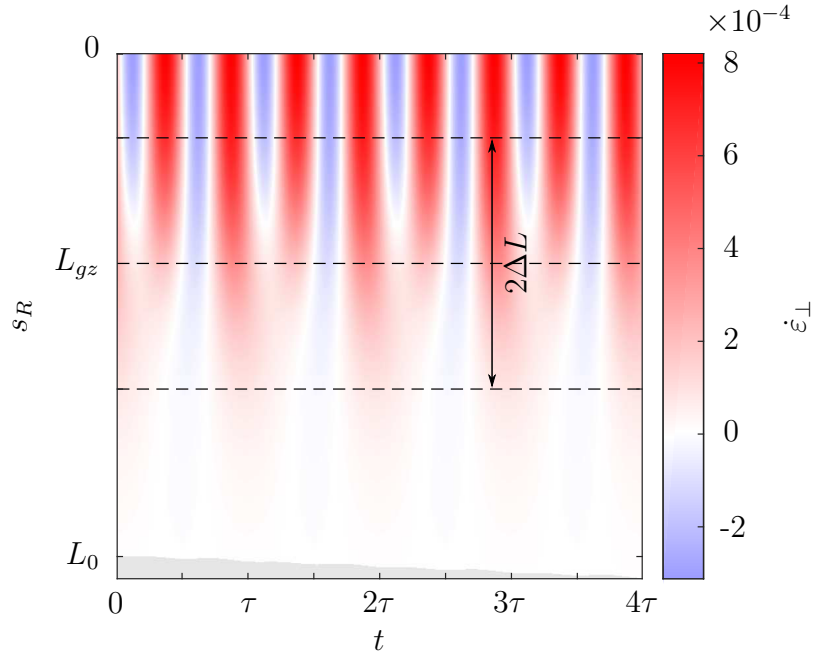


Figure 5.10: **Simulated spatio-temporal diagram of projected elongation.** Two oscillatory modes are visible in this diagram, with a transition around $s_R = L_{gz}$ and on a characteristic length of $2\Delta L$. Here, time is indicated in units of τ , the imposed period of nutation.

The motion displayed by the simulated rachis is shown in figure 5.9. Half a period of nutation is represented. The evolution in time is indicated by the color code: from blue to yellow. We see that the most important features of the nutation motion are qualitatively reproduced. As a matter of fact, the simulated motion is a periodical pendulum-like motion, nodding from right to left. The curvature variations are indeed localized downstream from the apex. When $\dot{\epsilon}_0$ and ω are appropriately tuned—i.e. $\dot{\epsilon}_0 \ll \omega$ —the rachis freezes a straight shape downstream of the growth zone, as it is the case in figure 5.9.

What about the measurement of the projected elongation rate $\dot{\epsilon}_{\perp}$? A simulated spatio-temporal diagram of $\dot{\epsilon}_{\perp}$ is shown in figure 5.10. The spatio-temporal diagram is presented in terms of reversed arclength s_R in order to highlight the growth zone—from $s_R = 0$ to $s_R = L_{gz}$ —and the bending zone of length $2\Delta L$ and centred on $s_R = L_{gz}$. In a similar way than in figure 5.3, we see that the projected elongation rate—as a function of time—has an oscillatory behaviour. Like in our experimental measurements, this oscillatory behaviour is different near the base and near the apex.

This is easily confirmed by performing a wavelet transform of the projected elongation signals $\dot{\epsilon}_{\perp}(s, t)$ for each point between $s_R = 0$ and $s_R = L_0$. Like in figure 5.4,

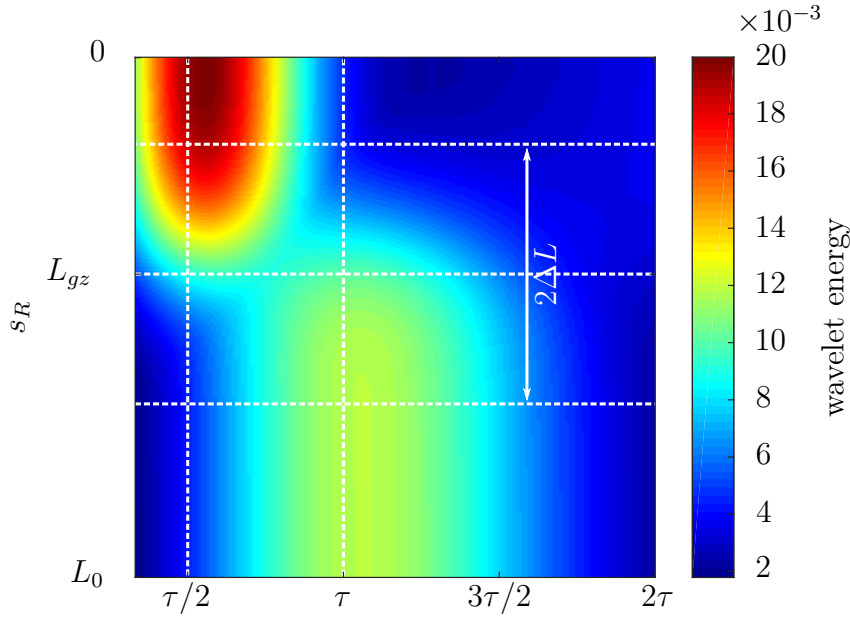


Figure 5.11: **Spatial distribution of energy for different frequencies.** This graph was obtained thanks to a wavelet transform of the data presented in figure 5.10. The two dominant modes roughly correspond to the imposed nutation period $\tau = 2\pi/\omega$ and $\tau/2$. The mode associated to the projection effects ($\tau/2$) is strong near the apex while the mode associated to differential elongation (τ) is strong near the base.

the spatial distribution of energy of the different modes can then be studied (see figure 5.11). The wavelet analysis once again puts forward two space-frequency domains. Above $s_R = L_{gz}$, we see that the dominant mode has roughly a period corresponding to τ , the imposed period of nutation. Meanwhile, below $s_R = L_{gz}$, the dominant mode has roughly a period $\tau/2$ —i.e. roughly twice the frequency of nutation. Referring to equation (5.2) and to the definition of the differential elongation rate $\dot{\delta}$, we understand that the observed fundamental mode is a signature of the differential elongation of the tissues. Then, as discussed in section 5.1.3, the second harmonic is a consequence of the variation of projection effects. Finally, figure 5.4 confirms that the zone of transition between the two modes is centred around $s_R = L_{gz}$. It furthermore seems that the maximal level of energy for each mode are reached for $s_R = L_{gz} - \Delta L$ and $s_R = L_{gz} + \Delta L$.

Rough estimation of experimental parameters

We have described the results of our simulations qualitatively. We now want to use this model to extract some information—possibly quantitative—from our experimental measurements. A first approach is to try and reproduce the features of our experimental graphs (see figures 5.3 and 5.4). Our model indeed relies on a

great number of parameters. The great freedom provided by the model can turn to be a burden when it comes to fit our experimental data. Fortunately, some of the parameters of the model can be measured or estimated.

Knowing what part of the rachis is observed, we can easily measure the radius. Here, we have $R = 0.26 \pm 0.05 \text{ mm}$. The frequency of the motion is also known. A somewhat averaged measurement of the nutation frequency is provided by figure 5.4. With a period of about 2.1 h , we have a pulsation $\omega \simeq 3 \text{ h}^{-1}$. At last, $\dot{\varepsilon}_0$ can be roughly estimated from figure 5.3. As a matter of fact, the initial and final lengths are known and allow to compute the elongation rate over the duration of the experiment. Here, we can estimate $\dot{\varepsilon}_0 \simeq 1.4 \times 10^{-2} \text{ h}^{-1}$.

Then, note that figures 5.3 and 5.4 display both the fundamental frequency and its second harmonic. As showed earlier, in the framework of the model the transition between the two modes occurs around $s_R = L_{gz}$. Here, the transition seems to occur around $s_R \simeq s_{ref}$ (see figure 5.4). So, in first approximation we can hypothesize that $s_{ref} \simeq L_{gz}$. The distance from the apex to the reference point has been measured and $s_{ref} \simeq 23.6 \text{ mm}$. A good first guess for L_{gz} is thus given by $L_{gz} = 23.6 \text{ mm}$.

As previously discussed, the transition between the two oscillatory modes of $\dot{\varepsilon}_\perp$ is achieved over a typical length of $2\Delta L$. Since we do not observe the whole rachis, it is likely that we are not able to see the complete transition between the two modes in figure 5.4. The observation of this figure tells us that $2\Delta L$ is at least 8 mm . A point of comparison is furthermore provided by the results of Chapter 4 where ΔL was obtained by a different method.

Unfortunately, for the experiment studied here, top view takes are not available. So, it is not possible to access $\Delta\phi$ directly. We can at best restrict ourselves to the following reasonable interval $5^\circ \leq \Delta\phi \leq 20^\circ$. For the same reason, no measurement of the out-of-plane curvature κ_\perp of the rachis is available. So, it is *a priori* not possible to estimate the intensity $\dot{\delta}_0$ of differential elongation. But, provided estimations for $\Delta\phi$, R , ΔL and ω , equation (5.9) gives an estimation of $\dot{\delta}_0$.

Finally, our experimental graphs only track a given part of the rachis. Initially, the extremities of the part of interest are located at $s_R = s_{ref} - 11 \text{ mm}$ and $s_R = s_{ref} + 6 \text{ mm}$. Our simulated data have thus to be limited in space to faithfully reproduce our experimental data. To do so, the trajectories of the initial boundaries of the segment of interest have computed. The final spatio-temporal diagram of $\dot{\varepsilon}_\perp$ is then cropped according to these two extremal trajectories.

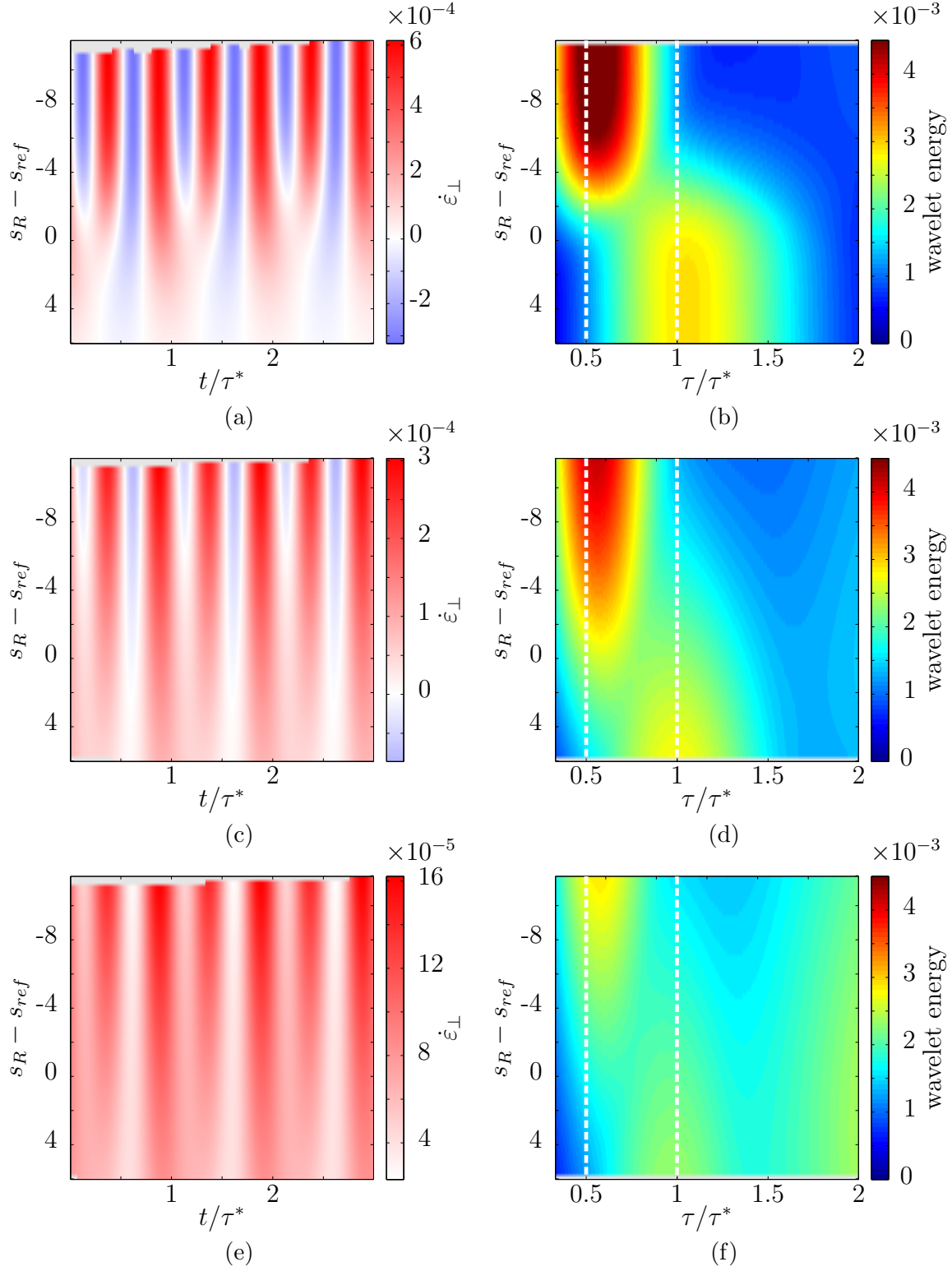


Figure 5.12: **Results for three different simulations.** Each line corresponds to a run of the simulation for a different value of ΔL . Parameter $\dot{\delta}_0$ is adjusted in order to keep $\Delta\phi$ constant. The spatio-temporal graph of $\dot{\epsilon}_\perp$ is shown in the left column. The spatial distribution of wavelet energy is shown in the right one. (a–b) Occurrence of local contractions, $\dot{\epsilon}_0 = 1/4\dot{\epsilon}_c$. (c–d) At the threshold of contraction, $\dot{\epsilon}_0 = \dot{\epsilon}_c$. (d–e) Local contractions forbidden, $\dot{\epsilon}_0 = 2\dot{\epsilon}_c$.

Let us now take a look at the impact of the variation of two parameters on the results of our simulations. The radius R and the pulsation ω are fixed by our measurements. We have then chosen $L_{gz} = 23.6 \text{ mm}$, $\dot{\epsilon}_0 = 1.4 \times 10^{-2} \text{ h}^{-1}$ and arbitrarily fixed $\Delta\phi = 10^\circ$. All the previous parameters are kept constant during the simulation. In contrast, we have chosen to let ΔL free. Since we work with fixed motion ($\Delta\phi$ and ω kept constant for all simulations), the value of $\dot{\delta}_0$ is completely determined by the other parameters. The diagrams presented in figure 5.12 show the results of the simulation for three sets of parameters. The parameter ΔL has been chosen to explore the following growth scenarios:

- (i) occurrence of local contractions, here $\dot{\epsilon}_0 = 1/4\dot{\epsilon}_c$, see figures 5.12a and 5.12b
- (ii) limit of contraction, i.e. $\dot{\epsilon}_0 = \dot{\epsilon}_c$, see figures 5.12c and 5.12d
- (iii) absence of local contractions, here $\dot{\epsilon}_0 = 2\dot{\epsilon}_c$, see figures 5.12e and 5.12f

These scenarios respectively correspond to $\Delta L = 4.8 \text{ mm}$, $\Delta L = 19.4 \text{ mm}$, and $\Delta L = 38.8 \text{ mm}$. The qualitative difference between the several diagrams of projected elongation is striking. As ΔL get greater and greater, we see that the fundamental mode—of period τ^* —becomes more and more difficult to observe. This is confirmed by the spatial distributions of energy (see right column of figure 5.12). This is due to two effects. First, because of equation (5.9), when ΔL increases, $\dot{\delta}_0$ has to decrease to keep $\Delta\phi$ constant. In consequence, the amplitude of the fundamental mode decreases. In addition to that, increasing ΔL means increasing the zone over which the transition between the two modes occurs. So, the fundamental mode and its second harmonic are localized farther and farther away from the reference point $s_R = s_{ref}$. At some point, ΔL becomes so big that the observed zone of the rachis only contains a part of the transition zone, preventing us to observe the oscillatory modes of $\dot{\epsilon}_\perp$. This is somewhat equivalent to zooming in initial transition zone of figure 5.12e.

The qualitative comparison of figures 5.12b, 5.12d and 5.12e with figure 5.4 suggests that the optimal value for ΔL is comprised between $\Delta L = 4.8 \text{ mm}$ and $\Delta L = 19.4 \text{ mm}$. Of course, these values rely on the initial choice for all the other parameters. Interestingly enough—with this initial set of parameters—this leads to $\dot{\epsilon}_0 < \dot{\epsilon}_c$. Local contractions might thus be at play, but our lack of knowledge on other parameters such as $\Delta\phi$ prevent us from concluding. Can we go a step further?

In order to go beyond this difficulty, another approach is to try and *fit* our experimental distribution of energy (see figure 5.4). Doing so requires to be able to

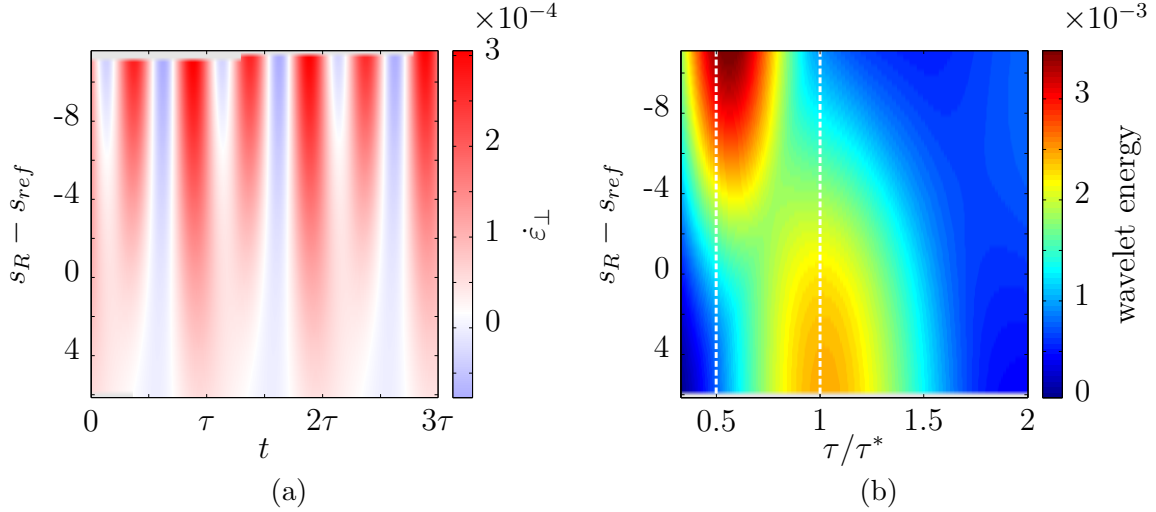


Figure 5.13: **Optimal result of the fitting procedure.** Here are presented the spatio-temporal diagram of projected elongation (a) and the spatial distribution of wavelet energy (b). The optimal parameters obtained after 10^4 iterations are: $\Delta\phi = 8.0^\circ$, $L_{gz} = 20.6 \text{ mm}$, $\Delta L = 12.2 \text{ mm}$ and $\dot{\delta}_0 = 4.5 \times 10^{-3} \text{ h}^{-1}$. The two last parameters have been fixed at $\dot{\epsilon}_0 = 1.4 \times 10^{-2} \text{ h}^{-1}$ and $R = 0.26 \text{ mm}$.

quantitatively compare the experimental and simulated distributions of energy. We have chosen the following score

$$\eta = \sum_i \sum_j (M_{i,j}^{exp} - M_{i,j}^{sim})^2 \quad (5.12)$$

which is basically the sum of the squared difference of the elements of the two normalized⁵ energy distributions matrices M^{exp} and M^{sim} . The aim of the fitting procedure is to reach an—minimal—optimal value for η .

For the purpose of our fit, we have reduced the number of parameters by fixing $R = 0.26 \text{ mm}$ and $\dot{\epsilon}_0 = 1.4 \times 10^{-2} \text{ h}^{-1}$. The initial values of the other parameters L_{gz} , ΔL and $\Delta\phi$ are randomly chosen. The last parameter $\dot{\delta}_0$ is fixed by equation (5.9). Then, the evolution of the parameters is ruled by a Metropolis-like algorithm. At each iteration, the parameters have a certain probability to change value. The set of parameters is first updated, a new simulated distribution of energy is then computed and the score η is updated. This technique is advantageous in the sense that it allows to explore the space of the parameters automatically.

Having initially fixed $R = 0.26 \text{ mm}$ and $\dot{\epsilon}_0 = 1.4 \times 10^{-2} \text{ h}^{-1}$, the optimal parameters given by our fit after 10^4 iterations are $\Delta\phi = 8.0^\circ$, $L_{gz} = 20.6 \text{ mm}$, $\Delta L = 12.2 \text{ mm}$ and $\dot{\delta}_0 = 4.5 \times 10^{-3} \text{ h}^{-1}$. The results of our fitting procedure are shown in figure 5.13. The visual comparison of the experimental and simulated

⁵The energy distribution matrices have been normalized by the difference between their maximum and minimum.

figures bring out some discrepancies.

Let us compare the spatial distributions of wavelet energy (see figures 5.13b and 5.4). We notice that the wavelet energies of the fundamental mode and the second harmonic are comparable in the experimental distribution of energies whereas it is not the case in figure 5.13b. As a matter of fact, we see that the energy of the fundamental mode ($\tau/\tau^* = 1$) remains lower than the energy of the second harmonic ($\tau/\tau^* = 1/2$).

Another remark—rising from the comparison of figures 5.3 and 5.13a—lies in the mean value of the signals $\dot{\epsilon}_\perp(s, t)$ for a given arc length in the spatio-temporal diagrams. In particular, our experimental data show that the oscillations of $\dot{\epsilon}_\perp$ are centered around 0 near the apical end of our sample (see figure 5.3). This however clearly not the case in the result of our simulations (see figure 5.13a).

Otherwise, the output of our fitting procedure shows a good qualitative agreement with our experimental data. The two modes are indeed observed. More importantly, they are approximately located in the expected regions, i.e. the fundamental mode is observed $s_R - s_{ref} > 0$ while the second harmonic is found in the region described by $s_R - s_{ref} < 0$. The length of the transition zone also appears to be reasonable⁶ as it allows to observe both modes. It is difficult to comment on the value of $\Delta\phi$, but $\Delta\phi = 8.0^\circ$ is at least qualitatively consistent with the typical values of $\Delta\phi$ and seems reasonable considering the available pictures of the motion. At last, we see that the optimal parameters bring $\dot{\epsilon}_0/4\dot{\delta}_0 = 0.78$ thus suggesting the occurrence of local contractions.

5.3 Discussion and partial conclusion

The previous chapters have pinpointed possible regulation mechanisms underlying both the growth and the posture regulation of *Averrhoa carambola* leaves. In particular, our results from Chapter 4 have unearthed the specific spatial organization of elongation and differential elongation, but in a averaged way, at the scale of the whole organ. However, the growth and motions of the carambola leaves is dynamic by essence. Our main goal in this fifth chapter was thus to determine the elongation and differential elongation fields at high spatial and temporal resolutions to account for the dynamics of growth and motions.

Our technique to measure elongation along the rachis by combining time-lapse photography and image-to-image correlation (Bastien et al., 2016) however revealed

⁶We can foresee in figure 5.4 that $\Delta L \simeq 8 \text{ mm}$ with the possibility that the observed transition is not complete.

insufficient in the case of an organ with enhanced out-of-plane motions. Our measurements are clearly affected by artefacts (see figure 5.3) which are actually a consequence of the nutation motion, as discussed in section 5.1.3. Unfortunately, these artefacts of geometrical origin might be 10 to 100 times bigger than our signals of interest. Rather than changing our technique, our approach consisted in trying to extract as much information as possible from our biased measurements of the *projected* elongation. With this initial goal in mind, we have built a kinematic model of nutation which benefits happened to be of broader interest.

A model accounting for the kinematics of nutation Armed with the experimental characterisation of the elongation and differential elongation fields of Chapter 4, we have defined a new kinematic model for growth and nutation in compound leaves (section 5.2.1). The originality of our model is twofold. First, contrary to the vast majority of models of nutation, our model is not an attempt to explain the emergence of the motion (Mugnai et al., 2007; Stolarz, 2009). In the framework of kinematics, the origin of nutation oscillations is somewhat irrelevant. They are consequently introduced *ad hoc* in the definition of the differential elongation $\dot{\delta}$. Second, it is growth itself—more precisely, the spatial organization of elongation and differential elongation—which at the base of our model.

Despite the great number of parameters—eight—involved in our model, it provides a quite light framework, enabling us to link all the parameters through simple relations (section 5.2.1, ‘Restricting the range of the parameters’).

The simulations based on our model showed a good qualitative agreement with nutation, reproducing quite faithfully the main features of the motion (see figure 5.9). Furthermore, our simulations have successfully reproduced—at least qualitatively—our experimental measurements of the projected elongation field $\dot{\epsilon}_{\perp}$ (compare figure 5.3 to figures 5.10, 5.12 (left column) and 5.13a). In particular, the puzzling presence of two frequencies in the measurements of $\dot{\epsilon}_{\perp}$ have been reproduced (compare figure 5.4 to figures 5.11, 5.12 (right column) and 5.13b) and explained as an evidence of the differential elongation of the tissues (see section 5.2.2, ‘Typical simulation result’). Altogether, this brings further support to our observations and results from Chapters 3 & 4, as the observed profiles for the elongation and differential elongation allow to effectively reproduce the nutation motion.

Measuring the elongation of moving organs remains challenging Regarding our initial aim, our model only provided approximate and macroscopic information on the elongation behaviour of the rachis at this stage. The model indeed sheds

a new light on our experimental data (figures 5.3 and 5.4) and allows to estimate important quantities involved in the kinematics of growth such as the lengths of the growth and bending zones (L_{gz} and $2\Delta L$) respectively. A naive fit of the spatial distribution of wavelet energy has been performed (see figure 5.13) and has provided the following estimations: $L_{gz} \simeq 20.6 \text{ mm}$ and $\Delta L \simeq 12.2 \text{ mm}$. We can compare these values to those obtained for a different experiment in Chapter 4 (indicated with a prime here). We had $L'_{gz} \simeq 33.4 \text{ mm}$ and $\Delta L' \simeq 20.8 \text{ mm}$. Of course, the values in the experiment of Chapter 4 are higher but stay in the same order of magnitude than in the present experiment. Considering the fact that the two rachis were of radius $R = 0.26 \text{ mm}$ and $R' = 0.6 \text{ mm}$, the different techniques used and the possible biological variations, those differences are not so surprising. Moreover, these values are compatible with mentions of centimetric growth and bending zones in the literature (Millet et al., 1988).

The estimation of the other parameters— $\dot{\epsilon}_0$, $\Delta\phi$ and $\dot{\delta}_0$ —is much more delicate. As a matter of fact, the fit of the spatial distribution of wavelet energy does not account for the value of $\dot{\epsilon}_0$ since it is not involved in the expression of the amplitude of the fundamental mode and the second harmonic (see Appendix C). For this reason, we have estimated it thanks to the elongation of the studied sample in figure 5.3. An approximation is made here: that the sample elongates at a constant and homogenous rate $\dot{\epsilon}_0$ which cannot be the case according to our model. Our coarse approximation of $\dot{\epsilon}_0 \simeq 1.4 \times 10^{-2} \text{ h}^{-1}$ is however consistent with $\dot{\epsilon}'_0 \simeq 1.9 \times 10^{-2} \text{ h}^{-1}$ measured in Chapter 4. Finally, the value of $\dot{\delta}_0$ depends on $\Delta\phi$ which is difficult to check but seems reasonable, as already discussed. In any case, our estimation $\dot{\delta}_0 \simeq 4.5 \times 10^{-3} \text{ h}^{-1}$ is also comparable to $\dot{\delta}'_0 \simeq 7.0 \times 10^{-3} \text{ h}^{-1}$.

Considering our current method to experimentally measure elongation and differential elongation, we see that our model hardly gives precise quantitative information on the growth behaviour of our samples. Further efforts on our data set and on the model might bring more precise estimations of the parameters. For instance, it might be possible to estimate $\Delta\phi$ from the oscillations of the individual trajectories observed in figure 5.3. However, to cope with the growth of moving organs, it appears that a different method of measurement might be needed. In order to get rid of the variations of projection effects induced by nutation, a natural idea is to access the 3D geometry of the rachis. A collaboration with Franck Hétroy-Wheeler and Julien Pansiot—computer scientists specialized in 3D motion capture—has been engaged in this way and should bring precise unbiased measurements of both elongation and differential elongation.

Indirect evidences of local contractions

The benefits of our model to the description of *Averrhoa carambola* growth have been discussed. Can we now go further and use it to other ends? In Chapter 4, we have studied the rhythms of nutation. As a matter of fact, our results have unearthed the slow amplitude modulation of nutation. The growing rachis goes through daily bursts of activity. These nutation tides rely on bursts of differential elongation. What is then the exact nature of this differential elongation? Reversible or irreversible? The framework brought by our kinematic model of nutation gives us a tool to analyse and understand such variations of differential elongation. In particular, could they be linked to local contractions along the rachis?

As discussed in section 5.2.1, there exist a threshold $\dot{\epsilon}_c$ in $\dot{\epsilon}_0$ under which local contractions occur. Interestingly enough, we have seen that for the experiment described in this chapter, $\dot{\epsilon}_0/\dot{\epsilon}_c = 0.78$. As for the experiment presented in Chapter 4, we see that for the averaged parameters we have $\dot{\epsilon}'_0/\dot{\epsilon}'_c = 0.67$. These values have to be considered carefully as they are not the output of direct measurements and are possibly affected by large errors. For both experiments however, this *suggest* that the average behaviour on the duration of the experiments involves contraction. So, the next step is naturally to spot when and where such contractions could occur.

To do so, I propose to quickly re-analyse and discuss the experiment of Chapter 4 at the light of our model. Here, we will split the experiment in several parts, depending on the occurrence of a nutation tide. This was done manually on figure 4.4 and is thus necessarily subjective and imperfect. From here, we can first determine $\dot{\epsilon}_0$ and $\dot{\delta}_0$ by applying the same method and fit than in Chapter 4. The result of this procedure is shown in figure 5.14. We see that for points belonging to a nutation tide we systematically have $\dot{\epsilon}_0/\dot{\epsilon}_c < 1$. Regarding points not belonging to a tide, the situation is not clear though. For two points, we fit systematically failed. For the remaining points, contraction is suggested in one case over two. Here again, these values should be considered carefully.

Another way to look at contraction events during nutation is by studying the evolution of the angular amplitude $\Delta\phi$ of the motion (see figure 5.15). For a given set of parameters, it is possible to define an angle $\Delta\phi_c = \Delta L^2/(2N\pi RL_{gz})$ above which contractions must occur. Here, N corresponds to the number of nutation oscillations a material point undergoes before leaving the bending zone and is somehow linked to $\dot{\epsilon}_0$. For the experiment of Chapter 4, we have approximately $20 \leq N \leq 30$. These two limits have been indicated in figure 5.15. We see that for every point belonging

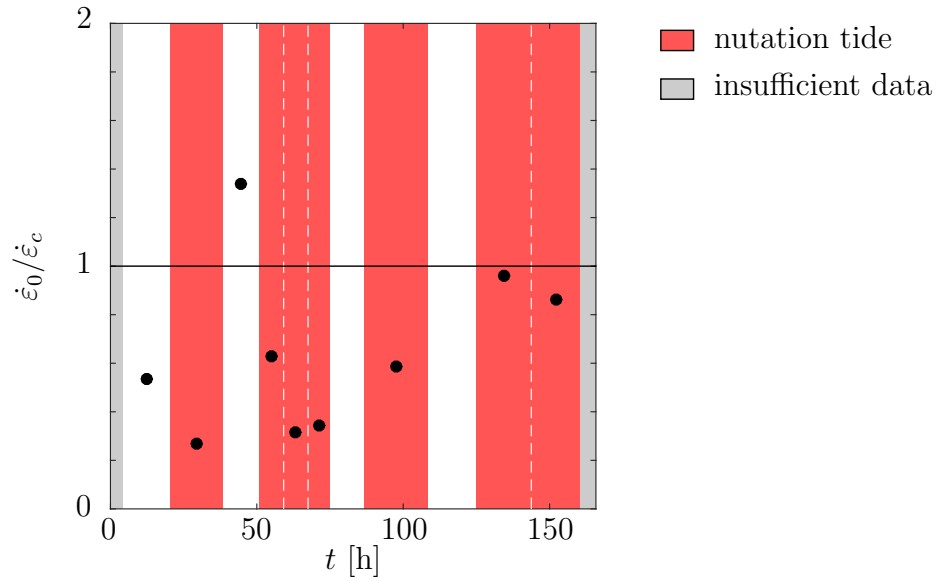


Figure 5.14: **Evolution of the contraction status in time.** In the framework of our model, if $\dot{\epsilon}_0/\dot{\epsilon}_c < 1$ then the rachis locally contracts. Otherwise, contractions are not possible. Red background indicates the occurrence of nutantion tides. There are no points around $t = 80$ h and $t = 120$ h because data could not be properly fitted.

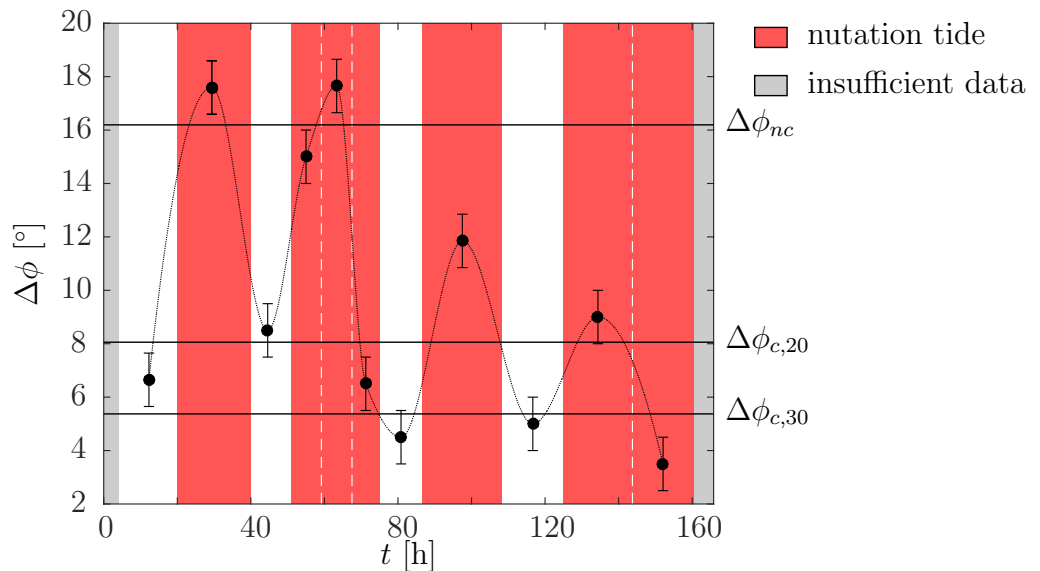


Figure 5.15: **Evolution of $\Delta\phi$ in relation with contraction and nutantion surges.** The angular amplitude of nutantion has been determined for each part of the experiment. The thin black dotted line is a mere indication of the evolution of $\Delta\phi$. Error bars represent the measurement error of $\pm 1^\circ$. Horizontal black lines represent the threshold angle $\Delta\phi_{nc}$ for three values of N . Red background indicates the occurrence of nutantion tides.

to a nutation tide, $\Delta\phi$ is greater than the limits $\Delta\phi_{c,20}$ and $\Delta\phi_{c,30}$. In contrast, points not belonging to a nutation tide are below or near $\Delta\phi_{c,20}$ and $\Delta\phi_{c,30}$. There thus seems to be an alternation between phases with and without contractions in the motion.

Then, we can also define an angle $\Delta\phi_{nc}$ above which contractions are mandatory for any value of $\dot{\epsilon}_0$, corresponding to the limit of $\Delta\phi$ for the minimal physical value of N . Here, we have estimated $\Delta\phi_{nc}$ by arbitrarily taking $N = 5$, which seems a quite low limit. We then see on figure 5.15 that two nutation tides have $\Delta\phi > \Delta\phi_{nc}$. For such motions, the local contraction of tissues may thus be mandatory.

As already discussed in Chapter 1, contractions have been measured in (circum)nutating organs (Berg & Peacock, 1992; Caré et al., 1998), and have also been suggested to be involved in other growth motions such as gravitropism for example (Berg et al., 1986). More precisely, Caré and coworkers have actually shown that individual cells undergo reversible volume variations in the bending zone of *Phaseolus vulgaris* (Caré et al., 1998). Moreover, some authors have also proposed that growth itself is not sufficient to drive circumnutation and that reversible process should be considered (Millet et al., 1988).

Taking into account the lack of precision of our preliminary results, we can say that contractions might also be involved in the case of *Averrhoa carambola* nutation. This is indicated by the global $\dot{\epsilon}_0/\dot{\epsilon}_c$ ratios, but also by figures 5.14 and 5.15. In complete agreement with the results of Caré and coworkers, our model furthermore predicts that if contractions occur, then they should be localized within the bending zone of the organ⁷. Then, in the framework of our model, we show that local contractions are not a compulsory prerequisite to the nutation motion. Beneath the physical limit $\Delta\phi_{nc}$, motions can either involve contractions or not. On experimental grounds, while it is not still perfectly clear, our results seem to suggest that contractions are however involved in nutation, in particular during nutation tides (see figures 5.14 and 5.15).

What mechanisms could now be at the origin of such reversible contractions? A careful observation of the convex and concave faces of nutating *Phaseolus vulgaris* stems showed that cells on the concave face were rippled while cells on the convex face were fully swollen (Millet et al., 1984). Based on previous evidences of variations of osmotic potential in the bending zone, Caré *et al.* have proposed that these reversible volume variations result from turgor variations. It is also possible that

⁷More generally, the spatial patterns of elongation described by these authors is consistent with our measurements and model.

more subtle mechanical effects are involved. For instance, the nutation motion could also induce the compression of the tissues on the concave face of the bending organ. At last, these reversible length variations could be indirectly linked to variations in the elastic properties of the cell wall, which we will investigate in the next chapter.

Partial conclusion In this chapter we have developed a kinematic model of growth and nutation, based on our previous experimental characterization of the spatial patterns of elongation and differential elongation involved in *Averrhoa carambola* nutation. Being consistent with our own characterizations of nutation, but also with further observations in the literature, it seems that our model gathers the essential features of the nutation kinematics.

We have also seen how a precise measurement of the elongation field of a moving plant organ is a delicate task. Our kinematic model did not allow a rigorous quantitative analysis of our experimental results yet. It however allowed us to understand the nature of the observed measurement artefacts. In particular, we have been able to pinpoint the signature of differential growth in our biased measurements.

The nature of this differential elongation has now to be investigated at a lower organization scale, namely at the cell wall level.

Chapter 6

Towards the microscopic aspects of plant growth

Contents

6.1	Mechanical heterogeneities within tissues	132
6.1.1	Atomic force microscopy as a tool for plant mechanics . . .	132
6.1.2	Experimental protocol	133
6.1.3	Data analysis	138
6.1.4	Results	140
6.2	Cell wall composition heterogeneities	145
6.2.1	Preliminary results	148
6.3	Discussion and partial conclusion	151

A major characteristic of plant cells is the rigid cell wall they are encased in. Julius von Sachs and Julius von Wiesner already stressed the importance of the cell wall as early as the 19th century. The cell wall is not only essential to give rigidity to the plant, but it is also plays an important role in its growth. As discussed in Chapter 1, on a mechanical point of view, plant growth is ruled by both the turgor pressure and the resistance of the cell wall. The mechanical properties of the cell wall partly ensue from the chemical status of its components.

The nutation motion is underlaid by the differential elongation of the rachis, possibly with the contribution of reversible length variations. During nutation, the lateral faces of the rachis must then undergo different elongation rates. We now want to take benefit from the intimate link between growth and motions to explore the microscopical aspects of growth. The aim of this sixth chapter is thus to investigate

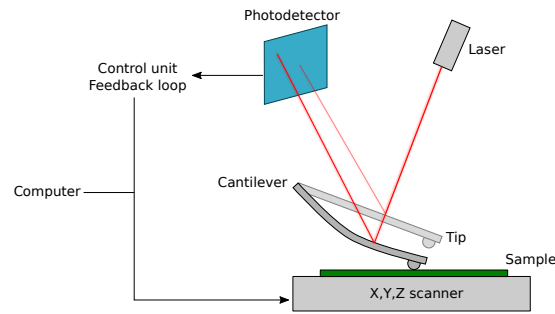


Figure 6.1: **Simplified picture of an atomic force microscope.** The illustrated operating mode is the contact mode. Inspired from (Milani et al., 2013).

how this differential growth translates in terms of mechanics and biochemistry of the cell wall.

6.1 Mechanical heterogeneities within tissues

6.1.1 Atomic force microscopy as a tool for plant mechanics

Atomic force microscopy (AFM) is a very high-resolution imaging technique that was originally developed to image surfaces at the atomic scale (Binnig et al., 1986). Such a resolution can be achieved by using a physical probe to image the surface. In the case of the AFM, the probing element is an ultra-light and deformable cantilever beam with a rigid tip on its bottom surface. A laser is constantly pointed at the cantilever top surface and is reflected to a photodetector. When approached to the sample, the tip extremity is submitted to interatomic forces. Because of its very low mass, the cantilever is very flexible and the repulsive forces bend the cantilever. This bending results in the displacement of the laser beam on the photodetector which can finally be linked to the local height of the probed surface. We see here that the AFM can be used both to measure forces and to determine the probed surface topology. The original operating mode of the AFM relies on keeping the interaction forces between the tip and the sample constant. This is made possible by a feedback loop involving the measurement of the force and the control of piezoelectric drives that allow to adjust finely the tip position (see figure 6.1).

The atomic force microscope is a versatile tool and is being used in several domains including solid state physics, polymer chemistry or cell biology. In cell biology, one of the main interests appears to have been surface-imaging of animal living cells in a non-destructive manner (Milani et al., 2013). Another application of the AFM is the determination of the mechanical properties of biological samples. This particular

use of the AFM is the one we will be concerned with for the rest of this study.

To perform mechanical measurements—contrary to the original AFM operating mode—the cantilever is brought to direct contact with the sample in order to indent it, as pictured in figure 6.1. This contact mode is made of three phases: approach, contact and retract. The vertical position of the cantilever and its deflection are recorded during the whole process. During the approach phase, the cantilever gets closer and closer to the sample. Then, the contact between the cantilever tip and the sample is established. The cantilever keeps being lowered, the tip of cantilever is sunk further down into the sample: both indentation depth and cantilever deflection increase. The indentation stops once the measured deflection of the cantilever reaches its setpoint¹. Finally, the retract phase begins and the cantilever is pulled up to its initial z-position. However, extend and retract phases are not equivalent. The sample may adhere to the cantilever tip and exert a force on it. When the cantilever is high enough compared to the sample, adhesion ceases. Moreover, differences in the approach and retract phases might be induced by dissipative phenomena such as viscosity (Milani et al., 2013).

If the cantilever is properly calibrated, it becomes possible to link the deflection of the cantilever to the applied force and to draw force-displacement curves. Such curves are the basic material from which the mechanical properties of the sample are extracted. To get the mechanical properties of the probed tissue, we need to establish a relation between the indentation depth and the force applied on the sample. This relation is given by the Hertz contact model. The Hertz model hypothesizes that the sample is an isotropic and linear elastic medium occupying a half space ; the cantilever tip is not deformable ; there is no interaction between the sample and the probe. Given this set of hypotheses and considering that we use a spherical probe on an incompressible half-plane, we have

$$F = E\sqrt{R}d^{3/2} \quad (6.1)$$

We see that given the force curve, the information about the position of the sample with respect to the tip (indentation depth) and the radius of the used tip, it becomes possible to extract the Young's modulus of the sample (Lin et al., 2007).

6.1.2 Experimental protocol

Our present aim is to take benefit from the nutation motion to gain insight on the mechanical changes implied by growth at the cell wall level. To this end, we resort

¹Maximum value of the cantilever deflection set by the user

to two different experimental techniques: time-lapse photography and Atomic Force Microscopy (AFM).

Technical protocol

The first step of the protocol is to record the motion of the rachis. This is done by placing a camera above the leaf—top view, with the camera as horizontal as the geometry of the plant allows—of interest and performing time-lapse photography. This step is designed to pinpoint the bending zone and to give us the direction of the motion at the moment of the experiment. The choice of the time interval δt of the time-lapse photography is ruled by the need of having a clear information on the position of the bending zone at the moment when we cut down the leaf for sample preparation. For our different experiments, δt was taken equal to 2.5 min.

The moment when the leaf is cut has to be chosen carefully. We want to make sure that we do not take a sample at the moment when differential growth nullifies for example. One could be tempted to cut the leaf when it is at one of its extreme positions in the nutation process. Doing so has two severe drawbacks. First, when the leaf reaches an extreme position, the motion gets slower, and it might be difficult to determine the actual direction of nutation. Moreover, differential growth is supposedly low near to an extreme position. In Chapter 2, we have described the implications of a the hypothesis a nutation motion only driven by differential growth. In particular, we have deduced that differential growth has to be maximal at the moment when the rachis is straight— ϕ globally nullifies—and minimal near to an extreme position. Even if the results of Chapter 4 and Chapter 5 suggest that nutation do not only rely on differential growth, we refer to these simple deductions. We have consequently decided to cut the leaf when it approaches (or just leaves) the straight-shape step of nutation.

Once the leaf has been cut, it is preserved from dessication in a moist box. The next step is the sample preparation strictly speaking. As mentioned in Chapter 2, *Averrhoa carambola* is a hairy plant. Its epidermis is densely covered with long and curved trichomes. These trichomes prevent the cantilever from reaching the epidermal cells. So, in our case, it is not possible to probe the mechanics of the epidermis—as it is done for *Arabidopsis thaliana* hypocotyls for example (Peaucelle et al., 2011). For this reason, we perform cross sections of the rachis and probe the mechanics of its inner tissues. Doing so has an advantage: the elasticity of the tissues will be probed directly in their direction of growth, contrary to most indentation experiments on plant material. Then, several samples are taken from

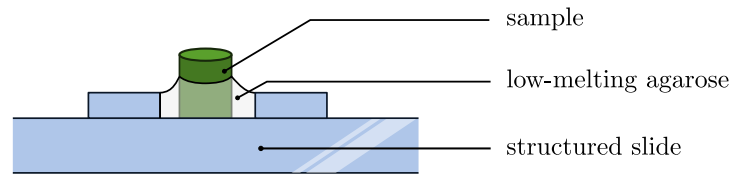


Figure 6.2: **Illustration of the sample preparation.** The cross-sections of the rachis are placed vertically on structured microscopy slides and embedded in low-melting agarose. This protocol was adapted from (Peaucelle, 2014).

the bending zone with a razor blade and are then arranged vertically on the slide (see figure 6.2).

One of the major challenges in using fresh tissues is to make sure that they stay immobile during the AFM measurements. To overcome this difficulty, samples are placed on a slightly modified microscopy slide and then embedded in low-melting agarose. To ensure the stability of the whole preparation—*a priori* agarose slips on glass, and vertical samples might not be as stable as horizontal ones—the microscopy slide has been prepared beforehand (see figure 6.2). Slides are structured glass canals where to place the sample, and with deep scratches. Altogether, this allows a better adhesion of agarose on glass and minimizes sample stability issues during the measurement process (Peaucelle, 2014).

The prepared slice is then immersed in a saturated mannitol solution. While this solution helps keeping the samples hydrated, it also plasmolyses the tissues. The tissues being plasmolysed, it means that we will only probe the properties of the cell wall material. However, plasmolysis is not an instantaneous process. The plasmolysis status of the tissue should be carefully considered before starting any measurement.

Two questions naturally arise from this remark. What is the plasmolysis dynamics? What is the effect of plasmolysis on our AFM measurements? A possible approach to answer this question is to scan a given region of the sample of interest repeatedly, compute the mean and the standard deviation of the Young’s modulus over the scanned region and finally observe the temporal evolution of these quantities.

As we can see on figure 6.3, the longer the sample has been immersed in mannitol, the lower is the average Young’s modulus E_m . In the first minutes after immersion, E_m quickly decays. It then stabilizes after 18 minutes of immersion. Here, the difference between the maximum of E_m and its minimum is approximately 6 kPa (*i.e.* around 20 % of the initial value of E_m). This experiment indicates that we

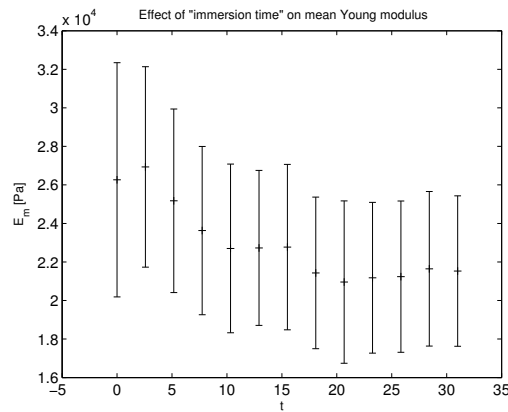


Figure 6.3: **Plasmolysis dynamics and plasmolysis effects on Atomic Force Microscopy measurements.** The same region is scanned repeatedly and the evolution of its average Young's modulus E_m is traced. Error bars represent the standard deviation over the AFM map.

should wait at least twenty minutes after immersion in mannitol to begin AFM measurements and avoid errors due to incomplete plasmolysis.

Finally, the prepared slide is placed under the AFM and enclosed in a moist atmosphere to avoid a quick evaporation of the mannitol solution.

Sample orientation

The thorniest part of sample preparation is to determine its orientation on the microscopy slide. To properly correlate the direction of the motion and the mechanical properties of the tissues, it is decisive to be certain of the orientation of the sample. Fortunately, we can make good use of several anatomical clues to orient our samples.

Leaves often have a bilateral symmetry. That is to say that their midveins define an axis of symmetry. Thus, two opposite faces—usually the lateral ones—are approximate mirror images of each other. In this case, the adaxial and abaxial faces are usually different. What about the rachis of *Averrhoa carambola*? We have already seen in Chapter 2 that mature rachis have a radial symmetry, but developing rachis present a clear bilateral symmetry. The symmetry of the lateral sides consequently helps to distinguish the adaxial and abaxial faces. The adaxial face of the rachis is flatter than the abaxial one. In a schematic way, we could say that the section of the rachis have the shape of a heart or even of a triangle (see figure 6.4a).

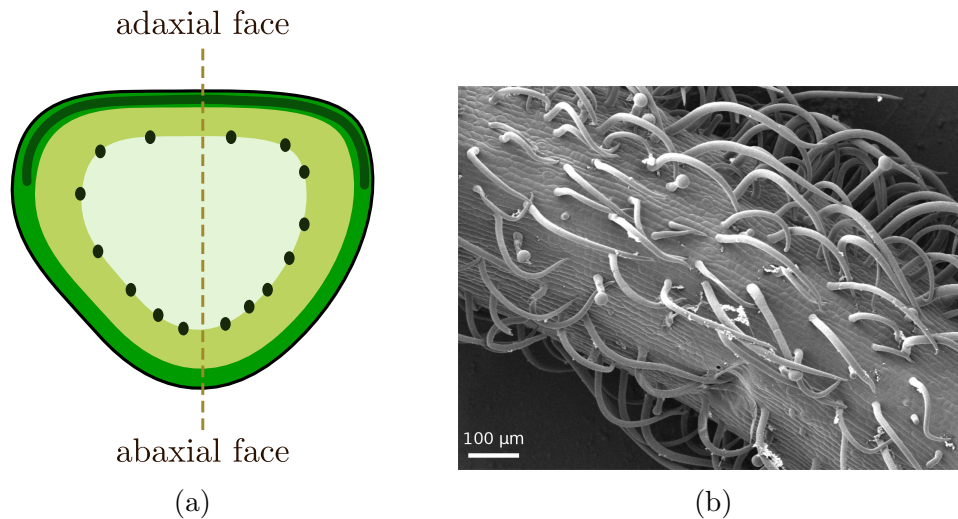


Figure 6.4: **Useful clues to determine the orientation of a sample.** (a) Simplified picture of a cross-section of *Averrhoa carambola* rachis. The bilateral symmetry of the rachis allows a clear distinction between the lateral faces and the abaxial/adaxial faces. Flatness, chloroplast and vessel densities allow to distinguish the adaxial and abaxial faces from one another. (b) The rachis is covered with trichomes that all point toward the apex.

Two other anatomical clues are helpful. In the developing rachis, it appears that the density of primordial vessels is higher in the lower part of the section than in the higher one. At last, most of the time, the adaxial face contains more chloroplasts, and consequently looks greener, than the abaxial one. This last point is also valid for mature rachis and is a strong clue to help in determining the orientation of any sample.

We already discussed an orientation convention in Chapter 2. We keep considering the rachis in the same way: from the petiole to the apex. This defines the right and left sides of the rachis. It is thus important to know ‘where the apex is’ when we look at a given sample. A reliable indicator of this is the direction of the trichomes. As we can see, the trichomes are all oriented in the same direction: their sharp ends actually point toward the apex (see figure 6.4b).

Knowing the direction of the motion, and knowing the orientation of the sample, we are now able to distinguish the concave and the convex sides of the rachis. This finally allows us to compare the mechanical properties of two regions with supposedly different growth behaviours.

Choice of the different parameters

The AFM device can be tuned at many levels, and several types of AFM tips can be used. This gives a high number of parameters to choose. Some of these parameters are likely to impact the final result of our mechanical measurements. Among them, three parameters are of superior importance: bead diameter, indentation depth and indentation speed.

The choice of which tip to use for AFM measurements is of great importance. The resolution of the measurements obviously depends on the tip. All of the cantilevers used for these measurements bear a $25\ \mu\text{m}$ diameter bead. This diameter allows us to observe the elasticity pattern at a scale close enough to the cellular scale. A greater diameter might also be adapted to our study. Indeed, we are interested in the differences of Young's modulus within the tissues of the rachis. Probing the elasticity at a greater scale (some cells) might already be sufficient to bring out such heterogeneities.

Indentation depth is not directly controllable. It is the result of the deformation of the probed material—and obviously depends on its mechanical properties—under the action of the indentation force applied by the cantilever. In our experiments it was generally of $1 - 5\ \mu\text{m}$.

6.1.3 Data analysis

The AFM allows to probe the mechanics of the sample on $100\ \mu\text{m} \times 100\ \mu\text{m}$ regions. These regions are reduced to a certain amount of points depending on the chosen spatial resolution. For each of these points, the AFM raw output is a set of two 'force versus height' curves. One of these curves corresponds to the extend phase measurement while the other one corresponds to the retract phase. In these curves, the force corresponds to the force applied on the biological sample and the height corresponds to the z-position of the cantilever².

As discussed in section 6.1.1, the Hertz contact model allows to retrieve the Young's modulus of the tissue. But, in the frame of the Hertz contact model, we first need to get force versus indentation depth curves. That is to say that we need to determine the position of the contact point or, to put it in other words, the position of the sample relative to the initial position of the cantilever. In simple cases, this can be done by pinpointing the change of slope in the force-height curve.

²The used AFM does not provide the absolute position of the cantilever but only its position relative to its initial position.

What does this change of slope mean? It corresponds to the transition between a resistance-free displacement of the cantilever—no change in the applied force while the cantilever is displaced—and the displacement of the cantilever with a mechanical resistance—any displacement of the cantilever induces a change in the applied force. Most of the time however, this change of slope is hard to detect. For this reason, the position of the contact point is fitted by the dedicated JPK data analysis software. Once the contact point has been determined, the analysed force-height curve can be transformed in force versus indentation depth curves. From this point, it becomes possible to fit the Hertz contact model to the considered curve.

The described analysis has to be repeated twice—extent and retract curves—for each point of a scanned area. When this is complete, a map of the rigidity—or any other available information— of the area can be built. In such a map, each point corresponds to a single AFM measurement and is associated to the retrieved Young's modulus. Hence, we can build two maps corresponding to the extent and retract measurements. Maps are actually matrices built from the output files of the AFM thanks to Matlab and are thereafter workable for statistical analysis for instance.

A single AFM map covers 10^{-2} mm^2 while a typical rachis transverse area is of the order of several tenths of mm^2 . Numerous maps are thus needed to image the whole sample or at least a part of it. To obtain a proper image of the sample, we then need to align all these maps. The alignment of the maps cannot be done automatically since the cantilever is displaced across the sample during the experiment and the AFM does not record the absolute $X - Y$ coordinates of the cantilever. In addition to that, the sample is sometimes not completely stable in the agarose layer and may be continually drifted because of repeated contacts with the cantilever. To go beyond these issues, a picture of the cantilever over the sample is taken for each map. The resulting pictures are aligned manually. The map position within the sample is known thanks to the initial position of the cantilever in the aligned pictures. However, the position of the maps over the studied sample is not perfect. In general, we do not precisely know where the bead is placed under the used cantilever³. Strictly speaking, we retrieve the position of the maps relative to each other.

The individual maps that are obtained can now be processed and corrected if needed. Rigidity maps can be affected by numerous sources of error. In particular, we are sometimes forced to probe the agarose layer. Some measurements might also be disturbed by the presence of a trichome or of some unwanted material on top the

³The cantilevers used during my thesis were manually built by Alexis Peaucelle. As a result, the position of the bead under the cantilever is not known.

sample. Thanks to simple filters on the sample height and rigidity, we can exclude aberrant points or regions external to the sample. Parts of the map that were affected in some manner but cannot be excluded by simple filtering are manually masked.

In this whole part, we are seeking mechanical heterogeneities within the growing tissues of *Averrhoa carambola* rachis. Because of the nutation motion, we basically expect one side of the rachis to be stiffer than the other. To reveal such a behaviour, it is sufficient to use relative rigidity values. I have made the choice to use only relative Young's modulus values partly for this reason, but also because it makes the protocol simpler—the cantilever calibration is no longer relevant—and less dependent to calibration issues. As a result, all the rigidity maps that will be presented hereafter are in percentage of the global average Young's modulus of the considered sample E_m .

6.1.4 Results

Full-mapping of the rachis

A first approach to explore the inner mechanics of the rachis is to realize a complete AFM scan of a sample. As already discussed in section 6.1.3, such an experiment is costly in the sense it requires to perform a large number of AFM maps. But, doing so will allow to comparing the mechanical properties of the different tissues of the rachis and eventually to pinpoint tissues more likely to be relevant for our study. Such a map is presented in figure 6.5.

First, we see that the rigidity of the inner tissues of the rachis is quite heterogeneous. The Young's modulus values E are mostly comprised in $0 \leq E \leq 5E_m$, where E_m is the global average of E . Then, it seems that the softest tissues are found in the center of the sample while the stiffest tissues are found on its periphery. This is somewhat consistent with the description of the inner tissues made in Chapter 2. As a matter of fact, the most central tissue of the rachis—the medullar parenchyma—is constituted of large thin-walled cells. On the contrary, the outermost layers have thicker cell walls and are relatively much smaller. It could reasonably be expected for the parenchyma to be softer than the rest of the tissues.

This sample had been taken in the bending zone of the growing rachis. So, can we spot a mechanical heterogeneities that could correlate with the motion? Actually, we see that the highest values of E/E_m are found on the left half of figure 6.5. Not only can we spot patches of high relative rigidity, but the mean values of E/E_m also

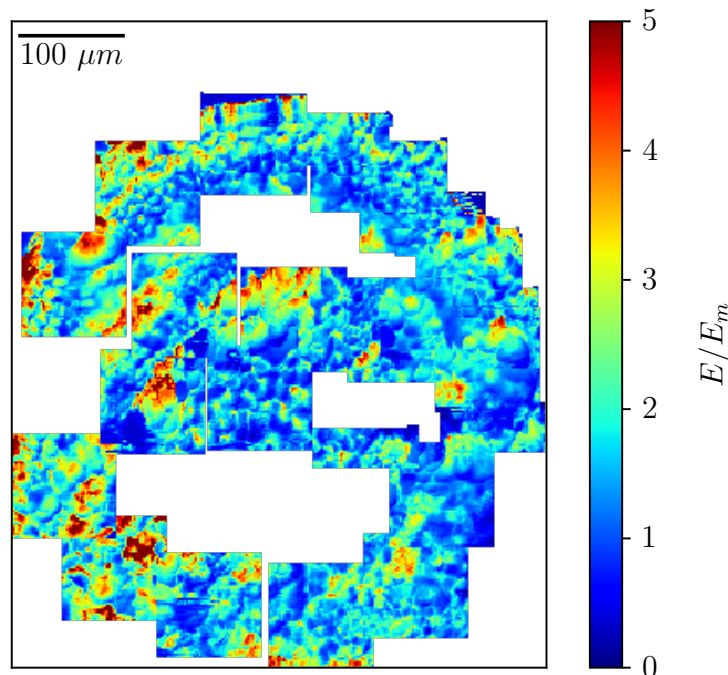


Figure 6.5: **Global rigidity mapping of the rachis' inner tissues.**

seem greater in the left maps. We thus see that there is a gradient of rigidity in the tissues of the rachis. Could these variations be linked to the nutation motion?

Focusing on peripheral tissues

Mapping the rigidity of a whole rachis cut have put forward the mechanical heterogeneities resulting from the diversity of the inner tissues of the rachis. The presented experiment also displayed a rigidity gradient between the faces of the rachis. Does such a rigidity gradient correlate with the nutation motion?

The peripheral tissues of our sample seem of particular interest since they display mechanical inhomogeneities. Besides, as discussed in Chapter 2, these tissues undergo important anatomical changes. So, we are now going to focus on these specific tissues.

Here, accordingly to the protocol described in section 6.1.2, a time-lapse movie of the leaf was systematically realized to determine the direction of the motion. Then, like previously, series of AFM maps were realized on the inner tissues of the rachis. We confined the measurements to the peripheral tissues, trying to probe the same tissues consistently throughout the experiment. Thanks to the orientation criteria described earlier, we have split our individual AFM maps in two populations: those belonging to the concave and convex faces of the rachis. To compare

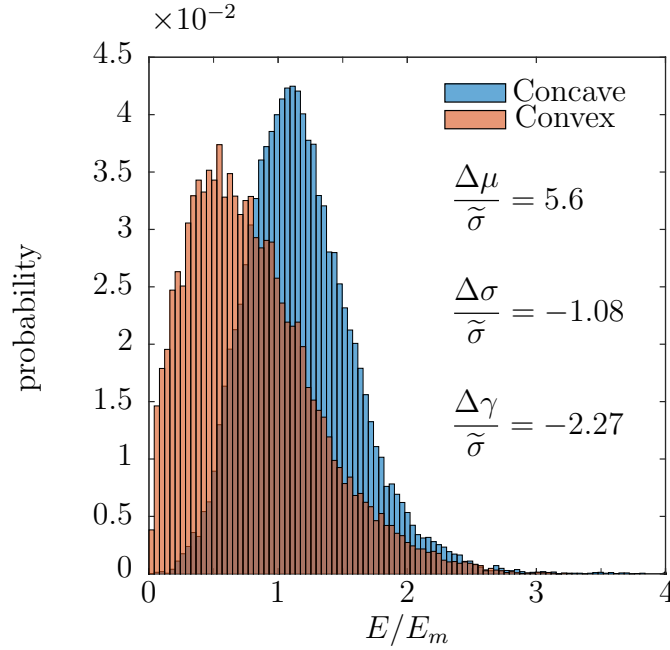


Figure 6.6: **Relative rigidity histograms of the inner peripheral tissues.** The histograms of the concave and convex faces of the rachis are drawn separately, in blue and red respectively. The three first moments of the distributions are compared and normalized by an estimation of the variability in E ($\Delta X \equiv X_{concave} - X_{convex}$). This sample belongs to the experiment 1, and is labelled 1.

these two populations, we have built the histograms of the relative rigidities E/E_m (see figure 6.6). To be able to quantitatively compare the characteristics of these histograms, we have measured different moments of the distributions: their mean μ_i , their standard deviation σ_i and their skewness γ_i^4 . Finally, to assess the significance of the observed differences between the characteristics of the distributions, we normalize the differences in the different scores by a measurement of the local variations of E/E_m , noted here $\tilde{\sigma}$. The local variations of E/E_m are quantified by computing the standard deviation on a small neighbourhood around each pixel of each map. Finally, $\tilde{\sigma}$ corresponds to the median of this quantity.

In the case of the experiment presented in figure 6.6, we see that the histograms of the concave and convex faces are qualitatively different. Not only the modes of the distributions are clearly different, but their global shapes also differ. We see that the distribution of E/E_m for the concave face is almost symmetrical, looking like a Gaussian distribution. In contrast, the convex distribution is asymmetrical and

⁴The skewness is basically a measurement of the asymmetry of a distribution. It corresponds to the standardized centred third moment $\gamma_i = \langle X - \mu_i \rangle^3 / \sigma_i^3$. A positive skewness indicates that the distribution leans to the left, on the contrary a distribution with negative skewness leans to the right.

	$\mu_{concave}$	μ_{convex}	$\Delta\mu/\tilde{\sigma}$	$\gamma_{concave}$	γ_{convex}	$\Delta\gamma/\tilde{\sigma}$
Experiment 1						
sample 1	1.18	0.80	5.60	0.76	0.90	-2.27
sample 2	1.10	0.90	3.14	0.17	1.20	-15.6
Experiment 2						
sample 1	1.10	0.92	3.37	0.32	0.50	-3.29
Experiment 3						
sample 1	1.06	0.96	1.03	0.87	0.91	-0.48
sample 2	1.06	0.95	1.25	1.00	1.54	-5.77

Table 6.1: **Recapitulation of the distributions characteristics.** This table gathers the different comparison scores—mean, standard deviation and skewness—for the relative rigidity histograms shown in figures 6.6 and 6.7). For all the displayed quantities, $\Delta X \equiv X_{concave} - X_{convex}$. Data is presented in the same order than the figures.

shifted towards low relative rigidities. At first glance, we thus see that in average the convex face of the rachis is softer than the concave face. The difference of the means is significative since we have $\Delta\mu = 5.6\tilde{\sigma}$. Besides, the skewness scores confirm that both distributions lean to the left (see table 6.1), that is to say that there is a tendency to over-represent the low E/E_m . Finally, $\Delta\gamma = -2.27\tilde{\sigma}$ confirms the visual impression of figure 6.6: the asymmetry of the distribution of E/E_m is more marked for the convex face.

So, if we accept that the nutation motion is driven driven elongation—with possible irreversible and reversible contributions—these first results suggest a correlation between the rigidity of the tissues and their elongation rate. More precisely, the experiment pictured in figure 6.6 suggests that the tissues with the highest elongation rate—on the convex face—have a lower rigidity than the tissues with the lowest elongation rate—on the concave face. Here, the relative difference between the Young’s moduli of the faces is of about 40% (see table 6.1).

In order to test the reproducibility of these results, we have performed further experiments. Four additional rigidity mappings of the peripheral tissues of the rachis are presented in figure 6.7. The characteristics of the different distributions and their comparison are gathered in table 6.1.

First, we see that the two samples of experiment 1 provide qualitatively equivalent results (compare figures 6.6 and 6.7a). We recover two distinguishable distributions of relative rigidities. As previously, the convex tissues are in average softer than the

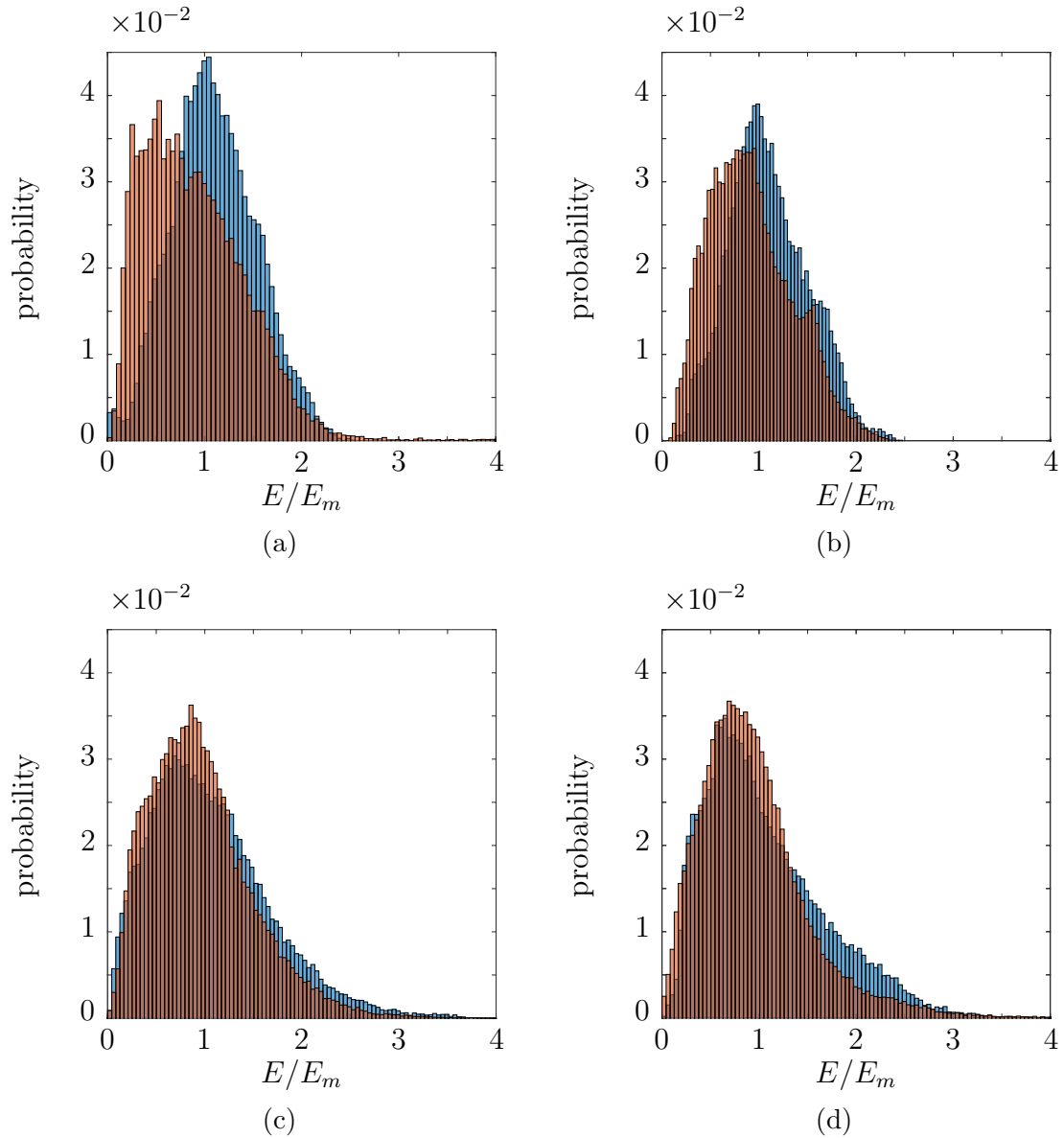


Figure 6.7: **Additional relative rigidity histograms.** The results for four other samples are shown here. (a) Second sample from experiment 1 (same experiment than in figure 6.6). (b) A single sample from experiment 2. (c–d) Two samples from experiment 3. The red and blue histograms correspond to the convex and concave faces respectively. The comparison of the histograms characteristics is summed up in table 6.1.

tissues of the concave face. Moreover, we find again a marked asymmetry in the case of the convex distribution. In quantitative terms, the two means are significantly different with $\Delta\mu = 3.14\tilde{\sigma}$. Similarly, for the skewness scores, we have $\Delta\gamma = -15.6\tilde{\sigma}$. Notably, we see that the relative difference between the Young's moduli of the faces is now reduced to 20% (against 40% previously). So, we see here that two samples from the same experiment—and thus the same rachis—display important quantitative differences that will need to be discussed. Interestingly enough, we see that the only sample from experiment 2 also displays the characteristic behaviour of the samples of the two previously discussed samples (see figure 6.7b and table 6.1).

As for the third and last experiment, the global behaviour is different from the three previous cases (see figure 6.7c–d). For the two samples of experiment 3, the tissues of the convex face remain softer than those of the concave face but the mean values of the E/E_m distributions are not as well separate. In both cases $\Delta\mu \simeq \tilde{\sigma}$. The observation of figures 6.7c–d shows that the asymmetry of relative rigidity distributions is more pronounced than for the previous experiments. This is particularly true in the case of the tissues of the concave face. Moving on a more precise description of the distributions, we see that the tissues of the concave face present a slightly more important number of points with $E > E_m$ than tissues on the convex face. Notably, in the case of the second sample where the difference in skewness is important (see figure 6.7d, $\Delta\gamma = -5.77\tilde{\sigma}$).

In summary, we have investigated the possibility of mechanical heterogeneities within the tissues of the nutating rachis. As a matter of fact, our results are based on few experiments and might be matter to some debate, inviting us to remain cautious. Our results show evidences of inhomogeneities of the elastic properties of the cell wall, correlating with the direction of the nutation motion.

6.2 Cell wall composition heterogeneities

The rachis of *Averrhoa carambola* presents clues of mechanical heterogeneities in its bending zone. As discussed in Chapter 1, the mechanics of the cell wall is greatly influenced by its biochemical status. So, can we now pinpoint biochemical heterogeneities within the inner tissues of the nutating rachis? In particular, the methylesterification of a family of pectins—homogalacturonans—has recently drawn much attention in the plant biomechanics community. The biochemical status of the cell wall can be assessed by different means. One of the most widespread techniques is immunohistochemistry. In this section, I will first quickly introduce the principles

of immunohistochemistry. Then, I will present the preliminary results we have obtained on the composition of the cell wall.

Quick introduction to immunohistochemistry

The aim of immunohistochemistry is to localize certain proteins of interest within a whole tissue. This is performed by taking benefit of the mechanisms of the immune system. We use antibodies specific of the antigen (here a protein) of interest. These antibodies will then react with the antigens of interest and bind to them exclusively. The used antibodies are usually linked to a fluorophore that allows the detection of the antibody-antigen complexes under fluorescence microscopy. Two methods are then possible to prepare an immunohistochemistry observation: the direct and indirect methods. The direct method relies on the injection of a single antibody bearing a fluorophore. In contrast, in the case of the indirect method, two antibodies are sequentially injected in the tissues. The primary antibody is not labelled and directly binds to the antigen of interest. Then, a secondary antibody—specific to the primary antibody—is injected in the tissues and binds on the primary antibody. These secondary antibodies bear a fluorescent tag that allows the detection of the antigen of interest. The different steps of the indirect labelling method are pictured in figure 6.8.

Here, we will use the indirect labelling method. This method indeed requires additional steps for the sample preparation before observation. In this sense, the preparation is more tedious and might potentially undergo more experimental difficulties. The indirect labelling method however presents several advantages. The signal is amplified in comparison with the direct labelling method. Actually, secondary antibodies can bind to several parts of a single primary antibody. Having several secondary antibodies binding a primary antibody results in more fluorescent signal per targeted antigen. Furthermore, the indirect labelling method is less constraining to use. The direct method requires to have antibodies specific to each antigen of interest also linked to a fluorescent tag. For the indirect method, the secondary antibodies are rather versatile since they are not specific to a single antigen but to a whole family of antibodies (e.g. anti-rat or anti-rabbit antibodies).

Experimental protocol

Performing immunohistochemistry requires a delicate preparation of the samples. First, the tissues of interest have to be taken and fixed. The fixation process results in the death of the cells of the sample but allows us to maintain the sample in its original biological state. This is realized thanks to a bath in paraformaldehyde and

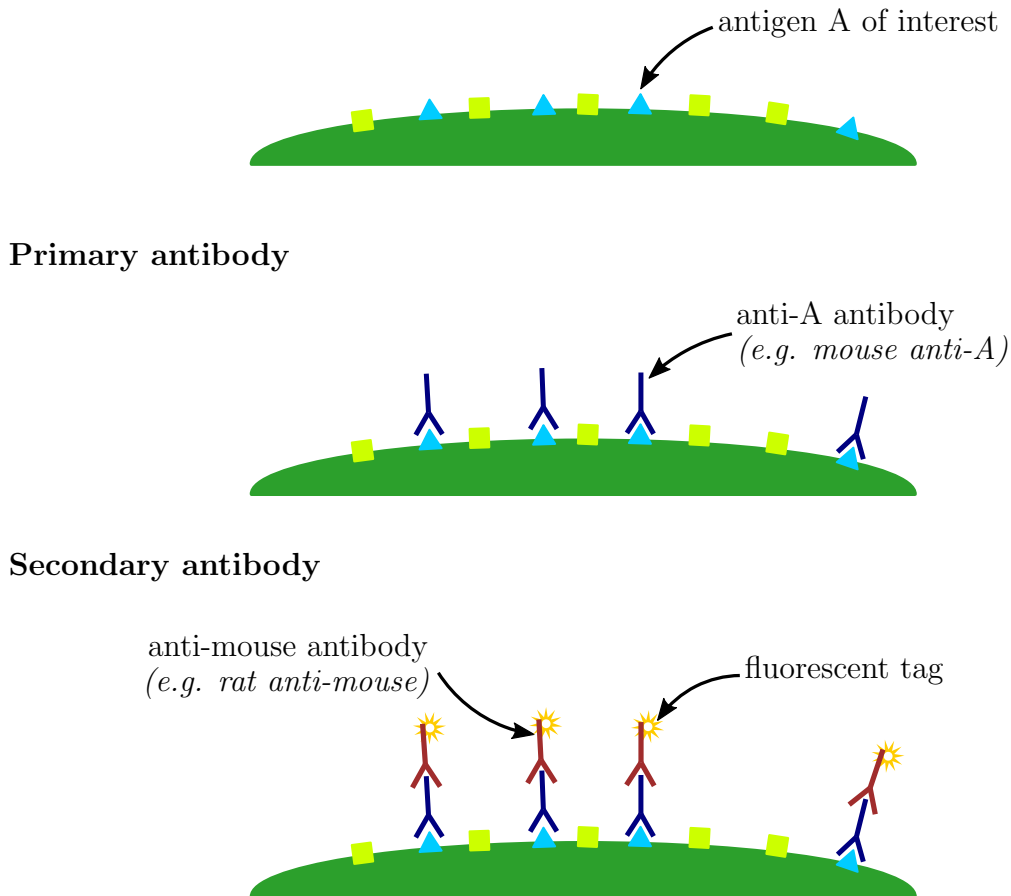


Figure 6.8: **Illustration of the indirect labelling principle.** A first antibody, specific to the antigen A is introduced. This primary antibody has been extracted from an animal species (mouse, rabbit, rat, ...). Then, a secondary antibody is injected, specific to the primary antibody (i.e. anti-mouse, anti-rabbit or anti-rat, ...). This second antibody is bound to a fluorophore (or fluorescent tag) and allow to observe the localization of the antigen A of interest within the studied tissues.

a slow dehydration of the tissues. The sample is then embedded in a more or less solid material—resin or wax—to facilitate its slicing. The samples are then sliced thanks to a microtome and mounted on microscopy slides and dewaxed. In our case, slices of 5 μm have been realized.

Then begins the immunostaining strictly speaking. The sliced samples are first progressively rehydrated and placed in a buffer. The nature of the buffer might depend on the nature of the antibodies used for the experiment⁵. The primary antibody is injected over the microscopy slide and let to react overnight. After washing the samples with the adequate buffer, the secondary antibody is introduced and let to react for at least 12 *h* in the dark, to avoid bleaching. Finally, the samples are washed a last time and the microscopy slides sealed. The samples are now ready for observation under a confocal microscope.

Tested antibodies

Here, we want to assess if the mechanical heterogeneities observed in the inner tissues of the *Averrhoa carambola* rachis are correlated with biochemical heterogeneities. We are going to focus on the homogalacturonans, which can be either methylesterified or de-methylesterified. Several antibodies are available to discriminate the homogalacturonans in the cell wall depending on their degree of esterification. The 2F4 antibody specifically binds to lowly methylesterified pectins—degree of esterification up to 40%—forming Ca^{2+} -cross links. On the contrary, LM20 and JIM7 antibodies do not bind to unesterified homogalacturonans. These three antibodies will thus allow us to compare the methylesterification status in the cell wall of *Averrhoa carambola*.

6.2.1 Preliminary results

In this section, I will present the results obtained for a single experiment. The presented samples were taken in the bending zone of the rachis and prepared according to the experimental protocol we have just described.

Since we are mostly interested in a possible antagonism between the lateral faces of the rachis, the images from our immunohistochemistry experiments have been locally averaged on a small neighbourhood of pixels. These coarse-grained images help revealing patches and zones with different signal intensity.

⁵In the case of a complex material like the cell wall, additional treatments might be needed to facilitate the action of the primary antibody. This is for example the case for cellulose labelling. Degrading part of the cell wall pectins frees regions of the cellulose microfibrils useful to binding

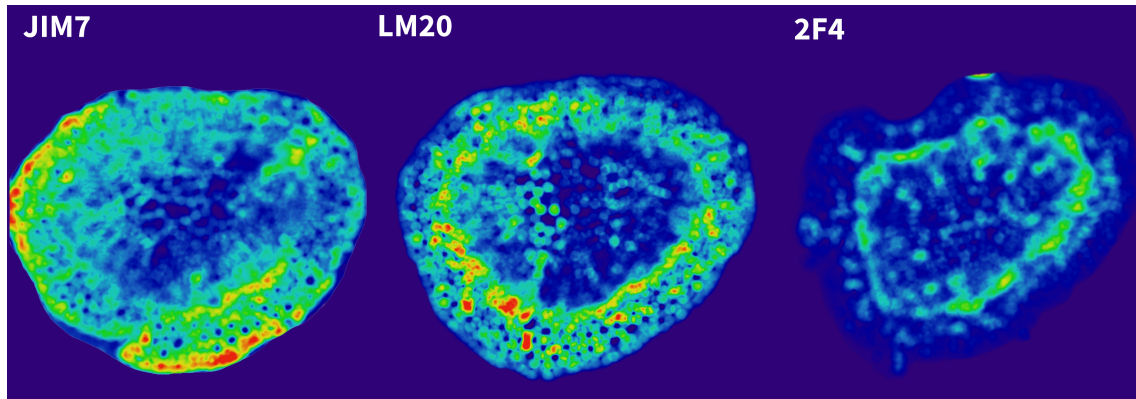


Figure 6.9: **Evidences of cell wall composition heterogeneities in the bending zone.** The immunostaining images have been coarse-grained and re-aligned for the three antibodies. JIM7 and LM20 display consistent asymmetries of de-methylesterification. 2F4 seems to show the complementary asymmetry. Color maps cannot be compared from a sample to another. Colors evolve from blue to red.

The results of the whole procedure are shown in figure 6.9. In this figure, three samples taken in the bending zone of the rachis are presented. Each one of them is labelled with a different antibody: JIM7, LM20 or 2F4. Note that the colormaps should not be used are not comparable from a sample to another. Their respective minimum and maximum values do not match. These have been chosen in order to enhance the contrast and the visualization of heterogeneities within a single sample. The three different samples have been oriented in a similar way to compare the spatial repartition of the signal intensity.

First, we see that—for all three samples—the signal intensity presents some degree of heterogeneity. In all the cases shown in figure 6.9, the central tissues have a weaker signal intensity than the peripheral tissues⁶. Furthermore, the samples all seem to exhibit an antisymmetry of composition heterogeneity between their lateral faces. Interestingly enough, it looks like JIM7 and LM20 asymmetries are oriented likewise. On figure 6.9, we indeed see that the JIM7 labelling shows large signal intensities on its left half, with two strong zones at the top and bottom. The LM20 sample returns the strongest signal intensities on its left lateral face, rather at the bottom. In both cases, the upper part of the right face appears weaker. The zones of high intensity do not exactly match but overlap to a large extent.

On the contrary, it looks like the sample labelled by 2F4 antibodies has the complementary asymmetry (see figure 6.9, right sample). As a matter of fact, we see that in this case, the strongest signal intensities are found in the right half of

and labelling.

⁶It should however been noticed that the coarse-graining process is sensible to the size of the cells and to the thickness of their walls. Then, medullar parenchyma being characterized by large thin-walled cells, the coarse-grained values are necessarily lower than elsewhere in the sample.

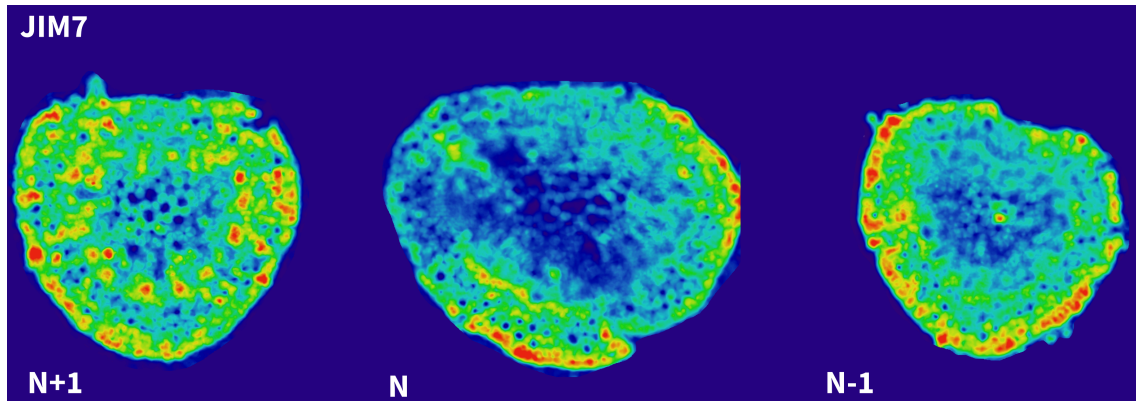


Figure 6.10: **Evidences of cell wall composition heterogeneities along the rachis.** Here are presented three samples labelled with JIM7 from three successive interleaflets arranged from apex to base. The interleaflet N corresponds to the bending zone. Colors evolve from blue to red.

the sample.

These simple observations are consistent with the specificity of the used antibodies. On the one hand, JIM7 and LM20 both indicate that homogalacturonans with high degrees of esterification are rather found on the left half. On the other hand, homogalacturonans with low degrees of esterification are indicated by 2F4 and found in the opposed face of the rachis.

We have just seen that there exist evidences of heterogeneities or an antisymmetry in the degree of esterification of the homogalacturonans constituting the cell wall in the bending zone. Can we also spot hints of variations of the methylation degree along the rachis? In addition to the samples previously presented, we have also taken samples in the two neighbouring interleaflets. Following the numbering convention established in Chapter 2, the interleaflets are labelled from base to apex: N-1, N, N+1. The interleaflet N thus corresponds to the centre interleaflet which samples we have just studied.

Here, a sample per interleaflet—labelled with JIM7—is shown in figure 6.10. The samples are arranged by increasing distance to the apex of the rachis. In the case of interleaflet N+1, apart from some spots of higher methylation, the signal intensity is quite homogeneous. Then, in the case of the interleaflet N-1, we see that the peripheral tissues exhibit the higher degrees of esterification. This is particularly true for the outermost layers of cells. The adaxial face of the sample and the central tissues also appear to have a lower intensity. Apart from that, here again the signal is quite homogeneous. The analysis of the patterns of JIM7 labelling suggests that the antisymmetry of the methylation status for the lateral faces of the growing rachis

is particularly pronounced in the bending zone.

6.3 Discussion and partial conclusion

The growth and nutation of *Averrhoa carambola* have been shown to be underlaid by differential elongation. Hints of reversible contractions during nutation naturally question the nature of this differential elongation. This is why this sixth chapter brought the study of *Averrhoa carambola* growth and motions to the tissue and cell wall scales. Two entangled aspects of the microscopic growth mechanisms have thus been explored: the cell wall mechanics and the cell wall biochemistry. Our main question was here to determine whether mechanical and biochemical heterogeneities could correlate with nutation and differential growth.

Nutation could correlate with elasticity heterogeneities at the tissue scale

The elasticity of the inner tissues of the bending zone have been probed with Atomic Force Microscopy (AFM). Our aim was to specifically pinpoint a mechanical antagonism between the lateral faces of the nutating rachis. A first global mapping of the rachis confirmed the anticipated enhanced mechanical heterogeneities within the peripheral tissues of the rachis (see Chapter 2 and figure 6.5). We consequently targeted these tissues in the following experiments.

By keeping track of the orientation of our samples (see figure 6.4) we were able to assess the link between the direction of the motion and the mechanical properties of the inner tissues. Doing so, we have evidenced differences in the relative elasticity of the concave and convex faces of the nutating rachis (see figures 6.6 and 6.7). Differences have been quantified by studying the relative elasticity distributions for each face. Our results have first revealed significant differences in the average elasticity. In our experiments, the convex face of the rachis is in average softer than the concave face by 10 to 40% (see table 6.1). Significant differences in the distributions' skewnesses were also noticed. This is a more subtle effect however. It seems that the distribution of relative elasticity of the convex side has a tendency to be lean toward the low values of relative elasticities. In other words, even in cases where the average elasticities of the two lateral faces are close (eg. figures 6.7c–d), the convex face presents fewer zones of high relative elasticity than the concave face. It thus appears that the direction of nutation correlates with the inner elastic properties of the tissues: the rachis bends toward its softer lateral face.

However, these results must be considered with caution, for several reasons. First, the low number of performed experiments do not allow to draw any definitive

conclusion. Second, we see that our third experiment shows less clear results (see figures 6.7c–d). How can these differences between experiments be explained? It is possible that the mechanical antagonism of the lateral faces depends on the characteristics of nutation (eg. its amplitude or its velocity). Another source of variability is the position of the sample in the bending zone. The thickness of our samples—several hundreds of micrometers—combined with the strong spatial variations of elongation (see Chapter 4 & 5) could indeed explain the observed variability. Further experiments have thus be conducted to ascertain the mechanical antagonism of the lateral faces of the rachis and its correlation to the direction of nutation.

Could this mechanical anisotropy correlate with growth? As discussed in Chapter 1, plant growth is an irreversible process which relies on the plastic properties of the cell wall. Our AFM measurements do not probe the plastic but the elastic properties of the cell wall. So, the observed mechanical anisotropy could naturally be interpreted as a signature of ongoing elastic processes. However, several studies have established a correlation between the irreversible growth and the elastic properties of the cell wall.

In our case, the convex face is expected to have a greater elongation rate than the concave face. Thus, this would suggest that low Young’s moduli are correlated with high elongation rates and inversely. This would be consistent with previous findings for single cells such as *Chara corallina* internodes (Proseus et al., 1999) and *Papaver rhoeas* pollen tube (Zerzour et al., 2009) ; or for the apical meristem of both *Arabidopsis thaliana* and tomato plants (Peaucelle et al., 2011; Kierzkowski et al., 2012). Our results on *Averrhoa carambola* could thus bring further support to the correlation of the elastic properties of the cell wall and the growth rate in a tissue context.

Hints of biochemical heterogeneities The next step consisted in assessing the possible biochemical changes involved in the cell wall. Here, we have specifically investigated the methylesterification status pectins constituting the cell wall. In the same way than for the mechanical properties of the tissues, we have here focused on seeking an antagonism between the lateral faces of the rachis. An averaged information is thus sufficient. This is why we have used coarse-grained images (see figures 6.10 and 6.9).

Our first results show that—in the bending zone of the rachis—the degree of esterification of homogalacturonans is not homogeneous within our samples (see figure 6.9). Moreover, we do see a antagonism between the lateral faces of the rachis. Although biological repetitions are obviously needed in order to confirm this

tendency, the observation of the methylesterification asymmetry in these specific samples is quite certain. As a matter of fact, three different antibodies—JIM7, LM20 and 2F4—have consistently revealed the same asymmetry (see figure 6.9). We have then investigated the evolution of this biochemical antagonism along the rachis. Samples have been taken in the neighbouring interleaflets and submitted to the same experimental protocol. Our results suggest that such an asymmetry—at least of this magnitude—is localized to the bending zone of the rachis. As discussed in the case of the elastic properties, the heterogeneities of methylesterification might undergo quick spatial variations within the bending zone.

Here again, the interpretation of these preliminary results should be done carefully. By resorting on coarse-grained images, we have overlooked at the possibility of cell wall thickness and cell size inhomogeneities within the tissues. To take this possibility into account, further immunohistochemistry labelling experiments should include a cellulose labelling. Doing so would also allow us to perform a proper quantification of the signal intensity across the cell walls⁷.

Establishing a correlation between the direction of the observed methylesterification heterogeneities and the direction of nutation requires to perform immunohistochemistry assays in which we keep track of the orientation of the sample. We have actually performed such experiments, but they have not been analysed at the moment of this manuscript. From these new experiments, we will be able to assess if there exists a correlation with the direction of the motion, and thus possibly with elasticity and growth. In particular, it will be interesting to check in the case of *Averrhoa carambola* if the high degrees of esterification correspond to stiffer tissues like predicted by the classical view on pectins (see Chapter 1) and observed in the case of the pollen tube for example (Parre & Geitmann, 2005). On the contrary, high degrees of esterification could also correlate with soft tissues like in the case of *Arabidopsis thaliana* meristem (Peaucelle et al., 2011).

Partial conclusion In conclusion, this chapter has revealed the mechanical and biochemical heterogeneities involved in differential growth. In both cases, an antagonism between the lateral faces of the nutating rachis has been observed, localized within the bending zone. Assuming that irreversible growth was involved in nutation, we were then able to hypothesize a correlation between the elastic properties of the inner tissues to growth, thus building a putative scenario consistent with pre-

⁷*Averrhoa carambola* tissues actually are autofluorescent. Unfortunately, this autofluorescence is weak and not specific to the cell wall: organelles such as amyloplasts and chloroplasts also emit light. As a result, the autofluorescence signal does not allow a proper quantification.

vious literature (see figure 6.11 for a graphical sum-up). Further work should enable us to go a ascertain these first results but also to go a step further and determine a link between the chemical status of the cell wall and growth.

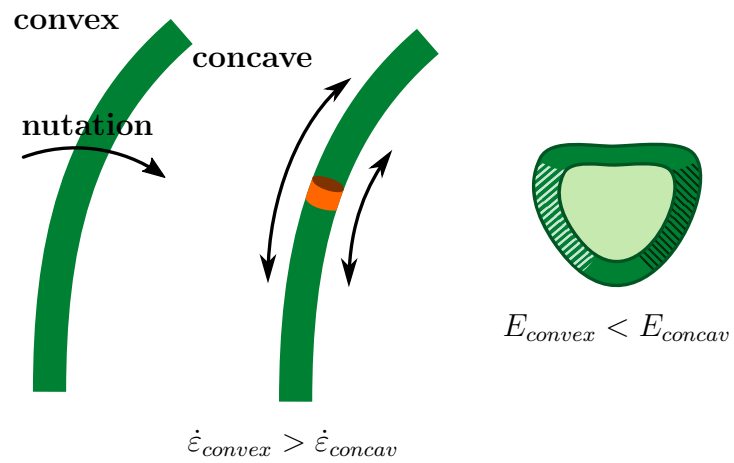


Figure 6.11: Putative scenario for a growth-elasticity correlation in nutation.

Chapter 7

Conclusion & prospects

The foundation of this work lies in the intimate links between plant motions, growth and several aspects of development. This is why, in contrast with numerous studies on plant motions, we have left aside the notion of still plants set in motion by a certain trigger to embrace the idea of evermoving plants. In this whole thesis, plant motions have been considered as an outward signal of the microscopic growth processes. In this sense, we have been able to investigate several aspects of growth—kinematics, mechanics and biochemistry—at different scales. Let us now summarize the different results brought by our approach and draw outlooks for further research.

Our works have been focused on the motions of *Averrhoa carambola* compound leaves. Of course, *Averrhoa carambola* does not offer the mutant arsenal of *Arabidopsis thaliana* but it is a more complete model for the study of plant motions. This statement relies on the diversity and the extent of *Averrhoa carambola* motions, but also on the fact that they are widespread motions. Following our idea according to which the logic of growth motions lies in their temporal succession, we have then studied the successive unfurling and nutation motions.

The unfurling motion and the associated hook shape is typical of many organs and compound leaves. The reproducibility of this shape presages posture regulation processes. Thanks to a simple ‘flipping’ test, we have verified that the shape of *Averrhoa carambola* compound leaves indeed results from active processes. From then on, the specificities of the unfurling motion may be helpful to the posture regulation of the leaves. In particular, we have shown that the unfurling motion involves prominent changes of the spontaneous curvature but also a gradient of flexural rigidity along the rachis of the leaves. The changes in the stiffness of the tissues are besides underlined by the maturation of the tissues via lignification.

The characterization of nutation then revealed the spatial patterns of elongation and differential elongation at the scale of the whole leaf. As many other organs, the compound leaves of *Averrhoa carambola* show an apical growth. It is thus characterized by a growth zone. More importantly, we have shown that the differential elongation was localized within a bending zone, at the basal extremity of the growth zone.

Based on these observations, we have built a kinematic model of growth and nutation. This model successfully reproduces the main features of nutation, and might thus incorporate the essential components of growth and nutation kinematics. In that sense, it provides a general framework to study the interplays between growth and nutation.

Another part of our study of nutation focused on its dynamical aspects. We have seen that nutation is not a steady process as the amplitude of the motion undergoes periodical bursts—that we refer as nutation tides or nutation surges—on a circadian basis. The well-defined periodicity of these nutation tides suggests inner clock.

The dynamical behaviour of nutation also implies variations of elongation and differential elongation. To go beyond our averaged growth profiles, we have tried to investigate the occurrence of such variations by measuring precisely the elongation of nutating rachises. Our measurements were however greatly affected by artefacts due to the nutation motion itself.

So, the question of the spatial and time variations of the elongation behaviour remain unanswered for the moment. Getting a proper characterization of the growth of a moving organ requires a new measurement technique implying 3D reconstruction of the rachis. We are confident that such techniques could lead to advances in the characterization of growth and differential growth dynamics.

Here, our kinematic model of nutation helped us retrieve important qualitative information from our biased measurements however. Importantly, we have been able to spot a signature of differential elongation within our measurements.

Our model has also brought forward that dynamical changes of the elongation and differential elongation could lead to local contractions of the rachis. Local contractions of plant tissues have already been discussed, but our model clarifies the conditions for their occurrence. The confrontation of the model to our experimental data suggests that local contractions are indeed observed, particularly during nutation tides. In agreement with previous works (Caré et al., 1998), we hypothesize that these contractions correspond to local variation of the turgor pressure.

Differential elongation having been evidenced, we have then naturally tried to pinpoint the associated variations at the scale of the tissue. While our results still

need confirmation, they are encouraging. We have been able to put forward elasticity heterogeneities between the lateral faces of the rachis, correlated with the direction of the motion. Hints of a biochemical antagonism—based on the esterification degree of pectins—have also been observed. The continuation of these works should allow us to confirm these observations, and thus to establish a link between growth, mechanics and the esterification degree of pectins in the case of *Averrhoa carambola*.

A natural extension of the microscopical aspect of our work would be to determine the time and spatial variations of the observed mechanical and biochemical antagonisms. Doing so would allow a better understanding of the link between differential elongation and the status of the cell wall. For example, the existence of time delays between the changes in the cell wall and the motion could help to understand the biological processes giving rise to oscillatory motions.

In this part of our work, we hope to have provided a proof of concept on the possibility to make use of motions to study the physiological implications of growth at the scale of tissues, such as stems and rachises.

Besides the direct questions our results have raised, we can draw more general questions and perspectives on the shape, growth and rhythms of plants.

Biological basis of the link between elongation and differential elongation

In the case of nutation, differential elongation takes place at the basal end of the growth zone, where elongation decays. This specific localization of differential elongation is puzzling. Could there be a direct link between the local rate of elongation of an organ and its propensity to undergo differential growth? The nutation motion implies periodical oscillations of the elongation rate within the bending zone. So, it seems that asynchrony of elongation rises in the tissues coming out the growth zone. What would be the biological basis for such a behaviour?

Mechanics and nutation Nutation is often presented as a result of irreversible differential growth. However, contractions are known to be involved in nutation (Caré et al., 1998) and have been indirectly observed in our case. It is likely that, in the general case, nutation actually results from a mix of irreversible and reversible length variations. These contractions could result from simple turgor variations, but could also be the result of compressions. As a matter of fact, considering the possibility of turgor variations and the heterogeneities of elasticity within the bending zone, it is possible to imagine that the bending of the rachis puts the concave face under compression and the concave face in tension. The resulting stresses could then be sensed by the plant and used a feedback on nutation and/or entertain oscillations.

This idea is not exactly new, as it was suggested by Johnsson as soon as 1979 (refer to (Peacock & Berg, 1994)) but our renewed observations of local contractions somewhat revives it. It is furthermore supported by numerous studies on the effects of mechanical stress on growth (Baskin, 2015). Despite several authors encouraging the modelling of mechanical effects in nutation, this issue has remained—to the best of my knowledge—untackled for the moment. Instead, models of nutation mainly revolve around two ideas: endogenous oscillations or oscillations triggered by gravitropic overshooting (Mugnai et al., 2007). There is evidence of an interplay between graviception and nutation (Mugnai et al., 2007; Baskin, 2015), and a mechanical-based model of nutation could not account for such effects (Peacock & Berg, 1994). But it could however bring a new light on nutation.

Posture regulation As already discussed, the reproducibility of the hook shape and the associated unfurling motion suggest posture regulation processes of the leaf. Similarly, *Averrhoa carambola* leaves systematically reach a flat and straight state. The question of how exactly the shape of the leaf is regulated is now asked.

Our simple experiments from Chapter 3 have allowed us to characterize several geometrical and mechanical quantities of the growing leaf. This experimental protocol could be augmented and include coarse growth kinematics characterization. Doing so, we would be able to explore the posture regulation processes of the leaf. In particular, we have postulated in Chapter 3 that the rachis may maintain—through the regulation of its flexural rigidity—a zone of high stress and/or strain as a mean to enhance autotropism. These ideas could be tested by deforming locally the plant, for instance.

Another question that arises from the observation of *Averrhoa carambola* growth and motion is the possibility of a role for nutation in posture regulation. As a matter of fact, nutation occurs at the basal end of the growth zone and upstream from the lignification zone. Nutation corresponds to the last bending motion during the development of the leaf. If, as discussed earlier, nutation does imply mechanical stress within the tissues, it is possible to imagine that it allows enhanced autotropism before definitely freezing the shape of the rachis. Preliminary results in the lab show that, when grown on a rotating clinostat the leaves show dramatically reduced nutation. More importantly, their final shapes clearly differ from the regular leaf shape: they show a prominent torsion along the rachis and the leaflets are consequently no longer coplanar.

Oscillatory motions are widespread among plant organs. Circumnutation and nutation are certainly the most famous examples of this kind, but simple leaves also display oscillatory motions. Their blades undergo fluttering motions around their midrib before reaching flatness (e.g. *Persea americana* or *Quercus sp.*). Our

thoughts on the topic remain speculative, but a role for oscillatory motions in posture regulation could give an explanation to their long questioned ubiquity and purpose.

At last, let us underline that we have solely studied two of the motions of a single plant—*Averrhoa carambola*—under the specific prism of development. The perspectives drawn here are thus necessarily too specific. Considering the rich behaviour of plants and the fascinating diversity of their motions, there is no doubt that future studies—focused on other motions or adopting different approaches—will unearth interesting results for plant sciences. We hope to have demonstrated how the long-known—and long overlooked—plant growth motions are rich and worth further study.

Bibliography

- Armon, S., Efrati, E., Kupferman, R., & Sharon, E. (2011). Geometry and mechanics in the opening of chiral seed pods. *Science*, 333(6050), 1726–1730.
- Barceló, A. R. (1997). Lignification in plant cell walls. *International review of cytology*, 176, 87–132.
- Barlow, P., Parker, J., & Brain, P. (1994). Oscillations of axial plant organs. *Advances in Space Research*, 14(8), 149–158.
- Baskin, T. I. (1986). Redistribution of growth during phototropism and nutation in the pea epicotyl. *Planta*, 169(3), 406–414.
- Baskin, T. I. (2005). Anisotropic expansion of the plant cell wall. *Annu. Rev. Cell Dev. Biol.*, 21, 203–222.
- Baskin, T. I. (2015). Ultradian growth oscillations in organs: Physiological signal or noise? In *Rhythms in Plants* (pp. 3–17). Springer.
- Bastien, R. (2010). *Formes et mouvements gravitropiques des tiges végétales: Modèle universel et phénotypage*. PhD thesis, Université Paris Diderot.
- Bastien, R., Bohr, T., Moulia, B., & Douady, S. (2013). Unifying model of shoot gravitropism reveals proprioception as a central feature of posture control in plants. *Proceedings of the National Academy of Sciences*, 110(2), 755–760.
- Bastien, R., Douady, S., & Moulia, B. (2014). A unifying modeling of plant shoot gravitropism with an explicit account of the effects of growth. *Frontiers in Plant Science*, 5.
- Bastien, R., Douady, S., & Moulia, B. (2015). A Unified Model of Shoot Tropism in Plants: Photo-, Gravi- and Propio-ception. *PLOS Computational Biology*, 11(2), e1004037.
- Bastien, R., Legland, D., Martin, M., Fregosi, L., Peaucelle, A., Douady, S., Moulia, B., & Höfte, H. (2016). KymoRod: a method for automated kinematic analysis of rod-shaped plant organs. *The Plant Journal*, 88(3), 468–475.

- Bastien, R. & Meroz, Y. (2016). The kinematics of plant nutation reveals a simple relation between curvature and the orientation of differential growth. *PLoS computational biology*, 12(12), e1005238.
- Bell, P. R. (1959). The movement of plants in response to light. *Darwin's biological work: Some aspects reconsidered*, (pp. 1–47).
- Berg, A. R., MacDonald, I. R., Hart, J. W., & Gordon, D. C. (1986). Relative elemental elongation rates in the etiolated hypocotyl of sunflower (*Helianthus annuus* L.)—a comparison of straight growth and gravitropic growth. *Botanical gazette*, 147(4), 373–382.
- Berg, A. R. & Peacock, K. (1992). Growth Patterns in Nutating and Nonnutating Sunflower (*Helianthus annuus*) Hypocotyls. *American Journal of Botany*, 79(1), 77.
- Beusmans, J. M. H. & Silk, W. K. (1988). Mechanical Properties within the Growth Zone of Corn Roots Investigated by Bending Experiments. II. Distributions of Modulus and Compliance in Bending. *American Journal of Botany*, 75(7), 996.
- Binnig, G., Quate, C. F., & Gerber, C. (1986). Atomic force microscope. *Physical review letters*, 56(9), 930.
- Bizet, F., Hummel, I., & Bogeat-Triboulot, M.-B. (2015). Length and activity of the root apical meristem revealed in vivo by infrared imaging. *Journal of Experimental Botany*, 66(5), 1387–1395.
- Bruce, R. (1785). An Account of the Sensitive Quality of the Tree *Averrhoa Carambola*. In a Letter from Robert Bruce, M.D. to Sir Joseph Banks, Bart. P.R.S. *Philosophical Transactions of the Royal Society of London*, 75(0), 356–360.
- Buda, A., Zawadzki, T., Krupa, M., Stolarz, M., & Okulski, W. (2003). Daily and infradian rhythms of circumnutation intensity in *Helianthus annuus*. *Physiologia Plantarum*, 119(4), 582–589.
- Caré, A.-F., Nefed'ev, L., Bonnet, B., Millet, B., & Badot, P.-M. (1998). Cell elongation and revolving movement in *Phaseolus vulgaris* L. twining shoots. *Plant and cell physiology*, 39(9), 914–921.
- Charzewska, A. & Zawadzki, T. (2006). Circadian Modulation of Circumnutation Length, Period, and Shape in *Helianthus annuus*. *Journal of Plant Growth Regulation*, 25(4), 324–331.

- Chavarría-Krauser, A., Nagel, K. A., Palme, K., Schurr, U., Walter, A., & Scharr, H. (2008). Spatio-temporal quantification of differential growth processes in root growth zones based on a novel combination of image sequence processing and refined concepts describing curvature production. *New Phytologist*, 177(3), 811–821.
- Chebli, Y. & Geitmann, A. (2017). Cellular growth in plants requires regulation of cell wall biochemistry. *Current Opinion in Cell Biology*, 44, 28–35.
- Clément, R., Blanc, P., Mauroy, B., Sapin, V., & Douady, S. (2012). Shape self-regulation in early lung morphogenesis. *PLoS One*, 7(5), e36925.
- Cosgrove, D. J. (1987). Wall relaxation and the driving forces for cell expansive growth. *Plant physiology*, 84(3), 561–564.
- Cosgrove, D. J. (2005). Growth of the plant cell wall. *Nature reviews. Molecular cell biology*, 6(11), 850.
- Cosgrove, D. J. (2015). Plant cell wall extensibility: connecting plant cell growth with cell wall structure, mechanics, and the action of wall-modifying enzymes. *Journal of experimental botany*, 67(2), 463–476.
- Couturier, E. (2009). *Plis et formes des feuilles*. PhD thesis, Université Paris Diderot.
- Darwin, C. & Darwin, F. (1880). *The power of movement in plants*. John Murray, London.
- de Candolle, A. P. (1832). *Physiologie végétale, ou, Exposition des forces et des fonctions vitales des végétaux : pour servir de suite à l'organographie végétale, et d'introduction à la botanique géographique et agricole*. Béchet Jeune, Paris.
- Dornbusch, T., Michaud, O., Xenarios, I., & Fankhauser, C. (2014). Differentially Phased Leaf Growth and Movements in Arabidopsis Depend on Coordinated Circadian and Light Regulation. *The Plant Cell*, 26(10), 3911–3921.
- Dumais, J. & Forterre, Y. (2012). “Vegetable Dynamicks”: The Role of Water in Plant Movements. *Annual Review of Fluid Mechanics*, 44(1), 453–478.
- Durand-Smet, P., Chastrette, N., Guiroy, A., Richert, A., Berne-Dedieu, A., Szecsi, J., Boudaoud, A., Frachisse, J.-M., Bendahmane, M., Hamant, O., et al. (2014). A comparative mechanical analysis of plant and animal cells reveals convergence across kingdoms. *Biophysical journal*, 107(10), 2237–2244.

- Endo, Y., Sakamoto, J., Kashiwano, Y., Yokota, H., Nakamura, S., & Kinoshita, E. (2010). A biomechanical study on burst mechanisms of plant fruit: stress analysis of pericarps before bursting. *Journal of the mechanical behavior of biomedical materials*, 3(7), 512–519.
- Erickson, R. O. & Sax, K. B. (1956). Elemental growth rate of the primary root of *zea mays*. *Proceedings of the American Philosophical Society*, 100(5), 487–498.
- Feldman, M. (2011). Hilbert transform in vibration analysis. *Mechanical systems and signal processing*, 25(3), 735–802.
- Feynman, R. P., Leighton, R. B., & Sands, M. L. (1964). *The Feynman Lectures on Physics: electromagnetism and matter*, volume 2. Redwood City, California: Addison Wesley Publishing Company.
- Firn, R. & Myers, A. (1989). Plant movements caused by differential growth—Unity or diversity of mechanisms? *Environmental and Experimental Botany*, 29(1), 47–55.
- Forterre, Y. (2013). Slow, fast and furious: understanding the physics of plant movements. *Journal of Experimental Botany*, 64(15), 4745–4760.
- Forterre, Y., Skotheim, J. M., Dumais, J., & Mahadevan, L. (2005). How the venus flytrap snaps. *Nature*, 433(7024), 421.
- Franssen, J., Cooke, S., Digby, J., & Firn, R. (1981). Measurements of Differential Growth Causing Phototropic Curvature of Coleoptiles and Hypocotyls. *Zeitschrift für Pflanzenphysiologie*, 103(3), 207–216.
- Fukaki, H., Fujisawa, H., & Tasaka, M. (1996). Gravitropic response of inflorescence stems in *Arabidopsis thaliana*. *Plant Physiology*, 110(3), 933–943.
- Galvão, V. C. & Fankhauser, C. (2015). Sensing the light environment in plants: photoreceptors and early signaling steps. *Current opinion in neurobiology*, 34, 46–53.
- Geitmann, A. & Ortega, J. K. (2009). Mechanics and modeling of plant cell growth. *Trends in Plant Science*, 14(9), 467–478.
- Heathcote, D. G. (1966). A New Type of Rhythmic Plant Movement: Micronutation. *Journal of Experimental Botany*, 17(4), 690–695.
- Isnard, S. & Silk, W. K. (2009). Moving with climbing plants from Charles Darwin's time into the 21st century. *American Journal of Botany*, 96(7), 1205–1221.

- Kierzkowski, D., Nakayama, N., Routier-Kierzkowska, A.-L., Weber, A., Bayer, E., Schorderet, M., Reinhardt, D., Kuhlemeier, C., & Smith, R. S. (2012). Elastic domains regulate growth and organogenesis in the plant shoot apical meristem. *Science*, 335(6072), 1096–1099.
- Lin, D. C., Dimitriadis, E. K., & Horkay, F. (2007). Robust strategies for automated AFM force curve analysis—I. Non-adhesive indentation of soft, inhomogeneous materials. *Journal of biomechanical engineering*, 129(3), 430–440.
- Lion, C., Simon, C., Huss, B., Blervacq, A.-S., Tirot, L., Toybou, D., Spriet, C., Slo-mianny, C., Guerardel, Y., Hawkins, S., & Biot, C. (2017). BLISS: A Bioorthogonal Dual-Labeling Strategy to Unravel Lignification Dynamics in Plants. *Cell Chemical Biology*, 24(3), 326–338.
- Litz, R. & Griffis, J. (1989). Carambola (*averrhoa carambola* l.). In *Trees II* (pp. 59–67). Springer.
- Llorens, C., Argentina, M., Rojas, N., Westbrook, J., Dumais, J., & Noblin, X. (2016). The fern cavitation catapult: mechanism and design principles. *Journal of The Royal Society Interface*, 13(114), 20150930.
- Lockhart, J. A. (1965). An Analysis of Irreversible Plant Cell Elongation. *Journal of Theoretical Biology*, 8, 264–275.
- Manda, H., Vyas, K., Pandya, A., & Singhal, G. (2012). A complete review on: *Averrhoa carambola*. *World Journal of Pharmacy and Pharmaceutical Sciences*, 1(1), 17–33.
- Marder, M. (2015). The place of plants: Spatiality, movement, growth. *Performance Philosophy*, 1(1), 185–194.
- McClung, C. R. (2006). Plant circadian rhythms. *The Plant Cell*, 18(4), 792–803.
- Milani, P., Braybrook, S. A., & Boudaoud, A. (2013). Shrinking the hammer: micromechanical approaches to morphogenesis. *Journal of Experimental Botany*, 64(15), 4651–4662.
- Millet, B., Melin, D., & Badot, P.-M. (1988). Circumnutation in *Phaseolus vulgaris*. i. growth, osmotic potential and cell ultrastructure in the free-moving part of the shoot. *Physiologia Plantarum*, 72(1), 133–138.
- Millet, B., Melin, D., Bonnet, B., Ibrahim, C. A., & Mercier, J. (1984). Rhythmic circumnutation movement of the shoots in *Phaseolus vulgaris* L. *Chronobiology international*, 1(1), 11–19.

- Moulia, B., Coutand, C., & Julien, J.-L. (2015). Mechanosensitive control of plant growth: bearing the load, sensing, transducing, and responding. *Frontiers in Plant Science*, 6.
- Moulia, B., Coutand, C., & Lenne, C. (2006). Posture control and skeletal mechanical acclimation in terrestrial plants: implications for mechanical modeling of plant architecture. *American Journal of Botany*, 93(10), 1477–1489.
- Moulia, B., Fournier, M., & Guitard, D. (1994). Mechanics and form of the maize leaf: in vivo qualification of flexural behaviour. *Journal of Materials Science*, 29(9), 2359–2366.
- Mugnai, S., Azzarello, E., Masi, E., Pandolfi, C., & Mancuso, S. (2007). Nutation in plants. In *Rhythms in Plants* (pp. 77–90). Springer.
- Ortega, J. K. (1985). Augmented growth equation for cell wall expansion. *Plant physiology*, 79(1), 318–320.
- Palin, R. & Geitmann, A. (2012). The role of pectin in plant morphogenesis. *Biosystems*, 109(3), 397–402.
- Parre, E. & Geitmann, A. (2005). Pectin and the role of the physical properties of the cell wall in pollen tube growth of solanum chacoense. *Planta*, 220(4), 582–592.
- Patil, A., Koli, S., Patil, D., & Phatak, A. (2012). A comprehensive review of an important medicinal plant — averrhoa carambola l. *Pharmacognosy Communications*, 2(2).
- Peacock, K. & Berg, A. (1994). Effect of mechanical stress on sunflower (helianthus annuus l.) hypocotyl growth. *Annals of Botany*, 74(6), 661–666.
- Peaucelle, A. (2014). Afm-based mapping of the elastic properties of cell walls: At tissue, cellular, and subcellular resolutions. *Journal of visualized experiments: JoVE*, (89).
- Peaucelle, A., Braybrook, S., & Höfte, H. (2012). Cell wall mechanics and growth control in plants: the role of pectins revisited. *Frontiers in Plant Science*, 3.
- Peaucelle, A., Braybrook, S. A., Le Guillou, L., Bron, E., Kuhlemeier, C., & Höfte, H. (2011). Pectin-Induced Changes in Cell Wall Mechanics Underlie Organ Initiation in Arabidopsis. *Current Biology*, 21(20), 1720–1726.
- Peaucelle, A., Louvet, R., Johansen, J. N., Höfte, H., Laufs, P., Pelloux, J., & Mouille, G. (2008). Arabidopsis Phyllotaxis Is Controlled by the Methyl-Esterification Status of Cell-Wall Pectins. *Current Biology*, 18(24), 1943–1948.

- Peaucelle, A., Wightman, R., & Höfte, H. (2015). The Control of Growth Symmetry Breaking in the Arabidopsis Hypocotyl. *Current Biology*, 25(13), 1746–1752.
- Peters, W. S. & Tomos, A. D. (2000). The mechanic state of “inner tissue” in the growing zone of sunflower hypocotyls and the regulation of its growth rate following excision. *Plant Physiology*, 123(2), 605–612.
- Pouliquen, O., Forterre, Y., Bérut, A., Chauvet, H., Bizet, F., Legué, V., & Moulia, B. (2017). A new scenario for gravity detection in plants: the position sensor hypothesis. *Physical Biology*, 14(3), 035005.
- Proseus, T. E., Ortega, J. K., & Boyer, J. S. (1999). Separating growth from elastic deformation during cell enlargement. *Plant Physiology*, 119(2), 775–784.
- Quattrocchi, U. (1999). *CRC World dictionary of plant names: Common names, scientific names, eponyms, synonyms, and etymology*. CRC Press.
- Reyssat, E. & Mahadevan, L. (2009). Hygromorphs: from pine cones to biomimetic bilayers. *Journal of the Royal Society Interface*, 6(39), 951–957.
- Rivière, M., Derr, J., & Douady, S. (2017). Motions of leaves and stems, from growth to potential use. *Physical Biology*, 14(5), 051001.
- Ruggeberg, M., Speck, T., Paris, O., Lapierre, C., Pollet, B., Koch, G., & Burgert, I. (2008). Stiffness gradients in vascular bundles of the palm *Washingtonia robusta*. *Proceedings of the Royal Society B: Biological Sciences*, 275(1648), 2221–2229.
- Sadeghi, A., Mondini, A., Del Dottore, E., Mattoli, V., Beccai, L., Taccola, S., Lucarotti, C., Totaro, M., & Mazzolai, B. (2016). A plant-inspired robot with soft differential bending capabilities. *Bioinspiration & biomimetics*, 12(1), 015001.
- Saghir, S. A. M., Sadikun, A., Khaw, K.-Y., & Murugaiyah, V. (2013). Star fruit (*averrhoa carambola* l.): From traditional uses to pharmacological activities. *Boletín Latinoamericano y del Caribe de Plantas Medicinales y Aromáticas*, 12(3).
- Schleicher, S., Lienhard, J., Poppinga, S., Speck, T., & Knippers, J. (2015). A methodology for transferring principles of plant movements to elastic systems in architecture. *Computer-Aided Design*, 60, 105–117.
- Schopfer, P. (2006). Biomechanics of plant growth. *American journal of botany*, 93(10), 1415–1425.
- Schuster, J. & Engelmann, W. (1997). Circumnutations of *Arabidopsis thaliana* Seedlings. *Biological Rhythm Research*, 28(4), 422–440.

- Sharrock, R. (1660). *The history of the propagation & improvement of vegetables by the concurrence of art and nature*. A. Lichfield for T. Robinson, Oxford.
- Silk, W. K. (1992). Steady Form from Changing Cells. *International Journal of Plant Sciences*, 153(3, Part 2), S49–S58.
- Silk, W. K. & Beusmans, J. M. H. (1988). Mechanical Properties within the Growth Zone of Corn Roots Investigated by Bending Experiments. I. Preliminary Observations. *American Journal of Botany*, 75(7), 990.
- Silk, W. K. & Erickson, R. O. (1978). Kinematics of Hypocotyl Curvature. *American Journal of Botany*, 65(3), 310.
- Silk, W. K. & Erickson, R. O. (1979). Kinematics of Plant Growth. *Journal of Theoretical Biology*, 76(4), 481–501.
- Silk, W. K., Hsiao, T. C., Diederhufen, U., & Matson, C. (1986). Spatial distributions of potassium, solutes, and their deposition rates in the growth zone of the primary corn root. *Plant Physiology*, 82(3), 853–858.
- Silk, W. K., Lord, E. M., & Eckard, K. J. (1989). Growth patterns inferred from anatomical records empirical tests using longisections of roots of zea mays l. *Plant Physiology*, 90(2), 708–713.
- Skotheim, J. M. & Mahadevan, L. (2005). Physical Limits and Design Principles for Plant and Fungal Movements. *Science*, 308(5726), 1308–1310.
- Somers, D. E. (1999). The physiology and molecular bases of the plant circadian clock. *Plant Physiology*, 121(1), 9–20.
- Someya, N., Niinuma, K., Kimura, M., Yamaguchi, I., & Hamamoto, H. (2006). Circumnutation of arabidopsis thaliana inflorescence stems. *Biologia plantarum*, 50(2), 287–290.
- Speck, T. & Burgert, I. (2011). Plant Stems: Functional Design and Mechanics. *Annual Review of Materials Research*, 41(1), 169–193.
- Stolarz, M. (2009). Circumnutation as a visible plant action and reaction: Physiological, cellular and molecular basis for circumnutations. *Plant Signaling & Behavior*, 4(5), 380–387.
- Stolarz, M., Krol, E., Dziubinska, H., & Zawadzki, T. (2008). Complex relationship between growth and circumnutations in *Helianthus annuus* stem. *Plant Signaling & Behavior*, 3(6), 376–380.

- Tamiya, T., Miyazaki, T., Ishikawa, H., Iriguchi, N., Maki, T., Matsumoto, J. J., & Tsuchiya, T. (1988). Movement of water in conjunction with plant movement visualized by nmr imaging. *The Journal of Biochemistry*, 104(1), 5–8.
- Theophrastus (1916). *Enquiry into plants*. Harvard University Press.
- Thimann, K. V. & Schneider, C. L. (1938). Differential Growth in Plant Tissues. *American Journal of Botany*, 25(8), 627.
- Tomos, A. D., Malone, M., & Pritchard, J. (1989). The biophysics of differential growth. *Environmental and Experimental Botany*, 29(1), 7–23.
- Ulrich, E. (1911). Leaf movements in the family oxalidaceae. In *Contributions from the Botanical Laboratory of the University of Pennsylvania* (pp. 212–242). University of Pennsylvania.
- Vanden Driessche, T. (2000). Nutations in Shoots and in Desmodium Lateral Leaflets, Nyctinastism and Seismonastism in Mimosa pudica. Comparison and Evolution of Morphology and Mechanism. *Biological Rhythm Research*, 31(4), 451–468.
- Vincent, O., Roditchev, I., & Marmottant, P. (2011). Spontaneous firings of carnivorous aquatic utricularia traps: temporal patterns and mechanical oscillations. *PLoS One*, 6(5), e20205.
- Walter, A., Spies, H., Terjung, S., Küsters, R., Kirchgeßner, N., & Schurr, U. (2002). Spatio-temporal dynamics of expansion growth in roots: automatic quantification of diurnal course and temperature response by digital image sequence processing. *Journal of experimental botany*, 53(369), 689–698.
- Webster, C. (1966). The recognition of plant sensitivity by English botanists in the seventeenth century. *Isis*, 57(1), 5–23.
- Went, F. W. (1926). On growth-accelerating substances in the coleoptile of *Avena sativa*. In *Proc. Kon. Ned. Akad. Wet.*, volume 30 (pp.1).
- Whippo, C. W. & Hangarter, R. P. (2006). Phototropism: bending towards enlightenment. *The Plant Cell*, 18(5), 1110–1119.
- Whippo, C. W. & Hangarter, R. P. (2009). The "sensational" power of movement in plants: A Darwinian system for studying the evolution of behavior. *American Journal of Botany*, 96(12), 2115–2127.

- Zamil, M. S. & Geitmann, A. (2017). The middle lamella—more than a glue. *Physical Biology*, 14(1), 015004.
- Zerzour, R., Kroeger, J., & Geitmann, A. (2009). Polar growth in pollen tubes is associated with spatially confined dynamic changes in cell mechanical properties. *Developmental biology*, 334(2), 437–446.
- Zhang, Q., Cheetamun, R., Dhugga, K. S., Rafalski, J. A., Tingey, S. V., Shirley, N. J., Taylor, J., Hayes, K., Beatty, M., Bacic, A., et al. (2014). Spatial gradients in cell wall composition and transcriptional profiles along elongating maize internodes. *BMC plant biology*, 14(1), 27.

Image credit

Figure 1.1a, page 2

Drawings by P. H. W. Taubert from *Leguminosae* (1891)

Public domain

Figure 1.2, page 3

Illustration by J. W. Buel from *Sea and Land* (1887)

Public domain

Figure 1.7, page 11

Illustration by LadyofHats from Wikicommons Media

https://commons.wikimedia.org/wiki/File:Plant_cell_structure-en.svg

Public domain

Minor modifications: Some details of the original image have been withdrawn for simplicity. An emphasis has been put on identifying structures specific to plants.

Figure 1.9, page 14

Figure adapted from (Cosgrove, 2005)

Illustration material by LadyofHats from Wikicommons Media

Public domain

https://commons.wikimedia.org/wiki/File:Turgor_pressure_on_plant_cells_diagram-es.svg

Figure 2.1a, page 25

Forestowlet ([https://commons.wikimedia.org/wiki/File:Averrhoa_carambola\(Star_fruit\)_06.JPG](https://commons.wikimedia.org/wiki/File:Averrhoa_carambola(Star_fruit)_06.JPG)), <https://creativecommons.org/licenses/by-sa/4.0/legalcode>

Figure 2.1b, page 25

Tau'olunga (https://commons.wikimedia.org/wiki/File:Averrhoa_carambola_flowers.jpg), 'Averrhoa carambola flowers', <https://creativecommons.org/licenses/by-sa/3.0/legalcode>

Figure 2.1c, page 25

SMasters (https://commons.wikimedia.org/wiki/File:Carambola_Starfruit.jpg), 'Carambola Starfruit', <https://creativecommons.org/licenses/by-sa/3.0/legalcode>

Appendices

Appendix A

Graviception, proprioception and hook shape

Contents

A.1 The graviproprioceptive model	175
A.1.1 Origin of the model	176
A.1.2 A suitable model for <i>Averrhoa carambola</i> ?	177
A.2 Adaptation of the model	177
A.2.1 Definition of the model	177
A.2.2 Growth-dependent parameters	178
A.3 Results	179

Thanks to careful observations, one is often able to bring out a couple of important contributions in a phenomenon. Building a consistent model based on these few contributions allows to check if they are sufficient to explain the observed phenomenon in the first place. Here we tried to understand if graviception and proprioception were enough to describe the unfurling of *Averrhoa carambola* leaves.

A.1 The graviproprioceptive model

Here I propose an insight on a specific model called the graviproprioceptive model—or the AC model—and discuss its relevance in the specific case of *Averrhoa carambola*.

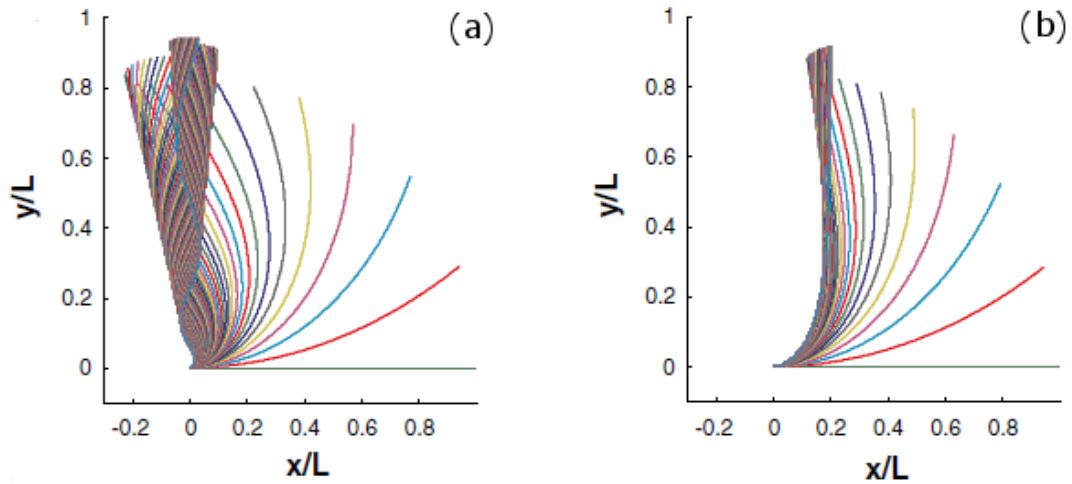


Figure A.1: Results of simulation for the gravitropic response of a tilted stem. (a) Without the proprioceptive term (A model), the stem oscillates and is unable to converge to a stationary shape. (b) The addition of the proprioceptive term (AC model) makes the stem converge to a stationary vertical shape. Figures from (Bastien et al., 2013).

A.1.1 Origin of the model

The graviproprioceptive model was introduced by Bastien and coworkers (Bastien et al., 2013, 2014) as an attempt to grasp the behaviour of plants undergoing gravitropism. Their approach lies on a geometrical analysis of the development of plants and on an analysis of the symmetries of the problem. They argue that, on a geometrical point of view, if we neglect the variations of radius along the plant organ (stem, rachis, central rib, etc.) we can simplify the problem to a flexible rod problem. The main modification induced by gravitropism is a modification of the curvature along the organ. Since it is done without torsion, the local orientation and curvature are sufficient to describe the geometry of the organ. Hence,

$$\partial_t C(s, t) = \phi(A, C) \quad (\text{A.1})$$

(where s is the arc length along the plant organ and t is the time, A the local angle of the stem with respect to the up vertical and C is the local curvature defined as $\frac{dA}{ds}$). Considering that we are here interested in a plant organ trying to recover an alignment with the vertical, the straight and vertical state ($A = 0, C = 0$) must be a stable solution of the previous equation. The system must satisfy $A \rightarrow -A$ and $C \rightarrow -C$ symmetries together. Thus, only the odd terms remain in the development around the stable solution. At first order, we end up with the following equation :

$$\partial_t C(s, t) = \beta A(s, t) + \gamma C(s, t) \quad (\text{A.2})$$

The βA term corresponds to the graviceptive term. If the angle is positive, it must imply a diminution of the curvature in order to have $A \rightarrow 0$ and the plant to become vertical again. Similarly, the term γC corresponds to a proprioceptive term. If C becomes too negative, it must imply a counter-balancing in order to have the plant organ straight in the end. Thus, Bastien and coworkers finally propose the graviproprioceptive model :

$$\partial_t C(s, t) = -\beta A(s, t) - \gamma C(s, t) \quad (\text{A.3})$$

where β and γ are positive constants. One other feature of this model is that growth does not appear in a first time. However, the authors assume that growth (and processes leading to the curvature of the organ) can only occur in a confined region – the growth zone – represented by the length L_{gz} . Growth is then added and convergence of the shape can only be reached under certain conditions I am not going to discuss here.

A.1.2 A suitable model for *Averrhoa carambola* ?

Since we want to explain the relation between morphogenetic motions and posture regulation in the case of *Averrhoa carambola* leaves, the previously described model appears to be promising. The unrollment of the rachis in a plane associated with the stabilization of the leaf at a well-regulated gravity set angle is *a priori* likely to be linked to gravitropism. The same idea applies to nutation motions out of the plane containing the rachis but it is of course not possible to simulate nutation with such a 2D model. Nevertheless, the development of *Averrhoa carambola* leaves look to be strongly influenced by gravitropism and autotropism. Previous results in the lab have highlighted that *Averrhoa carambola* possesses a growth zone situated at a fixed distance of the apex of the rachis. This zone matches with the curved zone of the rachis.

For all these reasons, we have chosen to use this model in order to try to simulate the rich dynamics of the leaves development. However, we propose in the following section some modifications to adapt it to our specific case.

A.2 Adaptation of the model

A.2.1 Definition of the model

The problem of the growth of the leaves is slightly different than the previous problem. Here we want the extremity of the rachis to be aligned with the downward

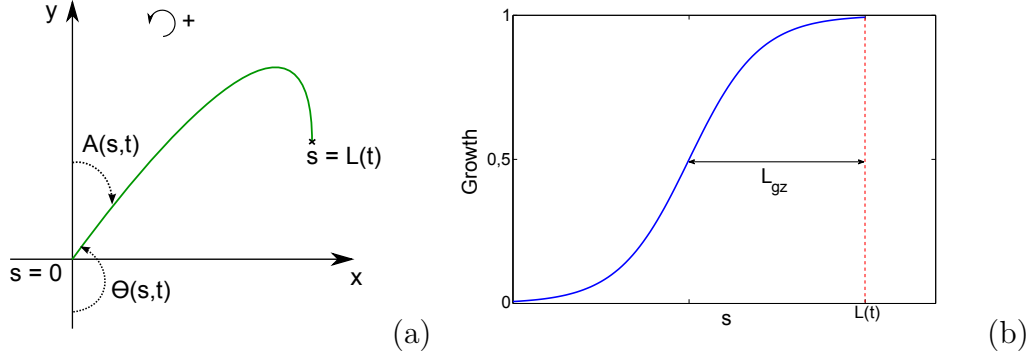


Figure A.2: (a) Parametrization of our problem. The angles are counted positive anti-clockwise, s is the arc length starting at the basis of the rachis. The origin is set to the basis of the rachis. (b) Example of growth distribution along the rachis ($\dot{\varepsilon}_0 = 1$ here)

vertical. Then it is more convenient to use θ than A as we will have $\theta \rightarrow 0$ at the extremity of the rachis (see figure A.2). Moreover, we have to inverse the effect of the gravitropism. The arc length s is now defined along the rachis of the leaf. The origin is set at the basis of the rachis and the position of the rachis is denoted by $L(t)$.

The change of orientation of the angles has no consequences on eq. A.3 because of the symmetries of the model. Now, considering θ and $C = \frac{d\theta}{ds}$ combined with a reversed gravitropism, we end up with :

$$\partial_t C(s, t) = -\beta\theta(s, t) - \gamma C(s, t) \quad (\text{A.4})$$

We also included growth in the model in agreement with our experimental observations (apical growth). We chose the following function :

$$\dot{\varepsilon}(s, t) = \frac{\dot{\varepsilon}_0}{2} \left(\tanh \left(\frac{L(t) - L_{gz} - s}{L_d} \right) + 1 \right) \quad (\text{A.5})$$

where $\dot{\varepsilon}$ is the elongation rate, $\dot{\varepsilon}_0$ its amplitude, L_{gz} is the length of the growth-zone and L_d is a characteristic length determining the length over which growth decays. The idea that motivated this choice is that we wanted a smooth function sharing characteristics with the step function used by Bastien and coworkers.

A.2.2 Growth-dependent parameters

The second modification that we made to the graviproprioceptive model is that we introduced a dependence on growth for the parameter β . Bastien and coworkers

assumed that gravitropic response can only occur where there is growth, so, as previously, we propose a smooth step-like function for the $\dot{\epsilon}$ -dependence of β . Because of the observations of Y. Corre we want the curvature zone and the growth zone to match, so we propose :

$$\beta(s, t) = \frac{\beta_0}{2} \left(\tanh \left(\frac{L(t) - L_{gz} - s}{L_d} \right) + 1 \right) \quad (\text{A.6})$$

where β_0 is the amplitude of the gravitropic term. The proprioceptive term was not modified in our model in a first time. However, a growth-dependence could be introduced for γ too. It has been noticed that curvature of the leaves is only subject to little changes under high elongation rate conditions. We could think of a smoothed step function, decreasing when elongation rate increases and converging to a non-zero minimum value for example.

A.3 Results

This model was implemented in Matlab thanks to a basic Newton algorithm. As a matter of fact, our goal is not to perform a very precise simulation but to check if the modified graviproprioceptive model is able to reproduce approximately the evolution of the shape of the leaves.

As shown on the different pictures, the model produces shapes that look like *Averrhoa carambola*. The choice of the parameters is of course arbitrary and I have tuned them in a lot of combinations. One parameter seems to be more important than the others in the similarity of the shapes, that is the length of the growth zone. If the growth zone is not sufficiently long, it results in a weak curvature of the hook and the extremity of the leaf cannot be vertical.

The absence of proprioceptive term leads to aberrant shapes, as in the case of *Arabidopsis thaliana*. This suggests that proprioception is essential in the posture regulation of *Averrhoa carambola* too.

This model gives promising results and confirms that proprioception and graviception are fundamental to explain the unfurling motion and the posture regulation of the leaves of *Averrhoa carambola* during its development.

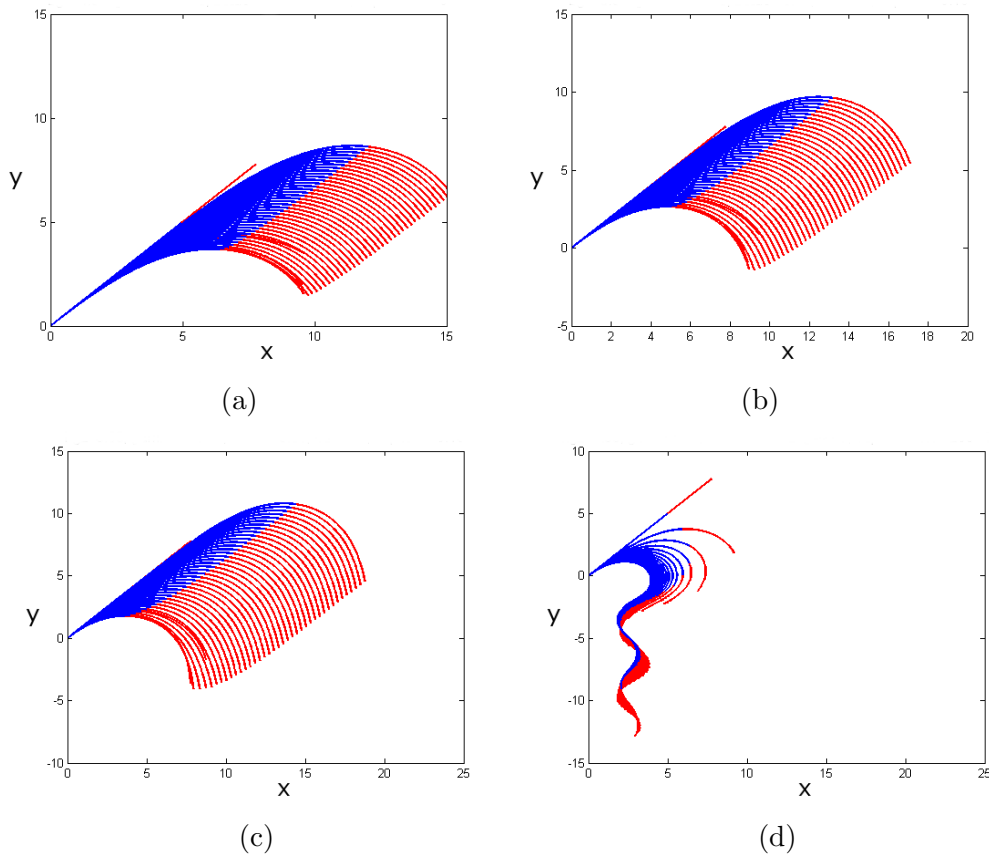


Figure A.3: Results of my simulations. The three first graphs are with increasing L_{gz} and show the importance of the length of the growth zone (represented in red). A long growth zone is required for good agreement with the shape of the leaves. Last graph shows that proprioception is fundamental in posture regulation on the leaves.

Appendix B

Mechanics of the rachis: additional insights

Contents

B.1 Viscous deformation of the rachis	181
B.2 Useful calculations	181

B.1 Viscous deformation of the rachis

The experiment presented in the second section of Chapter 3, we have flipped the rachis upside-down at several moments of its development to assess the role of its self-weight on its shape. For each experiment, we have also let the rachis in this upside-down position for 30 min (see figure B.1).

We have thus observed that deformations amplified after 30 min, under the self-weight of the leaf and leaflets. This is the signature of the viscous properties of the rachis at the macroscopical scale. We have limited our study to the elastic deformations of the rachis (or at least to the deformations underwent in a short period of time). However, the extent of the viscous deformation of the rachis invites to further investigation, as the normally observed shape should partly result from the viscous properties of the rachis also.

B.2 Useful calculations

In this appendix, I propose to completely derive the beam theory properties used to compute the mechanical properties of the rachis at the macroscopic scale. Let us

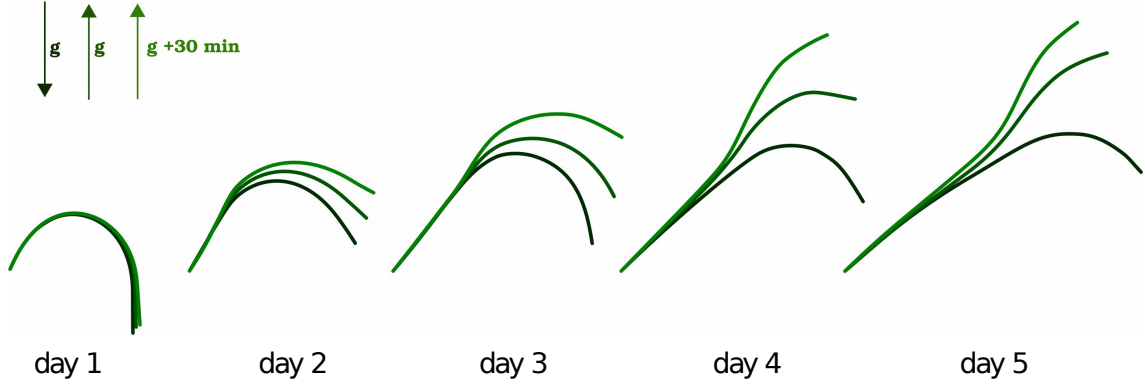


Figure B.1: Viscous deformation of the rachis. For each day of experiment, three conformations are overlaid. In dark green, the initial conformation of the rachis. In medium green, the rachis when it reaches the upside-down position (elsatic deformation). In light green, the rachis after 30 min in the flipped position. We see that deformations amplify after 30 min.

consider the situation depicted in the following figure and the associated conventions.

Consider a random force F with linear origin:

$$\vec{F}(s) = F_x(s)\vec{e}_x + F_z(s)\vec{e}_z = \int_0^s f_x(s')ds'\vec{e}_x + \int_0^s f_z(s')ds'\vec{e}_z$$

Note that the vectors of the cartesian basis can be expressed in terms of \vec{n} and \vec{t} from the Frenet basis:

$$\forall s, \begin{cases} \vec{e}_x = -\cos(\theta)\vec{n} + \sin(\theta)\vec{t} \\ \vec{e}_z = \sin(\theta)\vec{n} + \cos(\theta)\vec{t} \end{cases}$$

We can now determine N and T in the general case, the normal and the tangential forces respectively:

$$\vec{F}(s) = [-F_x(s)\cos\theta(s) + F_z(s)\sin\theta(s)]\vec{n}(s) + [F_x(s)\sin\theta(s) + F_z(s)\cos\theta(s)]\vec{t}(s)$$

$$\begin{cases} N(s) = -F_x(s)\cos\theta(s) + F_z(s)\sin\theta(s) \\ T(s) = F_x(s)\sin\theta(s) + F_z(s)\cos\theta(s) \end{cases}$$

Let us express the momentum Γ exerted on the left side of the beam by the right

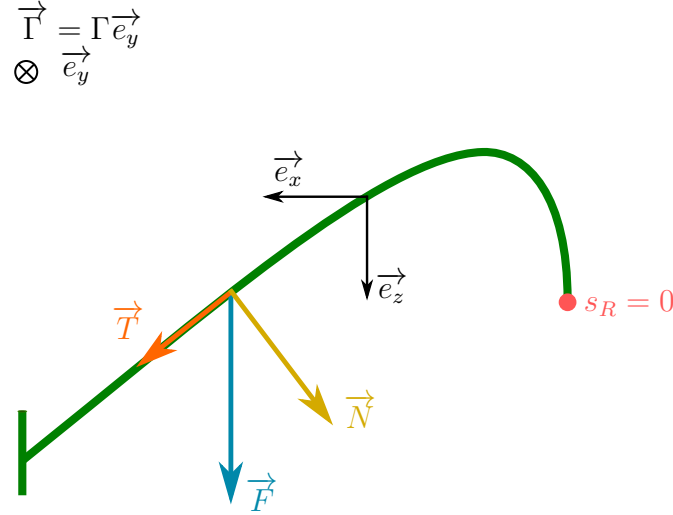


Figure B.2: **Parametrization of our mechanics problem.** We define a global right handed Cartesian coordinate system $(\vec{e}_x, \vec{e}_y, \vec{e}_z)$. Consider an arbitrary force \vec{F} applied on the rachis at $s_R = s$. \vec{F} can be decomposed into two components, relative to the local geometry of the rachis: a tangential component \vec{T} and a normal component \vec{N} . The sign convention for an arbitrary torque Γ is indicated.

side of the beam at each point s :

$$\begin{aligned}\vec{\Gamma}(s) &= \int_0^s \overrightarrow{MM'}(s') \wedge d\vec{F}(s') \\ &= \int_0^s \begin{pmatrix} x(s') - x(s) \\ 0 \\ z(s') - z(s) \end{pmatrix} \wedge \begin{pmatrix} f_x(s') \\ 0 \\ f_z(s') \end{pmatrix} ds' \\ \Rightarrow \Gamma(s) &= \int_0^s [(z(s') - z(s))f_x(s') - (x(s') - x(s))f_z(s')] ds'\end{aligned}$$

Let us differentiate Γ with respect to s :

$$\begin{aligned}\frac{d\Gamma}{ds}(s) &= \int_0^s f_x(s') ds' \left(-\frac{dz}{ds}(s) \right) - \int_0^s f_z(s') ds' \left(-\frac{dx}{ds}(s) \right) \\ &= -F_x(s) \cos\theta(s) + F_z(s) \sin\theta(s) \\ &= N(s)\end{aligned}$$

This relation is very useful in our case. It allows one to compute the momentum exerted by the self-weight on the rachis by integrating its normal component over s . In our specific case, the force F will reduce to the weight P (which is colinear to \vec{e}_z). Assuming that the rachis is a cylinder, we can write down P in terms of the volumic mass of the rachis ρ , the gravitational acceleration g and the cross section

area A :

$$\vec{P}(s) = P(s)\vec{e}_z = \int_0^s \rho g A(s') ds' \vec{e}_z$$

$$\Gamma'(s) = N(s) = P(s) \sin\theta(s)$$

Moreover, in the general case we can write:

$$\begin{cases} \Gamma_+(s) = B(s)(C_+(s) - C_0(s)) \\ \Gamma_-(s) = B(s)(C_-(s) - C_0(s)) \end{cases}$$

Which rises:

$$B = \frac{\Gamma_+ - \Gamma_-}{C_+ - C_-}$$

$$C_0 = \frac{1}{2} \left[C_+ + C_- - \frac{\Gamma_+ + \Gamma_-}{B} \right]$$

$$E = \frac{B}{I} = \frac{1}{I} \frac{\Gamma_+ - \Gamma_-}{C_+ - C_-}$$

Finally, in the case of a cylinder we get:

$$E = \frac{B}{I} = \frac{2}{\pi R^4} \frac{\Gamma_+ - \Gamma_-}{C_+ - C_-}$$

Appendix C

Kinematic model of nutation: useful calculations

Contents

C.1 Angular amplitude of the motion	185
C.2 Threshold of contraction	186
C.3 Amplitude of the second harmonic term	187

In this appendix, I propose to detail some useful calculations for the kinematic model of nutation presented in Chapter 5.

C.1 Angular amplitude of the motion

One of the most important features of the nutation motion is of course its angular amplitude. One of the aim of our model is to infer the growth laws of the observed rachis thanks to simple measurements. The measurement of $\Delta\phi$ is among them. Most of the time, we thus want to perform simulations at a fixed $\Delta\phi$. This requires to understand the links between $\Delta\phi$ and the other parameters. The angular amplitude of the motion is fixed by the curvature variations on the rachis. Let us then first determine the evolution of curvature for a given motion.

We have seen that—in the case of nutation—the variations of curvature are directly linked to the differential elongation of the tissues by

$$\dot{\kappa} \simeq \frac{1 - R^2 \kappa^2}{R} \dot{\delta}$$

In the case of the observed motions, it seems reasonable to state that $R \ll 1/\kappa$. For example, in the case of the experiment detailed in Chapter 4, we have $R = 0.6 \text{ mm}$ and $1/\kappa \simeq 3 \text{ cm}$. In a first approximation, and by neglecting the time dependence of s_0 , we thus have

$$\begin{aligned}\dot{\kappa} &\simeq \frac{\dot{\delta}_0}{R} \left(1 - \tanh^2 \left(\frac{s - s_0}{\Delta L} \right) \right) \sin \omega t \\ \text{so, } \kappa &\simeq -\frac{\dot{\delta}_0}{R\omega} \left(1 - \tanh^2 \left(\frac{s - s_0}{\Delta L} \right) \right) \cos \omega t\end{aligned}$$

The local orientation of the rachis is then obtained by spatially integrating κ , and by fixing the orientation of the base at $\phi(s=0) = 0$.

$$\begin{aligned}\phi &= -\frac{\dot{\delta}_0}{R\omega} \int \left(1 - \tanh^2 \left(\frac{s - s_0}{\Delta L} \right) \right) ds \cdot \cos \omega t \\ &= -\frac{\dot{\delta}_0 \Delta L}{R\omega} \left[\tanh \left(\frac{s - s_0}{\Delta L} \right) + \tanh \left(\frac{s_0}{\Delta L} \right) \right] \cos \omega t\end{aligned}$$

Finally, the angular amplitude of the motion is measured at the apex, *i.e.* $s = L_{tot}$. Granted that $L_{tot} - L_{gz} \gg \Delta L$ and $L_{gz} \gg \Delta L$ we have

$$\Delta\phi = \frac{2\Delta L \dot{\delta}_0}{R\omega}$$

C.2 Threshold of contraction

Depending on the growth parameters— $\dot{\varepsilon}_0$ and $\dot{\delta}_0$ —local contractions can either be allowed or forbidden. Let us now determine the value of the threshold of contraction. The total growth of a lateral face of the rachis is given by

$$\dot{\varepsilon}_{tot} = \dot{\varepsilon} \pm \dot{\delta}$$

depending on the considered side. The threshold of contraction is then simply given by

$$\begin{aligned} \forall(s, t), \dot{\varepsilon}_{tot} &\geq 0 \\ \forall(s, t), \dot{\varepsilon} \pm \dot{\delta} &\geq 0 \\ \forall(s, t), \frac{\dot{\varepsilon}_0}{2} \left(1 + \tanh \left(\frac{s - s_0}{\Delta L} \right) \right) \pm \dot{\delta}_0 \left(1 - \tanh^2 \left(\frac{s - s_0}{\Delta L} \right) \right) \sin \omega t &\geq 0 \end{aligned}$$

Considering that $\dot{\varepsilon}_0$ and $\dot{\delta}_0$ are both definite positive, it is thus sufficient to have

$$\begin{aligned} \forall s, \frac{\dot{\varepsilon}_0}{2} \left(1 + \tanh \left(\frac{s - s_0}{\Delta L} \right) \right) - \dot{\delta}_0 \left(1 - \tanh^2 \left(\frac{s - s_0}{\Delta L} \right) \right) &\geq 0 \\ \forall s, \frac{\dot{\varepsilon}_0}{2} - \dot{\delta}_0 \left(1 - \tanh \left(\frac{s - s_0}{\Delta L} \right) \right) &\geq 0 \end{aligned}$$

Since $0 \leq 1 - \tanh \left(\frac{s - s_0}{\Delta L} \right) \leq 2$, it is then sufficient to have

$$\dot{\varepsilon}_0 \geq 4\dot{\delta}_0$$

We can finally define two equivalent thresholds of contraction, in $\dot{\varepsilon}_0$ or $\dot{\delta}_0$. These thresholds indeed depend on the spatial distribution of elongation initially chosen.

C.3 Amplitude of the second harmonic term

The total projected elongation of a side of the rachis is given by

$$\dot{\varepsilon}_{\perp}^{tot} = \left(\dot{\varepsilon} \pm \dot{\delta} \right) - \dot{\phi} \tan \phi$$

The expressions of the $\dot{\varepsilon}$ and $\dot{\delta}$ terms are already known, as they define our model. We immediately see that they respectively correspond to a term a null frequency and a term at the fundamental frequency ω . Let us now derive the expression of the geometrical term $\dot{\phi} \tan \phi$ and show that, indeed, it corresponds to the term at frequency 2ω .

We already know from the previous section the expression of ϕ . Its time derivative is simply given by

$$\dot{\phi} = \frac{\dot{\delta}_0 \Delta L}{R} \left[\tanh \left(\frac{s - s_0}{\Delta L} \right) + \tanh \left(\frac{s_0}{\Delta L} \right) \right] \sin \omega t$$

In the case where $\phi \ll 1$, we can approximate $\dot{\phi} \tan \phi$ to $\dot{\phi} \phi$ at the first order in ϕ . The geometrical term of projection then reads

$$\begin{aligned} \phi \dot{\phi} &= - \left(\frac{\dot{\delta}_0 \Delta L}{R \omega} \right)^2 \omega \left[\tanh \left(\frac{s - s_0}{\Delta L} \right) + \tanh \left(\frac{s_0}{\Delta L} \right) \right]^2 \cos \omega t \cdot \sin \omega t \\ &= - \frac{1}{2} \left(\frac{\dot{\delta}_0 \Delta L}{R \omega} \right)^2 \omega \left[\tanh \left(\frac{s - s_0}{\Delta L} \right) + \tanh \left(\frac{s_0}{\Delta L} \right) \right]^2 \sin 2\omega t \end{aligned}$$

So, finally we confirm that the geometrical term of projection is responsible for the observation of the second harmonic (and possibly higher harmonics at higher orders in ϕ). The observation of the fundamental mode in our measurements is thus a signature of the oscillations of elongation rate and of differential elongation.

